UNIVERSITY OF OXFORD
DEPARTMENT OF COMPUTER SCIENCE

A computational framework for understanding the dynamics of signalling pathways

ALI CIGARI
UNIVERSITY COLLEGE, OXFORD





A thesis submitted for
the degree of Doctor of Philosophy.
Trinity 2017

Abstract

Signalling pathways are subcellular networks that enable the cell to respond to its microenvironment. Abnormal function of a signalling pathway is a hallmark of carcinogenesis and developmental diseases. The signalling cascades in these pathways involve biochemical interactions that can lead to highly nonlinear cellular responses. Studies of signalling pathways often involve the proposal of models based on experimental data that are difficult to quantify and reproduce. Due to the nature of the experimental procedures, the experimental results can often be qualitative or at best semi-quantitative. As a result, the data and models proposed in different studies can often appear inconsistent.

The canonical Wnt pathway, overactive in 90% of colorectal cancer cases, is not immune to these problems. A review of the literature reveals many seemingly inconsistent experimental results and models regarding the pathway dynamics. This makes the Wnt pathway a natural candidate for investigation using a new model selection framework using qualitative experimental data.

The steps involved in our model selection framework are as follows. We propose a set of candidate mathematical models that may be consistent with experimental observations. Using a qualitative cost function, we explore the output of these models to investigate whether they can reproduce qualitatively similar outputs to the experimental observations. Any consistent candidate models are analysed further using sensitivity analysis and *in silico* experiments, before new *in vitro* experiments are proposed to discriminate between remaining models.

Our literature review of the Wnt pathway revealed that a major source of discrepancy is the way in which Wnt stimulation leads to the initial accumulation of the Wnt-target β-catenin. Before studying this problem, we introduce a set of candidate models to study the first steps in the Wnt signalling cascade involving the Axin scaffolding protein that degrades β-catenin and the LRP6 co-receptor, which facilitates deactivation of this process. Using our framework, we reduce the number of suitable candidate models from twelve to four and propose new *in vitro* experiments to discriminate between these models further. In a multi-disciplinary study, we carry out these experiments in the laboratory to discriminate between the remaining candidate models.

Our results suggest that Axin can interact with LRP6 independently of Wnt, and that Wnt stimulation leads to Axin-driven LRP6 phosphorylation. We build on our initial candidate models and introduce β-catenin and further details of the pathway in a new set of candidate mathematical models. We compare these models to experimental results from three different studies of the pathway, which have proposed different models for the pathway. We establish that one of our candidate models can qualitatively reproduce the results from all three studies. According to this model, the first steps that lead to accumulation of β-catenin upon Wnt stimulation is sequestration of Axin at the membrane. Beyond the first half hour, dephosphorylation of Axin allows levels of β-catenin to increase further.

The existence of seemingly inconsistent experimental results and models is not unique to the Wnt pathway. Thus we believe that the framework developed in this thesis could be adapted for use in other studies of signalling pathways to understand the underlying networks of individual pathways and their crosstalk.

Acknowledgements

The last four years of my life have been interesting to say the least. I have had one of toughest years of my life, combined with some of the happiest periods I remember, surprisingly, not the least the last few months. I am sad to be finishing my D.Phil. but I do not think I have ever been as excited as I am now about starting the next chapter of my life.

A few thank you's are certainly in order. First of all I would like to thank all my supervisors: Professor Helen Byrne, Dr Joe Pitt-Francis, Professor David Gavaghan, Professor Eric O'Neill, and Dr Alexander Fletcher. I hope they all know how much I have valued their support, both on a personal level and on an academic level.

I would also like to give a big thank you to my sister, Shadi. Words cannot explain what she has done for me over the years, so I will not try to. I would also like to give a big thank you to my parents, Hossein and Sedigheh, who have also supported me every step of the way, specially when I had the crazy idea of quitting a successful career to start a D.Phil.

I would also like to mention all of my lab mates in Oncology. Thank you for the help in the lab and the friendships outside it.

There are also so many friends I would like to thank. I will not name anyone personally, but you know who you are. I am happy to have met you, be it in Cambridge, London, Oxford or further afield. Thank you for being with me, during the good times and the bad.

Finally, I would also like to thank everyone in my life for putting up with me and my hobbies, specially the rowing and the cycling. Doing sports has been such a huge part of my life, and I am grateful for all the support I have received to pursue these pastimes.

Contents

1 Introduction **1**
1.1 Motivation . . . 1
1.2 Research questions . . . 3
1.3 Thesis structure . . . 4

2 Literature review **7**
2.1 Introduction . . . 7
2.1.1 β-catenin . . . 8
2.1.2 The Wnt family of proteins . . . 10
2.1.3 Frizzled family of receptors . . . 11
2.1.4 Arrow/LRP5/LRP6 . . . 12
2.1.5 Dishevelled . . . 13
2.1.6 Axin . . . 14
2.1.6.1 Axin feedback loops . . . 15
2.1.7 APC . . . 15
2.1.8 E-cadherin . . . 16
2.1.9 The role of YAP/TAZ . . . 16
2.1.10 Other agonists and antagonists of the Wnt pathway . . . 17
2.2 Models of the Wnt pathway . . . 17
2.2.1 Verbal models . . . 18
2.2.1.1 Reduced affinity of β-catenin for Axin . . . 20
2.2.1.2 Direct inhibition of GSK3-phosphorylation of β-catenin by LRP6 phosphorylated at PPPSP motifs . . . 21
2.2.1.3 Inhibition of ubiquitination of β-catenin facilitated by APC . . . 21
2.2.1.4 YAP enhances binding of β-TrCP to Axin and β-catenin ubiquitination . . . 22
2.2.1.5 Sequestration of GSK3 inside MVBs . . . 22
2.2.2 Mathematical models . . . 22
2.2.2.1 Compartmentalised models . . . 25
2.3 Overview of experimental data used in models of signalling pathways . 26
2.3.1 Western blot detection . . . 26
2.3.2 Co-immunoprecipitation (co-IP) studies. . . . 27
2.3.3 Reading co-IP/Western blot results . . . 27
2.3.4 Parameter Identifiability . . . 29
2.3.5 Modelling based on population scale experimental results . . . 31
2.4 Summary and what is to come... . . . 31

3 Model selection **33**
3.1 Introduction . . . 33
3.2 Literature Review . . . 34
3.2.1 Classical methods of parameter inference and model selection . . 34
3.2.2 Bayesian methods of parameter inference and model selection . . 35
3.2.3 Approximate Bayesian Computation . . . 36
3.3 Methods . . . 37

3.3.1 ABC SMC technique . . . 37
3.3.2 Multi-start CMA-ES Algorithm . . . 39
3.4 Case study 1: Spread of infectious diseases . . . 40
3.4.1 Dataset from outbreak of common-cold in Tristan da Cunha collected in October 1967 . . . 42
3.4.2 Synthetic dataset . . . 42
3.4.3 Results . . . 42
3.4.3.1 Dataset from outbreak of common-cold in Tristan da Cunha collected in October 1967 . . . 43
3.4.3.2 Synthetic dataset . . . 44
3.5 Case study 2: model selection in signalling pathways . . . 53
3.5.1 Nondimensionalization . . . 54
3.5.2 Qualitative fitting and satisfaction metrics . . . 55
3.5.3 Analytical model selection . . . 56
3.5.4 Results . . . 57
3.6 Discussion . . . 60

4 A reduced core model of the Wnt pathway **65**
4.1 Introduction . . . 65
4.2 Methods . . . 67
4.2.1 Qualitative description of our mathematical models . . . 67
4.2.1.1 Modelling the effect of Wnt . . . 70
4.2.2 Candidate models . . . 70
4.2.3 Mathematical representation of our candidate models . . . 71
4.2.4 Implementation of the mathematical model . . . 75
4.2.4.1 Steady state analysis . . . 76
4.2.5 Model selection . . . 76
4.2.5.1 Parameter values for the multi-start CMA-ES technique 79
4.3 Results . . . 81
4.3.1 Sensitivity analysis . . . 83
4.3.2 *in silico* experiments . . . 84
4.3.3 Reject more detailed models . . . 86
4.3.4 Proposing further experiments . . . 86
4.4 Simplification of the reduced core model . . . 88
4.4.1 Summary of the chapter so far . . . 88
4.4.2 Simplifying the model . . . 90
4.4.3 Steady state analysis . . . 93
4.4.4 Target model output . . . 95
4.4.5 Exploring the model output . . . 96
4.4.6 Further model analysis . . . 96
4.4.7 Final remarks about the simplified candidate model S_1 . . . 97
4.5 Discussion . . . 99

5 Experimental work **101**
5.1 Introduction . . . 101
5.2 Materials and Methods . . . 104
5.2.1 Cell culture . . . 104
5.2.2 Ligands, inhibitors and conditioned media . . . 104
5.2.3 Immunofluorescence . . . 105

5.2.4 Protein complex immunoprecipitation (Co-IP) . . . 106
5.2.5 Western blot . . . 108
5.3 Results . . . 110
5.4 Discussion . . . 111

6 A new model of the Wnt pathway **113**
6.1 Introduction . . . 113
6.2 Extension 1: Introducing the destruction complex . . . 114
6.2.1 Introduction . . . 114
6.2.2 Methods . . . 114
6.2.2.1 Qualitative description of our mathematical models . . 115
6.2.2.2 Candidate models . . . 118
6.2.2.3 Mathematical representation of our candidate models . 120
6.2.2.4 Implementation of the mathematical model . . . 121
6.2.2.5 Experimental observations . . . 121
6.2.2.6 Steady state analysis . . . 122
6.2.2.7 Model selection . . . 124
6.2.2.8 Parameter values for the multi-start CMA-ES technique 126
6.2.3 Results . . . 126
6.2.3.1 Sensitivity analysis . . . 127
6.2.3.2 *in silico* experiments . . . 129
6.2.3.3 Summary so far . . . 130
6.3 Extension 2: β-catenin modifications in the destruction complex . . . 133
6.3.1 Introduction . . . 133
6.3.2 Methods . . . 133
6.3.2.1 Qualitative description of our mathematical models . . 133
6.3.2.2 Candidate models . . . 134
6.3.2.3 Mathematical representation of our candidate models . 137
6.3.2.4 Experimental observations . . . 138
6.3.2.5 Steady state analysis . . . 142
6.3.2.6 Model selection . . . 145
6.3.2.7 Parameter values for the multi-start CMA-ES technique 145
6.3.3 Results . . . 145
6.3.3.1 Sensitivity analysis . . . 150
6.3.3.2 *in silico* experiments: Kim et al. (2013) . . . 150
6.3.3.3 *in silico* experiments: Li et al. (2012) . . . 154
6.3.3.4 *in silico* experiments: Azzolin et al. (2014) . . . 154
6.4 Discussion . . . 156

7 Discussion **159**
7.1 Summary of the thesis . . . 159
7.2 Summary of the work in each chapter . . . 159
7.2.1 A note on reproducibility of experimental results . . . 161
7.3 Future work . . . 161
7.4 Final remarks . . . 163

I Appendices **165**

A Theoretical methods **167**
A.1 Image segmentation 167
A.2 Estimating number of Wnt ligands and receptors 168
A.2.1 Number of Wnt ligands in a typical *in vitro* experiment 168
A.3 Western blot quantification 168

B Cost vectors used in Chapters 4 and 6 **169**
B.1 Cost vectors for Chapter 4 169
B.2 Cost vectors for Chapter 6 170

C Parameter values for candidate models in Chapter 4 **173**

D Parameter values for candidate models in Chapter 6 **175**

Chapter 1

Introduction

1.1 Motivation

The ability of a cell to respond and adapt to its surrounding environment is fundamental to its survival. In multicellular organisms, a cell's response to its microenvironment enables it to become specialised, and to carry out specific functions (Krstic et al., 2017; Vermeulen et al., 2010). This response often involves changes to proteins, such as synthesis, degradation, phosphorylation or complex formation that enable the cell to function appropriately in the given environment.

Signalling pathways are subcellular networks that transfer a stimulus (e.g. binding of a ligand to a receptor at the cell membrane) across the cell via a series of biochemical cascades to a response to that stimulus (e.g. increase in transcription of a particular gene). The biochemical reactions involved in this signal transduction typically involve interactions between different proteins and conformational changes that enable the transfer of this signal within the cell and across neighbouring cells (Molnar et al., 2011).

The biochemical interactions that participate in signalling pathways can generate complicated dynamics depending on the stimulus and the cell's status. Moreover, crosstalk between signalling pathways is common (Song et al., 2015; Kay et al., 2017; Vert and Chory, 2011; Collu and Hidalgo, 2014). This means a signalling event in one pathway could change the behaviour in another pathway or the combined signal from both pathways triggers a response different to the one from each pathway (Vert and Chory, 2011). This can make the behaviour of signalling pathways highly nonlinear and in many cases hard to predict (Janson, 2012; Carballido-Landeira and Escribano, 2016; Tyson et al., 2003).

Abnormal function of a signal transduction pathway, for example due to mutations in its components, is a hallmark of carcinogenesis and developmental diseases (Bazigou and Rallis, 2007). In order to understand how these abnormalities lead to such diseases, it is important first to understand the signal transduction process in healthy cells.

As a result, one of the core research themes within Systems Biology is the study of signalling pathways (Alon, 2007; Alberghina and Westerhoff, 2005). The primary challenges are to understand the structure of the biochemical networks that define these pathways and how mutations within their components lead to incorrect cellular responses. Typically, such studies involve abstract models that describe these networks. These may be mathematical, e.g. using ordinary differential equations (ODEs), or verbal, using a word description to detail the network interactions (MacLean et al., 2015a).

A particular challenge in these studies is that the experimental results on which these models are based are often hard to interpret quantitatively (Bass et al., 2017; Gassmann et al., 2009; Taylor et al., 2013). Based on the experimental procedure the results are often qualitative or, at best, semi-quantitative (Pargett and Umulis, 2013; Bass et al., 2017). For example, levels of a particular protein may increase monotonically,

or follow a bell shape, but the exact levels of such changes can vary across experiments. Moreover, the experimental procedures and setup, and the initial states of the biological system can mean that seemingly contradictory results are observed in different studies or even within the same study by the same group of experimentalists. In addition, the sparsity of the available data adds further challenges to such studies. These challenges mean experimental results and models proposed in different studies can often appear contradictory (Metcalfe and Bienz, 2011).

One of the well-studied signalling pathways in vertebrates is the Wnt signalling pathway, which regulates many processes in the cell and its disruption is a hallmark of carcinogenesis (Zhan et al., 2017; Duchartre et al., 2016; Clevers and Nusse, 2012). In particular, 90% of colorectal cancer cases show overactivation of this pathway (Radtke and Clevers, 2005), with 75% of these cases carrying a mutation in APC, one of the core components of the canonical Wnt pathway (Morin et al., 1997). This makes the canonical Wnt pathway an ideal model system for exploring novel approaches to investigate the behaviour of signalling pathways in general.

Unsurprisingly, studies of the Wnt pathway also face the challenges described above. A review of the recent experimental research on the Wnt pathway reveals that the verbal models proposed for the pathway can also appear contradictory (MacDonald and He, 2012; Metcalfe and Bienz, 2011). The existing verbal models of the pathway have not been shown to be fully consistent with the experimental data, nor can the data be used to reject competing models. Similarly, mathematical modelling, and more importantly model parametrisation, based on such qualitative data can lead to inconsistent models.

There is therefore a growing need for a different approach in order to assess the available experimental data and establish whether seemingly inconsistent results can be reconciled. Accordingly, in this thesis, instead of carrying out quantitative analysis of models of the Wnt signalling pathway, we carry out qualitative comparisons of alternative quantitative models against the experimental data. Our aim is to determine whether seemingly inconsistent experimental observations can be unified under a mathematical framework.

Focusing on the Wnt pathway, we carry out a detailed literature review to propose a set of candidate models that may be consistent with different (and sometimes apparently contradictory) experimental observations. We represent these models using ODEs, and use our framework to capture their qualitative behaviour, and ask whether they may be qualitatively consistent with the experimental observations.

The steps in our model selection framework are as follows. First, we propose a set of candidate mathematical models that may be consistent with the experimental observations. Using the results from a single study, we propose a qualitative cost function that allows us to compare the quantitative output of our candidate mathematical models with the experimental data from that study. Within this study, we use an optimisation algorithm to explore the parameter space of each candidate model, and reject candidate models where we are unable to find suitable parameter values to reproduce the experimental results qualitatively. Using the feasible parameter values found for the remaining candidate models, we carry out further analysis on these models, in particular sensitivity analysis, and *in silico* experiments to compare the model outputs with other experimental observations not used in the original cost function.

If there are suitable experimental results available from different studies, we may

then propose different cost functions for each set of results and apply the above steps for each candidate model and cost function across these studies. If there are several candidate models that describe the observed experimental data across all studies, we then analyse the model outputs to propose new experiments that may be used to discriminate between them.

Using this framework, we first focus on the cell's initial response to Wnt stimulation. In particular, we question which reactions are fundamentally altered by binding of Wnt ligands to the receptors at the cell membrane; namely, the rate of recruitment of the scaffolding protein Axin to the membrane, or the phosphorylation of LRP6 co-receptor. We are able to establish that several of our proposed candidate models are consistent with the experimental observations from one of the recent studies of the Wnt pathway, and go on to propose new *in vitro* experiments that could discriminate between these models.

In order to explore the utility of this approach further I undertook training within the laboratory of my experimental supervisor. I subsequently spent a significant time period in the laboratory reproducing the experiments used in our framework and carrying out our new *in vitro* experiment to discriminate between the remaining candidate models. I experienced first-hand the challenges of experimental work, and the problems of reproducibility of experimental results that my experimental colleagues experience every day. The insights gained are explored further later in this thesis.

Following this experimental phase, we shift our focus to studying how Wnt stimulation leads to deactivation of the multiprotein complex termed the destruction complex, and accumulation of the primary Wnt-target, β-catenin (see Chapter 2 for a detailed review). We apply our framework to three different sets of results concerning the deactivation of the destruction complex and show that under our framework, we are able to propose a unifying mathematical model of the Wnt pathway describing these seemingly inconsistent results.

In summary, using this approach, we can demonstrate that within this framework, even with relatively sparse, qualitative experimental results it is possible to discriminate between different candidate models. Additionally, the framework can guide us towards new experiments that could discriminate between any remaining candidate models. With regards to the Wnt pathway, we are able to use our framework to establish which reactions are most likely altered upon Wnt stimulation. Moreover, we are able to show that a single model can reconcile seemingly inconsistent experimental results.

It is important to note that the proposal of inconsistent verbal models of signalling pathways are not peculiar to the Wnt pathway; arising primarily from the experimental procedures that are widely used in these studies. Consequently, although we applied our framework to the Wnt pathway, it should be more widely applicable to other pathways. We hope that the framework can, in the future, be extended and used to discriminate between different models of signalling pathways, and guide experimentalists in designing future experiments.

1.2 Research questions

Here we rephrase the above motivation into explicit research questions. The overarching research question we would like to investigate is whether mathematical modelling

can help us discriminate between different verbal models of the canonical Wnt pathway proposed in different experimental studies. In particular, we study four specific questions:

1. Can we apply a computational framework to experimental results that are primarily semi-quantitative and qualitative, rather than quantitative, to infer suitability of different model structures in describing different experimental results?
2. Can we use such a framework, mathematical modelling using ordinary differential equations, and the current experimental results in the literature to understand the structure of the biochemical interactions that lead to recruitment to the membrane and deactivation of the destruction complex?
3. Can we propose and carry out new *in vitro* experiments that may clarify the structure of these interactions further?
4. Can we propose a minimalistic unifying model of the canonical Wnt pathway that may under different parameterisations explain the seemingly inconsistent experimental results that have led to proposals of different models of the canonical Wnt pathway?

1.3 Thesis structure

Chapter 2: Literature review. In the next chapter, we introduce the canonical Wnt pathway and provide a detailed review of the recent biological literature involving some of its key components. We summarise some of the latest verbal models of the canonical Wnt pathway, focusing on the steps that lead to deactivation of an important multiprotein complex at the centre of the pathway, termed the destruction complex. We then summarise some of the important mathematical models of the canonical Wnt pathway before discussing the problem of data quality in studies of signalling pathways.

Chapter 3: Model selection. In this chapter, we introduce mathematical model selection and carry out a brief literature review. We compare our model selection technique based on CMA-ES optimisation algorithm to one based on approximate Bayesian computation. We apply the two techniques to two case studies. In the first case study, we follow Toni et al. (2009) and apply the techniques to SIR models studying the spread of infectious diseases. The second case study focuses on a simple signalling pathway and introduces the idea of qualitative model comparison. We discuss the advantages and disadvantages of each technique.

Chapter 4: A reduced core model of the Wnt pathway. In Chapter 4, we introduce a set of candidate models for the interactions between two core components of the Wnt pathway, Axin and LRP6. By applying our model selection framework to recent experimental results by Kim et al. (2013), we reduce the number of suitable candidate models from twelve to four and propose new *in vitro* experiments to discriminate between these models further. Because in this chapter we only study the cell's initial response to Wnt stimulation, in preparation for introducing further complexities in our candidate models and studying a more complete picture of the pathway, and in order to keep the problem of model selection tractable, we end the chapter by simplifying

the most suitable candidate model further. We show that this model can still describe key experimental dynamics.

Chapter 5: Experimental work. In this chapter, we describe our efforts to carry out the *in vitro* experiments proposed in Chapter 4 to discriminate between our remaining candidate models for the interaction between Axin and LRP6. We detail the materials and methods and summarise our results. We discuss why further work is needed to validate or reject the candidate models. We also discuss some of the problems we faced when carrying out experimental work.

Chapter 6: A new model of the Wnt pathway. In this chapter, we build on our initial candidate models. We introduce β-catenin and further details of the Wnt pathway in our models. We compare our candidate models to experimental results from three recent studies of the canonical Wnt pathway, each of which has proposed different verbal models for the Wnt pathway (Kim et al., 2013; Azzolin et al., 2014; Li et al., 2012). We show one of our candidate models is consistent with the three sets of experimental results.

Chapter 7: Discussion. In this final chapter, we summarise the work carried out in this D.Phil. and presented in this thesis. We highlight the main contributions of the work and describe some of its limitations. We outline some of the problems we faced carrying out multidisciplinary work and some of the lessons we learnt carrying out cell culture work from the point of view of a non-experimentalist. We discuss future works and potential extensions of this thesis.

Chapter 2

Literature review

2.1 Introduction

The Wnt signalling pathway is one of the fundamental signal transduction pathways in vertebrates. It regulates many processes in the cell, such as cell cycle progression and cell differentiation, and disruption of Wnt signalling is a hallmark of carcinogenesis and several developmental diseases such as Norrie or Tetra-amelia (Stamos and Weis, 2013; Valenta et al., 2012; Clevers and Nusse, 2012). The Wnt pathway is named after the hydrophobic Wnt family of proteins that bind to various receptors and co-receptors on the cell membrane, transferring extracellular cues into intracellular signals.

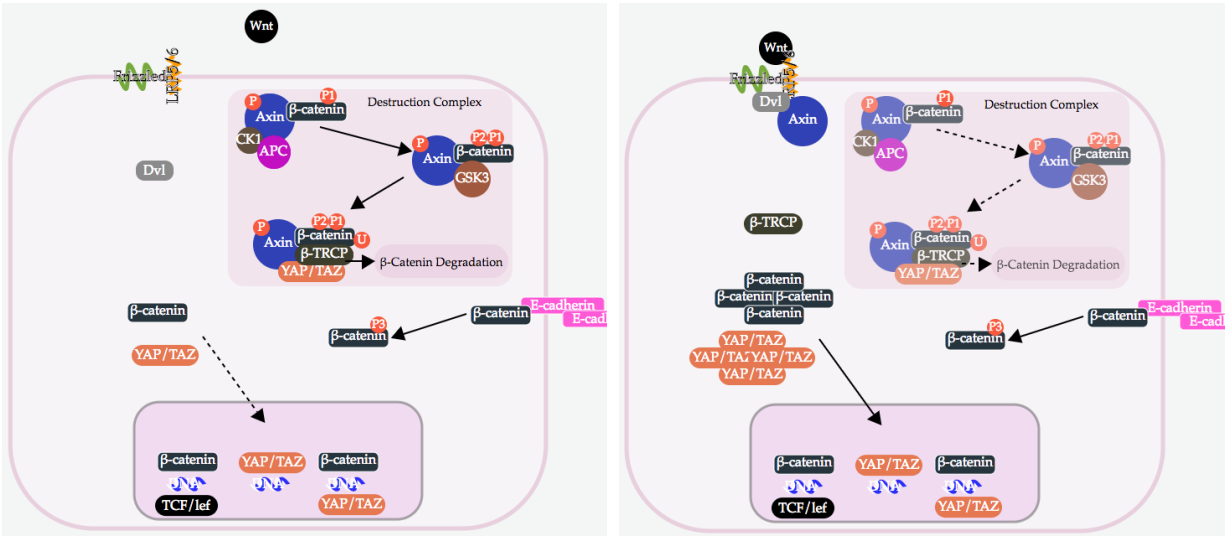
The Wnt pathway consists of two subsets: the canonical Wnt pathway, which regulates intracellular levels of the β-catenin protein; and the non-canonical pathways, such as the Planar Cell Polarity (PCP) pathway, which directs the alignment of cells within tissues (Amerongen, 2012). Our primary focus is the canonical Wnt pathway, which we simply refer to as the Wnt signalling pathway, unless otherwise specified.

Of particular interest in this thesis is the relevance of Wnt signalling to colorectal cancer (CRC), the fourth most common cancer in humans (Ferlay et al., 2012). CRC initiates in the layer of epithelial cells that cover the surface of the intestine in test-tube shaped glands called crypts (Reya and Clevers, 2005). Colorectal carcinogenesis occurs as a consequence of changes that disrupt normal crypt dynamics. Thus, elucidating the extracellular chemical signals and mechanical cues that control crypt homeostasis, and how mutations alter these is crucial to understanding the origins of CRC. Overactivation of the Wnt signalling pathway occurs in 90% of CRCs (Radtke and Clevers, 2005), with mutations in adenomatous polyposis coli (APC) occurring in 75% of CRC cell lines (Morin et al., 1997). It is therefore important to understand how these alterations allow neoplasms to develop and take over the healthy tissue. This may assist in identification of suitable drug targets. Before we may identify the effect of these mutations on cell and tissue, we need to understand the behaviour of Wnt signalling in healthy cells.

The Wnt pathway is highly conserved from invertebrates, including C. elegans and Drosophila, to vertebrates, including Xenopus and mammals (Valenta et al., 2012). Although we will primarily focus on the behaviour of the pathway in vertebrates and in particular mammals, most proteins and processes named here have orthologs or equivalents in invertebrates and many studies of the Wnt (or Wingless/Wg) pathway have been carried out in Drosophila.

Our understanding of the Wnt pathway is still very limited; however, a few steps are very well observed. In the absence of a Wnt stimulus (Figure 2.1A), β-catenin is marked by a multiprotein assembly, called the destruction complex, for degradation. The main components of the destruction complex are understood to be scaffolding proteins Axin and APC, and kinases GSK3 and CK1. Wnt stimulation leads to binding of Wnt ligands to Frizzled receptors and LRP5/LRP6 co-receptors (Figure 2.1B). This

leads to recruitment of several components of the destruction complex, and in particular the scaffolding protein Axin to the membrane, and deactivation of this complex in a not very well understood way. Deactivation of the destruction complex drives an increase in levels of β-catenin, which translocates to the nucleus, leading to transcription of various Wnt-target genes.



(A) Wnt off (B) Wnt on

FIGURE 2.1: Schematic of the canonical Wnt signalling pathway. In the absence of extracellular Wnt ligands (left), β-catenin is continuously degraded by a multiprotein complex termed the destruction complex, which causes β-catenin phosphorylation at residues S45 by CK1 and S33/S37/T41 by GSK3. Upon Wnt stimulation (right), the destruction complex is deactivated, causing β-catenin accumulation and Wnt target gene transcription. A large fraction of β-catenin is also found at the membrane, bound to E-cadherin in adherens junctions

The description above is a very simplified version of the events of the Wnt pathway. The Wnt pathway involves many proteins that go through various post-translational modifications, and has cross talk with several other important pathways, including Hippo (Azzolin et al., 2012; Piccolo et al., 2014), Delta-Notch and Hedgehog pathways (Takebe et al., 2011).

In the first part of this chapter, we introduce several proteins that play important roles in the Wnt pathway dynamics. We then describe several verbal and mathematical models of the pathway, and describe some competing verbal models for how the destruction complex is deactivated upon Wnt stimulation.

We then review several existing mathematical models of the Wnt pathway. We end by touching uppon data quality in studies of signalling pathways, and explain why caution must be exercised by both experimentalists and mathematicians before predictions are made using any such data.

2.1.1 β-catenin

The main target of the Wnt pathway, β-catenin, plays two different roles in the cell. It is a transcriptional coactivator, which can increase transcription of various genes by binding to the T-cell factor/lymphoid enhancer factor (TCF/Lef) family of transcription factors (Tetsu and McCormick, 1999). It also plays an important role in adherens

junctions by forming complexes with α-catenin and E-cadherin, and, in this way, connecting the actin cytoskeleton to the cell-cell junctions (Clevers and Nusse, 2012).

The role of β-catenin was first discovered in the 1980s. Its role in cell adhesion was discovered by Ozawa et al. (1989) as a binding partner of E-cadherin. Its role in gene transcription was discovered in Drosophila, via the β-catenin ortholog, Armadillo (Nusslein-Volhard et al., 1984).

Figure 2.2 displays a schematic of β-catenin and several of its binding partners. These binding partners share overlapping binding regions. For example, APC, E-cadherin and TCF/Lef bind to β-catenin via overlapping regions, meaning β-catenin cannot form complexes with these proteins at the same time, i.e. it has to choose between cell-adhesion, gene transcription and degradation (Valenta et al., 2012). Conformational changes in β-catenin may bias it towards its different roles. In Drosophila, Armadillo mutants have been produced that can perform exclusively its role in gene transcription or cell adhesion (Valenta et al., 2012).

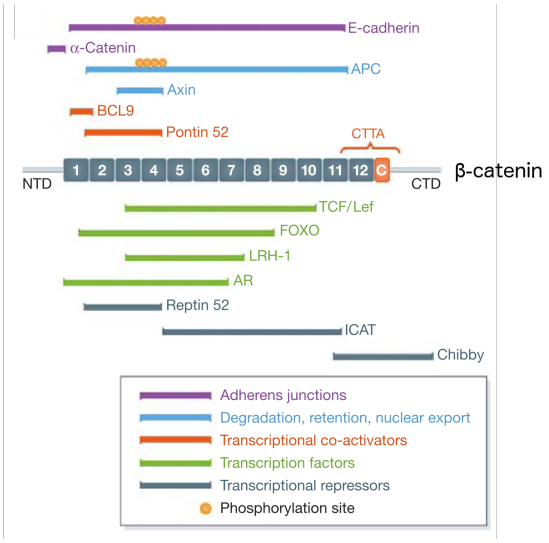


FIGURE 2.2: The β-catenin protein consists of a central region composed of 12 Armadillo repeats (numbered boxes), flanked by an amino-terminal domain (NTD) and a carboxy-terminal domain (CTD). Between the last Armadillo repeat and the flexible part of the CTD is the conserved helix-C (C). Coloured bars show experimentally validated binding sites for β-catenin interaction partners. Colour code: purple, components of adherens junctions; blue, members of the β-catenin destruction complex; red, transcriptional co-activators; green, transcription factors providing DNA binding; gray, transcriptional inhibitors. C-Terminal Transcriptional Activators (CTTA), the critical domain for their binding is marked by brackets. Little circles indicate phosphorylation sites on either E-cadherin or APC that enhance the interactions. Figure reproduced with permission of Springer from Valenta et al. (2012).

Since β-catenin is an important part of adherens junctions and a large fraction of β-catenin is bound to adherens junctions at the cell membrane, disruptions in adherens junctions could release β-catenin to the cytoplasm and may cause Wnt signalling. Herzig et al. (2007) observe that E-cadherin-negative cells failed to show higher levels of TCF transcription using the Top/flash report assay compared to E-cadherin positive cells (Herzig et al., 2007). However, other groups have observed an increase in β-catenin/TCF mediated transcriptional response in murine breast cells (Stockinger et al., 2001).

β-catenin may be phosphorylated in various sites which may increase its likelihood of taking part in a particular role in the cell. For example, phosphorylation at Y654 residue by Src can reduce its ability to bind to cadherins, while increasing its nuclear translocation and signalling ability (Huber and Weis, 2001; Veelen et al., 2011). Similarly, phosphorylation at S191 and S605 by JNK2 kinase has been observed to increase nuclear localisation of β-catenin (Wu et al., 2008), although the exact method of translocation of β-catenin into the nucleus is not yet well understood (Valenta et al., 2012).

Of particular interest to our thesis is β-catenin phosphorylation that occurs in the destruction complex. CK1 phosphorylates the S45 residue (Amit et al., 2002; Liu et al., 2002), which primes β-catenin for phosphorylation by GSK3 at T41, leading to successive phosphorylation at S37 and S33. This creates a binding site for β-TrCP (Yost et al., 1996; Liu et al., 2002; Wu and He, 2006). β-TrCP recruits β-catenin to the Skp1/Cul1/F-box/β-TrCP (SCFβ-TrCP) E3 ubiquitin ligase complex, which leads to β-catenin degradation via the 26S proteasome (Hart et al., 1999).

β-catenin may also be marked for degradation in a β-TrCP independent manner, in particular via Siah-1 (Liu et al., 2001) and Jade 1 (Chitalia et al., 2008). Siah-1 degradation is in fact independent of β-catenin phosphorylation via the destruction complex, however, it has been proposed that the rates of degradation of β-catenin independently of the destruction complex, cannot be significant (Hernández et al., 2012).

2.1.2 The Wnt family of proteins

In mammals there are 19 different genes for Wnt proteins, each approximately 40 kDa in size (Schweizer and Varmus, 2003). They are secreted into the extracellular space by Wnt-secreting cells such as Paneth cells (Gregorieff et al., 2005), and are typically found bound to the cell membrane or the extracellular matrix (Mikels and Nusse, 2006a). Wnt signalling often acts on a relatively short range between neighbouring cells (Clevers and Nusse, 2012). It can shape tissues as it can give polarity and asymmetry to cells, e.g. during cell division, daughter cells close to Wnt beads show higher levels of nuclear β-catenin and pluripotency (Habib et al., 2013).

The difference in the roles different Wnt ligands play is not well understood. Some Wnt ligands predominantly lead to canonical signalling while others activate non-canonical signalling only. It has also been observed that ligands can work in a cooperative manner (Miller et al., 2012). Most *in vitro* studies of the canonical Wnt pathway use human or murine Wnt3A ligands to stimulate cells.

The structure of Wnt proteins and how they interact with receptors at the membrane is also not well understood, largely because researchers have found it difficult to generate the soluble Wnt protein fragments which are required for such studies (MacDonald and He, 2012). It has also been difficult to purify Wnt proteins. Indeed, most studies of the Wnt pathway use Wnt Conditioned Media. HEK293T cells are often transfected with a Wnt producing vector, or alternatively, cell lines such as L-Wnt-3A cells (available from ATCC) which are stably transfected with such a vector, are used to produce Wnt Conditioned Media, which is then used to stimulate other cells *in vitro*. It is important to note that Wnt Conditioned Media contains other proteins secreted by the Wnt producing cells, which may stimulate the cells in other unexpected ways.

Other Wnt ligands can also act to activate or inhibit canonical Wnt signalling in a receptor dependent manner. For example Wnt5A can inhibit β-catenin induced gene

transcription by binding to receptor orphan tyrosine kinase Ror2, whereas it can activate canonical Wnt signalling by binding to Frizzled 4 receptor (Mikels and Nusse, 2006b).

2.1.3 Frizzled family of receptors

Frizzled proteins are seven-transmembrane receptors. They are the main receptors for Wnt ligands and play central roles in cell proliferation, movement and polarity (Yu et al., 2012). Ten Frizzled proteins have been identified in mammalian cells. Different Wnt ligands activate Wnt signalling by binding to these different receptors. Partial redundancies in various Frizzled proteins have been observed in different tissue types. For example, Fzd4 and Fzd8 function redundantly in kidney development (Ye et al., 2011).

Yu et al. (2012) carried out a detailed review of interactions between Wnt ligands and Frizzled receptors (Figure 2.3). They found that Frizzled 2 and Frizzled 7 are capable of canonical Wnt signalling and are highly redundant with respect to one another. However, they admit that it is unclear how these redundancies occur, and whether signalling converges at the receptor level with formation of the same ligand/receptor complexes or indirectly further downstream.

It is well known that the Frizzled receptor is crucial to Wnt signalling, however its exact role and the mechanism of its activity is not well understood. The first crystal structure of binding of Wnt ligands to a Frizzled receptor was published in 2012 showing mouse Fzd8 CRD domain in complex with Xenopus Wnt8 ligand (Janda et al., 2012).

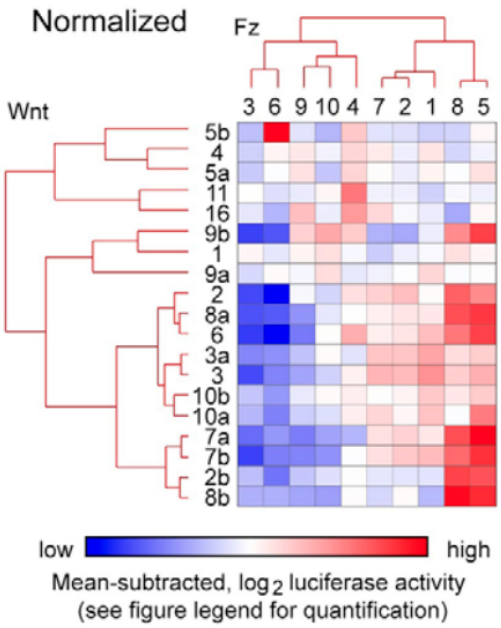
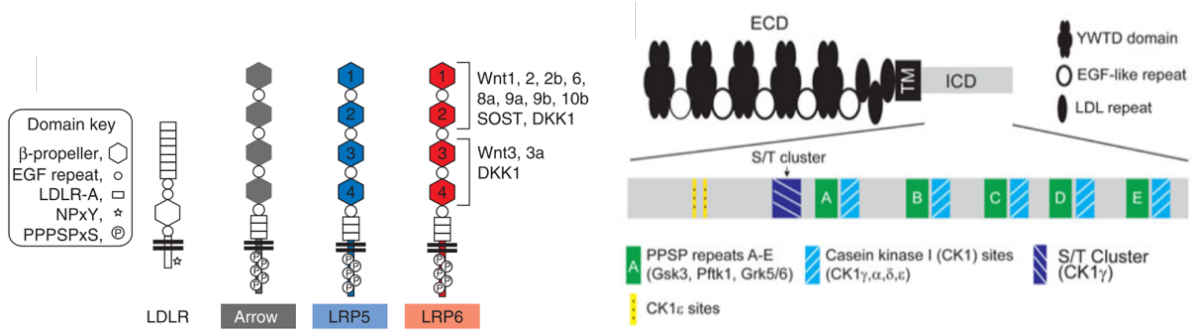


FIGURE 2.3: The activity of the canonical Wnt pathway upon transfection of STF cells (HEK293T cells stably expressing firefly luciferase reporter, which is a measure of canonical Wnt activity) with various mouse Wnt and Frizzled proteins alongside LRP5. Figure reproduced from Yu et al. (2012) with permission.

We refer readers to a recent publication by Wang et al. (2016) for a review of the latest research on the Frizzled family of receptors.



(A) (B)

FIGURE 2.4: Schematics of LRP6 protein. (A) Arrow, LRP5, and LRP6 are shown schematically together with LDLR. LRP6 binding to different Wnt proteins and antagonists SOST and DKK1 are shown. (B) LRP6 is a single-pass transmembrane protein. It has a modular extracellular domain (ECD), consisting of YWTD domains, EGF-like repeats, and LDL repeats. The intracellular domain (ICD) consists of PPPSP repeats (A–E), each juxtaposed with CK1 sites. Protein kinases promoting LRP6 signal transduction are indicated. Note that N-terminal phosphorylation by CK1ε is inhibitory to Wnt/LRP6 signalling. (A) is reproduced with permission of Cold Spring Harbor Laboratory Press from MacDonald and He (2012) and (B) is reproduced with permission of Springer from Niehrs and Shen (2010).

2.1.4 Arrow/LRP5/LRP6

LDL receptor-related proteins 5 and 6 (LRP5/LRP6) in vertebrates, or their Drosophila ortholog, Arrow, (henceforth referred to as LRP6 for simplicity) are single-span transmembrane proteins with approximately 1600 amino acid residues that play an important role in canonical and non-canonical Wnt signalling. They are believed to act as a co-receptor for Frizzled, forming a ternary complex with Frizzled and Wnt ligands (MacDonald and He, 2012), leading to Wnt signalling.

Different groups have established that Wnt ligands can bind directly to LRP6 (He et al., 2004). A single LRP6 protein may also be able to engage two different Wnt proteins simultaneously (MacDonald and He, 2012), adding further to the complexities of Wnt signalling. The schematic in Figure 2.4A shows where various ligands bind to the extracellular domain of LRP6. Figure 2.4B shows the structure of the LRP6 intracellular domain. LRP6 has five signature PPP(S/T)PxS motifs (often summarised to PPPSPxS or simply PPPSP) named A to E. These motifs are conserved from invertebrates to human. For consistency, from this point on we refer to these motifs as PPPSP. These motifs and, in particular, phosphorylation of several of their residues are believed to play important roles in the Wnt cascade. PPPSP phosphorylation by GSK3 primes LRP6 for phosphorylation at xS by CK1. We note that this contrasts with the β-catenin phosphorylation steps, where CK1 primes β-catenin for GSK3 phosphorylation. Most studies use an antibody that measures phosphorylation of the S1490 residue on the PPPSP motif A by GSK3, while similar regulations are observed on other motifs.

PPPSP motifs work in a cooperative manner. A single PPPSP motif is insufficient to stimulate Wnt signalling (Wolf et al., 2008; Niehrs and Shen, 2010); with at least four motifs required for competent Wnt signalling (MacDonald et al., 2008; Wolf et al., 2008).

LRP6 also has an S/T cluster, preceding the first PPPSP motif, which may be phosphorylated by CK1, and in particular residue T1479, which is phosphorylated by CK1γ

upon Wnt stimulation (Bilic et al., 2007). The importance of this phosphorylation in the Wnt cascade is not clear, particularly because it is not conserved in Drosophila (Zeng et al., 2008).

We remark that apart from the kinases described above, various other kinases are known to phosphorylate LRP6 at several sites in Wnt-dependent and Wnt-independent manners. We refer the reader to a review by Niehrs and Shen (2010) for a more detailed review of LRP6 phosphorylation.

Many studies of Wnt signalling involve mutants that have the LRP6 cytoplasmic region knocked out (called LRP6ΔC), or have the five motifs replaced by PPPAPxA or PPPAP, such that they can no longer be phosphorylated. These mutations lead to deactivation and lack of Wnt signalling. On the other hand, mutants lacking the extracellular domain of LRP6 (called LRP6ΔN) have constitutively active Wnt signalling (Wu et al., 2009; Zeng et al., 2005; MacDonald and He, 2012).

It is observed that Axin is recruited to LRP6 upon Wnt stimulation (Khan et al., 2007; Bilic et al., 2007), however, the exact method of recruitment is unclear; it may be direct, indirect or a combination of both (Piao et al., 2008; Zeng et al., 2008; MacDonald et al., 2008; Zeng et al., 2005). A Phosphorylated PPPSP motif is a docking station, unlike an unphosphorylated one (Tamai et al., 2004). However, Zeng et al. (2008) and Yamamoto et al. (2006) observe that Axin is required for LRP6 phosphorylation at PPPSP motifs. Phosphorylation by GSK3 of LRP6 at S1490, which is in the first of these motifs, is greatly enhanced upon overexpression of Axin (Yamamoto et al., 2006). These results suggest that there may be several alternative ways of recruitment of Axin to phosphorylated and unphosphorylated LRP6. Only Axin that can recruit GSK3 has been observed to phosphorylate LRP6 (Zeng et al., 2008), suggesting Axin might aid LRP6 phosphorylation by chaperoning GSK3 to the membrane and enhancing its availability there.

Frizzled is also required for PPPSP phosphorylation by GSK3 (Zeng et al., 2008). Indeed, preventing Frizzled/Dishevelled interaction halted this phosphorylation suggesting that Dishevelled plays a key role in Frizzled/Wnt induced phosphorylation of LRP6 (Zeng et al., 2008). The role of Dishevelled is discussed further below.

Another observation in the study of signalling via LRP6 is that caveolin, a family of membrane proteins important for endocytosis, is required for β-catenin accumulation upon Wnt stimulation (Yamamoto et al., 2006; Yamamoto et al., 2008). These studies found that LRP6 phosphorylation at S1490 and T1479 and LRP6 internalisation were required for Wnt signalling. Caveolin was found to be important for internalisation of LRP6 in lipid rafts, membrane micro domains that are enriched in cholesterol and glycosphingolipids (Yamamoto et al., 2006). We remark that these studies were performed using overexpression of LRP6 proteins, which may lead to increased endocytosis.

We also note that GSK3 plays two opposing roles in Wnt signalling. Cytoplasmic GSK3 can lead to degradation of β-catenin and inhibition of Wnt signalling, whereas GSK3 at the membrane can lead to its activation (MacDonald and He, 2012).

2.1.5 Dishevelled

Dishevelled (or simply Dvl) proteins (DVL1, DVL2, DVL3 in humans and Dsh in Drosophila and Xdsh in Xenopus) comprise approximately 700 amino acids and play important roles in Wnt signal transduction (MacDonald et al., 2008).

Dvl has three important domains called DIX, PDZ, and DEP. The PDZ and DEP

domains have been shown to be important for recruitment of Dvl to Frizzled and the plasma membrane. However, it is unclear whether Frizzled-Dvl interaction is primarily Wnt-driven (MacDonald and He, 2012). The DIX domain, on the other hand, can lead to polymerisation of DVL (Schwarz-Romond et al., 2005), and may lead to the dynamic assembly of protein-protein interactions such as between Axin and Dvl, and play an important role in the formation of aggregates at the membrane called the LRP6 signalosome (Bilic et al., 2007). Recently, it has been suggested that the DEP domain of Dvl is also essential to LRP6 signalosome formation by enabling dimerisation of Dvl proteins (Gammons et al., 2016). However, it has also been suggested these aggregates are, in fact, endocytic vesicles (Taelman et al., 2010). Dvl can associate with CK1ε and CK2, and become hyperphosphorylated upon Wnt stimulation (Willert et al., 1997), although the role of Dvl phosphorylation in Wnt signalling is not yet clear.

The Axin scaffolding protein has a similar DIX domain, which is called DAX in the literature to distinguish it from the Dvl DIX domain. It has been suggested that Axin oligomerization might also play an important role in β-catenin degradation (Fiedler et al., 2011). Axin is recruited to Dvl in overexpression studies, although again the interaction between Axin and Dvl and its role in Wnt signalling is unclear (Kishida et al., 1999).

Although it has been observed Dvl plays an important role in Wnt signalling, and in particular phosphorylation of LRP6, recruitment of Axin to the membrane and deactivation of the destruction complex, its precise role and the importance of its domains or phosphorylation at various residues are not well understood.

2.1.6 Axin

One of the primary members of the β-catenin destruction complex is the Axin scaffolding protein. There are two Axin genes in vertebrates, Axin1 and Axin2, which do not seem to vary in function (Stamos and Weis, 2013). Axin2 is a Wnt-target gene, leading to one of the well observed feedback loops in Wnt signalling (Jho et al., 2002). Going forward, we refer to the total Axin1 and Axin2 simply as Axin.

Axin is a tumour suppressor, with overexpression of Axin able to reduce levels of β-catenin in colorectal cancer cell lines (Behrens et al., 1998). It is a largely unstructured protein with binding sites for β-catenin, GSK3 and CK1 kinases, PP2A phosphotase and APC. It has been observed to enhance phosphorylation of β-catenin by CK1 and GSK3 by acting as a scaffold (Stamos and Weis, 2013).

Axin levels have been observed to vary across cell lines. Whereas Lee et al. (2003) observed low levels of Axin in Xenopus (0.02 nM), Tan et al. (2012) observed higher levels in a range of mammalian cell lines (e.g. 150 nM in HEK293T human embryonic kidney cells).

Levels of Axin are observed to drop upon Wnt stimulation (Li et al., 2012). This is most likely due to Axin dephosphorylation at various residues which is observed to reduce Axin stability (Yamamoto et al., 1999; Strovel et al., 2000). Although this drop might play an important role in long term Wnt response, initial accumulation of β-catenin occurs before any changes in levels of Axin are observed. β-catenin accumulation and increase in Wnt target gene mRNA were observed within the first 30 minutes to 2 hours after Wnt stimulation, whereas there is no noticeable drop in Axin concentration in this period (Li et al., 2012).

Axin phosphorylation might also play an important role in the cell's initial response to Wnt signalling. Phosphorylation of Axin by GSK3 at S497/S500 residues can increase its affinity for β-catenin (Kim et al., 2013). Kim et al. (2013) observed that Axin is dephosphorylated by protein phosphatase 1cγ (PP1cγ) at these sites upon Wnt stimulation. Luo et al. (2007) observed that PP1-driven dephosphorylation of Axin can reduce its affinity for GSK3. Similarly, Willert et al. (1999) observed that Wnt stimulation leads to dephosphorylation of Axin; however, they observed that this dephosphorylation was reduced by blocking protein phosphatase 2A (PP2A), and not PP1.

2.1.6.1 Axin feedback loops

Two well observed Axin feedback loops affect the canonical Wnt signalling. First, Axin2, has been shown to be a Wnt target gene (Jho et al., 2002; Leung et al., 2002). This provides a negative feedback loop on the canonical Wnt cascade as an increase in Wnt stimulation causes β-catenin accumulation, increasing transcription of Axin2 and hence increasing β-catenin degradation via the destruction complex. Second, Axin dephosphorylation via the LRP6 complex upon Wnt stimulation leads to destabilisation of Axin via enzymes tankyrase 1 and tankyrase 2 via an as yet unknown manner (Huang et al., 2009). This causes Axin levels to fall 4 to 5 hours after Wnt stimulation (Li et al., 2012) and creates a positive feedback loop as Wnt stimulation reduces the concentration of the destruction complex, increasing the affects of Wnt stimulation further.

2.1.7 APC

Mutations in the tumour suppressor APC occur in 75% of CRC cell lines (Morin et al., 1997), suggesting it plays a crucial role in controlling cell processes whose disruption can initiate carcinogenesis.

APC has binding sites for β-catenin and Axin (Stamos and Weis, 2013). Its phosphorylation by GSK3 and CK1 is enhanced in the presence of Axin and increases its affinity for β-catenin (Stamos and Weis, 2013). In addition to its role in the β-catenin destruction complex, APC has important roles in spindle formation, kinetochore attachment and microtubule stability (McCartney and Näthke, 2008). These roles might also explain why APC mutations are so common in CRC.

The exact role of APC in the destruction complex is not well understood. In a study involving purified proteins, increasing levels of APC in the presence of other components of the destruction complex failed to increase β-catenin phosphorylation (Stamos and Weis, 2013). However, it has been suggested that APC is necessary for β-catenin phosphorylation (Wang et al., 2014).

Recently Pronobis et al. (2017) used overexpression of the Drosophila APC2 and Axin proteins in human SW480 cells to study the role of APC and Axin. Their investigation revealed that non-functional APC2 and Axin mutants were able to complement each other to form a functioning destruction complex. They proposed that the destruction complex is able to recruit β-catenin using different domains of the APC and Axin scaffolding proteins. Moreover, the authors observed that although overexpression of some non-functional APC2 or Axin mutants did not lead to β-catenin degradation, this did inhibit Wnt target gene transcription as effectively as overexpression of full length APC2 or Axin, suggesting these proteins might play a role in sequestering β-catenin in the cytoplasm and away from the nucleus.

Su et al. (2008) observed that APC protects β-catenin from dephosphorylation by PP2A, and can facilitate its binding to the SCF/β-TrCP complex. APC's role in β-catenin ubiquitination is also supported by studies in colorectal cancer cell lines that carry mutations in APC (e.g SW480 and DLD-1) in which levels of phosphorylated β-catenin were unaltered (Su et al., 2008)

Since APC phosphorylation enables APC to bind to the same domain of β-catenin as Axin, it has also been proposed that APC might play a role in recycling Axin by removing phosphorylated β-catenin from the destruction complex (Kimelman and Xu, 2006). Similarly, APC has multiple binding sites for β-catenin with their affinity depending on APC's phosphorylation state. These observations suggest that phosphorylation state of APC is important for its function (Ha et al., 2004).

Localisation of APC in the cell may also influence its role in Wnt signalling. Brocardo et al. (2005) observed that truncated APC could shuttle between the cytosol and the nucleus more easily than full length APC; however, a more recent study failed to find a significant amount of APC2 in the nucleus, suggesting APC's nuclear transport might not play an important role in Wnt signalling (Roberts et al., 2012).

There are numerous other hypotheses about the role of APC in the destruction complex, although understanding the role of APC still remains extremely illusive (MacDonald and He, 2012).

2.1.8 E-cadherin

A large pool of β-catenin is bound to E-cadherin in Adherens junctions at the cell membrane and disruption in these junctions may affect Wnt signalling (Herzig et al., 2007; Stockinger et al., 2001). Repression of E-cadherin is a hallmark of Epithelial-mesenchymal transition (EMT), a key event in the generation of invasive tumours (Shin et al., 2010). The levels of E-cadherin are regulated by the canonical Wnt pathway in several ways. First, the Slug family of proteins is an inhibitor of E-cadherin transcription, and can itself be induced by β-catenin signalling (Conacci-Sorrell et al., 2003). Additionally, the protease ADAM10 is known to destroy the integrity of the Adherens junctions, and is itself transcribed by a Wnt target gene (Maretzky et al., 2005).

More recently, Huels et al. (2015) investigated the role E-cadherin plays in controlling normal cell behaviour when components of the canonical Wnt pathway are mutated. They observed that mutations in APC or GSK3 quickly lead to β-catenin accumulation in the small intestine and colon, whereas in the case of a single activating mutation of β-catenin, E-cadherin acted as a sink for the accumulated β-catenin. This meant it took longer for tumours to initiate in the small intestine and no tumours were observed in the colon, where there are higher levels of E-cadherin. Both a reduction in E-cadherin levels and a double mutation in β-catenin were shown to have a similar effect on Wnt signalling as mutations in GSK3 and APC.

These observations suggest that E-cadherin might play an important role in explaining how mutations in components of Wnt signalling leads to carcinogenesis.

2.1.9 The role of YAP/TAZ

Crosstalk has been observed between the canonical Wnt pathway and other fundamental subcellular pathways, such as the Hedgehog and Delta/Notch pathways (Takebe et al., 2011), and non-canonical Wnt signalling pathways (Amerongen, 2012). Wnt also

interacts with the Hippo pathway, which determines organ size by regulating cell proliferation and apoptosis in several ways (Piccolo et al., 2014). First, the transcriptional coactivators Yes-associated protein (YAP) and transcriptional coactivator with PDZ-binding motif (TAZ), targets of the Hippo pathway, share with β-catenin a common DNA-binding platform to transcribe several target genes involved in cell proliferation and viability (Piccolo et al., 2014). Next, Azzolin et al. (2014) showed that YAP/TAZ are part of the destruction complex and Wnt induces disassociation of YAP/TAZ from Axin. YAP/TAZ may then translocate to the nucleus and cause YAP target gene transcription. Unlike Azzolin et al. (2014), more recently Cai et al. (2015) failed to detect an increase in YAP/TEAD transcription factors reporter activity upon Wnt stimulation. More work is needed to explain these dependencies.

Azzolin et al. (2014) also detected a drop in Wnt transcriptional activity upon overexpression of YAP and a decrease in the association of β-TrCP with Axin1 upon depletion of YAP with short interfering RNAs (siRNAs). Hence, YAP/TAZ can act as mediators and inhibitors of Wnt signalling (Piccolo et al., 2014).

YAP/TAZ also transduce the mechanical effect of confluency and contact inhibition, with healthy proliferating cells in sparse cell cultures or cultures on stiff extracellular matrix showing nuclear localisation of YAP/TAZ (Aragona et al., 2013). YAP/TAZ effects are particularly important after oncogenic mutations. In wild-type epithelial cells YAP1 inhibition fails to reduce the rate of proliferation. However, after loss of APC, inhibition of YAP1 via YES1 kinase activity reverses cell hyperproliferation (Rosenbluh et al., 2012).

Our understanding of the crosstalk between the Hippo and canonical Wnt pathway is still rather limited. The complexities of the two pathway suggest that there may be an exciting opportunity for mathematical modelling of this crosstalk.

2.1.10 Other agonists and antagonists of the Wnt pathway

In additions to the proteins described above, many other agonists and antagonists of Wnt signalling form ligand-receptor complexes that regulate Wnt signalling (Niehrs, 2012). For example, R-spondins (roof plate-specific spondin) is a known activator of the canonical Wnt pathway (Wei et al., 2007). R-spondins promote continual Wnt stimulation by stabilising the Frizzled/LRP5/6 signalosome and halting its endocytosis (Mah et al., 2016). R-spondin 1 is required for the growth of mouse crypt organoids in Wnt conditioned media (Sato et al., 2009).

Frizzled-related proteins (sFRPs) and Wnt inhibitory protein (WIF), inhibit Wnt signalling by forming a complex with Wnt (Itasaki, 2003; Li et al., 2005b; Semënov et al., 2005), whereas proteins from the Dickkopf (DKK) and WISE/SOST families cause inhibition by binding to LRP6 co-receptors and disrupting the LRP6/Fzd complex formation (Glinka et al., 1998; Bovolenta et al., 2008). These antagonists bind to LRP6 in regions that overlap with sites for Wnt ligands, blocking the interaction of Wnt ligands with LRP6 (MacDonald and He, 2012) (see Figure 2.4A).

2.2 Models of the Wnt pathway

Signalling pathways can be modelled in a variety of ways; we consider two categories:

- **Verbal models** use words to describe the interactions between pathway components. They are usually proposed in experimental studies.

- **Mathematical (and rule-based) models** use a set of rules and/or mathematical equations, such as ordinary or stochastic differential equations, to describe the temporal and spatial dynamics of the pathway. Whereas traditional mathematical models may treat each conformational state of a protein as an individual species, rule-based or agent-based models treat proteins as agents, with sites that may be in different states.

In the next two sections, we summarise some of the recent verbal and mathematical models of the Wnt pathway. We will focus on the models that include components of the pathway that we study in later thesis chapters.

2.2.1 Verbal models

In the first part of this chapter, we introduced the main components of the canonical Wnt pathway and summarised some of the important experimental observations regarding their interactions, and the post-translational modifications that some of these proteins undergo.

Many verbal models of the canonical Wnt pathway have been published. Although all have added new insights, they differ in the assumptions they make about the primary steps that lead to the accumulation of β-catenin in the cell. Table 2.1 summarises some of these hypotheses, which we detail below.

A note on role of LRP6. As described in Section 2.1.4, the LRP6 co-receptor and the Wnt-dependent conformational changes it undergoes seem to play an important role in Wnt signalling. We note that various verbal models have been proposed for the role of LRP6 in initiating Wnt signalling and β-catenin accumulation. We highlight these below:

1. **LRP6 signalosome formation.** Wnt-driven Dvl-mediated polymerisation leads to formation of LRP6 signalosomes. Proximity of several co-receptors provides an enhanced platform for sequestration of Axin at the membrane and Wnt signalling (Bilic et al., 2007).
2. **LRP6 internalisation.** Wnt-driven, caveolin-mediated internalisation of LRP6 leads to LRP6 endocytosis. Localisation of LRP6 with components of the destruction complex in vesicles on the way to endocytosis leads to deactivation of the destruction complex (Yamamoto et al., 2006; Yamamoto et al., 2008).
3. **Initiation and amplification effects.** As an initial step, Wnt stimulation leads to recruitment of Axin to the membrane and LRP6, which drives LRP6 phosphorylation. Phosphorylated LRP6 becomes a docking station for Axin, and in particular, phosphorylated Axin (Kim et al., 2013), amplifying Wnt signalling (Kim et al., 2013; MacDonald et al., 2008).
4. **Inhibition of GSK3-phosphorylation of β-catenin by phosphorylated PPPSP motifs.** Phosphorylated LRP6 inhibits GSK3, which is bound to Axin, from phosphorylating β-catenin (Piao et al., 2008; Wu et al., 2009; Cselenyi et al., 2008).
5. **Substitution of β-TrCP by LRP6.** Wnt signalling leads to recruitment of Axin to LRP6, which removes β-TrCP from the destruction complex (Azzolin et al., 2014). Li et al. (2012) propose a similar model where Wnt stimulation leads to dissociation of β-TrCP from Axin.

We remark that caveolin is observed with LRP6 in studies proposing models (1) and

Primary Step	Description	Reference
Signalosome formation/Sequestration of Axin at the membrane	Recruitment of Axin to Frizzled/LRP6 complex at the membrane leads to sequestration and inactivation of destruction complex.	(Bilic et al., 2007)
Reduced affinity of Axin to β-catenin	Dephosphorylation of Axin (e.g at S497/S500 residues) leads to reduced affinity to β-catenin.	(Kim et al., 2013; Jho et al., 1999)
Degradation of Axin	Wnt stimulation leads to destabilisation and degradation of Axin.	(Yamamoto et al., 1999; Strovel et al., 2000; Li et al., 2012)
Direct inhibition of β-catenin phosphorylation	Phosphorylated PPPSP motifs of LRP6 can lead to direct inhibition of GSK3 phosphorylation of β-catenin.	(Wu et al., 2009; Piao et al., 2008; Cselenyi et al., 2008)
Dissociation of APC from the destruction complex	Dissociation of APC from the Axin–GSK3 complex.	(Valvezan et al., 2012)
Dissociation of GSK3 from the destruction complex	PP1-driven dephosphorylation of Axin leads to lower affinity to GSK3.	(Luo et al., 2007)
Dissociation of β-TrCP from the destruction complex	Release of ubiquitin β-TrCP from the destruction complex scaffolding protein, Axin.	(Azzolin et al., 2014)
Inhibition of β-catenin ubiquitination	Inhibition of β-catenin ubiquitination and not β-catenin phosphorylation while in complex with Axin.	(Li et al., 2012)
LRP6 internalisation	Caveolin-dependent LRP6 internalisation into vesicles alongside Axin and other components of the destruction complex leads to inhibition of GSK3/recruitment of β-catenin to Axin.	(Yamamoto et al., 2006; Yamamoto et al., 2008)
MVB formation	Formation of multivesicular bodies (MVB) sequesters GSK3 from β-catenin.	(Taelman et al., 2010)

TABLE 2.1: Summary of mechanisms that have been proposed in verbal models of the canonical Wnt pathway to contribute to inactivation of the destruction complex and accumulation of β-catenin. We include illustrative references for each hypothesis, but note that for most there are many other publications supporting each hypotheses.

(2), so they are describing the same system using two different models. Models (1) and (3) (and similarly models (1) and (5)) could be mutually consistent with each other, such that LRP6 signalosome formation increases the rate of recruitment of Axin to the membrane. Finally, if unphosphorylated Axin has a lower affinity for β-TrCP, models (3) and (5) could also be consistent.

A note on β-catenin degradation by the destruction complex. There are four primary steps that β-catenin goes through before being degraded via the destruction complex: (i) recruitment to the destruction complex, (ii) phosphorylation by CK1, (iii) phosphorylation by GSK3, and (iv) ubiquitination by β-TrCP. A major discrepancy among existing Wnt pathway models lies in which of these steps are assumed to be altered by

Wnt signalling. Figure 2.5 summarises the competing hypotheses.

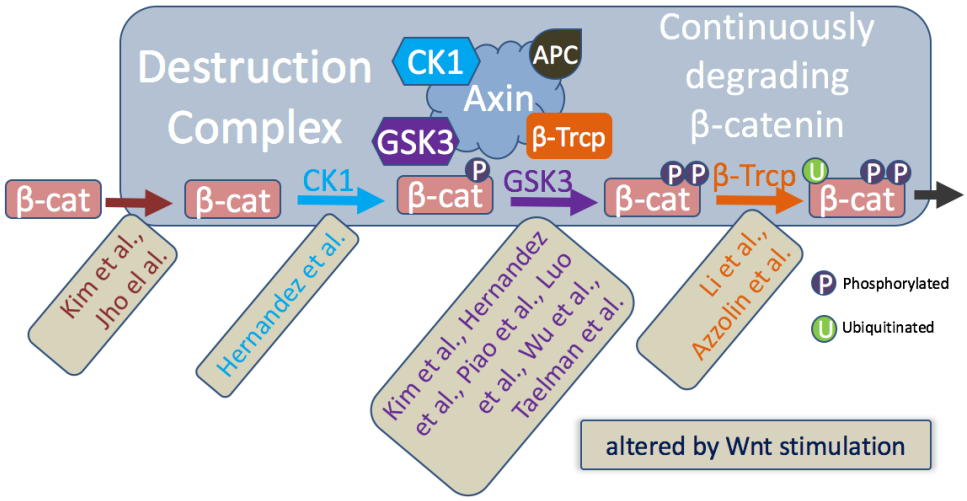


FIGURE 2.5: Schematic of the steps involved in β-catenin degradation via the destruction complex. There have been different proposals on how Wnt stimulation alters the dynamics of the destruction complex, leading to accumulation of β-catenin in the cell. Kim et al. (2013) and Jho et al. (1999) observed a reduced interaction between β-catenin and Axin, an important member of the destruction complex. Hernández et al. (2012) proposed that Wnt reduces the rate of phosphorylation of β-catenin by CK1 and GSK3. Other groups have proposed that Wnt reduces the rate of phosphorylation by GSK3 (Kim et al., 2013; Luo et al., 2007; Wu et al., 2009; Taelman et al., 2010), whereas Li et al. (2012) and Azzolin et al. (2014) suggested that Wnt reduces the ubiquitination rate of β-catenin. We only include some illustrative references for each step.

In the remainder of this section, we review some of the publications that have proposed verbal models about how Wnt signalling alters the behaviour of the destruction complex.

2.2.1.1 Reduced affinity of β-catenin for Axin

Kim et al. (2013) carry out their study in two mammalian cell lines; HEK293T cells and L-cells using endogenous protein levels. Similar to earlier studies, they observe that Axin is recruited to LRP6 within the first half hour of Wnt stimulation. Interestingly they noticed that levels of Axin in complex with LRP6 return to their original levels within 2 hours, while levels of β-catenin stay elevated, and levels of phosphorylated LRP6 remain higher than their "Wnt-off" levels.

Kim et al. (2013) developed a new antibody for Axin phosphorylated by GSK3 at the S497 and S500 residues as originally observed by Jho et al. (1999). By using overexpression of PP1cγ and using PP1 inhibitor, Tautomycin (TM), they showed that levels of phosphorylated Axin are controlled by the balance between GSK3-driven phosphorylation and PP1-driven dephosphorylation of these residues. They observe that Wnt stimulation leads to Axin dephosphorylation at these residues.

Kim et al. (2013) hypothesised what impact Axin dephosphorylation could have on its conformational state. Having shown that the Axin-DIX domain binds to Axin-BCD (β-catenin binding domain) in the absence of GSK3, but fails to bind in its presence, they proposed that dephosphorylation of Axin leads to its inactivation in what they call "intramolecular autoinhibition". They also showed that levels of β-catenin

binding to Axin-BCD are inversely proportional to levels of Axin-DIX binding to Axin-BCD, suggesting increased levels of β-catenin act as a safeguard mechanism for reactivating Axin and keeping levels of β-catenin under control.

Similar to earlier studies, Kim et al. (2013) also detected an increase in levels of LRP6 phosphorylated at S1490 residue, one of the five PPPSP motifs on LRP6, upon Wnt stimulation. They suggest that Axin-bound GSK3 enables phosphorylation of LRP6 upon Wnt stimulation. They also observed that phosphorylated LRP6 binds preferentially to Axin phosphorylated at S497/S500. They proposed that this amplification effect, proposed in earlier work by Zeng et al. (2008), leads to selective recruitment of phosphorylated Axin to the membrane, its dephosphorylation and increasingly rapid inactivation of the destruction complex (Kim et al., 2013).

2.2.1.2 Direct inhibition of GSK3-phosphorylation of β-catenin by LRP6 phosphorylated at PPPSP motifs

Piao et al. (2008), Wu et al. (2009), and Cselenyi et al. (2008) have all observed that phosphorylation of PPPSP motifs on LRP6 is important in the inhibition of phosphorylation of β-catenin by GSK3 *in vitro*. Piao et al. (2008) and Wu et al. (2009) both observed that injection of phosphorylated PPPSP peptide into Xenopus embryos leads to axis duplication, which is a sign of increased Wnt signalling.

Wu et al. (2009) used recombinant proteins to show that dually phosphorylated PPPSPxS peptides (which we again refer to PPPSP for consistency) directly inhibit GSK3-phosphorylation of β-catenin. Using assays containing Axin, β-catenin, CK1 and GSK3, they observed that addition of phosphorylated PPPSP motifs only affects phosphorylation of β-catenin at the S33/S37 and T41 residues and not its phosphorylation at S45 by CK1. They found that motifs A, C and E in particular had the strongest inhibitory effect on β-catenin phosphorylation.

Wu et al. (2009) also found that phosphorylated PPPSP peptides inhibit GSK3 activity independently of Axin. They concluded that PPPSP does not effect interactions between Axin and GSK3 and more likely inhibits GSK3 activity directly.

Piao et al. (2008) made a similar observation that phosphorylated PPPSP motifs (and not the unphosphorylated motifs) play an important role in the inhibition of GSK3β. They also observed that the S/T cluster of LRP6 is crucial for binding of GSK3β to LRP6.

2.2.1.3 Inhibition of ubiquitination of β-catenin facilitated by APC

Li et al. (2012) found that ubiquitinated β-catenin accumulates in a complex with Axin after proteasomal degradation is halted via the MG132 proteasome inhibitor, suggesting β-catenin is degraded while still in complex with Axin, contrary to previous assumptions that it was released from Axin after phosphorylation by GSK3.

Li et al. (2012) argue that Wnt stimulation inactivates the final step of the destruction complex by releasing β-TrCP from the destruction complex, thereby preventing it from marking β-catenin for ubiquitination. This argument is based on their finding that β-TrCP failed to co-immunoprecipitate with Axin upon Wnt stimulation after degradation was halted using MG132. Additionally, the authors failed to detect Axin in complex with LRP6 in several Wnt-unresponsive cell lines. When full-length APC

was reintroduced into cell lines with APC truncation (e.g. SW480 and DLD1), Li et al. (2012) observed reduced Wnt pathway activity. They also observed an increase in levels of ubiquitinated β-catenin in DLD1 and SW480 cells transfected with central region of APC, once degradation was after stimulation with MG132. They concluded that APC plays an important role in ubiquitination of β-catenin.

They proposed a model where Wnt stimulation (or APC mutations) prevents the destruction complex from marking β-catenin for ubiqutination, and frees the destruction complex to recruit further β-catenin. This saturates the destruction complex and enables levels of β-catenin to increase.

2.2.1.4 YAP enhances binding of β-TrCP to Axin and β-catenin ubiquitination

Azzolin et al. (2014) made similar observations to those reported by Li et al. (2012). They found that β-TrCP fails to co-immunoprecipitate with Axin after Wnt stimulation. Unlike several other studies (Kim et al., 2013; Khan et al., 2007; Li et al., 2012), where levels of Axin in complex with LRP6 fall after the first hour of Wnt stimulation, they found that levels of this complex continued to increase in the first 4 hours after Wnt stimulation.

Azzolin et al. (2014) also investigated the effect of YAP/TAZ on the β-catenin destruction complex. They showed that YAP/TAZ are part of the destruction complex and Wnt induces disassociation of YAP/TAZ from Axin. They detected a drop in Wnt transcriptional activity upon over-expression of YAP and a decrease in the association of β-TrCP with Axin upon depletion of YAP with short interfering RNAs (siRNAs). They proposed that YAP plays an important role in allowing binding of β-TrCP to Axin, thereby facilitating ubiquitination of β-catenin within the destruction complex.

2.2.1.5 Sequestration of GSK3 inside MVBs

An alternative verbal model of the canonical Wnt pathway proposes that Wnt signalling requires sequestration of GSK3 within multivesicular bodies (MVBs) (Taelman et al., 2010). This introduces two layers of membrane between GSK3 and its substrates, in particular β-catenin, inhibiting phosphorylation of its substrates. Taelman et al. (2010) found that proteins essential for MVB formation are required for Wnt signalling. They also found that GSK3 colocalised with endocytosed Wnt ligands. GSK3 also relocated into compartments that could be MVBs or lysosomes.

Interestingly, using β-catenin siRNA, they found that β-catenin was required for sequestration of GSK3 in MVBs, introducing the possibility of another feedback loop in Wnt signalling. Localisation of proteins in MVBs is often followed by their degradation via lysosomes. Hence a drop in levels of GSK3 may be expected according to this model. It is unclear how this model is consistent the observations that levels of GSK3 are unchanged upon Wnt stimulation (Metcalfe and Bienz, 2011).

2.2.2 Mathematical models

There are a large number of mathematical models of the canonical Wnt pathway, which differ in complexity (see Table 2.2), the species included, and their assumptions about how Wnt acts on the cell. In Table 2.3 we summarise some of the ways in which Wnt stimulation has been assumed to act in several recent mathematical models. We discuss

a few of these recent models below and refer the reader to Lloyd-Lewis et al. (2013) for a more detailed review.

Model	Number of Parameters	Number of dependent variables
Chen et al. (2014)	63	29
MacLean et al. (2015b)	31	19
Song et al. (2014)	31	17
Haack et al. (2015) (basic model)	23	8
Lee et al. (2003)	22	15
Barua and Hlavacek (2013)	21	410 (29 independent reactions only)
Leeuwen et al. (2007)	10	11
Kogan et al. (2012)	20	7
Mazemondet et al. (2012)	17	4
Schmitz et al. (2013)	16	11
Our candidate models H_{xy}	16	6
Our candidate models S_x	7	3
Our candidate models M_{xy}	13	6
Our candidate models N_{xy}	15	8
Mirams (2008)	5	1

TABLE 2.2: Summary of the complexity of existing mathematical models of the canonical Wnt signalling pathway, as quantified by the number of parameters and dependent variables. For simplicity, we exclude parameters used to represent a Wnt stimulus in each model. Note that although some models use mass action rules to describe biochemical interactions, many others assume more complicated nonlinear interaction terms.

Lee et al. (2003) introduced the first mathematical model of the canonical Wnt signalling pathway, which they calibrated using experimental data from *Xenopus* egg extracts. The Lee model comprises a set of Ordinary Differential Equations (ODEs) governing the temporal dynamics of Wnt pathway components, such as Axin, APC, GSK3, Dvl, TCF and β-catenin. It focuses on the formation of the destruction complex from its constitutive parts (Axin, APC and GSK3). Synthesis and degradation of Axin and β-catenin are modelled, with total levels of other proteins assumed constant. Wnt is assumed to control the rate of activation of Dvl, with activated Dvl leading to break up and deactivation of the destruction complex.

Lee et al. (2003) use conservation laws and fast kinetics approximations to reduce their system from fifteen to seven ODEs. They model Wnt stimulation using a dimensionless variable W, $W = 0$ denotes unstimulated or reference, $W = 1$, the stimulated state, and $W > 1$ the hyperstimulated state. They also consider a transient Wnt stimulation by imposing a time-dependent exponential decay on W.

Lee et al. (2003) used their model to study the effect on the half life of β-catenin of changes in concentrations of Axin, GSK3 and Dvl in the absence of Wnt stimulation. While they observed similar qualitative results experimentally, they noticed that their model over-estimates the effect of Axin and GSK3 for high concentrations of Dvl. They argue that in cells expressing full-length APC, Axin-independent degradation does make a significant contribution to the total β-catenin flux; however, with a 50% loss in APC, that contribution becomes important in determining total levels of β-catenin.

Wnt dependent reaction	Brief description	Reference
Activation of Dvl	Wnt stimulation increases rate of activation of Dvl, which deactivates the destruction complex. Lee et al. (2003) detail the deactivation of the destruction complex by break up of its components.	Lee et al. (2003) and MacLean et al. (2015b)
Phosphorylation of LRP6 by CK1	Wnt is modelled as a species, which binds to LRP6 and Frizzled, enabling phosphorylation of LRP6 by CK1. phospho LRP6 recruits and sequesters Axin, leading to deactivation of the destruction complex.	Haack et al. (2015)
Axin degradation	The rate of Axin degradation increases upon Wnt stimulation, reducing the levels of destruction complex available to mark β-catenin for degradation.	Leeuwen et al. (2007)
Break up of destruction complex	Wnt stimulation leads to inactivation of the destruction complex by causing it to decompose to its constitutive parts.	Leeuwen et al. (2007) and Song et al. (2014)
Conformational change in β-catenin	β-catenin exists in two conformations, with different binding affinity for transcriptional factors. Wnt controls the rate of this conformational change.	Leeuwen et al. (2007)
CK1 and GSK3 phosphorylation of β-catenin	Wnt stimulation reduces the rate of phosphorylation of β-catenin.	Hernández et al. (2012)
Deactivation of the destruction complex	Wnt stimulation increases the rate of deactivation of the destruction complex	Schmitz et al. (2013)

TABLE 2.3: Summary of the key assumptions used in some of the existing mathematical models of the canonical Wnt pathway regarding the effect of Wnt stimulation on cells. Some mathematical models focus on β-catenin and the changes it goes through prior to its degradation (Hernández et al., 2012), while others include descriptions of the destruction complex (Leeuwen et al., 2007; Lee et al., 2003), focus on interactions at the membrane (Haack et al., 2015), consider the dual role of β-catenin in signalling and cell adhesion (Leeuwen et al., 2007), or study the role shuttling between nucleus and cytoplasm (MacLean et al., 2015b; Schmitz et al., 2013).

They suggest that if the rate of Axin-independent degradation varies across tissues, their model could explain why APC loss may be oncogenic in certain tissues.

Leeuwen et al. (2007) incorporated the role of β-catenin in cell adhesion in their model, but unlike Lee's mathematical model, their model did not explicitly include the role of APC and GSK3. Leeuwen et al. (2007) consider two hypotheses. Under the first hypothesis, there is competition between E-cadherin and the signalling machinery for β-catenin. Under the second hypothesis, β-catenin can undergo a conformational change (to a closed form) upon Wnt stimulation (Gottardi and Gumbiner, 2004), which reduces its affinity for α-catenin, an important part of the adherens junctions, meaning β-catenin is more likely to bind to TCF/LEF. Wnt controls the rate of deactivation of the destruction complex, and can also (under the second hypothesis) promote conformational change (or closing) of the β-catenin.

Leeuwen et al. (2007) used their mathematical model to show that measuring levels of cadherin-mediated cell adhesion upon Wnt stimulation might enable one to discriminate between their two hypotheses. They also suggested that their model predictions about the level of functional APC needed for malignant transformation are consistent with experimental observations by Li et al. (2005a).

Hernández et al. (2012) combined experimental work with mathematical modelling to study the destruction complex in more detail. They designed a simple ODE model of β-catenin phosphorylation by CK1 and GSK3 in the destruction complex and its ubiquitination. They exploited experiments in various human cell lines to determine which steps in the destruction complex must be altered by Wnt stimulation. By assuming that β-catenin phosphorylation reactions are in quasi-steady-state, they concluded that Wnt signalling does not affect the rate of ubiquitination of β-catenin, in contrast to assertions made by Azzolin et al. (2014) and Li et al. (2012), whereas it must reduce the rate of phosphorylation of β-catenin by CK1 and GSK3. They also argued that any degradation of β-catenin that occurs independently of the destruction complex must be negligible. Finally, they discussed two possible scenarios for the state of the destruction complex, namely whether GSK3 and CK1 are always in association with Axin or whether they may engage or disengage from Axin at various steps, and suggest either is possible given their results.

Song et al. (2014) used mathematical modelling and *in vivo* experiments to study the competition of β-catenin between cell adhesion and signalling. The authors assumed a secondary role for APC in transporting β-catenin to the cell membrane. Their mathematical model predicts that whereas both APC and β-catenin mutations can result in β-catenin accumulation and increased Wnt signalling, only the former increases cell-cell adhesion. They validated this prediction by showing that APC-mutated cells migrate at a slower pace in murine intestinal crypts *in vivo*.

2.2.2.1 Compartmentalised models

Most mathematical models of the Wnt pathway, including the models we propose later in this thesis, treat the cell as a well mixed system. As we have discussed in the first part of this chapter, Wnt signalling involves the formation of large protein complexes, including the LRP6 signalosome, Adherens junctions and the destruction complex, and movement of various key pathway proteins to different locations in the cell, including recruitment of the destruction complex to the membrane and signalosome formation, or translocation of β-catenin into the nucleus (Lloyd-Lewis et al., 2013). Some mathematical model have investigated the role of spatial variations in Wnt signalling. For example, MacLean et al. (2015b) and Schmitz et al. (2013) used ODE models to study the role of nuclear/cytoplasmic transportation of the destruction complex and β-catenin on the dynamics of the Wnt pathway, and Haack et al. (2015) used a stochastic multi-compartmental model to study the effect of lipid-raft-dependent Wnt signalling on driving cell fate.

Adding spatial variations to mathematical modelling of Wnt signalling adds further challenges with regards to model fitting and availability of suitable experimental observations, which need to be considered.

2.3 Overview of experimental data used in models of signalling pathways

The verbal and mathematical models reviewed above illustrate recent efforts to increase our understanding of the canonical Wnt pathway. Although these models have given insights into the workings of the pathway, differences in the assumptions and the models proposed to describe the experimental observations indicate that our understanding of the canonical Wnt pathway remains limited.

Mathematical models provide a complementary approach to verbal models, enabling us to gain insights into the dynamics of multiple nonlinear biochemical interactions (MacLean et al., 2015a). A major source of uncertainty is the value of model parameters, such as reaction rate constants, which are difficult to observe experimentally. In such cases, mathematical models are often fitted to experimental results to estimate a suitable set of parameter values.

When studying the temporal dynamics of signalling pathways, time course experiments are often used as target data in model fittings. Such experiments usually include steps like the following:

- samples containing cells of interest are prepared in several dishes,
- a stimulus (e.g. Wnt) is added to the samples for different time periods,
- the samples are collected at the end of the allocated time,
- the samples are probed for levels of a particular target that may be compared to the mathematical model output.

The final step might involve different techniques, including qPCR (to e.g. measure levels of mRNA expression), immunofluorescence (to e.g. measure protein localisation), and many more. However, the most common techniques used involve Western blot detection. We give a brief description of this technique below.

2.3.1 Western blot detection

Western blot (WB) or **protein immunoblot** is widely used in experimental studies of signalling pathways to measure the levels of a particular protein in a sample. Figure 2.6 displays the various steps involved in carrying out a Western blot:

- **Sample preparation:** Several samples may be prepared. These may include for example (1) stimulation of the cells for different periods with the same stimuli, (2) stimulation with different stimuli, or (3) using cell lines transfected to express different levels of a particular protein. Samples are lysed using a suitable buffer and suitable technique to ensure the proteins of interest are preserved in the lysate.
- **Gel electrophoresis:** The samples are loaded onto a gel which separates the samples depending on their size and electric charge. Each gel can run slightly differently so results of Western blots should be compared within that particular gel.
- **Membrane transfer:** Using electroblotting, the separated proteins are transferred onto a membrane which may be probed for proteins of interest.
- **Blocking, primary and secondary antibody incubation:** The membrane, which now carries the separated proteins on one side is blocked using a suitable solution to avoid non specific binding of antibodies before being incubated with the primary antibody for the protein of interest, and then a secondary antibody that

can specifically detect the primary antibody. The membrane is often cut at appropriate points to incubate against antibodies for proteins of different weight at the same time.

- **Detection and analysis:** Finally, the membrane is incubated in a suitable substrate, which interacts with the secondary antibody and produces a signal corresponding to the levels of the protein of interest.

Results of Western blots are often described as semi-quantitative (Pargett and Umulis, 2013), meaning that the readout from a Western blot is not the actual protein levels, but a transformation of these levels in the sample. This transformation can vary depending on the exact procedure carried out, and can vary from lab to lab and, in fact, from experiment to experiment. Figure 2.7 illustrates how the signal strength from a Western blot varies depending on protein levels. It is important to carry out a Western blot in the linear range for the detection procedure used.

It is common to quantify the results of Western blots. This is often carried out in experimental studies (for example, see figures in Li et al. (2012) and Kim et al. (2013)). These quantifications can give markedly different results (see Figure 2.8). It is hence generally not appropriate to compare the levels of a particular protein from one experiment to another.

2.3.2 Co-immunoprecipitation (co-IP) studies.

Many studies of the canonical Wnt pathway have used co-IPs to measure dynamic changes in interaction between core components of the Wnt pathway upon Wnt stimulation. Here we summarise a typical co-IP procedure:

- **Lysate preparation.** In a similar fashion to Western blots, cells are lysed using an appropriate lysis buffer. It is important to ensure that the lysis buffer preserves interactions between the proteins of interest.
- **Beads incubation.** The lysates are incubated with beads and the primary antibody for the IP protein. The beads bind to the primary antibody which in turn binds to the IP protein. Any proteins in complex with the IP protein also remain in complex with the beads.
- **Westen blot.** Western blot detection, as described above, is carried out on the proteins after they are eluted from the beads.

As for the Western blot procedure described above, co-IP protocol must be optimised for the complex of interest. In particular, it is important to use the correct buffer, antibody and procedure to ensure maximum specific binding of the antibody to the IP protein while in complex with other proteins of interest.

2.3.3 Reading co-IP/Western blot results

Figure 2.9 represents a typical output from a co-IP study. We will use this example to illustrate how one might read and interpret such output. There are two sets of columns present under "IP" and "input". The input column contain the results of Western blot detection on the lysates without incubation with beads. These data should represent the total levels of each protein in the samples after 0, 0.5 and 2 hours of Wnt stimulation. Each row represents detection using the antibody against the given protein named in the right hand side. For example the first row under input columns suggests that levels of β-catenin are much higher in the samples after 2 hours compared to after 30 minutes of Wnt stimulation, which is itself higher than β-catenin levels without any

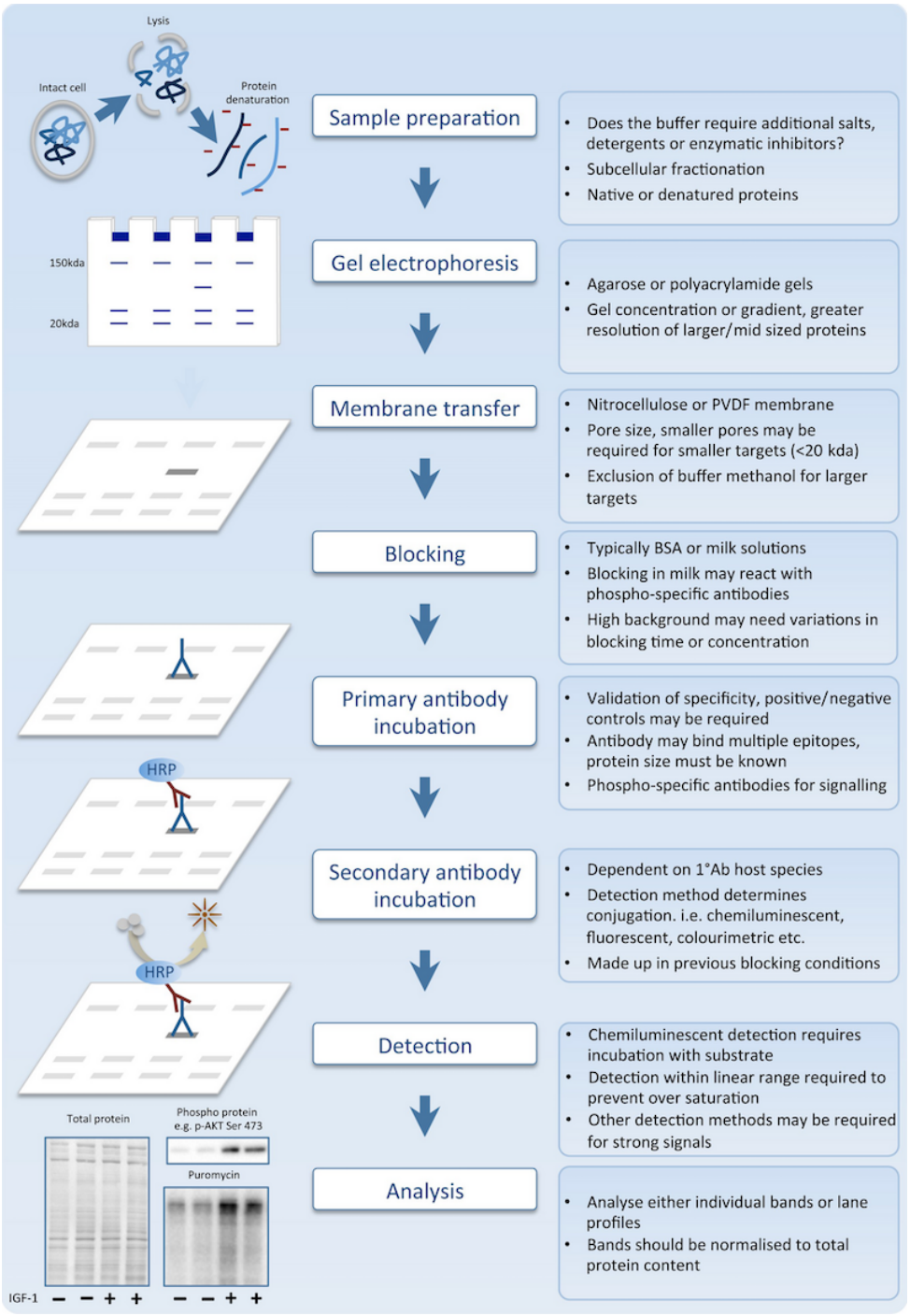


FIGURE 2.6: There are several steps involved in carrying out a Western blot. Each step in the procedure can vary greatly among different experimental labs. Many factors affect the details that needs to be followed at each step including the materials and equipment available or the protein of interest. Moreover, the steps often require optimisation to produce a suitable final output. All these mean that results from Western blots are semi-quantitative. Figure reproduced from Bass et al. (2017) under Creative Commons Attribution License (CC BY).

Wnt stimulation.

The IP columns show Western blot detection after the IP procedure. the "Axin IP" columns represent the proteins that bound to the anti-Axin antibody and the IP beads after the incubation period. Using the first row as an example, we can observe

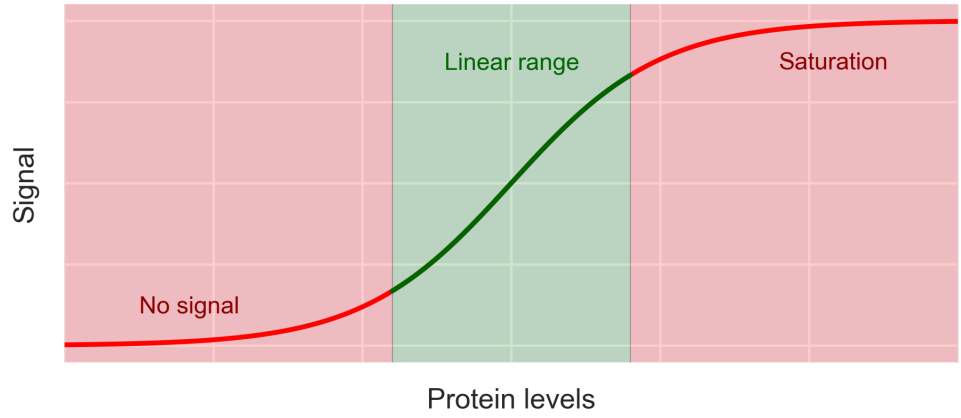


FIGURE 2.7: When carrying out Western blots, we must ensure that the system's linear range of detection is used. This range can vary depending on the blotting procedure, the protein of interest, the antibodies and substrates used, and the various incubation times. Beyond this range, the blot's signal strength may not correspond to the levels of protein in the sample.

that levels of β-catenin in complex with Axin drop from 0 to 30 minutes after Wnt stimulation before increasing again at 2 hours. The "con IP" column represent the sample that was incubated with beads and IGG antibody (a control antibody which should not bind to our proteins of interest). An empty column suggests that the beads did not bind non specifically to the various proteins of interest, validating the Axin IP.

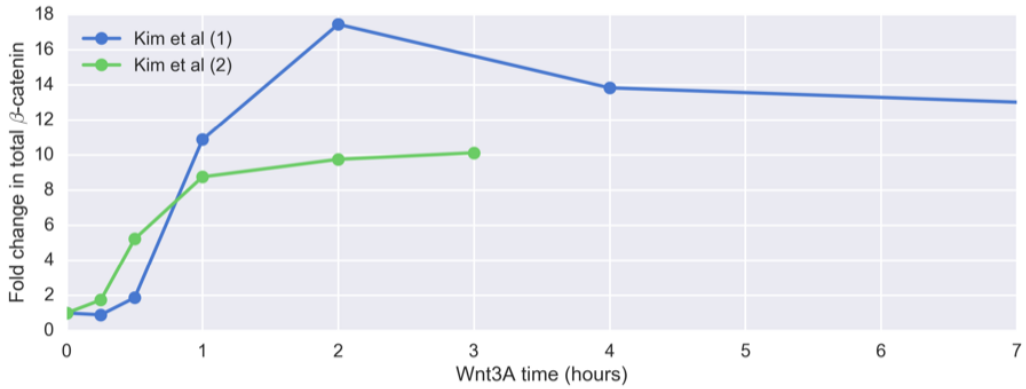
Mathematical models can be fitted to results from such experiments (e.g. Lee et al. (2003) and MacLean et al. (2015b) and many more) using sum of squared errors distance metrics that measure the distance between experimental observations and the mathematical model output. However, given the semi-quantitative nature, other fitting methods, such as satisfaction metrics, may be more appropriate (Pargett and Umulis, 2013). These metrics are defined such that if a particular requirement is satisfied, the distance is zero; otherwise the distance of the output from the edge of the satisfaction area is considered. We discuss satisfaction metrics further in Chapter 3.

2.3.4 Parameter Identifiability

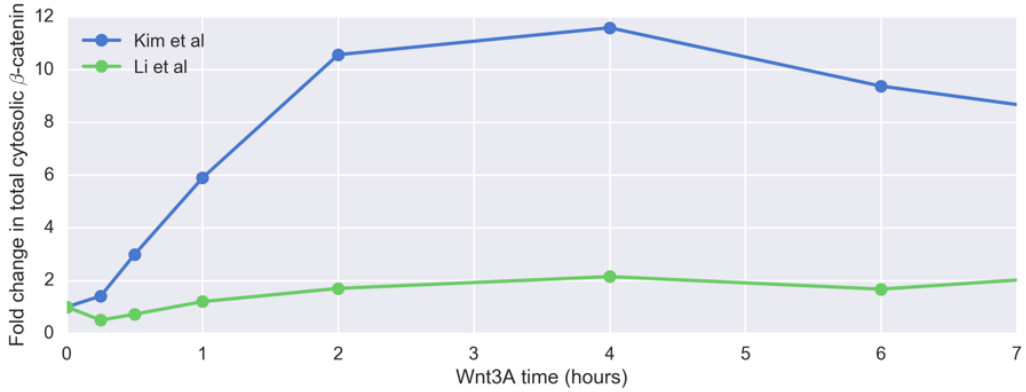
Parameter identifiability, i.e. the ability to find unique estimates of the true parameter values from experimental observations, is a significant hurdle in mathematical modelling of biological systems. Hines et al. (2014) demonstrate that even simple models of biochemical interactions could suffer from this problem, where markedly different parameter values provide equally good fits to the experimental data. Parameter identifiability could be structural (e.g. due to redundancies existing in model structure), or practical (e.g. due to the quality of the available experimental data (Raue et al., 2009)).

Parameter values for mathematical models of the Wnt pathway have been estimated from experimental results (Lee et al., 2003), however, parameter identifiability has not been investigated in such studies.

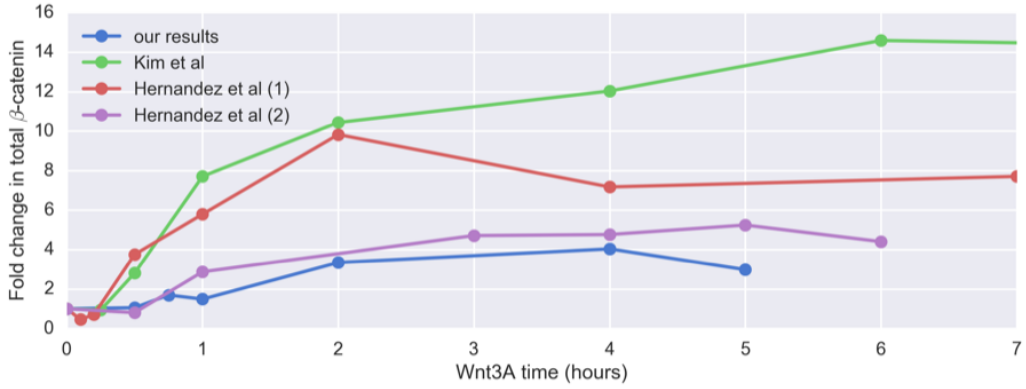
Several recent experimental studies of the Wnt pathway have provided time course results for levels of core Wnt pathway proteins (Li et al., 2012; Azzolin et al., 2014; Kim et al., 2013; Hernández et al., 2012). However, since these experiments have depended on semi quantitative techniques (e.g. Western blots, co-IP's), parameter identifiability remains a challenge. Despite this shortfall, it should still be possible to combine such semi-quantitative results alongside mathematical modelling to improve



(A) L-cells



(B) HEK293T



(C) RKO

FIGURE 2.8: Quantification of experimental results measuring fold change in levels of β-catenin upon Wnt stimultion in different studies in (A)L-cells, (B) HEK293T cells, and (C) RKO cells using the technique described in Appendix A. Different studies have yielded markedly different result. All results are from Western blots apart from our results which use immunofluorescence.

our understanding of the Wnt pathway. In particular, mathematical model selection may be used to select structures that are consistent with experimental observations and reject ones that are not.

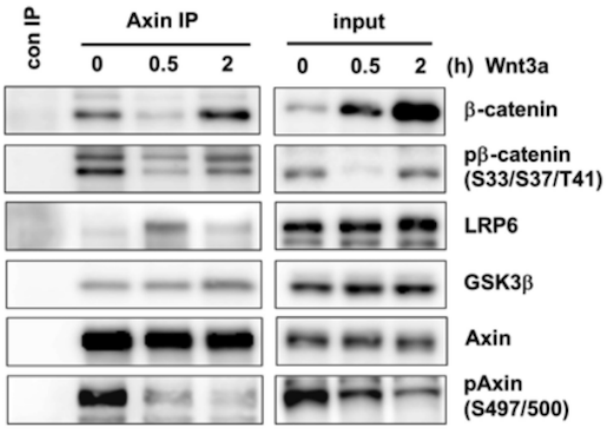


FIGURE 2.9: Example of a co-IP experiment ran using an anti-Axin antibody. The IP columns include the samples collected from the IP beads, so represent the levels of each protein pulled down in the IP experiment alongside Axin. The input columns include the samples before incubation with the beads, and hence should show the total protein levels in each sample. Figure reproduced from Kim et al. (2013) with permission.

2.3.5 Modelling based on population scale experimental results

By using experimental procedures such as Western blots and co-IP's to propose and fit models for subcellular signalling pathways, we are assuming that the observed population dynamics represent the dynamics of individual cells. In the intestinal crypts, certain cells are essential for Wnt secretion, driving Wnt signalling in neighbouring cells (Valenta et al., 2016). However, cell lines that are often used in *in vitro* experiments of Wnt pathway are not believed to secret Wnt. In these *in vitro* experiments, Wnt signalling in one cell, is not believed to effect signalling in neighbouring cells. However, in other pathways, such as Delta-Notch, where subcellular signalling in one cell directly alters the signal in a neighbouring cell (e.g. leading to alternating cellular patterns in the intestinal crypts) (Kay et al., 2017), caution must be exercised.

2.4 Summary and what is to come...

In this chapter we have provided a brief review of the biological literature involving the interactions between the core components of the Wnt pathway. We have summarised existing verbal models of the pathway. We have outlined the competing hypotheses about the deactivation of the destruction complex, and in particular the role played by LRP6. We have also reviewed some of the recent mathematical models of the Wnt pathway, starting with the first model of the pathway by Lee et al. (2003). In particular, we have detailed the different assumptions about where Wnt is assumed to act in these models.

We remark that none of the mathematical models have investigated the role that the LRP6 co-receptor and its conformational changes might play in the deactivation of the destruction complex and initiation of the Wnt signalling cascade. This is where our study of the Wnt pathway is focused as we believe mathematical modelling can reconcile differences in some of the experimental results.

We also touched briefly on the quality of data used in studies of signalling pathways and parameter identifiability. We recognised that with the existing procedures estimating suitable parameter values for a mathematical model of the Wnt pathway is

extremely difficult. Hence, instead of focusing parameter inference, we will focus on model selection in our study of the canonical Wnt pathway.

By recognising the qualitative or semi-quantitative nature of the available experimental data, we develop a framework that enables us to study the structure of the canonical Wnt pathway and thereby select the most suitable mathematical model among several candidate models.

In the next chapter we introduce the primary step in our model selection procedure which is based on the CMA-ES optimisation technique. We apply this technique to two case studies and compare its performance to a model selection technique based on Approximate Bayesian Computation (ABC). We use our results of this comparison to establish why we use the CMA-ES technique to study the Wnt pathway in Chapters 4 and 6.

Chapter 3

Model selection

3.1 Introduction

Signalling pathways are often modelled using ordinary differential equations (ODEs) (Alon, 2007). They may contain a large number of parameters which may be difficult to measure directly. There has been a large focus in systems biology on estimating parameter values for such models by fitting their outputs to experimental results (Toni et al., 2009; MacLean et al., 2015a; Vyshemirsky and Girolami, 2008).

As highlighted in Chapter 2, experimental observations and verbal modelling alone have proved insufficient in clarifying the dynamics of signalling pathways. Rather than parameter estimation, a primary contribution of mathematical modelling in this field may be to provide model selection techniques that enable us to discriminate between competing models of a signalling pathway.

Given the complexity of problems in systems biology, it is often intractable, or at least difficult, to enumerate all candidate models that are consistent with a set of experimental observations. Coghill et al. (2008) proposed a method called qualitative system identification that enables a modeller to discriminate between candidate model structures of signalling pathways. They studied the glycolysis pathway by considering thousands of possible combinations by which the 15 species of interest might interact. After several months of computation time on a 65 node cluster, they reduced the number of candidate models from 27,254 to 35. Using an alternative approach, Lee et al. (2003) proposed the first mathematical model of the canonical Wnt pathway, which involved 15 species, without discussing competing model structures that may be consistent with observed experimental results.

We believe that there is a middle ground between rigorous model selection and ad-hoc model proposals. By taking a multidisciplinary approach, and combining prior knowledge, mathematical modelling, experimental work and a detailed review of the literature, it should be possible to propose a small set of candidate models for the pathway of interest. If these candidate models are analysed using model selection techniques, they could inform us further about the appropriate structure of the signalling pathway, and may enable us to discriminate between competing structures by identifying further targeted experiments. In line with our view, there has recently been a shift towards model selection rather than parameter estimation. Model selection techniques are being developed and used to identify the models that may best reproduce biological observations (MacLean et al., 2015b; Kirk et al., 2013; Vyshemirsky and Girolami, 2008).

We start this chapter by summarising several model selection techniques, focusing on the classical or frequentist approach and the Bayesian approach. We then introduce the technique we use to study the canonical Wnt pathway in Chapter 4 together with an alternative based on Approximate Bayesian Computation (ABC) (Toni et al., 2009). Finally, we compare the two methods by applying them to two case studies.

3.2 Literature Review

Two main approaches are used for parameter estimation and model selection: these are the classical or frequentist approach and the Bayesian approach. In the former, the correct parameter values of a model are assumed to be fixed, and any difference between the model output and observed experimental results viewed as errors in quantities such as measurements. In this approach, one considers a confidence interval (CI), where the probability associated with the CI (e.g. 95%) is the probability that the CI covers the true parameter value. In the Bayesian approach, we do not consider parameter values to be fixed. Instead the uncertainty observed in the experimental observations are propagated to the parameter values, such that probability distributions of these parameters determine the range of feasible model parameter values.

3.2.1 Classical methods of parameter inference and model selection

One of the most widely used techniques for model selection is classical hypothesis testing. Typically, a null hypothesis (e.g. H_0: a coin used in a series of coin tosses is fair) and an alternative hypothesis (e.g. H_1: the coin is not fair) are proposed. Through an appropriate statistical test (e.g. two-tailed Binomial test), the null hypothesis may be rejected if there is sufficient evidence that the observed experimental results are unlikely (e.g. if the *p-value*, the probability of the observed results under hypothesis H_0 is less than a threshold, such as 0.05) (Neyman and Pearson, 1933; Cedersund and Roll, 2009).

An important function in many parameter inference and model selection techniques is the likelihood function. The likelihood function of a model or hypothesis H, with parameter vector θ_H for a set of observations x is defined as:

$$L_H(\theta_H|x) = P(x|\theta_H, H), \tag{3.1}$$

where $P(x|\theta_H, H)$ is the probability density function under model H, given parameter vector θ_H. The likelihood is a function of the parameter vector θ_H, and describes the probability of data x being observed given parameter vector θ_H under model H. Under the frequentist approach one might estimate the appropriate parameter vector $\hat{\theta}_H$ for a set of observations by maximising the likelihood function (maximum likelihood estimation or MLE).

If the models being studied are nested, i.e. the null hypothesis is a special case of the alternative, the likelihood ratio test is commonly used for model selection. Notice in the likelihood ratio test, the alternative model is always more complicated than the null hypothesis, a simple comparison of maximum likelihood values is not sufficient, and a statistical test is required. If the models are not nested, or when several models are being compared it may be appropriate to use alternative measures. For example, Akaike's Information Criterion (AIC):

$$\text{AIC}_H = -2 \log L_H(\hat{\theta}_H|x) + 2n_H, \tag{3.2}$$

may be suitable, where $\hat{\theta}_H$ is the parameter vector corresponding to the maximum likelihood, and n_H is the number of parameters in model H. While the first term is a measure of goodness of fit, the second term penalises complicated models. The best fit is then provided by the model with the lowest AIC value, although there is no guarantee that such a model is in fact a good fit (MacLean et al., 2015a).

We note that finding the maximum value of the likelihood function often involves a non-trivial non-linear optimisation, which may require careful investigation (Gould and Leyffer, 2003; Raue et al., 2013).

3.2.2 Bayesian methods of parameter inference and model selection

The use of Bayesian inference in parameter estimation and model selection has become increasingly more common in many scientific fields including systems biology (Wilkinson, 2007). This is for several reasons including the advantages they offer over existing frequentist methods, new inference techniques, increasing availability of off-the-shelf software packages and increasing computing power (Kirk et al., 2013).

Bayesian parameter estimation and model selection use new observations to update our existing belief of unknown model parameters (the prior distribution) by calculating an updated belief (the posterior distribution). This is possible thanks to the Bayes theorem:

$$P(\theta_H|x, H) = \frac{P(x|\theta_H, H)P(\theta_H|H)}{P(x|H)}, \tag{3.3}$$

where $P(\theta_H|x, H)$ is the posterior distribution, $P(x|\theta_H, H) = L_H(\theta_H|x)$ is the likelihood function, and $P(\theta_H|H)$ is the prior. $P(x|H)$ is the marginal likelihood or the evidence of the observation x under model H:

$$P(x|H) = \int_\theta P(x|\theta_H, H)P(\theta_H|H)\mathrm{d}^{n_H}\theta_H, \tag{3.4}$$

where $\int \mathrm{d}^{n_H}\theta_H$ represents integration over the n_H-dimensional parameter space. This can be difficult to evalulate in high-dimensional cases. Another challenge is that in many cases it is impossible to calculate a closed form for the posterior distribution $P(x|H)$. One special case where this is possible is the case of conjugate-distributions. For example, a Gaussian distribution with an unknown mean is a conjugate prior for a Gaussian likelihood function; meaning in such cases the posterior is also a Gaussian distribution.

These computational difficulties limited the use of Bayesian techniques for inference until the introduction of Markov Chain Monte Carlo (MCMC) methods (Gelfand and Smith, 1990). MCMC methods, such as Gibbs or Metropolis-Hastings samplers, allow sampling from the posterior distribution only up to the proportionality, i.e. without the need to calculate the normalisation constant, the evidence $P(x|H)$:

$$P(\theta_H|x, H) \propto P(x|\theta_H, H)P(\theta_H|H), \tag{3.5}$$

which removes the need to calculate the high dimensional integral in Equation (3.4).

Model selection

When considering model selection, given a set of m candidate models $H_i, i = 1, \ldots, m$, we may use Bayes theorem to update the probability of model H_i given observation x:

$$P(H_i|x) = \frac{P(x|H_i)P(H_i)}{\sum_{j=1}^{m} P(x|H_j)P(H_j)}. \tag{3.6}$$

We may then use the observation x to compare the posterior probabilities for any two models H_i and H_j:

$$\frac{P(H_i|x)}{P(H_j|x)} = \frac{P(x|H_i)P(H_i)}{P(x|H_j)P(H_j)}. \tag{3.7}$$

An important metric for Bayesian model selection is the Bayes Factor:

$$B_{ij} = \frac{P(x|H_i)}{P(x|H_j)}, \tag{3.8}$$

which may be re-written using Equation (3.7):

$$B_{ij} = \frac{P(H_i|x)/P(H_j|x)}{P(H_i)/P(H_j)}. \tag{3.9}$$

The Bayes factor B_{ij} may be interpreted as the ratio of posterior odds over the prior odds for H_i and against H_j. Kass and Raftery (1995) suggest the Bayes factor may be used to measure the evidence for and against a particular model versus another model (see Table 3.1). We remark that if we assume a uniform prior over all models, such that $P(H_i) = P(H_j)$, the ratio of the model posteriors is equal to the Bayes factor.

Bayes Factor B_{ij}	**Evidence for H_i and against H_j**
1-3	very weak
3-20	positive
20-150	Strong
> 150	Very Strong

TABLE 3.1: Kass and Raftery (1995) propose how Bayes factor should be used to compare evidence for and against two models.

Notice that in the problem of model selection unlike parameter inference, the integral in Equation (3.4) may not be avoided. In such cases methods such as Thermodynamic Integration (Vyshemirsky and Girolami, 2008) and Nested Sampling (Skilling and John, 2004; Feroz et al., 2009) may be used to estimate this integral numerically.

3.2.3 Approximate Bayesian Computation

The techniques discussed in the last two sections require calculation of the likelihood function, which may be intractable or expensive. In such cases, Approximate Bayesian Computation (ABC) methods may be employed to infer parameter values and perform model selection. Provided that a distance function can be defined to measure the goodness of fit between a model output x and an experimental observation x_0, ABC methods can be used to replace calculation of the likelihood with repeated simulation of the model.

The simplest ABC method is the ABC rejection sampler (Pritchard et al., 1999), which can have a very low acceptance rate. Inference in this algorithm is as follows. Sample a parameter set θ^* from the prior distribution $P(\theta)$. Simulate the model using the sampled parameter set to generate a model output x^*. Accept the sampled parameter set if the distance $d(x_0, x^*)$ between x_0 and x^* is less than the tolerance ϵ. The output of ABC rejection sampler will be a set of samples from a distribution $P(\theta|d(x_0, x^*) < \epsilon)$, which will be an approximation to the posterior distribution $P(\theta|x_0)$ as $\epsilon \to 0$.

Other methods include ABC MCMC (Marjoram et al., 2003), and ABC methods based on Sequential Monte Carlo (SMC) (Sisson et al., 2007; Toni et al., 2009). In the next section, we will detail an ABC SMC technique (Toni et al., 2009) and compare it to the multi-start Covariance Matrix Adaptation Evolutionary Strategy (CMA-ES) technique.

A note on summary statistics. In order to keep the problem of sampling from a high dimensional parameter space computationally efficient, the distance $d(x_0, x^*)$ is often replaced with distance between a set of summary statistics $d^*(S(x_0), S(x^*))$, which captures the important features of the experimental observations. If the summary statistics are sufficient then this leads to no loss of information compared to using all data points. However, often informative but not necessarily sufficient summary statistics are used.

3.3 Methods

As the experimental data we are using to study the structure of signalling pathways are semi-quantitative, we are not able to write down a suitable likelihood function for our candidate models. Therefore, we need to recruit *likelihood free* methods for model selection. In this section we will describe two such model selection techniques, one based on Approximate Bayesian Computation (Toni et al., 2009), and another based on the CMA-ES optimisation technique (Hansen, 2006). We apply the two techniques to different case studies to compare their performance. We find that the ABC SMC technique can account for model complexity during model selection and provide information about the range of suitable parameter values. On the other hand, CMA-ES is more computationally efficient and can perform model selection with considerably fewer model simulations.

Following Toni et al. (2009), our first case study focuses on the spread of infectious diseases. We apply the ABC SMC and CMA-ES to two datasets; a synthetic dataset where the correct model is known and a real dataset from an epidemiological study.

Our second case focuses on simple models of signalling pathways. We consider two candidate models of Feed Forward Loops (FFLs). We use one of the models to generate a synthetic dataset, before studying whether ABC SMC and CMA-ES are able to identify the correct model. We also introduce the concept of *qualitative comparison* of experimental results and model outputs, which we will use in our study of the canonical Wnt pathway in the next chapter.

3.3.1 ABC SMC technique

The aim of Approximate Bayesian Computation Sequential Monte Carlo (ABC SMC) is to develop an approximation to the posterior distributions of model parameters. In order to approximate these posterior distributions, ABC SMC uses a series of prescribed and decreasing population tolerance levels $\epsilon_0, \ldots, \epsilon_T$ (see e.g. Table 3.2) to calculate T intermediate approximations to the probability distributions for the parameter vector. In the first step, the algorithm samples the parameter vector from the priors, and points are accepted if their distance is within the step tolerance ϵ_0. Once a specific number of particles are accepted, the distribution of the new population and, in particular, the weights calculated for each particle, form the prior for the next set of samples. After the first population, particles are sampled from the particles accepted in the last population and perturbed using a perturbation kernel, before being accepted or rejected

using the new tolerance value. This process is repeated until the smallest tolerance is reached. The distribution of the final population is the algorithm's approximation to the posterior distribution of the parameter vector (Toni et al., 2009). Figure 3.1A summarises this process.

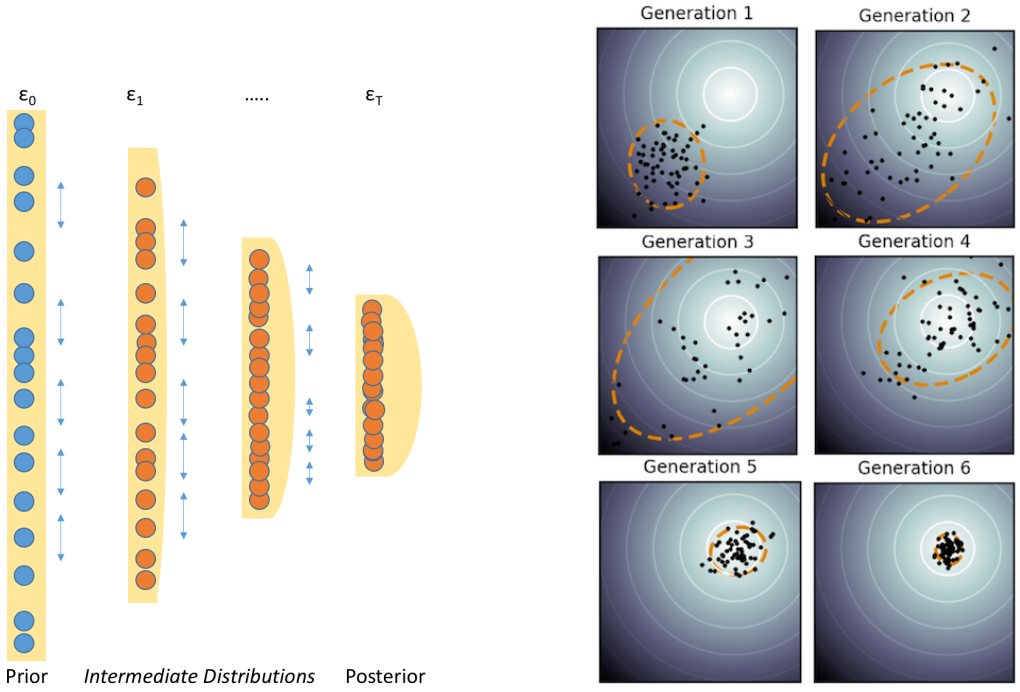


FIGURE 3.1: (A) Progress of ABC SMC algorithm in finding an approximation to the posterior distribution of a model parameter value in 1D. Particles are initially sampled and accepted from the prior. Accepted particles are then perturbed and accepted with a reduced tolerance in the next population. (B) Progress of CMA-ES algorithm in finding the minimum of a function in 2D. The black dots represent the sampled particles in each population. The white solid lines represent areas with the same function value. The orange dashed line represents a measure of the shape and size of the distribution of the current population. Figure reproduced from work by Nikolaus Hansen (Hansen, 2006) under Commons license.

The algorithm may also be used for model selection by introducing a new parameter $h = 1, \ldots, m$, which samples from the possible models under observation. Depending on which model is represented, each particle carries a parameter vector for the corresponding model. At each step in the ABC SMC model selection algorithm, we first sample from the model prior, before sampling from the particles corresponding to the sampled model. Particles are accepted or rejected and the populations are progressed as before.

If the algorithm fails to sample any particles from a particular model in a given population, that model is regarded as dead, and sampling continues with the remaining models. The weighted average of the number of particles remaining for each model in the final population may be used to calculate the model marginals and Bayes factors.

We used an improved implementation of *abc-sysbio* package (Liepe et al., 2010) for ABC SMC model selection. Our version, available at https://github.com/oofaish/abc-smc-bare, contains various bug fixes. We also implemented a new interface that enables the user to interact with the package programmatically without

Case Study	Particles	Populations	Population tolerances $\epsilon_0, \ldots, \epsilon_T$
one (common-cold)	1000	17	100.0, 90.0, 80.0, 73.0, 70.0, 60.0, 50.0, 40.0, 30.0, 25.0, 20.0, 16.0, 15.0, 14.0, 13.2, 12.8, 12.4
one (synthetic)	200	14	1000, 774, 599, 464, 359, 278, 215, 190, 170, 140, 120, 105, 100, 98
two (FFL networks)	50	5	1.0, 0.5, 0.4, 0.3, 0.25

TABLE 3.2: Algorithm parameter values under ABC SMC model selection. In the common-cold dataset, the same values were used as Toni et al. (2009). In the other case studies, the first population tolerance was chosen after trial and error to ensure the ABC SMC method has a reasonable acceptance ratio in the first population, while the rest of the population tolerances were chosen to be exponentially decreasing. The number of particles and number of populations were chosen again via trial and error to be low without the algorithm failing to sample all models in the first step or leading to a very low acceptance ratio.

using the SBML interface. The original *abc-sysbio* package assumes that all models are implemented as a system of ordinary differential equations, and solved using an ODE solver. Our implementation removes this assumption and allows arbitrary model definition and cost functions. It also provides improved tools for visualising the inference results. For our problem of interest, and in order to compare our results with Toni et al. (2009), most ABC SMC technique parameters were fixed at the default values prescribed by Liepe et al. (2010) and Toni et al. (2009). In particular, each particle was perturbed to another live model with probability 0.3. Moreover, a uniform parameter perturbation kernel $\mathcal{U}[-\sigma/2, +\sigma/2]$ was used where σ is the maximum range of the parameter being sampled in the last population. We remark that this differs from the perturbation kernel used by Toni et al. (2009), where the value of σ is fixed. However, as the results in Section 3.4.3.1 reveal, the model selection outcome is consistent with Toni et al. (2009). Table 3.2 summarises the remaining algorithm parameter values used in each case study. The aim of the first part of this chapter is to reproduce the results by Toni et al. (2009). In Section 3.4.3.1, we establish that we can replicate the results from Toni et al. (2009). We discuss the selection of the parameter values for the model selection algorithms further in Section 3.6.

3.3.2 Multi-start CMA-ES Algorithm

The main aim of our thesis is to develop a better understanding of the structure of signalling pathways. Since many experimental techniques generate outputs that are not quantitative, we hope to establish whether a particular mathematical model can replicate results that are qualitatively similar to the experimental observations. We seek to infer which structures are consistent with experimental observations and which are not, rather than necessarily to infer parameter values. Consequently, we focus on techniques that allow us to explore the output space and accept and reject model structures quickly.

The initial step in model selection is simple. We develop a metric that measures the distance between model output and the experimental observations, and attempt to minimise this metric globally. If all candidate mathematical models have similar levels of complexity, and if there is a clear favourite among these models (with the lowest distance to the experimental observations), that model is selected. We use a multi-start CMA-ES optimisation algorithm to tackle this global minimisation problem.

The Covariance Matrix Adaptation Evolutionary Strategy (CMA-ES) optimisation

algorithm (Hansen, 2006) starts from an initial estimate for the parameter vector and points are sampled from a multivariate normal distribution centred about this vector. The cost function J is calculated at each new sampled point, and a new mean is calculated using a weighted average of the lowest cost points, while the covariance matrix, which holds the pairwise correlation between the random variables corresponding to each element of cost vector, is updated to reflect a skew towards these low cost points (Hansen, 2006).

Figure 3.1B displays the progress of the CMA-ES algorithm in a typical minimisation run. We use the Python implementation of the CMA-ES algorithm (see: https://pypi.python.org/pypi/cma).

The multi-start technique initialises the CMA-ES algorithm at N different points to allow a better exploration of the parameter space. We select these N starting points at random in log space. The parameter vector corresponding to the lowest cost is selected as the final optimisation result.

Depending on the dimensionality of the parameter space, we initiate the algorithm at different numbers of starting points. For the problems considered in this chapter one starting point is sufficient. We discuss how to select and validate the number of starting points further in Chapter 4 where we deal with higher dimensional problems.

3.4 Case study 1: Spread of infectious diseases

We apply the two model selection techniques to four different SIR models that may describe the 'spread of infectious diseases. These models decompose the population into three or more distinct groups; susceptible (S), who do not have immunity to the given disease; infected (I), who are carrying the disease and can infect others; and recovered (R), who cannot be re-infected and cannot pass on the disease. An extension to the basic SIR model is the SEIR model which includes a population who have been infected, or Exposed (E) to the infection, and show signs of infection but are not yet infectious, unlike the infected (I) sub-population. Another extension is the SIRS model, where the recovered population could become re-susceptible after a period. The final alternative we consider is the SIR-delay model, where an infected person becomes infectious only after a latent period. This is implemented via a delay differential equation. The SIR-delay and SEIR models account for delays in becoming infectious, but in different ways. Table 3.3 displays a summary of these four models.

The temporal dynamics of each model may be formulated as a system of ordinary differential equations (ODEs), or delay differential equations for the SIR-delay model. We represent these systems of differential equations below. The colours red, blue and green represent the total susceptible, infected (and exposed), and recovered populations, respectively.

The SIRS model may be written as

$$\frac{\mathrm{d}S}{\mathrm{d}t} = B - \beta SI/N(t) - \mu S + \nu R, \tag{3.10}$$

$$\frac{\mathrm{d}I}{\mathrm{d}t} = \beta SI/N(t) - (\gamma + \mu)I, \tag{3.11}$$

$$\frac{\mathrm{d}R}{\mathrm{d}t} = \gamma I - (\mu + \nu)R, \tag{3.12}$$

where B and μ represent the Birth and Death rates, β is the contact rate between the

Model	Groups	Parameters in addition to SIR parameters	Equations	Notes
SIR	3 (susceptible, infected, recovered)		(3.10-3.12)	
SIRS	3 (susceptible, infected, recovered)	Re-susceptibility rate	(3.10-3.12)	Recovered population can become susceptible again.
SEIR	4 (susceptible, exposed, infected, recovered)	Latent period	(3.13-3.16)	Latent individuals show signs of infection but are not infectious.
SIR-delay	3 (susceptible, infected, recovered)	Latent period	(3.17-3.19)	A time-delay accounts for the delay between catching a disease and becoming infectious. A system of Delay differential equations (DDEs) is used to model the temporal dynamics.

TABLE 3.3: Summary of the four SIR-based models for studying the spread of infectious diseases in a population. The basic SIR model contains 5 parameters: birth rate, death rate, period before contact with an infected person, recovery period, and initial population.

susceptible and infected populations, $1/\gamma$ is the average infection period, and $1/\nu$ is average period before which a recovered person becomes susceptible again. $N(t) = S(t) + I(t) + R(t)$ represents the total population count at time t. The SIRS model simplifies to the SIR model when $\nu = 0$.

The SEIR model may be written as

$$\frac{\mathrm{d}S}{\mathrm{d}t} = B - \beta SI/N(t) - \mu S, \tag{3.13}$$

$$\frac{\mathrm{d}E}{\mathrm{d}t} = \beta SI/N(t) - (\epsilon + \mu)E, \tag{3.14}$$

$$\frac{\mathrm{d}I}{\mathrm{d}t} = \epsilon E - (\gamma + \mu)I, \tag{3.15}$$

$$\frac{\mathrm{d}R}{\mathrm{d}t} = \gamma I - \mu R, \tag{3.16}$$

where $1/\epsilon$ represents the average latent time for an exposed person.

Finally, the SIR-delay model may be written

$$\frac{\mathrm{d}S}{\mathrm{d}t} = B - \beta SI(t-\tau)/N(t) - \mu S, \tag{3.17}$$

$$\frac{\mathrm{d}I}{\mathrm{d}t} = \beta SI(t-\tau)/N(t) - (\gamma + \mu)I, \tag{3.18}$$

$$\frac{\mathrm{d}R}{\mathrm{d}t} = \gamma I - \mu R, \tag{3.19}$$

where τ represents the time period before an infected individual becomes infectious. All parameter values are assumed constant and positive. We did not nondimensionalize the SIR models for consistency with Toni et al. (2009).

For all simulations we assume the following initial conditions: one infected individual, with the rest of the population susceptible. These models were implemented in Python and solved numerically using the scipy (Jones et al., 2001) and pydelay (Flunkert and Schoell, 2009) packages.

In order to compare model outputs with observations, we sample the model outputs at n time points and compare the number of infected individuals and recovered individuals (I^i and R^i for $i = 1, \ldots, n$) with observations (I_0^i and R_0^i for $i = 1, \ldots, n$). For the SEIR model, members of the latent population E are considered infected, such that total infected individuals at time t is $I(t) + E(t)$. We calculate sum of squared errors to compare the model outputs with the true dataset:

$$J = \sum_{i=1}^{n} \left((I^i - I_0^i)^2 + (R^i - R_0^i)^2 \right). \tag{3.20}$$

3.4.1 Dataset from outbreak of common-cold in Tristan da Cunha collected in October 1967

In order to validate our implementation of the ABC SMC algorithm, we first tried to reproduce the model selection results from Toni et al. (2009). The authors investigate which SIR model best describes the outbreak of common-cold on an isolated island in the Atlantic Ocean with a population of 300 inhabitants. Table 3.4 contains the true dataset for this case study.

Day	1	2	3	4	5	6	7	8	9	10	11	12	13	14	15	16	17	18	19	20	21
Infected	1	1	3	7	6	10	13	13	14	14	17	10	6	6	4	3	1	1	1	1	0
Recovered	0	0	0	0	5	7	8	13	13	16	24	30	31	33	34	36	36	36	36	36	37

TABLE 3.4: Common-cold data from Tristan da Cunha collected in October 1967.

Table 3.5 summarises the priors used as input to the ABC SMC algorithm. The range of the prior distributions was used to bound the search space in the multi-start CMA-ES algorithm. We denote by $\mathcal{C}(x)$ a constant prior fixed at value x, and $\mathcal{U}(x, y)$ to represent a uniform prior over the interval (x, y).

3.4.2 Synthetic dataset

Here we apply the model selection methods to a problem where the true model is known. We generate synthetic data from the SEIR model and then compare the ability of each technique to recover this model. Column "True" in Table 3.5 details the parameter values used to generate the synthetic data. We note that we assume a population of 1000 individuals, and make the problem more realistic by adding Gaussian noise $\propto \mathcal{N}(0, 10^2)$ to the true output. We sample 20 data points from the time series of susceptible, infected and recovered populations.

3.4.3 Results

We applied the two model selection techniques to four SIR models (SIR, SIRS, SEIR and SIR-delay). We consider two different datasets. The first dataset is the common-cold data collected from Tristan da Cunba in 1967 and given in Table 3.4. Toni et al. (2009) applied the ABC SMC model selection technique to these data, and we replicate their computations to validate our implementation. For the second dataset, we apply the two model selection techniques to synthetic data generated using the SEIR model.

Parameter Sampled	Description	True (synthetic)	Units	Prior (synthetic)	Prior (common -cold)
B	Birth rate	0	individuals/day	$\mathcal{C}(0)$	$\mathcal{C}(0)$
μ	Death rate	0	1/day	$\mathcal{C}(0)$	$\mathcal{C}(0)$
$1/\beta$	Period before contact	2	days	$\mathcal{U}(1,10)$	$\mathcal{U}(1,10)$
$1/\gamma$	Recovery period	10	days	$\mathcal{U}(1,30)$	$\mathcal{U}(1,30)$
$1/\epsilon$	Latent period	7	days	$\mathcal{U}(1,10)$	$\mathcal{U}(0,5)$
τ	Latent period		days	$\mathcal{U}(1,10)$	$\mathcal{U}(0,5)$
ν	Re-susceptiblity rate		1/day	$\mathcal{U}(0,1)$	$\mathcal{U}(0,5)$
N	Initial population	1000	individuals	$\mathcal{C}(1000)$	$\mathcal{U}(37,100)$

TABLE 3.5: Description of parameters that appear in the SIR models of Section 3.4. The two model selection techniques were applied to two datasets, a synthetic dataset (generated using the SEIR model with values given in the "True" column) and the data of the outbreak of common-cold, as used by Toni et al. (2009). We used what we believe are reasonable priors (and bounds).

3.4.3.1 Dataset from outbreak of common-cold in Tristan da Cunha collected in October 1967

Figure 3.3B displays the progress of the model marginals (i.e. weight adjusted ratio of the number of accepted particles corresponding to each model at each population) alongside the population tolerance. Initially all models are equally likely, before the SIR-delay model becomes more favourable. As in Toni et al. (2009), the most favourable model switches from the SIR-delay to the SEIR model as the tolerance level drops. This plot is consistent with Figure 7 of Toni et al. (2009), where histograms for each population of particles are used to represent the model marginals.

Figure 3.3C shows how the ratio of accepted to sampled particles changes over successive populations. As the tolerance drops, the ratio also drops.

In Figure 3.4 we present our approximations to the posterior distributions for the parameter values in the SEIR model. The diagonal sub-figures display the approximation to the posterior distribution from the final population, whereas the non-diagonal terms display the cross-correlation between the different parameter values for all populations.

While the ABC SMC technique gives a measure of the model marginals, the CMA-ES technique only gives a measure of the goodness of fit of each model to the observations. Figure 3.2 displays the best fitting model outputs corresponding to parameter values found using CMA-ES, which are displayed in Table 3.6. The SEIR model produces an output closest to the experimental observations. However, all other models produce reasonable fits. Notice that the SIR model is a special case of the SIRS model, and given the same lowest cost, we would select the simpler SIR model.

Table 3.7 summarises these results from the two model selection techniques. In both cases the SEIR model gives the best 'fit', however, as we see in Figure 3.2, all four SIR models produce good fits to the experimental results and the fact that the SEIR model provides the lowest numerical cost is not particularly meaningful. Despite this remark, we note that using the ABC SMC technique we can calculate evidence for and against each model. For example, the Bayes factor for the SEIR model against the SIR-delay model is 5.83, which falls under 'Positive Evidence' according to Table

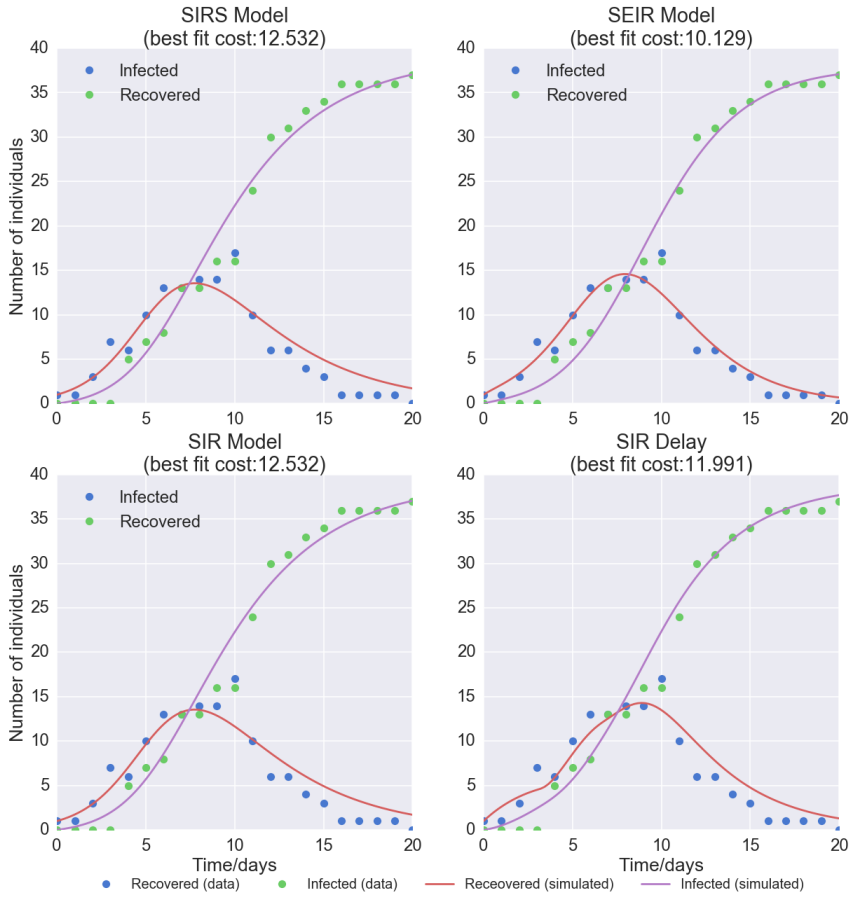


FIGURE 3.2: Results of fitting four different models for the spread of infectious diseases to common-cold data from Tristan da Cunha using CMA-ES. SEIR produces the closest output to the observations.

3.1. We note that the choice of final tolerance (12.4 in our study) is arbitrary, and it should be evident that if the ABC SMC technique was run to a lower tolerance and, in particular, for a tolerance below 12.0 (the lowest distance between SIR-delay model and the experimental observations), then the model marginal for the SEIR model would converge to 1.0 and the Bayes factor would suggest very strong evidence for the SEIR model against the SIR-delay model. This again reiterates that caution must be exercised when considering the results of such model selection techniques.

3.4.3.2 Synthetic dataset

Synthetic data was generated using the SEIR model with Gaussian noise added. Our aim here is to establish whether the two model selection techniques can recover the model that was used to generate the data. Table 3.9 summarises the results of the model selection. Using CMA-ES, we can find a parameter set for the correct model that has a cost 70% below the closest competitor (30.2, compared to costs of 180.8, 180.8 and 99.1 for the three incorrect models). Table 3.8 summarises the resulting parameter estimates while Figure 3.5 shows the best fits.

The ABC SMC technique also identified the correct model. Figures 3.6B and 3.6C show how the model marginals and acceptance ratios change as the population tolerances drop. We note that the marginal distribution converges to one as the population

	SIRS	SEIR	SIR	SIR-delay
N	41	39	41	39
$1/\beta$	0.85	1.84	0.85	2.21
$1/\gamma$	0.27	0.51	0.27	0.26
ν	0.00			
$1/\epsilon, \tau$		0.57		3.20

TABLE 3.6: The parameter values found by fitting each SIR model to the common-cold dataset using the CMA-ES technique.

Model	**Free Parameters**	**Lowest Cost (CMA-ES method)**	**Model Marginals (Toni et al., 2009) (17 iterations, final $\epsilon = 12.4$)**
SIRS	4	12.532	0
SEIR	4	10.129	0.85
SIR	3	12.532	0
SIR-delay	4	11.991	0.15

TABLE 3.7: Summary of results when ABC SMC and CMA-ES model selection techniques are applied to outbreak of common-cold data in Tristan da Cunh.

Sampled parameter	**SEIR (true values)**	**SIRS**	**SEIR**	**SIR**	**SIR-delay**
$1/\beta$	2	4.51	1.77	4.51	1.76
$1/\gamma$	10	18.08	8.74	17.44	17.44
ν		0.00			
$1/\epsilon, \tau$	7		8.17		7.72

TABLE 3.8: The parameter values used to generate the synthetic data using the SEIR model before addition of Gaussian noise $\propto \mathcal{N}(0, 10^2)$, alongside the parameter values found using the CMA-ES technique.

Model	**Free Parameters**	**Lowest Cost (CMA-ES method)**	**Model Marginals (Toni et al., 2009) (14 iterations, final $\epsilon = 98$)**
SIRS	3	180.8	0.0
SEIR (true)	3	30.2	1.0
SIR	2	180.8	0.0
SIR-delay	3	99.1	0.0

TABLE 3.9: Summary of model selection using ABC SMC and CMA-ES applied to synthetic data generated from SEIR model and Gaussian noise added. Both methods identify the correct model.

tolerance approaches the lowest cost found by the CMA-ES algorithm.

In Figure 3.6A we present the output from the particles sampled in the last population to illustrate the accepted range compared to the true data. With noisy data, ABC SMC can estimate the posterior distribution for the parameters that fit the true data. Figure 3.7 displays the approximation to the posterior distributions for the parameters in the SEIR model as fitted to the synthetic data in our case study.

As one might expect, the recovery period for infected individuals is negatively correlated with the latent period. Similarly the longer the recovery period, the shorter the

period before a susceptible individual gets infected (or the higher the rate of infection). Equally, the latent period is negatively correlated with the period before contact.

We also investigated how the results of model selection varies at different noise levels. We generated synthetic data using the SEIR model and added noise with different standard deviations to create a target dataset. We then used CMA-ES to investigate whether we are able to identify the correct model. Figure 3.8 displays how the lowest cost found under each model varies at different noise levels. At 5% noise, the technique often failed to identify the true model, however, in our analysis, at 1% it was able to identify SEIR model as the correct model. Moreover, at 1% noise, the lowest cost for the SEIR (true model) is at least 2.5 times lower than other models, whereas at higher noise levels, this ratio is much smaller, which should raise further questions about the reliability of the model selection results.

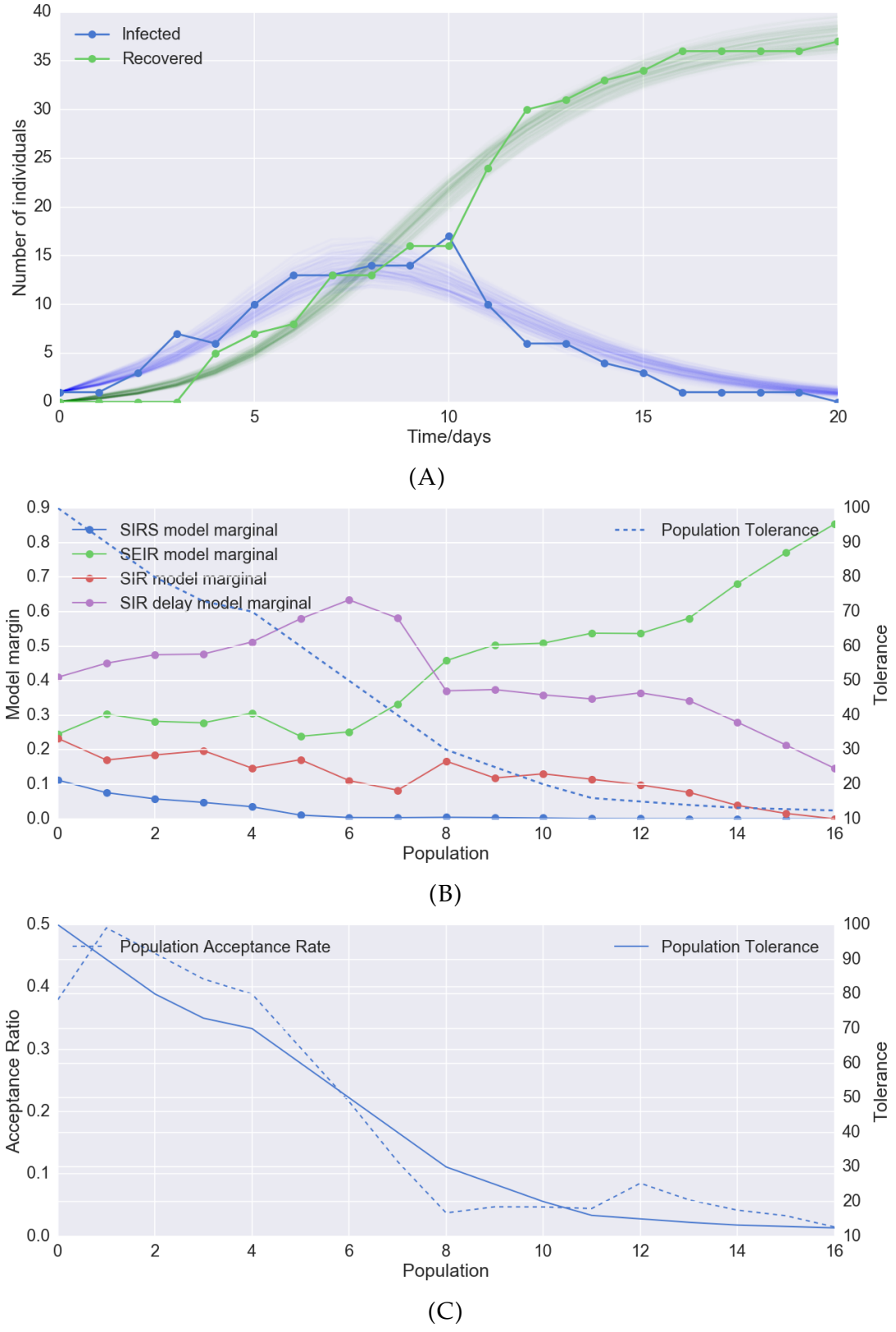


FIGURE 3.3: Reproducing model selection results for common-cold data from Tristan da Cunha from Toni et al. (2009). As the tolerance is reduced, SEIR, which has the lowest cost as found by CMA-ES algorithm, becomes more favourable. (A) The original data and model output from 200 particles with the highest weights from the last population. (B) The change in the model marginals as the tolerance ϵ drops in ABC SMC model selection. From populations zero to seven, the SIR-delay model seems to be the more suitable model. (C) Acceptance ratio for different populations of particles.

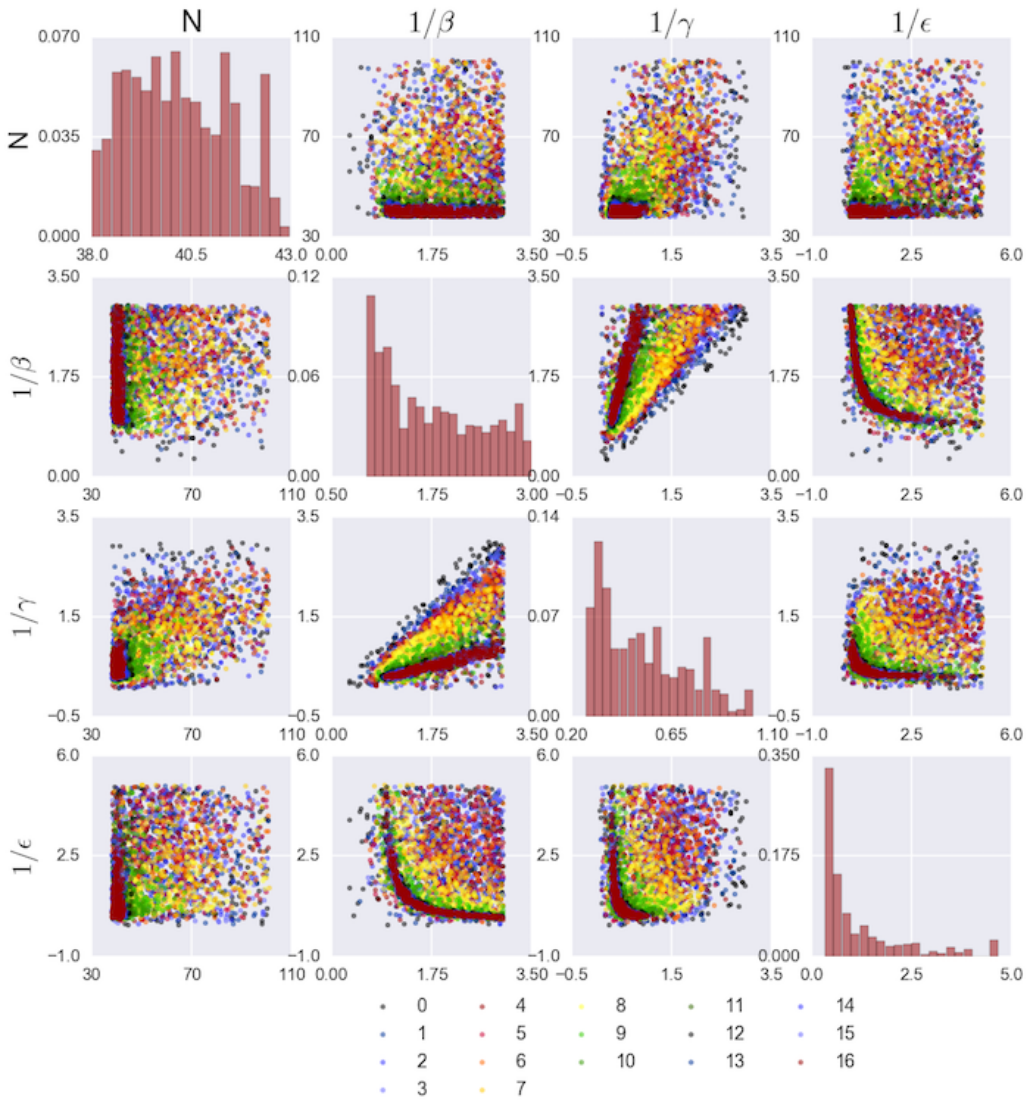


FIGURE 3.4: Parameter inference for the SEIR model fitted to common-cold data from Tristan da Cunha. A pair plot displaying an approximation to the posterior distribution for parameter values for the SEIR model and scatter plots of pair wise relationships between its parameter values. The histograms are from particles accepted under the final tolerance levels, whereas the scatter plots include values from particles accepted at intermediate tolerance levels during the ABC SMC algorithm. We remark that the ABC SMC final tolerance (12.4) is close to the lowest cost found by CMA-ES (10.129), however, the final approximation to the posterior distributions are still wide, suggesting that the model parameters are not identifiable from the given set of experimental observations.

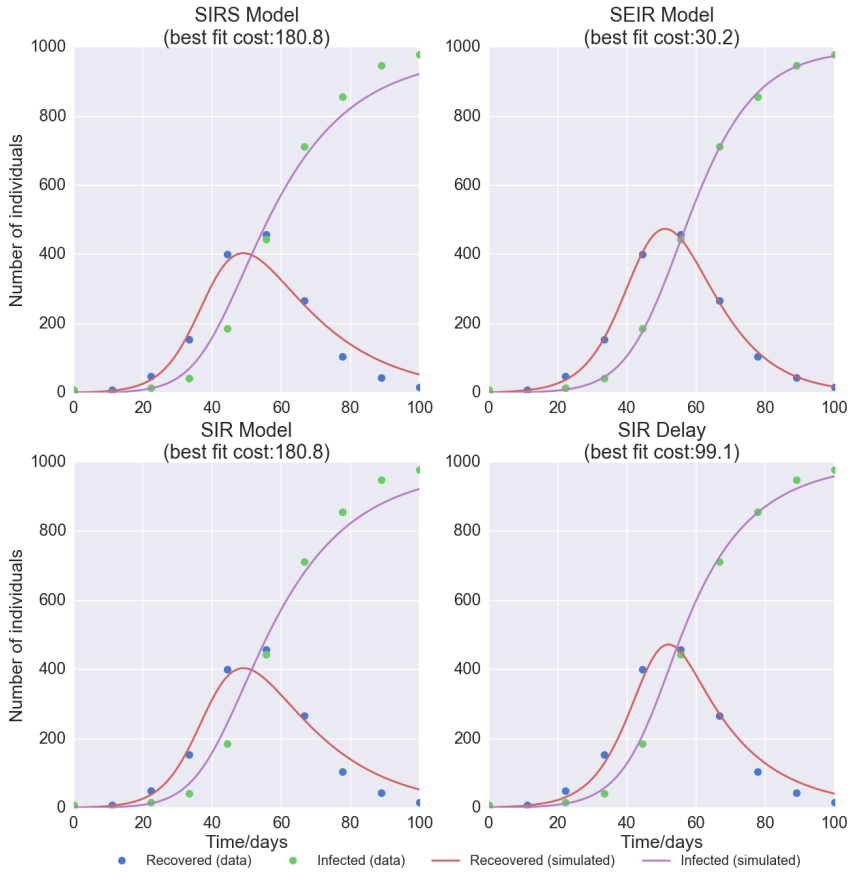
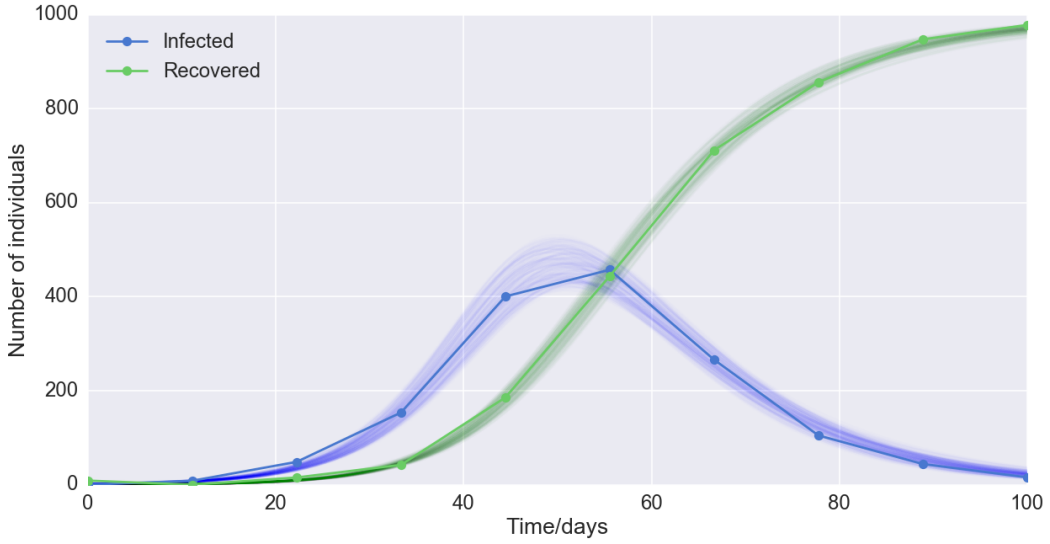
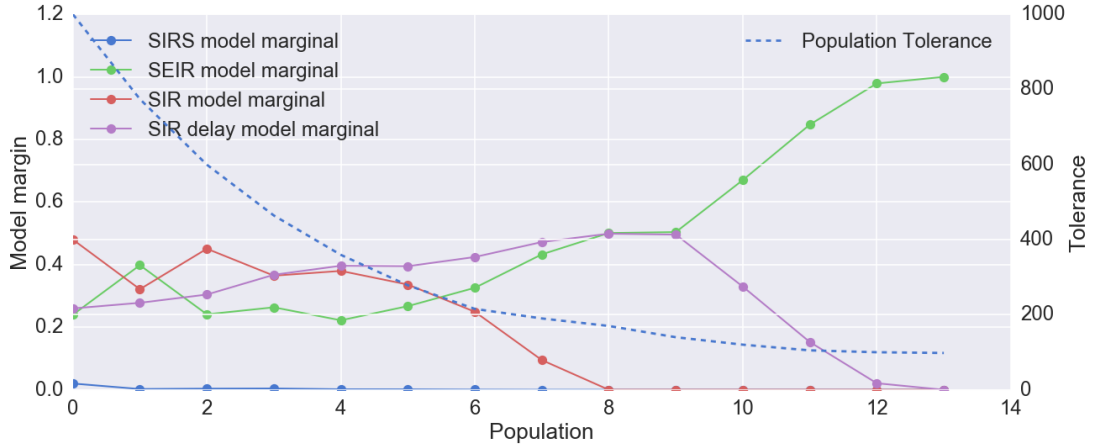


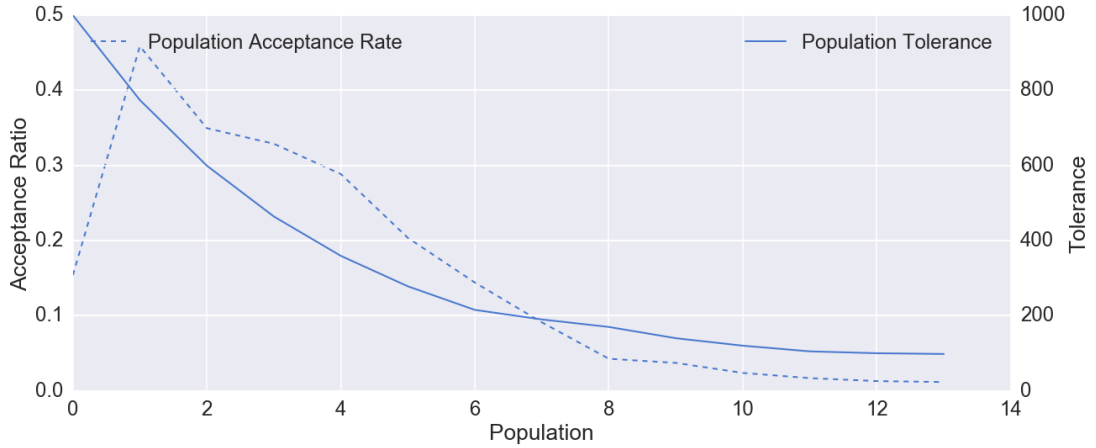
FIGURE 3.5: Results of fitting four SIR models to synthetic data generated from the SEIR model (see Equations (3.13)-(3.16); and added Gaussian noise. A simple sum of squared errors compares the simulated data and the true data at 20 time points. As expected the SEIR model has the lowest cost.



(A)



(B)



(C)

FIGURE 3.6: Model selection using ABC SMC. The SEIR model was used to generate synthetic dataset and Gaussian noise with standard deviation 10 was added to the 20 data points. ABC SMC identifies the correct model from SIRS, SEIR and SIR and SIR-delay models. (A) The true data and model outputs from all 200 particles from the last population. (B) The change in marginal values of model parameter and ϵ values for different populations. (C) Acceptance ratio for different populations.

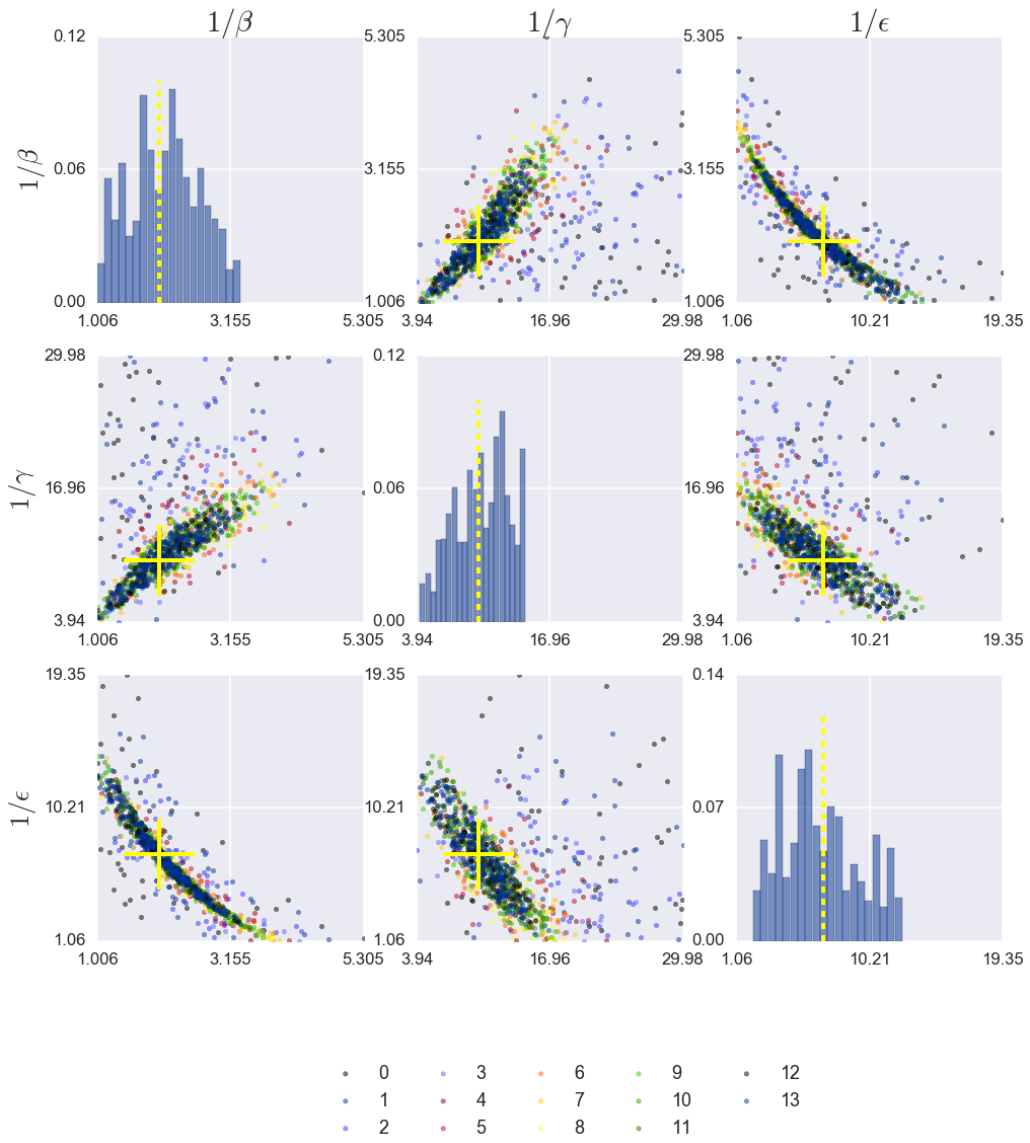


FIGURE 3.7: Parameter inference when fitting the SEIR model to synthetic data. A pair plot displaying an approximation to the posterior distribution for parameter values for the SEIR model (see Equations (3.13)-(3.16)) and scatter plots of pair wise relationships between the parameter values. The histograms are from the final population, whereas the scatter plots include values from intermediate populations. The parameter values used to generate the true data are marked in yellow and lie well within the range of the posterior distribution. We note that the final posterior distributions are very wide since we end ABC SMC model selection as soon as one of the model marginals reaches one. The ϵ for the final population is 98, which is much higher than the lowest distance found by CMA-ES at 30.2. We use 98 as the final population tolerance for the ABC SMC technique since the model marginal for the true model is 1 by this point.

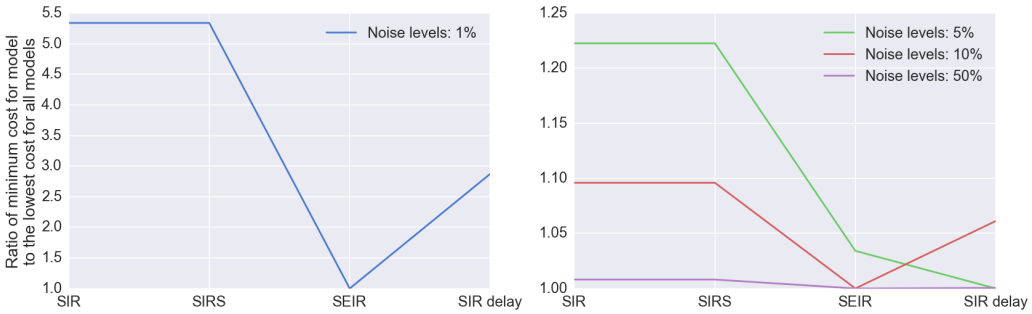


FIGURE 3.8: Effect of noise levels on results of model selection for the synthetic dataset under case study 1 (Notice the different scales on y-axes). We ran model selection using the CMA-ES technique for different noise levels: 1%, 5%, 10% and 50%. The comparison between ABC SMC and CMA-ES was carried out at 1%. As the noise level increases, the model selection becomes less reliable. Whereas at 1% noise, we were always able to recover the correct model, at higher noise levels, the technique often selected the wrong model (in the example here, at 5% noise, it incorrectly identifies SIR delay model as the correct model).

3.5 Case study 2: model selection in signalling pathways

The aim here is to verify that the two techniques can be used for model selection in studies of signalling pathways. We focus on two Feed Forward Loop (FFL) network motifs (Alon, 2007), which we describe below.

Transcription factors are proteins that regulate the transcription (i.e. the first steps in gene expression) of other proteins. We assume that protein X is a transcription factor for proteins Y and Z. Now suppose Y is a transcriptional co-regulator of protein Z, such that it can increase or decrease the expression of protein Z. Notice that we have not specified whether X and Y promote or repress the transcription of their target gene/protein Z. We consider two possible scenarios for this network (see Figure 3.9A), which we describe below. We assume further that the transcription of each protein starts (or stops) when the levels of its promoters (or repressors) rise above (or fall below) threshold values, and use time dependent system of ODEs to study the dynamics of the two networks:

- **Network 1:** X is a promoter of Y and Z, whereas Y is a repressor of Z, such that the rate of expression of Z is reduced when levels of Y increase:

$$\text{Network 1} \begin{cases} \dfrac{\mathrm{d}x}{\mathrm{d}t} = \beta_x - \alpha_x x, & (3.21) \\ \dfrac{\mathrm{d}y}{\mathrm{d}t} = \beta_y \theta(x > k_{xy}) - \alpha_y y, & (3.22) \\ \dfrac{\mathrm{d}z}{\mathrm{d}t} = \beta_z \theta(x > k_{xz})\theta(y < k_{yz}) - \alpha_z z, & (3.23) \end{cases}$$

- **Network 2:** X is a promoter of Z but a repressor of Y, while Y is a co-activator of Z:

$$\text{Network 2} \begin{cases} \dfrac{\mathrm{d}x}{\mathrm{d}t} = \beta_x - \alpha_x x, & (3.24) \\ \dfrac{\mathrm{d}y}{\mathrm{d}t} = \beta_y \theta(x < k_{xy}) - \alpha_y y, & (3.25) \\ \dfrac{\mathrm{d}z}{\mathrm{d}t} = \beta_z \theta(x > k_{xz})\theta(y > k_{yz}) - \alpha_z z, & (3.26) \end{cases}$$

where x, y, and z denote the concentration of proteins X, Y and Z at time t. β_x, β_y and β_z are transcription rates, and α_x, α_y and α_z are rates of degradation of X, Y and Z respectively. Parameters k_{xy}, k_{xz} and k_{yz} are threshold values at which gene transcription starts.

The piecewise constant function $\theta(b)$ takes the following values:

$$\theta(b) = \begin{cases} 1 \quad \text{if } b \text{ is TRUE} & (3.27) \\ 0.01 \quad \text{if } b \text{ is FALSE} & (3.28) \end{cases}$$

such that there is always a small background level of gene transcription. As an example, in Equation (3.23), the term $\theta(x > k_{xz})\theta(y < k_{yz})$ means that transcription of protein Z starts when levels of protein X are above a threshold (X is a promoter of Z), but levels of Y are below a certain threshold (Y is a repressor of Z).

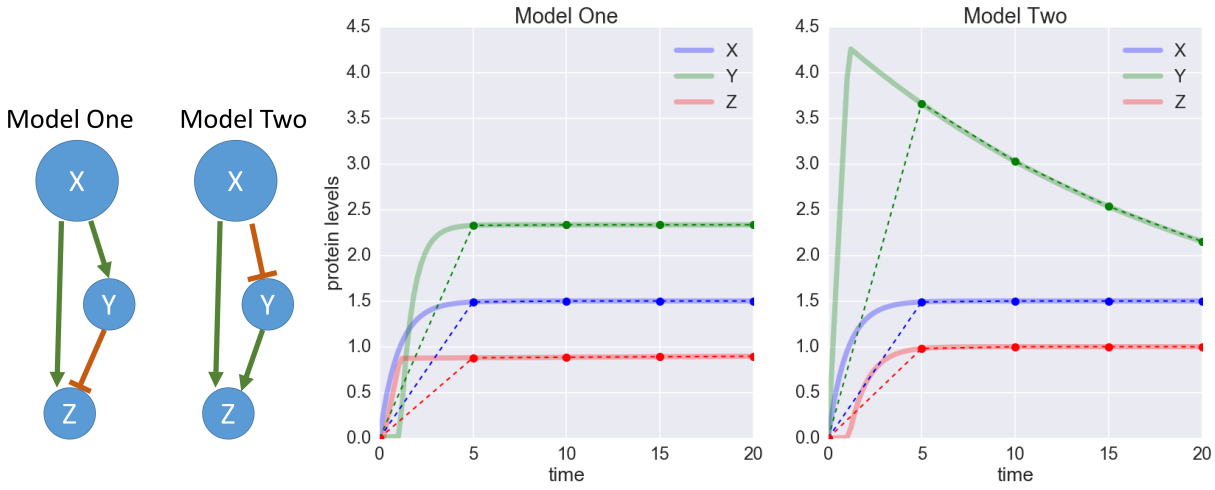


FIGURE 3.9: (A) The structure of the two Feed Forward Loops used in case study 2. (B) Example outputs from the two networks, after nondimensionalisation. The parameter values for model one are: $k_{xz} = 0.3, \alpha_y = 1.5, \alpha_z = 0.01, \beta_x = 1.5$ and $\beta_y = 3.5$. Parameter values for model two are $k_{xz} = 0.3, \alpha_y = 1.5, \alpha_z = 1.0, \beta_x = 1.5$ and $\beta_y = 4.0$. For both models we assume that the initial protein concentrations are all zero, such that at $t = 0$, $X = Y = Z = 0$. Notice the dashed lines represent the protein levels that may be assumed when only 5 time points are collected at $t = 0$, 5, 10, 15 and 20.

3.5.1 Nondimensionalization

By rescaling the variables in a model, nondimensionalization can be used to reduce the number of independent parameters in the model. This can inform us about parameter identifiability. Moreover, where quantitative estimates of model parameters exist, it enables us to estimate relative importance of different processes included in the model and thereby to justify neglect of certain processes. In case study one, we avoided nondimensionalization for consistency with Toni et al. (2009). In this second case study, we reduce the number of model parameter values by rescaling the protein concentrations x, y, and z, and time t as follows:

$$x^* = \frac{x}{k_{xy}}, y^* = \frac{y}{k_{yz}}, z^* = \frac{\alpha_x z}{\beta_z}, t^* = \alpha_x t.$$

Substituting these variable changes into Equations (3.21)-(3.23) and (3.24)-(3.26) yields the following nondimensionalized system of ODEs for the two FFL networks:

$$\text{Network 1} \begin{cases} \frac{\mathrm{d}x^*}{\mathrm{d}t^*} = \beta_x^* - x^* & (3.29) \\ \frac{\mathrm{d}y^*}{\mathrm{d}t^*} = \beta_y^* \theta(x^* > 1) - \alpha_y^* y^* & (3.30) \\ \frac{\mathrm{d}z^*}{\mathrm{d}t^*} = \theta(x^* > k_{xz}^*)\theta(y^* < 1) - \alpha_z^* z^* & (3.31) \end{cases}$$

$$\text{Network 2} \begin{cases} \frac{\mathrm{d}x^*}{\mathrm{d}t^*} = \beta_x^* - x^* & (3.32) \\ \frac{\mathrm{d}y^*}{\mathrm{d}t^*} = \beta_y^* \theta(x^* < 1) - \alpha_y^* y^* & (3.33) \\ \frac{\mathrm{d}z^*}{\mathrm{d}t^*} = \theta(x^* > k_{xz}^*)\theta(y^* > 1) - \alpha_z^* z^*, & (3.34) \end{cases}$$

where

$$\beta_x^* = \frac{\beta_x}{\alpha_x k_{xy}}, \quad \beta_y^* = \frac{\beta_y}{\alpha_x k_{yz}}, \quad \alpha_y^* = \frac{\alpha_y}{\alpha_x}, \quad \alpha_z^* = \frac{\alpha_z}{\alpha_x}, \quad k_{xz}^* = \frac{k_{xz}}{k_{xy}}. \tag{3.35}$$

Each network model now contains only five parameters instead of nine, reducing the dimensionality of the parameter space that needs to be explored and speeding up model selection without changing the system dynamics (see Figure 3.12). Henceforth, for simplicity we drop the $*$'s from the variable and parameter names.

We solve the models numerically using the *integrate.odeint* function in Python's scipy scientific package for $t = 0$ to $t = 20$ at 100 equally spaced time points. This function uses lsoda from FORTRAN library odepack and automatically adapts to solve stiff and non-stiff systems of first order ODEs using Backward Differentiation Formula (BDF) or Adams predictor-corrector methods respectively.

In Figure 3.9B, we present typical outputs from the two (nondimensionalised) models. We use the output generated by model two as the true dataset and employ model selection techniques to investigate whether it is possible to infer the correct model.

3.5.2 Qualitative fitting and satisfaction metrics

As described in Chapter 2, experimental data in studies of subcellular pathways is often semi-quantitative or qualitative. This means, for example, readouts from Western blots used to measure levels of proteins in a particular conformational state are a transformation of the real protein levels that can vary considerably depending on the specificity of the antibody used or the procedure followed to perform the Western blot.

As such, when performing model selection, we consider qualitative rather than quantitative outputs. That is, we investigate whether a given model can reproduce the same qualitative behaviour as the true output. We define our cost function using satisfaction metrics. Satisfaction metrics are defined such that if a particular requirement is satisfied, the cost is zero; otherwise a penalty proportional to the distance of the output from the edge of the satisfaction area is added to the cost function (Pargett and Umulis, 2013).

For example, if $x(t)$ is the model output at time t, and we require x to increase from $t = t_0$ to $t = t_n$, we may define the satisfaction distance as

$$J = \max(0, x(t_0) - x(t_n)). \tag{3.36}$$

The synthetic dataset we use is generated from model two (see Figure 3.9B). The qualitative features we aim to reproduce are:

- A monotonic increase in levels of protein Z. In other words, the gradient should be zero or positive. The satisfaction distance is defined as the lowest negative gradient of Z among all simulation points: $Q_i = \frac{z(t_j) - z(t_{j-1})}{\delta t}$, for $i = 1, \ldots, 100$.
- A bell shape in levels of protein Y.
  - Levels of Y should increase at least to 3.5 at $t = 5$: The satisfaction distance is defined as the distance between $y(t = 5)$ and 3.5 if $y < 3.5$,
  - Levels of Y should drop at least 1.5 times between $t = 5$ and $t = 20$. The satisfaction distance is defined as the distance between $\frac{y(t=5)}{y(t=20)}$ and 1.5 if this ratio is below 1.5.

We ignore changes in Protein X since it is monotonically increasing in all cases. Table 3.10 lists the elements of the cost vector. The final cost value is then given by

$$J = \sum_{i=1}^{3} w_i J_i^2, \tag{3.37}$$

where J_i and w_i are the cost elements and their associated weights.

We assume that all five model parameters in the nondimensionalized model are unknown. For model selection, we assume a uniform prior for each of these parameters $\propto \mathcal{U}[0, 10]$. We use 50 particles for the ABC SMC algorithm. For the CMA-ES algorithm we initiated the exploration of the parameter space at only one randomly selected point, with the four times the number of default particles.

Qualitative Requirement	**Quantity of Interest (Q_i)**	Value (J_i)	**Weight (w_i)**
Levels of Z should increase monotonically.	$\frac{z(t_j)-z(t_{j-1})}{\delta t}$	$\min_{j=1,\ldots,n}(0, Q_j)$	1
Levels of Y should increase at least to 3.5 at $t = 5$	$y(t = 5)$	$\min(0, Q_i - 3.5)$	1
Levels of Y should drop 1.5 times from the value at $t = 5$	$\frac{y(t=5)}{y(t=20)}$	$\min(0, Q_i - 1.5)$	1

TABLE 3.10: The elements of the cost vector used to compare model output with the true output. We assume values of y and z are calculated at n different time points $t = 0, \ldots, t_n = 20$. The exact levels of satisfaction boundaries are chosen to achieve a qualitative match to the experimental observations. We are not placing any requirements on when the turning point in Y should occur.

3.5.3 Analytical model selection

The two networks in this study can be solved analytically, without resorting to numerical methods. We assume zero initial conditions for all proteins and ignore background gene transcription.

Integrating equations (3.29) or (3.32) with $x(t = 0) = 0$ yields:

$$x = \beta_x(1 - e^{-t}). \tag{3.38}$$

Equation 3.38 indicates that $x(t)$ is an increasing saturating function of time for $\beta_x > 0$. We use Equation 3.38 to solve Equations (3.31) and (3.34) for y under models one and two. Under both models there is a regime change at $x = 1$. Setting $x = 1$ in Equation (3.38):

$$1 - e^{-t} < \frac{1}{\beta},$$
$$t < \log \frac{\beta}{\beta - 1} = t_0.$$

Under model one, assuming initial conditions of $y(t = 0) = 0$, we can solve Equation (3.31):

$$y = \begin{cases} 0 \quad t \leq t_0, & (3.39) \\ \frac{\beta_y}{\alpha_y}(1 - e^{\alpha_y(t-t_0)}) \quad t > t_0, & (3.40) \end{cases}$$

and similarly for model two:

$$y = \begin{cases} \frac{\beta_y}{\alpha_y}(1 - e^{-\alpha_y t}) & t \leq t_0, \quad (3.41) \\ \frac{\beta_y}{\alpha_y}(e^{\alpha_y t_0} - 1)e^{-\alpha_y t} & t > t_0. \quad (3.42) \end{cases}$$

We can hence deduce that under model one, $y(t)$ is an increasing saturating function of time t and model one cannot reproduce the qualitative behaviour produced by our synthetic dataset described in Section 3.5.2 and displayed in Figure 3.9B.

We summarise the results from the ABC SMC and CMA-ES model selection techniques in the next section and in doing so, confirm that they match this analytical result. We remark that such an analytical study is not possible for the more complicated pathways considered in later chapters of this thesis, making it essential to use the model selection techniques described in this chapter.

3.5.4 Results

We apply the two model selection techniques to two different Feed-forward loop network models. Unlike Case Study 1, we use a qualitative distance metric to account for the semi-quantitative nature of many biological experiments.

Model	Free Parameters	Lowest Cost (CMA-ES method)	Model Marginals (5 iterations, ϵ=0.25)
Model one	5	0.25 or 12.25	0.0
Model two (true)	5	0.00	1.0

TABLE 3.11: ABC SMC and CMA-ES model selection techniques applied to two FFL networks. Synthetic data was generated from model two, and a qualitative cost metric was used to compare the model outputs with the desired qualitative output. Both methods identify the correct model.

Table 3.11 summarises the results of model selection process. The CMA-ES method can find a set of parameters with zero cost for model two (i.e. the model satisfies all satisfaction metrics). It fails to identify a set of parameter values under model one that yield the correct qualitative output.

On some runs, CMA-ES failed to find the minimum value for the cost function for model one (i.e. 0.25) and converged to a local minimum at 12.25. These problems were resolved if either the number of particles or the number of starting points for the multi-start CMA-ES algorithm were increased. These do not change the final outcome of the model selection, however, they suggest that caution must be exercised when applying these techniques to problems where the solution is unknown.

ABC SMC suffered a different flaw where if we did not sample enough particles in each population (we settled on sampling 50 particles in each population), it incorrectly chose model one as the correct model. Again, this suggests that caution must be exercised when applying these model selection techniques.

In Figure 3.10 we plot the approximate posterior distributions for the parameter values found using ABC SMC. We note that unlike case study one, our distance metric

is now based on satisfaction metrics, since we are seeking a qualitative, rather than a quantitative fit. There is a large area of parameter space that satisfies our qualitative requirement. Hence the particles from the final population cover a wide area. The ABC SMC model selection yields a posterior distribution of parameter values that can be sampled if desired (see Figure 3.11C). This situation does not arise with CMA-ES as it generates a single set of suitable parameter values.

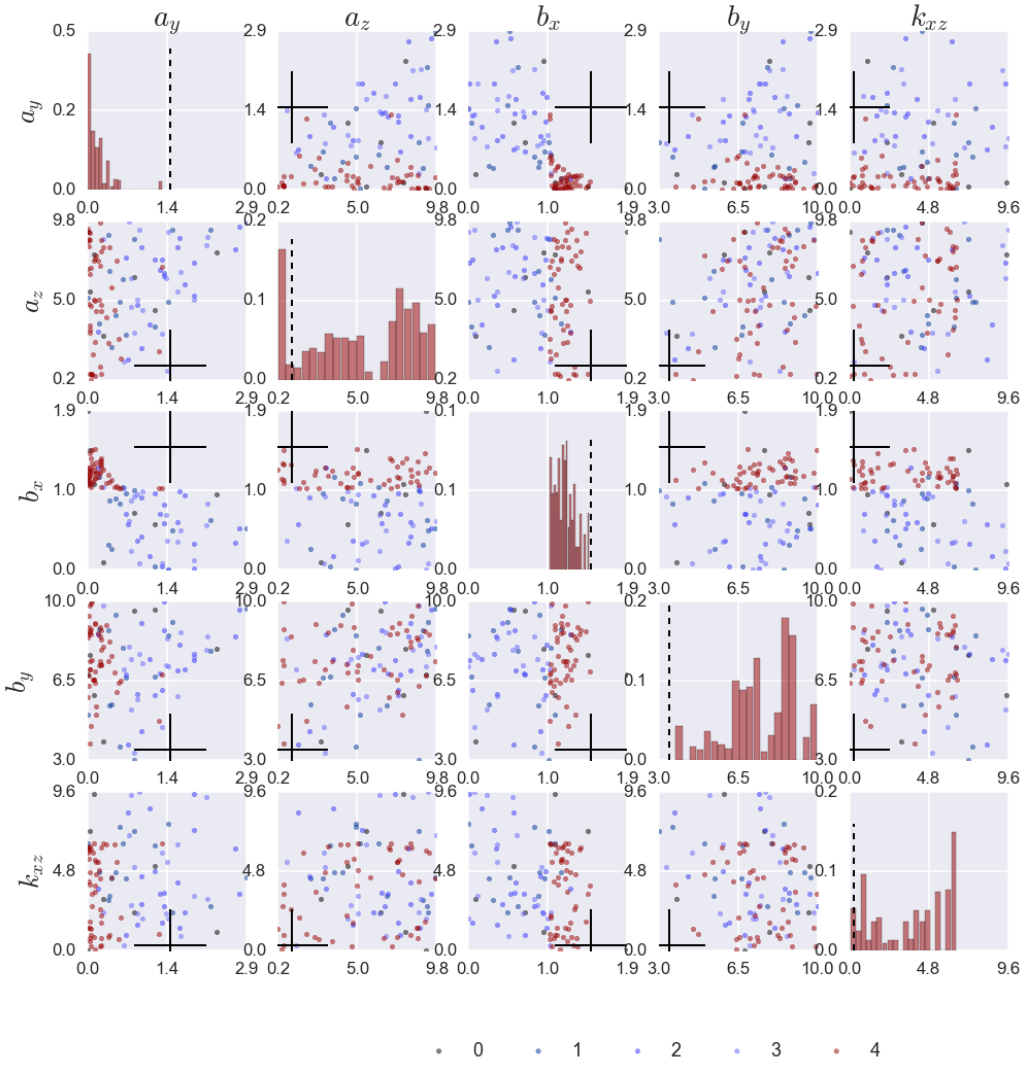
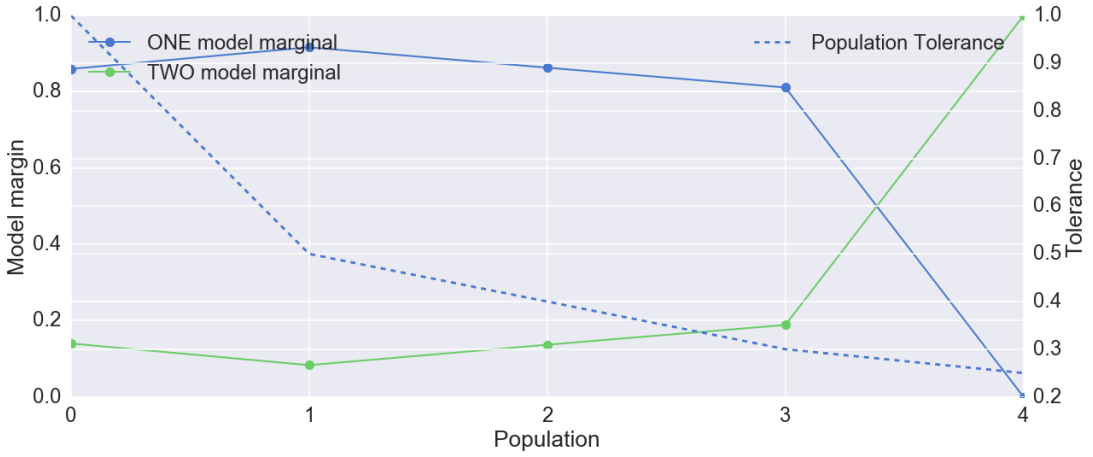
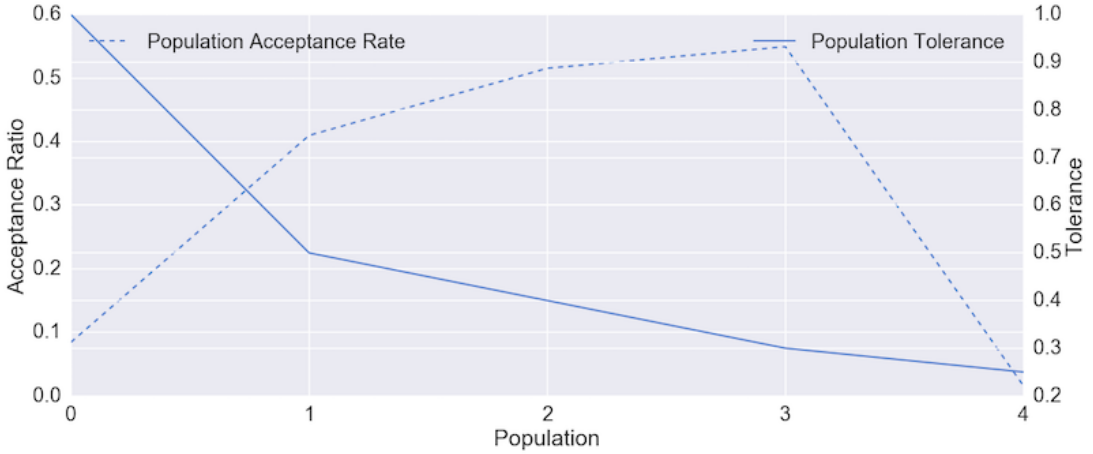


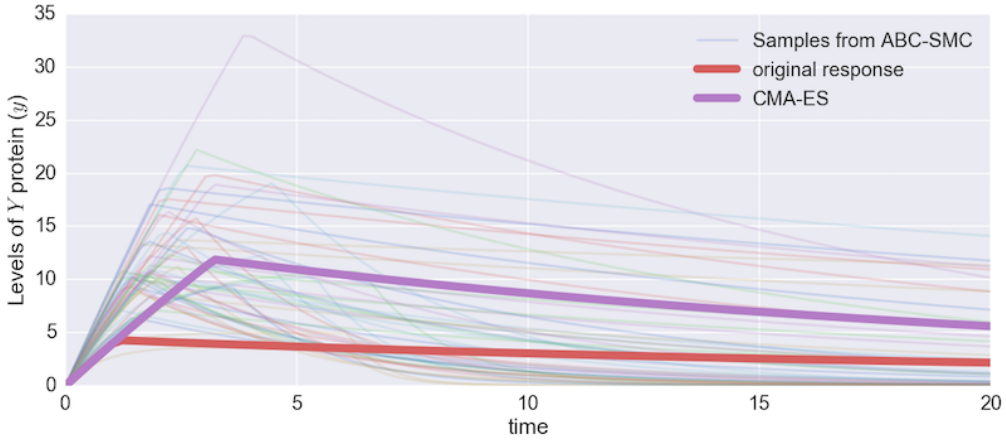
FIGURE 3.10: Distribution of particles accepted in the ABC SMC algorithm under model 2 (true model). The histograms are from the final population, whereas the scatter plots include all five particle populations. The black crosses and dashed lines show the true parameter values. The qualitative fit means that the range of suitable parameter values are wide and it is difficult to recover the original parameter values.



(A)



(B)



(C)

FIGURE 3.11: Results of model selection using ABC SMC and applied to a simple signalling pathway model. (A) The change in marginal values of model parameter and ϵ values for different populations. (B) Acceptance ratio for different populations. (C) The temporal dynamics of levels of protein Y, plotted using the parameter vector with lowest cost found using the CMA-ES technique and samples from final population of ABC SMC technique. The true parameter values are $k_{xz} = 0.3$, $\alpha_y = 1.5$, $\alpha_z = 1.0$, $\beta_x = 1.5$ and $\beta_y = 4.0$. The values recovered using the CMA-ES technique are: $k_{xz} = 1.32$, $\alpha_y = 0.04$, $\alpha_z = 0.99$, $\beta_x = 1.04$ and $\beta_y = 3.27$.

3.6 Discussion

In this chapter we introduced and compared two different model selection techniques that may be used to study signalling pathways. Since many experimental results in this field are semi-quantitative, we also introduced semi-quantitative/qualitative distance metrics. We focused on likelihood free model selection techniques since defining a tractable likelihood function is difficult when considering semi-quantitative distance metrics.

The first method, ABC SMC (Toni et al., 2009), a popular Approximate Bayesian Computation technique, considers model choice as an input parameter and uses a series of reducing tolerances to develop an approximation to the posterior distribution of appropriate model and parameter values for each model. In the second method, the cost function is minimised for each model using a multi-start CMA-ES algorithm. The model with the lowest global cost is considered the most suitable.

We applied these techniques to different case studies. Our first case study focused on the spread of infectious diseases. We used real and synthetic datasets to compare the two techniques. We then used the techniques to study signalling pathways. In this case study we incorporated qualitative comparison of model outputs and experimental results in order to mimic semi-quantitative experimental data.

According to Hansen (2006), the CMA-ES algorithm does not require extensive tuning of optimisation algorithm parameters, and the default parameter values were indeed suitable for our studies. The default number of particles in the initial population for each run of the algorithm in the multi-start regime has a default of $4+3\log(n_H)$ where n_H is the dimensionality of the parameter space. For global optimisation problems, an increase in this population size is recommended. In our tests, we found that the multi-start method and increasing the number of samples helped find the same minimum value. In high dimensional problems, multi-start facilitates the identification of parameter regions with different dynamics which can then be studied further (see Chapter 4 for details). In the first set of case studies, since we are not interested in studying different possible dynamics of the models, increasing the default population size four fold seemed sufficient for convergence to the global minimum. In the second case study, one start and the default number of particles were sufficient under the CMA-ES technique.

For ABC SMC, we used a different number of particles for each case study. For the synthetic example in the first case study, 200 particles were sufficient for model selection. With fewer particles the algorithm often failed to progress beyond the first population as it failed to sample all models, unless we increased the initial tolerance. In the common-cold dataset, 1000 particles were used for consistency with Toni et al. (2009). Finally, in the second case study, 50 particles were sufficient for correct model selection, any fewer particles and ABC SMC often failed to progress beyond the first population or selected the wrong model. It is interesting to note that although the second case study has a higher dimensionality compared to the first (five versus two to four), fewer particles were needed for correct model selection under both techniques. This is likely due to the satisfaction metrics, where the area in the parameter space that satisfies the required qualitative behaviour is relatively easier to locate.

The ABC SMC technique has many advantages compared to CMA-ES. If the primary objective is parameter inference, then the ABC SMC should be employed. Similar

to other Bayesian-based methods, the ABC SMC uses the experimental observations to approximate the posterior distribution for each of the model parameters. CMA-ES can generate single sets of suitable parameter values.

If we wish to explore different dynamics of a high dimensional problem, it may be appropriate to combine the two techniques. Initially, a multi-start CMA-ES algorithm may be used to locate different regions of parameter space that can describe the experimental observations. ABC SMC may then be applied to suitable priors defined around the parameter set found using CMA-ES. With a suitable quantitative distance metric (e.g. sum of squared errors), we can then use the results of the ABC SMC inference to inform us about the identifiability of model parameter values and sensitivity of model output to perturbations in parameter values.

For model selection, ABC SMC yields an approximation to the marginal likelihoods of each model, which may be used to calculate evidence for one model against another. CMA-ES only gives a measure of closeness of each model to the data. However, as observed in our case studies, the approximation to the model marginals given by ABC SMC are highly dependent on the choice of tolerances (Figures 3.3B, 3.6B). Caution must be exercised when considering such results.

An important factor to consider in model selection is model complexity and the problem of over-fitting. A simple model with a reasonable fit to the experimental observations may be preferable to a complex model, with more parameters, that fits the observations much better. Model selection criteria, such as AIC, penalise models with more parameters. Another advantage of the ABC SMC technique, alongside other Bayesian model selection techniques, is the automatic incorporation of the principle of Occam's razor. Bayesian-based approaches penalise higher dimensional models when calculating the evidence in Equation (3.4), unless the more detailed model is significantly better. CMA-ES, combined with semi-quantitative distance metrics, is unable to make such considerations and caution must be exercised when comparing models that differ markedly in their complexity.

Another concept we explored in this chapter is qualitative/semi-quantitative comparison and satisfaction metrics. Such methods are useful when experimental results are not quantitative. These enable us to quickly explore and compare model outputs with experimental observations and to establish whether the output exhibits similar behaviour to the experimental observations. One of the disadvantages of satisfaction metrics is that studying parameter identifiablity and sensitivity becomes impossible. Standard distance metrics (such as sum of squared errors) should be recruited to study parameter identifiablity once a suitable set of parameter values is found. Given the often large area of satisfaction, more than one model may be able to reproduce the experimental observations making the problem of model selection more difficult. However, until higher quality data becomes available, we believe these methods offer the best chance of improving our understanding of the dynamics of signalling pathways.

The primary advantage of CMA-ES over ABC SMC is speed. Figure 3.12 displays the number of model simulations required for ABC SMC and CMA-ES. For the nondimensionalized model, the difference for case study 2 where we use satisfaction metrics is substantial (1500 vs. 16000 on average). In our analysis, ABC SMC seems to particularly suffer when using satisfaction metrics, whereas CMA-ES quickly converges to the minimums for each model, ABC SMC initially gives a higher marginal probability to the incorrect model, and once the tolerance drops low enough it switches to the correct

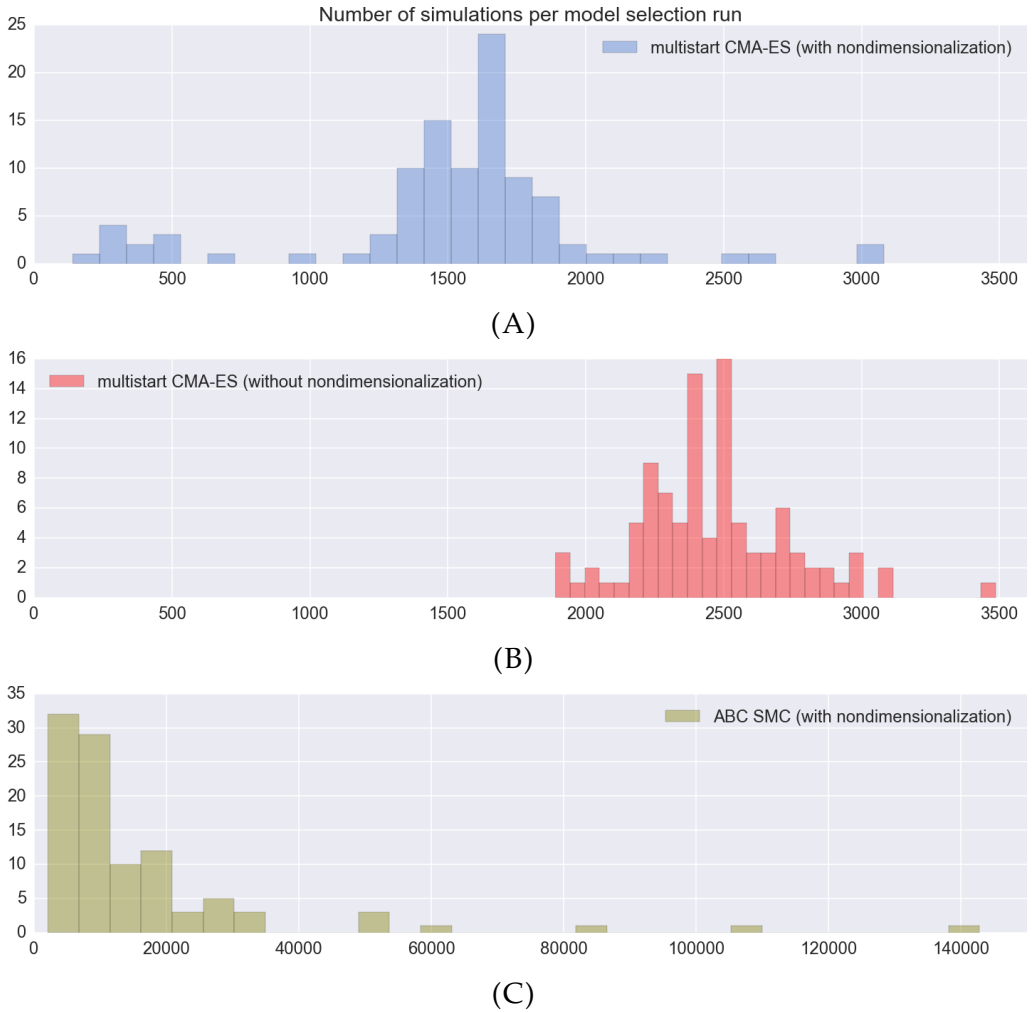


FIGURE 3.12: The distribution of total number of simulations required for model selection in case study 2 under (A) multi-start CMA-ES without model nondimensionalization, (B) multi-start CMA-ES with model nondimensionalization, and (C) ABC SMC with model nondimensionalization. Each model selection was run 100 times. ABC SMC required an average just under 16000 model simulations, whereas CMA-ES required on average 1500 and 2500 model simulations for the nondimensionalized and dimensionalized models respectively.

model. We experimented with different tolerance schedules, $\epsilon_0, \ldots, \epsilon_T$, without being able to improve this. Moreover, the candidate models being considered in our study of the canonical Wnt pathway have higher dimensionality than the models considered here (sixteen or seventeen versus five), meaning the extra speed offered by CMA-ES outweighs the benefits of ABC SMC. We experimented with running ABC SMC using different tolerance schedules and number of particles, without being able to improve the performance further. In future work it may be interesting to perform a more detailed investigation of the impact of the implementation parameter value on the speed and results of model selection. For these reasons we use CMA-ES for model selection in the remainder of this thesis. ABC SMC model selection has many advantages compared to CMA-ES. However, many of these advantages, such as parameter inference, are not fully utilised when using qualitative distance metrics.

In the second case study involving signalling pathways, we also demonstrated

how nondimensionalization may be used to reduce the dimensionality of the parameter vector, reducing the computational resources required for model selection. Figures 3.12A and 3.12B display the number of simulations required for model selection using the CMA-ES technique with and without nondimensionalization. Nondimensionalization speeds up model selection by reducing the average number of model simulations from 2500 to 1500. However, model selection using the dimensionalized model with the CMA-ES technique is still substantially faster than the process using the ABC SMC technique. Moreover, nondimensionalization, which involve manual analysis of the model system, can be time consuming and can slow down prototyping of new models. In our view, the small speed up (2500 vs 1500 model simulations), does not outweigh the time cost of nondimensionalization. Hence for the rest of this thesis, we avoid nondimensionalizing the models we propose, and instead apply CMA-ES to the dimensionalized model.

Our results in this chapter show that the CMA-ES technique may be used for model selection, providing an efficient method to explore the parameter space of candidate models without the need for extensive tuning of parameter values. We also showed that in face of qualitative experimental results, it may be possible to use satisfaction metrics to establish the most suitable model structures.

In the next chapter, we use the model selection techniques introduced here to study the canonical Wnt pathway. We will focus on the cell's initial response to Wnt stimulation. Recruiting the latest biological findings we introduce a set of candidate models that may be consistent with experimental observations, and use CMA-ES and satisfaction metrics to discriminate between these candidate models.

Chapter 4

A reduced core model of the Wnt pathway

4.1 Introduction

In the last chapter we introduced the idea of mathematical model selection. We showed that a technique based on a multi-start CMA-ES optimisation algorithm and satisfaction metrics can quickly select between mathematical models of a signalling pathway. In Chapters 1 and 2 we introduced the current state-of-the-art in modelling of the canonical Wnt pathway. We summarised various competing models proposed by various groups based on seemingly contradictory observations. In this chapter, and in Chapter 6, we use mathematical model selection to determine whether we can propose a model that is consistent with these observations. In this chapter we focus on the cell's initial response to Wnt stimulation.

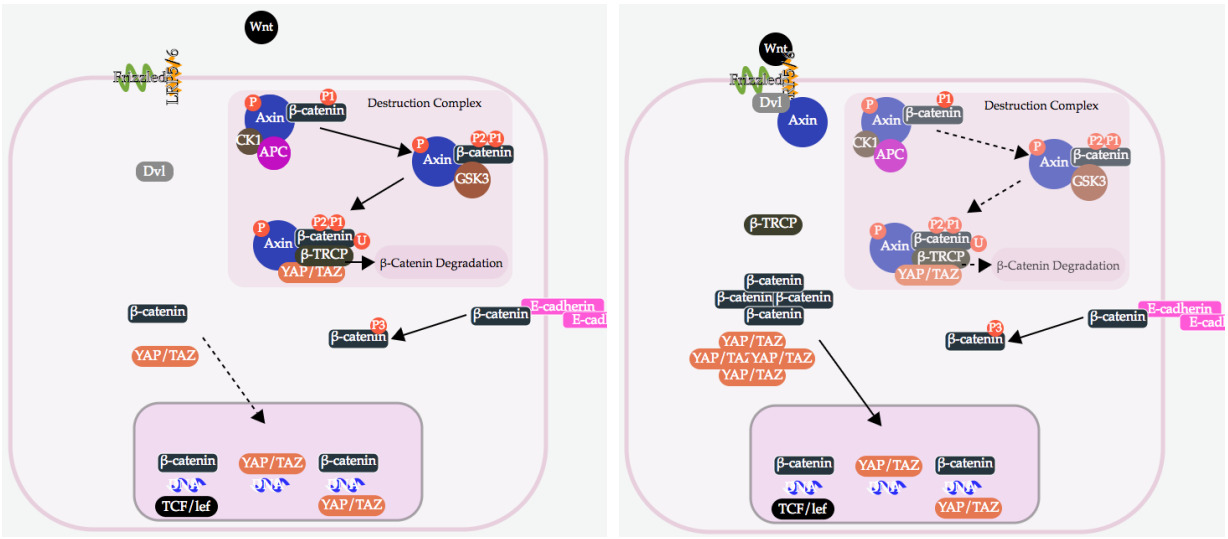
One of the earliest aspects of canonical Wnt signalling is exposure of the Frizzled transmembrane receptor and the Low Density Lipoprotein Receptor-related Protein 6 (LRP6) co-receptor, and its homolog LRP5, to extracellular Wnt ligands. This drives recruitment of the destruction complex, including Axin, APC and kinases GSK3 and CK1, to the membrane via the Dishevelled (Dvl) protein and its inactivation. As a result, β-catenin is not degraded by the proteasome, instead accumulating in the cytoplasm and translocating to the nucleus, where it causes Wnt target gene transcription. Figure 4.1 shows a schematic of the canonical Wnt pathway.

Wnt stimulation also leads to phosphorylation of the LRP6 at various sites. In particular, CK1 phosphorylates LRP6 at its threonine 1479 residue (Bilic et al., 2007) while GSK3 and CK1 can phosphorylate it at threonine/serine residues at one or more of its five PPPSP/PPPTP motifs (Zeng et al., 2005). Zeng et al. (2005) observe that GSK3 phosphorylation primes LRP6 for CK1 phosphorylation at these sites.

As described in Chapter 2, we break down the models of signalling pathways into two categories; verbal models, often proposed in experimental studies, and mathematical and rule based models. Various models of the canonical Wnt pathway have been proposed over the last two decades. Verbal models alone have failed to yield a model of the canonical pathway that unifies various, seemingly contradictory observations. Figure 2.5 in Chapter 2 summarises some of those discrepancies that lead to inactivation of the destruction complex.

Mathematical models offer a complementary approach to verbal models and can yield insight into the dynamics associated with the multiple nonlinear biochemical interactions that constitute the Wnt pathway. As demonstrated in Chapter 3, they can be used for model selection and also to generate experimentally testable predictions.

One of the aims of this thesis is to use mathematical modelling to explain seemingly contradictory experimental observations. Many recent studies have proposed that the conformational states of the LRP6 co-receptor and the Axin scaffolding protein contribute to inactivation of the destruction complex (Kim et al., 2013; Piao et al.,



(A) Wnt off (B) Wnt on

FIGURE 4.1: Schematic of the canonical Wnt signalling pathway. In the absence of extracellular Wnt ligands (left), β-catenin is continuously degraded by a multiprotein complex termed the destruction complex, which causes β-catenin phosphorylation at residues S45 by CK1 and S33/S37/T41 by GSK3. Upon Wnt stimulation (right), the destruction complex is deactivated, causing β-catenin accumulation and Wnt target gene transcription. A large fraction of β-catenin is also found at the membrane, bound to E-cadherin in Adherens junctions.

2008; Wu et al., 2009). To the best of our knowledge, none of the existing mathematical models of the canonical Wnt pathway have focused on these components of the canonical Wnt pathway.

Our literature review detailed in Chapter 2 revealed many as yet unanswered questions about the interactions between Axin and LRP6. There are some well reported observations with regards to interactions of these proteins, including recruitment of Axin to LRP6 (Bilic et al., 2007; Kim et al., 2013) and phosphorylation of LRP6 (Kim et al., 2013; Li et al., 2012). However, there are also inconsistencies, such as the observation that Axin is required for LRP6 phosphorylation (Wolf et al., 2008; Zeng et al., 2008), while unphosphorylated LRP6 does not in fact provide a docking site for Axin unlike phosphorylated LRP6 (Zeng et al., 2005). In addition, it is also unclear whether or not the first steps after Wnt stimulation is recruitment of Axin to LRP6 or LRP6 phosphorylation. For example, LRP6 aggregates are formed at the membrane upon Wnt stimulation. These aggregates lead to an increase in Axin recruitment to the membrane (Niehrs and Shen, 2010; Bilic et al., 2007). It is proposed that LRP6 phosphorylation is the consequence and not the cause of these aggregations (Niehrs and Shen, 2010; Bilic et al., 2007). These observations make it unclear whether Wnt signalling leads to an increase in rate of recruitment of Axin to the membrane (via the formation of aggregates), or an increase in LRP6 phosphorylation which then leads to recruitment of Axin. These are two of the primary hypotheses we are testing in this chapter. To address these questions, in this chapter we propose a set of candidate models with competing structures that may give us a better understanding of the ways in which these two proteins interact. The models differ in the biochemical interactions that are included, and those reactions that are regulated by Wnt. As in Chapter 3, we use the CMA-ES technique and satisfaction metrics to determine which models best describe

the experimental observations and use this to reduce the number of suitable candidate models.

We use sensitivity analysis and *in silico* experiments to reduce the space of suitable candidate models further, before proposing new experiments that may enable us to find the most suitable model.

The remainder of this chapter is structured as follows. In the Methods section, we give a detailed description of our candidate mathematical models. We first give a verbal description, detailing the assumptions on which the models are based. Next, we introduce our competing candidate models. We present the mathematical equations that define each mathematical model and outline the analysis we perform. In the Results section, we discuss the results of model selection. We then describe how we may simplify our candidate models while maintaining important features in the model. Finally, in the Discussion section we summarise our findings and describe the next steps in our work.

4.2 Methods

Several recent studies of the canonical Wnt pathway have focused on interactions between the LRP6 co-receptor and the Axin scaffolding protein (Kim et al., 2013; Haack et al., 2015), particularly the impact of phosphorylation of Axin and LRP6 as among the earliest steps leading to inactivation of the destruction complex. While some progress has been made, there are many open questions about these interactions and how conformational states of LRP6 and Axin might regulate them.

We propose a set of candidate mathematical models that differ in two ways. First, the reactions included in the different models may vary. Second, the reactions which are altered by Wnt stimulation may vary. By comparing these mathematical models with experimental results, we aim to elucidate how LRP6 and Axin contribute to the dynamics of the canonical Wnt pathway.

We note that due to lack of suitable experimental results, we do not explicitly model several other proteins that are observed to be fundamental to recruitment of Axin to the membrane and initiation of Wnt signalling, including Frizzled and Dvl.

4.2.1 Qualitative description of our mathematical models

We focus on LRP6 and Axin and study their phosphorylation, dephosphorylation and complex formation. Our candidate models are formulated in terms of 8 different species. We assume that Axin and LRP6 exists in one of two states; phosphorylated (represented by A_p and L_p) and unphosphorylated (represented by A_u and L_u). We also distinguish the four complexes that may form between them, denoting the complexes A_uL_u, A_pL_u, A_uL_p and A_pL_p by C_0, C_1, C_2 and C_3 respectively. Table 4.1 contains a summary of the dependent variables used in our models.

As discussed in Chapter 2, LRP6 has various sites that are phosphorylated upon Wnt stimulation. We consider only LRP6 phosphorylation by GKS3 at the S1490 residue (pS1490 LRP6). S1490 is part of one of the five PPPSP motifs on LRP6, which may be phosphorylated upon Wnt stimulation and are believed to cooperate in order to amplify Axin recruitment to LRP6 (MacDonald et al., 2008). We include this phosphorylation state for two reasons. First, Kim et al. (2013) propose that this conformational change increases the rate of recruitment of Axin phosphorylated at S497/S500 (pS497/500 Axin) to the membrane. Second, pS1490 LRP6 may cause direct inhibition

Dependent variable	Description
A_u	Concentration of Axin not phosphorylated at S497/S500
A_p	Concentration of Axin phosphorylated at S497/S500
L_u	Concentration of LRP6 not phosphorylated at S1490
L_p	Concentration of LRP6 phosphorylated at S1490
C_0	Concentration of Complex of L_u and A_u
C_1	Concentration of Complex of L_u and A_p
C_2	Concentration of Complex of L_p and A_u
C_3	Concentration of Complex of L_p and A_p

TABLE 4.1: Dependent variables used in our mathematical models.

of destruction complex activity (Piao et al., 2008; Wu et al., 2009; Cselenyi et al., 2008). We do not explicitly model phosphorylation of LRP6 by CK1 at the T1479 residue, since Axin may be recruited to the membrane without phosphorylation of LRP6 at this residue (Bilic et al., 2007).

We focus on Axin phosphorylation by GSK3 at residues S497/S500, which may play an important role in determining the activation state of the destruction complex and the recruitment of β-catenin to the destruction complex (Kim et al., 2013).

We restrict attention to the first 3 hours after Wnt stimulation and assume that total levels of Axin and LRP6 are fixed. A fall in both these levels are observed beyond 3-4 hours of Wnt stimulation (Kim et al., 2013; Khan et al., 2007; Li et al., 2012).

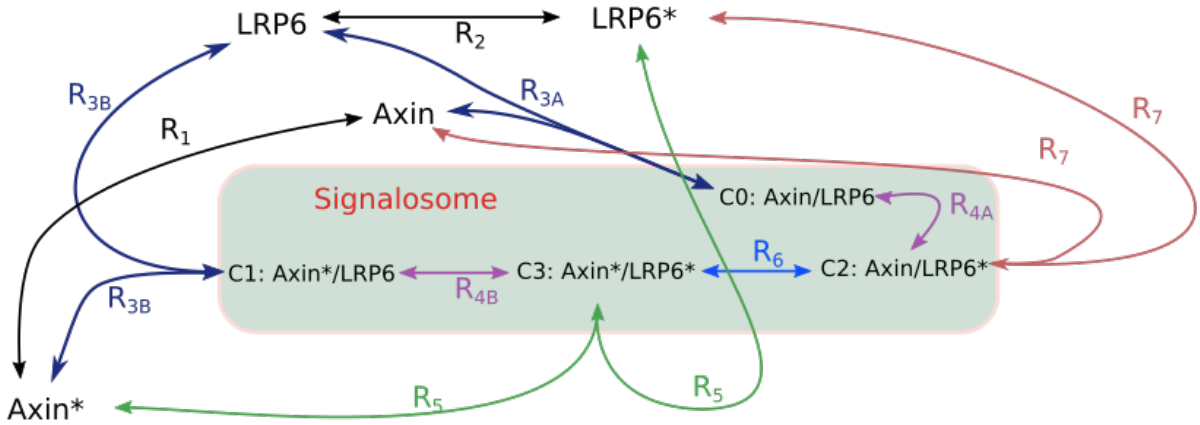


FIGURE 4.2: Schematic of our candidate mathematical models of the canonical Wnt pathway. These models describe the dynamics of phosphorylated and unphosphorylated Axin and LRP6 and the various complexes of Axin and LRP6 that they may form (see Table 4.1 for a summary of the dependent variables). '*' represent a phosphorylated protein. Black arrows indicate Wnt-independence under all model structures. Colours for other reactions match colours in Reactions (4.1)-(4.9). The rate constants for reaction R_i are given by $k_{\pm i}$, where the k_i's represent association or phosphorylation rates and the k_{-i}'s represent dephosphorylation or dissociation rates.

In Figure 4.2 we present a schematic of the 9 interactions included in our candidate mathematical models and we detail below the biological motivation/evidence underpinning each of these reactions. We view the cytosol, nucleus and membrane as a single well-mixed compartment and assume that all reactions take place in this compartment and ignore spatial variation in protein concentrations.

$$R_1: \quad \mathrm{A_u} \underset{k_{-1}}{\overset{k_1}{\rightleftharpoons}} \mathrm{A_p}, \tag{4.1}$$

$$R_2: \quad \mathrm{L_u} \underset{k_{-2}}{\overset{k_2}{\rightleftharpoons}} \mathrm{L_p}, \tag{4.2}$$

$$R_{3A}: \quad \mathrm{A_u} + \mathrm{L_u} \underset{k_{-3}}{\overset{k_3}{\rightleftharpoons}} \mathrm{C_0}, \tag{4.3}$$

$$R_{3B}: \quad \mathrm{A_p} + \mathrm{L_u} \underset{k_{-3}}{\overset{k_3}{\rightleftharpoons}} \mathrm{C_1}, \tag{4.4}$$

$$R_{4A}: \quad \mathrm{C_0} \underset{k_{-4}}{\overset{k_4}{\rightleftharpoons}} \mathrm{C_2}, \tag{4.5}$$

$$R_{4B}: \quad \mathrm{C_1} \underset{k_{-4}}{\overset{k_4}{\rightleftharpoons}} \mathrm{C_3}, \tag{4.6}$$

$$R_6: \quad \mathrm{C_2} \underset{k_{-6}}{\overset{k_6}{\rightleftharpoons}} \mathrm{C_3}, \tag{4.7}$$

$$R_5: \quad \mathrm{A_p} + \mathrm{L_p} \underset{k_{-5}}{\overset{k_5}{\rightleftharpoons}} \mathrm{C_3}, \tag{4.8}$$

$$R_7: \quad \mathrm{A_u} + \mathrm{L_p} \underset{k_{-7}}{\overset{k_7}{\rightleftharpoons}} \mathrm{C_2}. \tag{4.9}$$

Reactions R_1 and R_2 represent the Wnt-independent phosphorylation and dephosphorylation of Axin and LRP6. It has been observed that Axin is required for LRP6 phosphorylation (Zeng et al., 2008). Therefore, we assume that Axin ($\mathrm{A_u}$ and $\mathrm{A_p}$) can form a complex with unphosphorylated LRP6 ($\mathrm{L_u}$). This interaction is represented by reversible reactions R_{3A} and R_{3B}.

Kim et al. (2013) observed that pS1490 LRP6 binds preferentially to pS497/500 Axin compared to unphosphorylated Axin. Reaction R_5 represents this increased affinity between pS497/500 Axin ($\mathrm{A_p}$) for pS1490 LRP6 ($\mathrm{L_p}$).

GSK3 is known to stay bound to Axin upon its dephosphorylation (Kim et al., 2013; Li et al., 2012). Kim et al. (2013) proposed that GSK3 is recruited via Axin to facilitate LRP6 phosphorylation. Thus we assume that LRP6 may be phosphorylated while in complex with both Axin states and represent this by reactions R_{4A} and R_{4B}. Kim et al. (2013) observed that Axin is dephosphorylated upon Wnt stimulation, and proposed that this is due to recruitment of Axin to LRP6. In Reaction R_6, we assume that Axin in complex with LRP6 can be dephosphorylated upon Wnt stimulation. Additionally, LRP6 phosphorylation my occur in the absence of Axin dephosphorylation (Kim et al., 2013). We hence assume that phosphorylation of LRP6 in reactions R_{4A} and R_{4B} precedes the observed dephosphorylation of Axin in reaction R_6.

Upon Wnt stimulation, levels of Axin in complex with LRP6 have been observed first to rise and then to drop (Kim et al., 2013; Khan et al., 2007). We include reaction R_7 to represent the release of Axin from LRP6 after Axin has been dephosphorylated.

In some candidate models, we assume that there is always the same basal level of recruitment of Axin to pS1490 LRP6. In these candidate models, $k_{\pm 5} = k^*_{\pm 5} + k_{\pm 3}$, while $k_7 = k_3$ and $k_{-7} = k^*_{-7} + k_{-3}$. In other candidate models we assume $k_7 = 0$. We will discuss this in more detail later.

4.2.1.1 Modelling the effect of Wnt

Most existing mathematical models of the Wnt pathway account for Wnt stimulation in one of two ways. Lee et al. (2003), Leeuwen et al. (2007) and Hernández et al. (2012) view it as an externally prescribed function of time that acts on certain reactions. On the other hand, Haack et al. (2015) and Mazemondet et al. (2012) view Wnt as a dependent variable which is produced, degraded and interacts with other model variables. For simplicity, we follow Lee et al. (2003), representing Wnt stimulation as an exponential function of time, that changes from the "Wnt-off" value to the "Wnt-on" with a time constant of 1 to 20 minutes to account for reactions not included in our mathematical models. This time delay is in line to the delay observed by Hernández et al. (2012). The exact mathematical function used to represent Wnt stimulation is given in Equation (4.24).

We compare our candidate mathematical models with *in vitro* experiments, in which the number of Wnt3A ligands is typically 500 times higher than the number of LRP6 co-receptors (see Section A.2 in Appendix A). Since we focus on the first 3-4 hours after Wnt stimulation, we neglect any drop in Wnt levels over time.

4.2.2 Candidate models

Candidate models differ structurally in two ways and we use the notation H_{xy}, where x and y are positive integers, to refer to different candidate models. The subscript x indicates which reactions are altered by Wnt, while the subscript y indicates how Axin interacts with LRP6 and structural differences between the models.

Subscript $x = 1, 2, 3, 4, 5$ or 6 determines which reaction rates are altered upon Wnt stimulation:

- **x=1:** LRP6/Axin binding (k_3 in reactions R_{3A}, R_{3B}, R_5 and R_7),
- **x=2:** LRP6 phosphorylation while in complex with Axin (k_4 in reactions R_{4A} and R_{4B}),
- **x=3:** LRP6/Axin binding (k_3 in reactions R_{3A}, R_{3B}, R_5 and R_7), and LRP6/Axin release (k_{-7} in reaction R_7),
- **x=4:** Dephosphorylation of Axin while in complex with LRP6 (k_{-6} in reaction R_6),
- **x=5:** Dephosphorylation of Axin (k_{-6} in reaction R_6) and release of Axin from LRP6 (k_{-7} in reaction R_7),
- **x=6:** Phosphorylation of LRP6 (k_4 in reactions R_{4A} and R_{4B}) and release of Axin from LRP6 (k_{-7} in reaction R_7).

Subscript y determine how LRP6 and Axin interact:

- **y=1: No basal level of Axin/pS1490 LRP6 binding.** Reaction R_7 is not reversible with $k_7 = 0$.
- **y=2: Basal level of Axin/pS1490 LRP6 binding.** $k_{\pm 5} = k^*_{\pm 5} + k_{\pm 3}$, $k_7 = k_3$ and $k_{-7} = k^*_{-7} + k_{-3}$, where $k^*_{\pm 5}$ and k_{-7} are independent of $k_{\pm 3}$.

We remark that we only consider candidate models where Wnt leads to an increase in rate of reactions. One may investigate whether Wnt in fact leads to a reduction in the rate of the reverse reaction (e.g. dissociation of Axin from LRP6(k_{-3}) or LRP6 dephosphorylation (k_{-4})), however, since we failed to find any commentary in the literature

highlighting such mechanisms with regards to the Wnt pathway and since it is computationally expensive to consider all possible model structures, we ignored any such model structure. However, future work could consider such candidate models, and investigate the differences in the Wnt pathway dynamics due to such structures.

4.2.3 Mathematical representation of our candidate models

In this section we explain how we translate the reactions introduced in Section 4.2.1 into mathematical functions and use them to construct the candidate mathematical models of the canonical Wnt pathway.

We assume that all reactions follow mass action kinetics, meaning that the rate at which a reaction proceeds is proportional to the product of the concentrations of the reactants. We remark that this means we ignore saturation of the reactions due to other, un-modelled, species. We note that as discussed in Section 2.1.5, Dvl may play an important role in recruitment of Axin to the membrane and LRP6 phosphorylation. However, given that Dvl's exact role in the Wnt pathway is not yet clear, and it is unclear if it is a rate limiting element, we avoid modelling it, and in particular assume that Axin's recruitment to the LRP6 co-receptor and LRP6 phosphorylation happens according to mass-action kinetics. This enables us to keep the models simple, however, this assumption may need to be re-visited in the future if our candidate models are unable to describe the observed experimental results.

We also use the principle of mass balance to construct the governing equations, assuming that the net rate at which a reactant is produced is equal to the sum of sources minus the sum of the sink terms. As an illustrative example, the temporal dynamics of the reversible reaction:

$$\mathrm{A} + \mathrm{B} \underset{k_-}{\overset{k_+}{\rightleftharpoons}} \mathrm{C} \tag{4.10}$$

are described by the system of ODEs:

$$\frac{\mathrm{d}C}{\mathrm{d}t} = k_+ AB - k_- C \tag{4.11}$$

$$\frac{\mathrm{d}A}{\mathrm{d}t} = -k_+ AB + k_- C \tag{4.12}$$

$$\frac{\mathrm{d}B}{\mathrm{d}t} = -k_+ AB + k_- C \tag{4.13}$$

where t represents time, k_+ and k_- are the forward and reverse reaction rates and concentration of proteins A, B and C are represented by A, B and C respectively.

Applying the above principles to the network defined by Reactions (4.1)-(4.9), we deduce that the temporal dynamics of the dependent variables can be described by the

following system of ODEs:

$$\frac{\mathrm{d}A_u}{\mathrm{d}t} = -r_1 \quad -r_{3a} - r_{3c} \quad +r_7, \tag{4.14}$$

$$\frac{\mathrm{d}A_p}{\mathrm{d}t} = r_1 \quad -r_{3b} \quad -r_5, \tag{4.15}$$

$$\frac{\mathrm{d}L_u}{\mathrm{d}t} = -r_2 - r_{3a} - r_{3b}, \tag{4.16}$$

$$\frac{\mathrm{d}L_p}{\mathrm{d}t} = r_2 - r_{3c} \quad -r_5 \quad +r_7, \tag{4.17}$$

$$\frac{\mathrm{d}C_0}{\mathrm{d}t} = r_{3a} \quad -r_{4a}, \tag{4.18}$$

$$\frac{\mathrm{d}C_1}{\mathrm{d}t} = r_{3b} \quad -r_{4b}, \tag{4.19}$$

$$\frac{\mathrm{d}C_2}{\mathrm{d}t} = r_{3c} \quad +r_{4a} \quad -r_6 - r_7, \tag{4.20}$$

$$\frac{\mathrm{d}C_3}{\mathrm{d}t} = r_{4b} + r_5 + r_6, \tag{4.21}$$

where

$$R_1: \quad r_1 = k_1 A_u - k_{-1} A_p,$$

$$R_2: \quad r_2 = k_2 L_u - k_{-2} L_p,$$

$$R_{3A}: \quad r_{3a} = k_3(w) A_u L_u - k_{-3} C_0,$$

$$R_{3B}: \quad r_{3b} = k_3(w) A_p L_u - k_{-3} C_1,$$

$$R_{4A}: \quad r_{4a} = k_4(w) C_0 - k_{-4} C_2,$$

$$R_{4B}: \quad r_{4b} = k_4(w) C_1 - k_{-4} C_3,$$

$$R_5: \quad r_5 = \begin{cases} k_5 A_p L_p - k_{-5} C_3 & \text{under models } H_{x1}, \\ (k_3(w) + k_5) A_p L_p - (k_{-3} + k_{-5}) C_3 & \text{under models } H_{x2}, \end{cases}$$

$$R_6: \quad r_6 = k_6 C_2 - k_{-6}(w) C_3,$$

$$R_7: \quad r_7 = \begin{cases} k_{-7}(w) C_2 & \text{under models } H_{x1}, \\ k_3(w) A_u L_p - (k_{-3} + k_{-7}(w)) C_2 & \text{under models } H_{x2}, \end{cases}$$

and k_i $(i = 1, \ldots, 6)$ represent association or phosphorylation rates and k_{-i} $(i = 1, \ldots, 7)$ represent dephosphorylation or dissociation rates. Here w indicates possible Wnt-dependence of a particular rate constant. The colours for each equation correspond to those used in the model schematic (see Figure 4.2).

Historically, most mathematical models of the Wnt pathway are based on systems of ODEs. Given their quantitative nature, ODE-based models have many advantages compared to verbal models that are common in many studies of the pathway, yet they are much simpler than spatial and stochastic models. Using a system of ODEs to describe the temporal dynamics of our candidate mathematical models encapsulates several assumptions.

First, we assume that randomness and stochastic nature of the interaction of our proteins of interest is not fundamental in driving the observed dynamics. Mazemondet et al. (2012) compared stochastic and deterministic modelling of the Wnt pathway. They established that for low levels of Axin, as observed by Lee et al. (2003), stochastic effects can play a part in determining the model dynamics, however these effects were not reproducible in their *in vitro* experiments in mammalian cell lines. This led them to

suggest that Axin levels may not be as low as proposed by Lee et al. (2003), in which case stochastic effects may be neglected. Moreover, Tan et al. (2012) also observe high levels of Axin, again suggesting stochastic effects might not be crucial in describing the dynamics of the Wnt pathway in mammalian cell lines. We remark that the PySB package we use in our framework can also solve a proposed model using stochastic simulators, either via the the Danos implicit state simulation algorithm for rule-based systems (Danos et al., 2007), or simulate the set of reactions stochastically using the the Gillespie algorithm (Gillespie, 1976). However, stochastic modelling has considerably higher computational cost, that will bring another complication to proposing new model structures and model selection.

Second, we ignore the spatial variations in protein concentrations in our candidate mathematical models. These variations may be modelled using different methods, such as compartmentalisations (e.g. the Shuttle model by MacLean et al. (2015b)). Our literature review revealed very little useful data with regards to localisation of Wnt pathway proteins upon Wnt stimulation. Moreover, in reality, most of the current commercially available antibodies are not suitable for immunofluorescence studies which may enable collection of such data. As such, model selection among candidate models that involves such details will be extremely difficult. Hence, in line with most other mathematical models of the Wnt pathway, we ignore spatial variations and assume a well-mixed system.

Dependent variable	Description	Initial Condition (nM)
A_u	Concentration of Axin not phosphorylated at S497/S500	0
A_p	Concentration of Axin phosphorylated at S497/S500	Variable
L_u	Concentration of LRP6 not phosphorylated at S1490	15
L_p	Concentration of LRP6 phosphorylated at S1490	2
C_0	Concentration of Complex of $\mathrm{L_u}$ and $\mathrm{A_u}$	0
C_1	Concentration of Complex of $\mathrm{L_u}$ and $\mathrm{A_p}$	0
C_2	Concentration of Complex of $\mathrm{L_p}$ and $\mathrm{A_u}$	0
C_3	Concentration of Complex of $\mathrm{L_p}$ and $\mathrm{A_p}$	0

TABLE 4.2: Dependent variables used in our mathematical models, and their initial values in the "Wnt-off" simulation (see Section 4.2.4). Starting at these initial conditions, we solve the system of ODEs numerically until we reach a steady state, before using these steady state values as initial conditions for solving the system under "Wnt-on" parameter values. We vary total levels of Axin, A_{tot}, by changing the initial conditions for A_p. See text for more details.

In Tables 4.2 and 4.3 we list the dependent variables and parameters used in our mathematical models, while Table 4.4 summarises the candidate models we consider.

By taking suitable combinations of Equations (4.14)-(4.21), it is possible to derive two conservation laws. In particular, summing Equations (4.14), (4.15) and (4.18)-(4.21) yields:

$$\frac{\mathrm{d}}{\mathrm{d}t}\big(\text{total Axin}\big) = \frac{\mathrm{d}}{\mathrm{d}t}\big(A_u + A_p + C_0 + C_1 + C_2 + C_3\big) = 0,$$

Parameter	Description	Unit
$k_{\pm 1}$	Rate of Axin phosphorylation/dephosphorylation (Wnt independent)	min^{-1}
$k_{\pm 2}$	Rate of LRP6 phosphorylation/dephosphorylation (Wnt independent)	min^{-1}
$k_{\pm 3}$	Rate of initial LRP6/Axin association/dissociation	$\mathrm{min}^{-1}\mathrm{nM}^{-1}$
$k_{\pm 4}$	Rate of LRP6 phosphorylation/dephosphorylation while in complex with Axin	min^{-1}
$k_{\pm 5}$	Rate of association/dissociation of pS497/500 Axin and pS1490 LRP6	$\mathrm{min}^{-1}\mathrm{nM}^{-1}$
$k_{\pm 6}$	Rate of phosphorylation/dephosphorylation of Axin while in complex with LRP6	min^{-1}
k_{-7}	Rate of release of unphosphorylated Axin from Axin/LRP6 complex	min^{-1}
A_{tot}, L_{tot}	Total Axin and LRP6	nM
w_3, w_4, w_{-7}	Wnt multipliers (see Section 4.2.4)	-
τ	Time constant (see Section 4.2.4)	-

TABLE 4.3: Parameters used in our mathematical models. Table 4.5 contains the ranges used to estimate these parameters during model selection.

while, summing Equations (4.16)-(4.21) supplies:

$$\frac{\mathrm{d}}{\mathrm{d}t}\big(\text{total LRP6}\big) = \frac{\mathrm{d}}{\mathrm{d}t}\big(L_u + L_p + C_0 + C_1 + C_2 + C_3\big) = 0.$$

That is, total levels of LRP6 and Axin are constant with respect to time:

$$A_{\text{tot}} = A_u + A_p + C_0 + C_1 + C_2 + C_3, \tag{4.22}$$
$$L_{\text{tot}} = L_u + L_p + C_0 + C_1 + C_2 + C_3. \tag{4.23}$$

where A_{tot} and L_{tot} are the total levels of LRP6 and Axin respectively. We can exploit these conservation laws to reduce the number of dependent variables in the candidate models from eight to six.

Candidate Model	Number of Independent Parameters	Wnt Dependent Reactions	Basal Axin/LRP6 Binding
H_{11}	17	LRP6/Axin binding	-
H_{12}	17	LRP6/Axin binding	✓
H_{21}	17	Bounded LRP6 phosphorylation	-
H_{22}	17	Bounded LRP6 phosphorylation	✓
H_{31}	18	LRP6/Axin binding and release	-
H_{32}	18	LRP6/Axin binding and release	✓
H_{41}	17	Bounded Axin dephosphorylation	-
H_{42}	17	Bounded Axin dephosphorylation	✓
H_{51}	18	Bounded Axin dephosphorylation and Axin/LRP6 release	-
H_{52}	18	Bounded Axin dephosphorylation and Axin/LRP6 release	✓
H_{61}	18	Bounded LRP6 phosphorylation and Axin/LRP6 release	-
H_{62}	18	Bounded LRP6 phosphorylation and Axin/LRP6 release	✓

TABLE 4.4: We study a few different candidate models that differ in terms of both the reactions that are included in the model and the reactions that are Wnt dependent. We aim to keep the candidate models simple, while including different structures that could be consistent with experimental observations. Independent parameters include reaction rates, conserved protein levels, Wnt multipliers and exponential growth time constant.

4.2.4 Implementation of the mathematical model

The candidate models were solved by first writing the reactions in Python using the PySB package (Lopez et al., 2014); this package automatically converts a set of chemical reactions to a system of ODEs. In order to improve computation time, instead of using the numerical methods provided by PySB, the ODEs were extracted automatically and solved using the *integrate.odeint* function in Python's SciPy scientific package (Jones et al., 2001). This function uses lsoda from the FORTRAN library odepack and automatically adapts to solve stiff and non-stiff systems of first order ODEs using Backward Differentiation Formula (BDF) or Adams predictor-corrector methods respectively.

We solved the system of ODEs at equidistant simulation time points of fifteen minutes, with the maximum number of steps between each time point (*mxstep* argument to *integrate.odeint*) increased to 10000. The solver automatically reduces the time step between the requested time points further to keep the estimated local error within relative and absolute tolerances (*rtol*, *atol*), which default to 10^{-8}. We used the default values for all other parameters. In our experience, the default value for *mxstep* lead to warnings due to the stiffness of the system for some of the sampled parameter values as the CMA-ES algorithm explored the parameter space. Moreover, as we will establish in Section 4.2.5.1, our implementation is able to find suitable parameter values for all synthetically generated random model outputs, which increases our confidence in accuracy of our numerical solutions. Finally, in order to increase confidence in validity of our numerical solution further, we attempted to recover suitable parameter values for a subset of the synthetically generated model outputs (see Section 4.2.5.1)

after reducing *mxstep* from 10000 to 1000, effectively coarsening the time step refinement. Using visual inspection, we picked model outputs that were particularly stiff. We failed to recover suitable parameter values in all these cases, whereas as we establish in Section 4.2.5.1 we are able to recover suitable parameter values with *mxstep* at 10000. Increasing *mxstep* above 10000 made no difference to our ability to recover suitable parameter values.

4.2.4.1 Steady state analysis

Bistability has been associated with various sub-cellular biological phenomena such as cell cycle progression (Tyson and Novák, 2010; Swat et al., 2004). Such a system could tolerate large changes in the value of underlying parameters while admitting a switch like behaviour. To our knowledge bistability has not been observed or proposed to be important in the canonical Wnt pathway.

We have not been able to obtain a concise analytic expression for the steady state(s) of Equations (4.14)-(4.21). Thus, we instead solve the ODE system to steady state numerically for a model parameter set. We note that if the ODE system admits more than one stable steady state, this method may miss one or more of the steady states.

Note on analysis with chemical reaction network theory (CRNT) toolbox. Chemical reaction network theory (CRNT) may be applied to biochemical networks to establish whether they may admit multiple steady states. We studied our candidate mathematical models using the CRNT Toolbox (Ellison et al., 2014), which calculates various properties of chemical networks in order to establish whether a particular network may admit multiple positive steady states. The results were inconclusive in suggesting whether bistability is possible or not, and so we do not detail them here.

4.2.5 Model selection

We apply multi-start CMA-ES as described in Chapter 3 to our candidate mathematical models to determine whether they can reproduce some of the recent experimental observations. This enables us to accept or reject certain model structures, and gives insight into the possible nature of the interactions between LRP6 and Axin.

For a sampled set of model parameters (see Table 4.5), we integrate the model in the "Wnt-off" state numerically from the initial conditions given in Table 4.2 until a steady state is reached. We assume the solution has reached steady state if the maximum absolute change in each dependent variable in the last hour of simulation is less than 1%. We continue simulating for a longer period if this is not achieved, up to a maximum time of 20 hours. This steady state was then used as the initial conditions when solving the mathematical model in the "Wnt-on" state until $t_{\text{final}} = 3 \text{ hours}$.

Wnt-dependent rate parameters changed over time from their "Wnt-off" to "Wnt-on" value using an exponential growth time-dependent function, where the exponential time can vary between 1 and 20 minutes (see Section 4.2.1.1). For example, assuming Wnt acts on reaction rate k_i, increasing it by a factor of w upon Wnt stimulation, we assume:

$$k_i^{\text{on}}(t) = k_i\Big(1 + (w-1)\big(1 - e^{(-t/\tau)}\big)\Big) \tag{4.24}$$

where w is the Wnt multiplier and τ is the exponential time constant, meaning $\tau \ln 2$ is the half life of the exponential growth. Figure 4.3 displays an example of this function.

Param	Description	Unit	Value	Details
L_{tot}	Total LRP6 concentration	nM	17	Bafico et al. (2001) calculate 2500-5000 molecules/cell in NIH3T3 cells. Average number of receptors per cell (3750) is converted to a concentration level using a membrane volume of 0.37pL for HEK293T cells (Tan et al., 2012).
A_{tot}	Total Axin concentration	nM	0.001-200	150 (HEK293T), 110 (MDCK), 30 (Caco-2), 30 (SW480), 20 (SW480APC) (Tan et al., 2012), 0.02 (Xenopus egg extracts) (Lee et al., 2003).
	Phosphorylation, dephosphorylation rates	min^{-1}	10^{-4}-10^{4}	Upper bound chosen to be one order of magnitude above highest measured by Rose and Dube (1976), and the lower bound chosen one order of magnitude below the lowest values found in mathematical models of the Wnt pathway.
	Association rates	nM^{-1} min^{-1}	10^{-5}-10^{6}	Northrup and Erickson (1992) argue that typical values for association rates are of order of $10^6\text{M}^{-1}\text{s}^{-1} = 10^6 \times 60 \times 10^{-9}\text{nM}^{-1}\,\text{min}^{-1} = 0.06\text{nM}^{-1}\,\text{min}^{-1}$. There is a large range of fitted parameter values in the relevant literature. We select upper and lower bounds that are one order of magnitude beyond the highest and lowest values fitted.
	Dissociation constants	nM	0.01-10^{4}	Upper and lower bounds chosen one order of magnitude beyond the values found in the relevant references (Lee et al., 2003; Wei et al., 2007). Other mathematical models of the Wnt pathway have found lower fitted rate constants, however we do not use these values as they are not backed by any experimental observations.
w_i^*	Wnt multipliers		1-100	Upon Wnt stimulation, Hernández et al. (2012) see up to a ten fold increase in inhibition of the rate of phosphorylation of β-catenin. We use an upper bound which is one order of magnitude beyond this value.
τ	Activation time constant		1-20	Exponential time constant used to calculate the speed of fold change in the rate of Wnt driven reaction, in line with values observed by Hernández et al. (2012).

TABLE 4.5: Range of parameter values used to explore the output of each candidate mathematical model. The upper and lower ranges for the rate constants are taken from a combination of measurements from biological experiments or values used in other mathematical models of the Wnt pathway.

A note on the range of parameters w. For candidate models H_{xy} in this chapter, we only consider cases where Wnt stimulation leads to an increase in a particular reaction rate. We believe this is justified due to several reasons. For example, LRP6 phosphorylation and levels of Axin in complex with LRP6 are both observed to increase upon Wnt stimulation. Similarly, Kim et al. (2013) hypothesise that Axin is actively released

from LRP6 after dephosphorylation upon Wnt stimulation. We believe these justify our assumptions that Wnt might lead to an increase in the rate of these reactions (namely rates k_3, k_4 and k_{-7}).

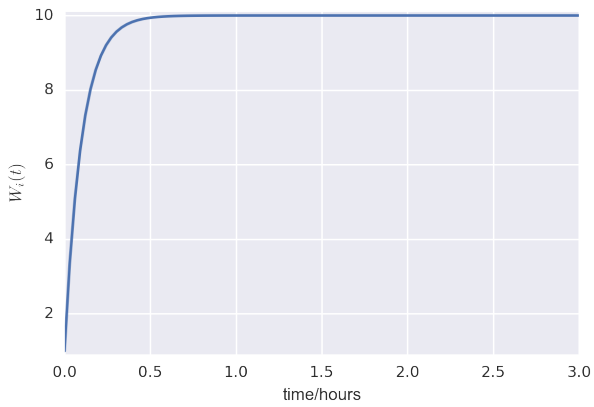


FIGURE 4.3: Externally prescribed dependent variables $W_i(t)$ drives the change in reaction rates upon Wnt stimulation in our mathematical models. This Figure shows a plot for $W_i(t) = (1 + (10 - 1)(1 - e^{60t/6})$, which corresponds to a multiplier of 10 and characteristic time of 6 minutes

We compare the output of each candidate mathematical model to data from experiments by Kim et al. (2013). The authors used Western blots and co-immunoprecipitation (co-IP) studies to measure the changes in levels of Axin and LRP6 in various phosphorylation states and in complexes with one another upon Wnt stimulation. They achieved similar results in two different human cell lines, HEK293T and L cells. We also note that similar results regarding interactions between Axin and LRP6 have been reported by Khan et al. (2007) and Li et al. (2012).

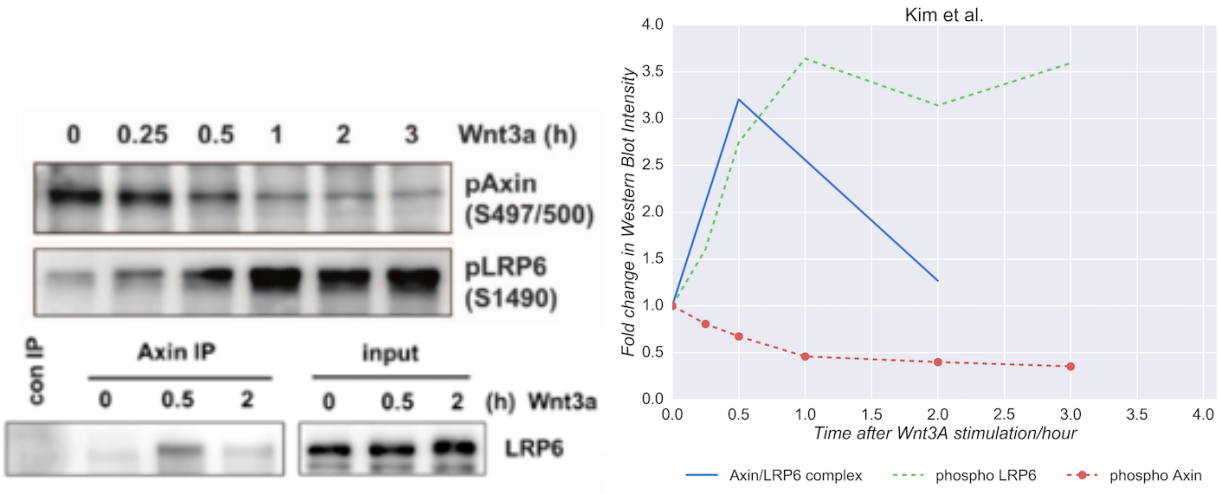
As mentioned in Chapters 2 and 3, the output from Western blots and co-IPs are semi-quantitative; they do not directly correspond to the concentration of the proteins being measured, but instead a transformation of these levels, which may vary depending on the experimental conditions and the specificity of the antibodies used (Pargett and Umulis, 2013). The quantitative output may also vary greatly from experiment to experiment depending on the initial state of the cells.

Given the expected variation in these values, we make a qualitative, rather than quantitative, comparison between the output of candidate models and the experimental observations. That is, we investigate whether a candidate model can reproduce the qualitative behaviours observed experimentally, such as a monotonic increase or a bell shape in a certain experimental output. As described in 3.5.2, we used satisfaction metrics to make model comparisons. Satisfaction metrics are defined such that if the requirement is satisfied, the cost is zero; otherwise a penalty is added to the cost function to represent the distance of the output from the edge of the satisfaction area (Pargett and Umulis, 2013).

In our study, the cost function that is optimised using multi-start CMA-ES is the l^2-norm of a cost vector, where each element of the cost vector aims to compare various properties of the model output with observations by Kim et al. (2013). Qualitatively, our primary requirements are that upon Wnt stimulation:

1. Total levels of pS497/500 Axin (i.e. $A_p + C_1 + C_3$) should drop monotonically;
2. Total levels of pS1490 LRP6 (i.e. $L_p + C_2 + C_3$) should increase monotonically;

3. Levels of LRP6/Axin Complex (i.e. $C_0 + C_1 + C_2 + C_3$) should increase within 30 minutes and then return to their original levels within 2 hours;
4. and the system should reach steady state within 90 minutes.



(A) (B)

FIGURE 4.4: Kim et al. (2013) stimulate human cell lines HEK293T and L Cells with Wnt3A ligands and use Western blots and co-immunoprecipitation studies to measure the change in concentration levels of various components of the Wnt signalling pathway. (A) Actual blots data in L cells (please see Section 2.3.3 of Chapter 2 on how to read such blots). (B) Quantification of these results using algorithm described in Appendix A, Section A.3. Total pS497/500 Axin, pS1490 LRP6 and Axin/LRP6 complex correspond to $A_p + C_1 + C_3$, $L_p + C_2 + C_3$ and $C_0 + C_1 + C_2 + C_3$ in our candidate model outputs respectively.

We developed a simple algorithm (See Appendix A) to convert the semi-quantitative experimental results by Kim et al. (2013) into quantitative values, shown in Figure 4.4. This allows us to fix reasonable edges for the satisfaction metrics when defining the elements of the cost vector. Table B.1 in Appendix B lists the exact elements of the cost vector used in our optimisation algorithm. The final cost is then given by

$$J = \sum_{i=0}^{8} w_i J_i^2, \tag{4.25}$$

where J_i and w_i are the cost elements and the associated weights.

4.2.5.1 Parameter values for the multi-start CMA-ES technique

In order to increase confidence that we are exploring the high dimensional parameter space of the candidate models appropriately using the multi-start CMA-ES technique, we investigate whether the multi-start CMA-ES technique can find appropriate fits to synthetic data generated from the candidate models.

For each of the twelve candidate models, we generate eight random vectors from the parameter space defined in Table 4.5 and use these to generate $12 \times 8 = 96$ synthetic model outputs.

We solve each model numerically as described earlier in the "Wnt-off" state until steady state and then in the "Wnt-on" state. We sample the model output at ten equidistant time points in the "Wnt-on" state. Since it is difficult to select an appropriate qualitative cost function for randomly generated model outputs, we calculate sum of squared errors to compare the model outputs with the synthetic model output. We accept any fits with a cost of below 0.001. For consistency with the problem of interest, we only include levels of pS497/500 Axin, pS1490 LRP6 and Axin/LRP6 complex when measuring the distance between the target data and model output.

We keep other CMA-ES algorithm parameter values at their default value, in particular using the default number of particles. We initiate CMA-ES at a randomly selected parameter vector $\boldsymbol{\theta}$ selected in log-space. Using log-space to calculate the initial optimisation points enabled a better exploration of the wide parameter space, which can span ten orders of magnitude. Unless a suitable fit is found, we restart the algorithm at a new randomly selected parameter vector. We continue this process until a suitable fit is found.

In all cases we confirmed that we are able to find a set of parameter values that reproduces the synthetic true output. As expected the original parameter vector was not identified.

In 72 of the 96 synthetic datasets, 10 or fewer restarts were enough to find a good fit, while for 3 of the 96 synthetic datasets, more than 80 optimisation runs were completed before a suitable fit was found. The highest number of optimisation runs completed before a suitable parameter set was found was 106. We note these results would be different for re-runs.

Using these results, we initialise CMA-ES at 112 randomly selected parameter vectors $\boldsymbol{\theta}$ selected in log-space. The parameter vectors corresponding to the lowest costs are selected as vectors with best fits. $112 = 7 \times 16$ was selected as it was higher than 106 (the highest number of restarts required to reproduce any of the synthetic model outputs) and to ease distribution of computational workload as our model selection was carried out on 16-core computers in a cluster.

Table 4.5 lists the range of parameter values used to explore the model outputs. The parameter vector $\boldsymbol{\theta}$ consists of:

- Phosphorylation and dephosphorylation rates ($k_{\pm 1}$, $k_{\pm 2}$, $k_{\pm 4}$, $k_{\pm 6}$),
- Association rates (k_3, k_5),
- Dissociation constants ($K_3 = k_{-3}/k_3$, $K_5 = k_{-5}/k_5$, $K_7 = k_{-7}/k_3$),
- Time constant τ,
- A subset of Wnt multipliers w_3, w_4, w_{-7}, depending on the candidate model structures,
- Total Axin levels A_{tot}.

Notice we use dissociation constants instead of dissociation rates as we could find several values for dissociation constants in the literature. These are then used to calculate the dissociation rates, k_{-3}, k_{-5} and k_{-7}.

The parameter vector $\boldsymbol{\theta}$ contains 16 or 17 parameters depending on the candidate model. We remark that we allow the total levels of Axin A_{tot} to vary during model selection to reflect the markedly different values quoted in the literature for the levels of Axin in different cell lines. We do not vary the total levels of LRP6 (L_{tot}) as we are only able to find one quoted value in the literature.

4.3 Results

We have proposed a set of candidate models that can be combined with semi-quantitative experimental data in order to gain insight into the interactions between LRP6 and Axin upon Wnt stimulation. We assume that Axin and LRP6 may exist in phosphorylated or unphosphorylated states. Axin and LRP6 may also form complexes that may lead to Axin dephosphorylation and LRP6 phosphorylation. The candidate models differ in their structure (i.e. interactions that define each model) and which reactions are altered by Wnt.

The parameter space of each candidate model is explored using the optimisation algorithm described earlier to find sets of parameter values with a good qualitative fit to experimental observations by Kim et al. (2013). We reject candidate models for which the algorithm fails to find a suitable parametrization. In Table 4.6 we identify those models for which we could find parameter values that yield a suitable qualitative fit to the experimental observations. In Figure 4.5 we present typical outputs from the successful candidate models. We rank the parameter sets found in ascending order of the corresponding cost from 0 to 111 (112 starting points). The exact parameter sets are provided in Appendix C.

Candidate Model	Wnt Dependent Reactions	Basal Axin/LRP6 Binding	% optimisation runs with a good qualitative fit
H_{11}	LRP6/Axin binding	-	4%
H_{12}	LRP6/Axin binding	✓	✗
H_{21}	Bounded LRP6 phosphorylation	-	14%
H_{22}	Bounded LRP6 phosphorylation	✓	9%
H_{31}	LRP6/Axin binding and release	-	10%
H_{32}	LRP6/Axin binding and release	✓	8%
H_{41}	Bounded Axin dephosphorylation	-	✗
H_{42}	Bounded Axin dephosphorylation	✓	✗
H_{51}	Bounded Axin dephosphorylation and Axin/LRP6 release	-	✗
H_{52}	Bounded Axin dephosphorylation and Axin/LRP6 release	✓	✗
H_{61}	Bounded LRP6 phosphorylation and Axin/LRP6 release	-	20%
H_{62}	Bounded LRP6 phosphorylation and Axin/LRP6 release	✓	16%

TABLE 4.6: The results of running the multi-start CMA-ES technique on the twelve candidate models H_{xy} to investigate whether they can reproduce the experimental results by Kim et al. (2013).

We remark that some of the remaining candidate models (e.g. H_{21}) are simpler versions of other models (e.g. H_{61}). We only choose the more detailed model if further analysis (such as *in silico* experiments and sensitivity analysis) suggest the simpler candidate models are unsuitable; we choose the simpler model if there is insufficient data to distinguish between the two.

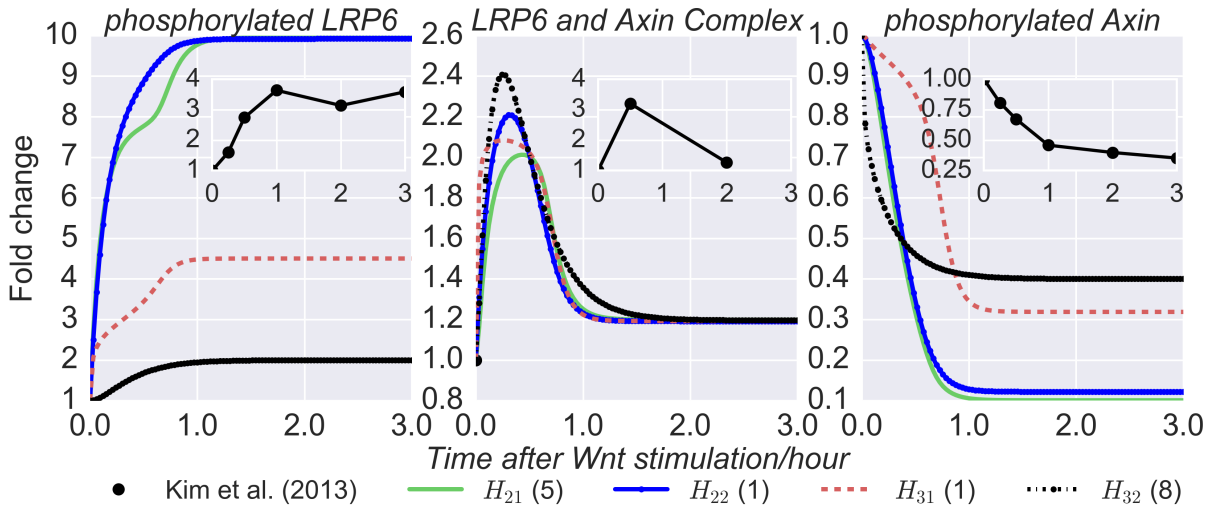


FIGURE 4.5: Example of best fits from four of the candidate models that we could find a set of parameter values that provide a good qualitative fit to the experimental observations by Kim et al. (2013) (we exclude candidate models H_{61} and H_{62} and only include the simpler versions of these model structures, namely H_{21} and H_{22}). The experimental observations are displayed in the inset plots. pS1490 LRP6, LRP6/Axin complex and pS497/500 Axin correspond to $L_p + C_2 + C_3$, $C_0 + C_1 + C_2 + C_3$ and $A_p + C_1 + C_3$ in our candidate model outputs respectively. The optimisation algorithm used to explore the parameter space is detailed in Section 4.2.5, and the details of the candidate models is summarised in Table 4.6. The number in bracket next to the candidate model name in the figure legend corresponds to the parameter set found using the optimisation algorithm. These parameter sets are given in Appendix C.

For candidate models H_{x1}, where pS1490 LRP6 binds to pS497/500 Axin only, in some cases we were able to find a good qualitative fit by making only one reaction rate Wnt dependent (rate of LRP6/Axin complex formation in H_{11}; rate of LRP6 phosphorylation in H_{21}). Increasing the rate of dephosphorylation of Axin upon Wnt stimulation was insufficient to describe the observed dynamics. Unsurprisingly, increasing the rate of release of Axin from LRP6 upon Wnt stimulation in addition to Axin/LRP6 recruitment (under H_{31}), or LRP6 phosphorylation (under H_{61}), was sufficient to describe the observed dynamics.

For candidate models H_{x2} where there is a basal level of Axin binding to pS1490 LRP6, increasing the rate of Axin/LRP6 complex formation upon Wnt stimulation (as in H_{12}) fails to describe the experimental observations. However, if the rate of LRP6 phosphorylation increases upon Wnt stimulation (as in H_{22}) it is then possible to explain the experimental observations. As before, we identify several sets of parameter values with suitable model outputs.

In order for candidate models H_{x2} to fit the experimental observations, an increase in the rate of recruitment of Axin to LRP6 (k_3) upon Wnt stimulation, must be combined with an increase in the rate of release of Axin from LRP6 after its dephosphorylation (k_{-7}). This structure corresponds to model H_{32}; we found several suitable parameter sets for this model.

It should be apparent from the plots in Figure 4.5 that several candidate models give good qualitative fits. That is, we could not discriminate between these mathematical models using these experimental observations. We note also that other suitable parameter sets may exist in regions of parameter space not explored by our algorithm.

In the next two sections we analyse these candidate models further.

4.3.1 Sensitivity analysis

Living organisms face perturbation on various levels from subcellular and genetic levels to organism levels. Robustness is a central feature of many systems in living organism (Stelling et al., 2004). Robustness might be achieved by several methods. For example, it could be due to redundancy, where different paths exist for carrying out the same functionality. Feedback loops are also known to increase robustness of subcellular pathways, where a system's output controls the effectiveness of the input signal on the system. Robustness might also be an inherent part of the design of a system (Stelling et al., 2004).

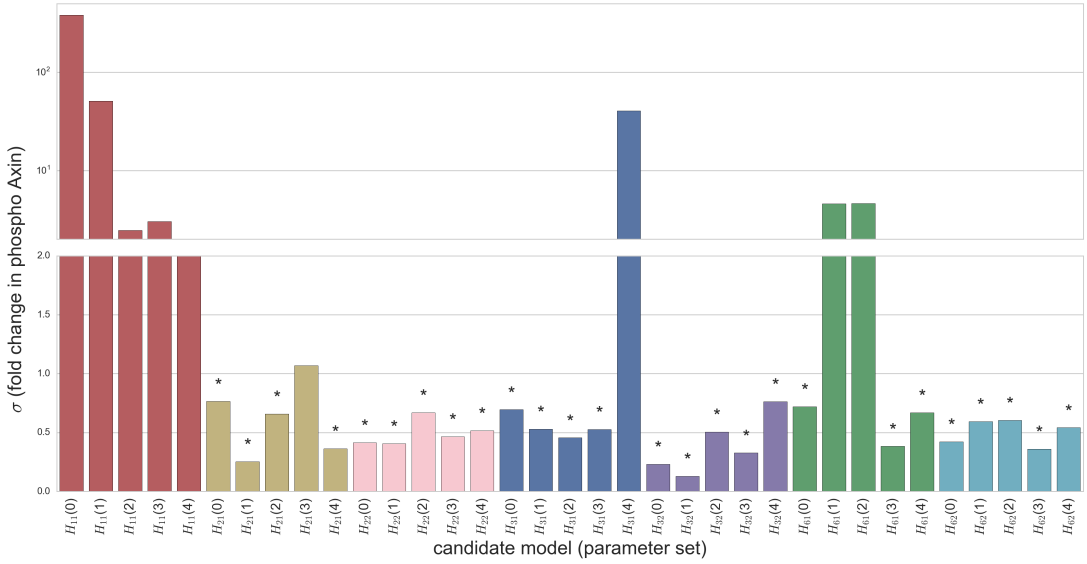


FIGURE 4.6: Standard deviation of control coefficients corresponding to fold change in total levels of pS497/500 Axin for various candidate models and parameter sets. We show up to 5 parameter sets for each candidate model. Each bar corresponds to one candidate model and parameter set combination. Lower values of the standard deviation correspond to a system that is more robust to perturbations in the values of rate parameters. * above a bar marks model and parameter combinations with a standard deviation of less than 1, which we accept as robust.

Goentoro and Kirschner (2009) use experiments on the RKO cell line and Xenopus embryos to show that the fold change in total levels of β-catenin upon Wnt stimulation is robust to perturbation in Wnt pathway machinery in the first few hours after Wnt stimulation. Since our candidate models is focused on the first few hours after Wnt stimulation, and known feedback loops involving Axin1, Axin2 or LRP6 operate on longer time periods, studying robustness of our the model outputs to perturbations in parameter values might provide us with further information about their suitability i.e. a means by which to discriminate between suitable candidate models.

As described earlier in this chapter, we represent active destruction complex, which can recruit and mark β-catenin for degradation by pS497/500 Axin in our candidate models. Drops in levels of pS497/500 Axin leads to an increase in levels of β-catenin (Kim et al., 2013). Since we do not model β-catenin in our candidate model, we instead investigate robustness of levels pS497/500 Axin to perturbation in model parameter values. Following Lee et al. (2003), we study the robustness in the model

with respect to changes in parameter values using control coefficients:

$$C^X_{\pm i} = \frac{k_{\pm i}}{X}\frac{\partial X}{\partial k_{\pm i}}, \tag{4.26}$$

where X denotes the fold change in total levels of pS497/500 Axin after 3 hours of Wnt stimulation. We use the standard deviation of all control coefficients to calculate a measure of system robustness to variation in all model parameters:

$$\sigma^X = \sqrt{\frac{1}{n}\sum_{\text{all } k_{\pm i}} (C^X_i - \mu^X)^2}, \tag{4.27}$$

where μ^X is the mean of all such control coefficients.

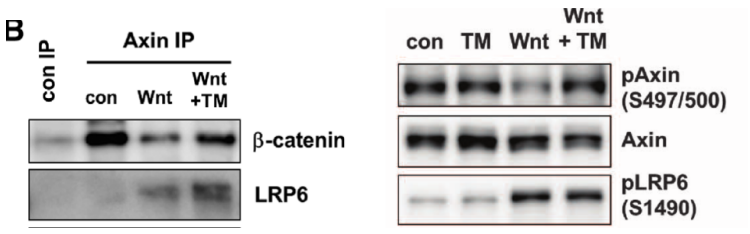
In Figure 4.6 we show how σ^X varies for different candidate models and feasible parameter sets identified in the last section.

Some of the candidate models and parameter sets are very sensitive to changes in parameter values. For example, a 1% change in the rate constants under candidate model H_{11} with parameter set 3, corresponds to on average a 3% change in fold change in levels of pS497/500 Axin over 3 hours. We can use these observations to reject non-robust parameter sets for each candidate model. * above a bar indicates the candidate model and parameter sets we are accepting as being most robust.

4.3.2 *in silico* experiments

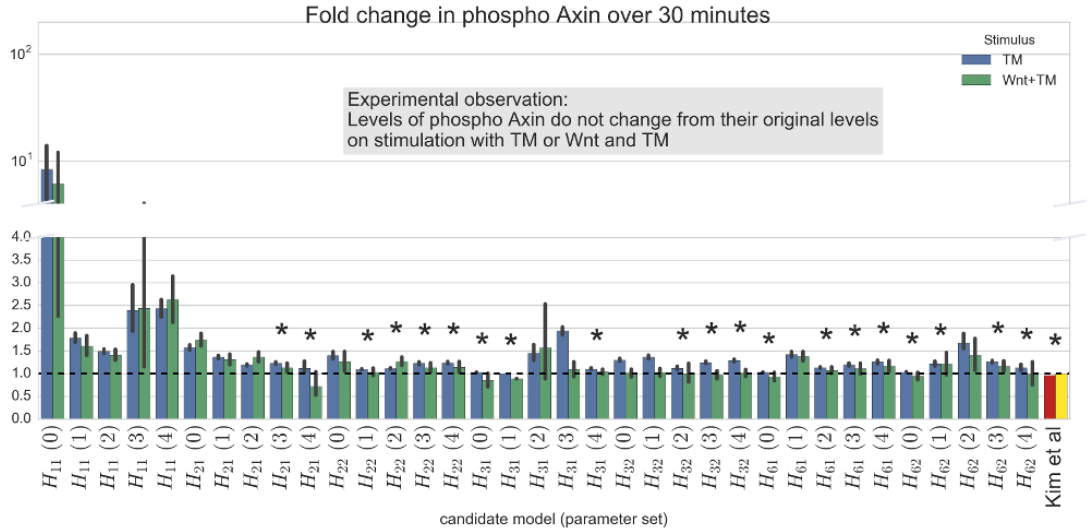
In addition to looking at the effect of Wnt stimulation on cells *in vitro*, Kim et al. (2013) also studied the impact of inhibitors such as the highly specific and potent PP1 inhibitor, Tautomycin (TM), on the interaction between Axin and LRP6 and their phosphorylation states (see Figure 4.7). Axin dephosphorylation upon Wnt stimulation likely reflects the counterbalance between GSK3 and protein phosphotase PP1 (Kim et al., 2013). They observed that treatment with TM did not affect levels of LRP6 phosphorylated at S1490 upon Wnt stimulation (third panel in Figure 4.7B), whereas it reduces the effect of Wnt on dephosphorylation of Axin (first panel in Figure 4.7B). Figure 4.7A suggests that TM also increases levels of LRP6 in complex with Axin compared to Wnt stimulation alone.

Using the candidate models and parameter sets found earlier, we run similar *in silico* experiments to study the response of each candidate model and parameter set to

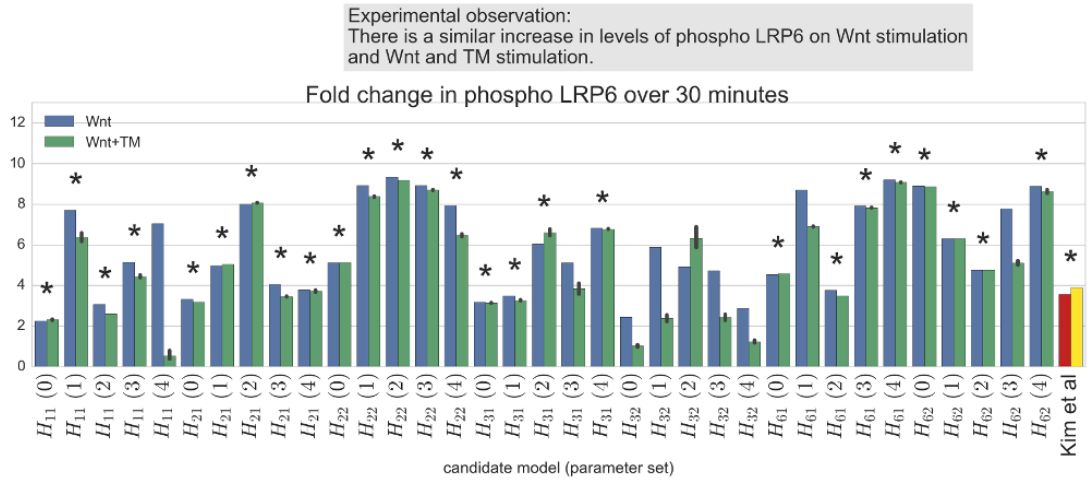


(A) L cells (B) HEK293T

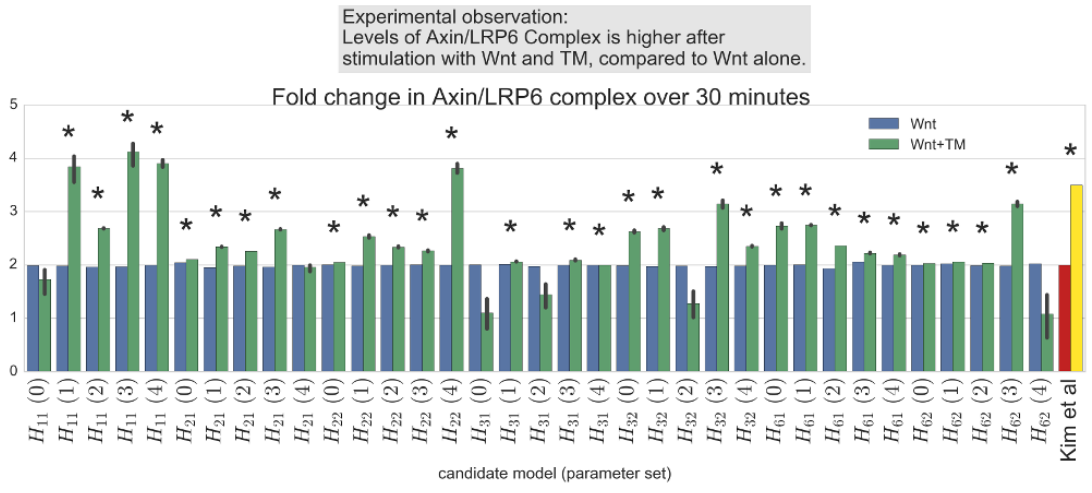
FIGURE 4.7: Kim et al. (2013) stimulated HEK293T cells or L cells with Wnt and/or the PP1 inhibitor, Tautomycin (TM) and measured levels of pS1490 LRP6, pS497/500 Axin, and LRP6 in complex with Axin after 30 minutes. We present the results from similar *in silico* experiments performed on each candidate model in Figure 4.8. We given an explanation on how to read such blots in Section 2.3.3 of Chapter 2.



(A)



(B)



(C)

FIGURE 4.8: *in silico* experiments on candidate models H_{xy} with *in vitro*. The final bars displayed in different colours are quantification of the equivalent *in vitro* experiments displayed in Figure 4.7 by Kim et al. (2013). We assume that stimulation with phosphatase inhibitor TM reduces the rate of dephosphorylation of Axin in complex with LRP6 (k_{-6}) by $90\% \pm 10\%$ (see text). Black lines above each bar represent a one standard deviation confidence interval. We stimulate the cells with TM alone, with Wnt alone, or with Wnt plus TM for 30 minutes. We show up to 5 parameter sets for each candidate model. * above a bar marks model and parameter sets that are qualitatively consistent with *in vitro* experimental observations.

a combination of TM and Wnt stimulation. We assume TM reduces the rate of Wnt-dependent dephosphorylation of Axin (k_{-6}) by $90\% \pm 10\%$ on a relative basis (i.e. 81%, 90% or 99%), without impacting other reaction rates in each candidate model. We note that we do not change the rates of LRP6 dephosphorylation nor Wnt-independent Axin dephosphorylation for the following reasons: levels of phosphorylated Axin remain unchanged from control upon stimulation with TM alone (notice the first two columns in the first row in Figure 4.7B), suggesting that TM does not significantly impact the Wnt-independent Axin dephosphorylation. Similarly, LRP6 phosphorylation is unchanged from unstimulated levels upon stimulation with TM alone, again suggesting that TM does not significantly alter dephosphorylation of LRP6.

The *in vitro* experiments that we seek to replicate are:

- (A) Levels of pS497/500 Axin do not change from their original levels on stimulation with TM, or Wnt and TM combined.
- (B) There is a similar increase in levels of pS1490 LRP6 upon stimulation with alone or Wnt and TM combined.
- (C) Levels of Axin/LRP6 Complex are higher after stimulation with Wnt and TM, compared to Wnt alone.

Figure 4.8 displays the results of these *in silico* experiments. The *'s above each bar mark parameter sets that are consistent with *in vitro* results. We accept candidate models that produce a similar qualitative output compared to the *in vitro* experiments. We accept any result that is within 30% of the target value. For example, in Figure 4.8A, where we expect the fold change in pS497/500 Axin to stay close to one, we accept any candidate models and parameter sets where this level is within 0.7 and 1.3. We can use these observations to reject some candidate models and parameter sets, such as candidate model H_{11}.

4.3.3 Reject more detailed models

We can use observations in Sections 4.3.1 and 4.3.2 to question the suitability of parameter sets/candidate model pairings that are not robust to parameter changes or do not reproduce other observed experimental results. For nested models, such as models H_{21} and H_{61} where H_{61} assumes two reactions are Wnt driven whereas H_{21} assumes only one is, we reject the more detailed model, i,e. model H_{61}. We similarly reject candidate Model H_{62} in favour of candidate model H_{22}. This enables us to reduce the number of suitable candidate models to four: H_{21}, H_{22}, H_{31} and H_{32}.

4.3.4 Proposing further experiments

We have now reduced the number of candidate models remaining to four: H_{21}, H_{22}, H_{31} and H_{32}. We now explain how we may be able to discriminate between these remaining candidate model by carrying out new experiments.

In Figure 4.9 we show how levels of pS1490 LRP6 in complex with Axin vary for the four remaining candidate models after Wnt stimulation. We may measure this quantity using a co-IP study. For example, a large increase after 2 hours will rule out candidate models H_{31} and H_{32}. However, it will not enable us to distinguish between models H_{21} and H_{22}.

In particular notice that the results of this experiment will inform us of the structure of the Wnt pathway in a significant way. Measuring the fold change in levels of

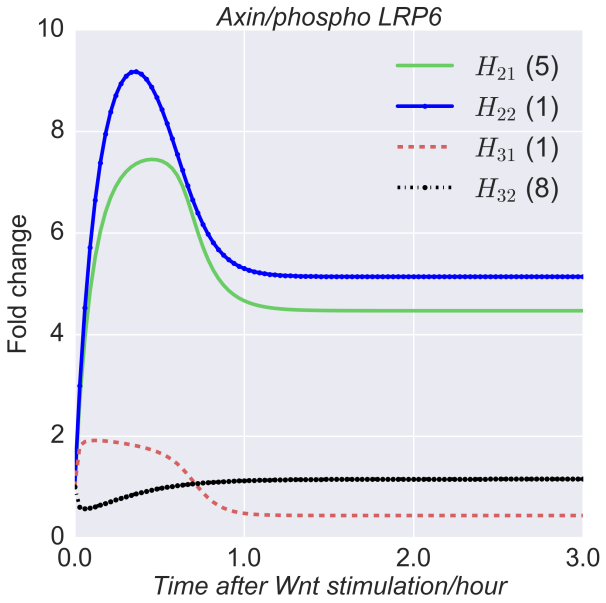


FIGURE 4.9: Measuring levels of Axin in complex with LRP6 phosphorylated at S1490 upon Wnt stimulation could enable us to determine which of our candidate models best describes the dynamics of the canonical Wnt pathway. However, it cannot discriminate between candidate models H_{21} and H_{22}.

Axin/pS1490 LRP6 complex after 3 hours of Wnt stimulation can tell us which reactions of the Wnt pathway are primarily Wnt driven according to our candidate models:

- An increase would suggest that the primary Wnt driven reaction is phosphorylation of LRP6 (reaction R_4).
- No increase or a drop in these levels would suggest that recruitment of Axin to LRP6 and its release are the dominant Wnt driven reactions (reactions R_3 and R_7).

This is one of the key results from this chapter of our work.

A note on results by Li et al. (2012). Similarly to the study by Kim et al. (2013), Li et al. (2012) studied the interaction between Axin and LRP6 upon Wnt stimulation (see Table 6.10 in Chapter 6 for a comparison between the results between these two studies.). We remark that their results did not include the changes in levels of pS497/500 Axin. Similarly to Kim et al. (2013), they observed that levels of Axin/LRP6 complex followed a bell-shape, however, they did not observe a drop to the original levels after 2 hours. We note that Li et al. (2012) also measured the levels of Axin in complex with pS1490 LRP6, which is the experiment we have proposed here. They do observe that these levels increase upon Wnt stimulation as predicted by our candidate models H_{21} and H_{22}, hinting at the suitability of these two models. However, in our opinion this does not validate these two candidate models fully since they observe slightly different results when looking at levels of Axin/LRP6 complex compared to Kim et al. (2013). Levels of Axin/LRP6, and Axin/pS1490 LRP6 complexes should be measured in the same experiment to enable discrimination between the remaining candidate models.

4.4 Simplification of the reduced core model

In Chapter 6 we will extend our candidate models of the canonical Wnt pathway to incorporate β-catenin and a more detailed description of the destruction complex. Introducing new species and biochemical reactions will increase the dimensionality of the model parameter space. In an effort to keep the problem computationally tractable (see Discussion in Chapter 6 and Figure 6.20), in this section we investigate whether we can further simplify the candidate model introduced here while retaining key qualitative behaviours.

4.4.1 Summary of the chapter so far

In this chapter, we have used the state-of-the-art biological literature to propose twelve candidate mathematical models that may describe a cell's initial response to Wnt stimulation. The candidate models focus on interactions between Axin and LRP6 and differ fundamentally in two ways. First, Wnt stimulation alters different reactions in each candidate model. Second, the candidate models vary in structure and in the biochemical reactions included.

We have developed a framework to explore the output of these candidate models and used it to reduce the number of suitable candidate models that are compatible with experimental observations. Figure 4.10 summarises the primary steps in the framework. We give further details of these steps below.

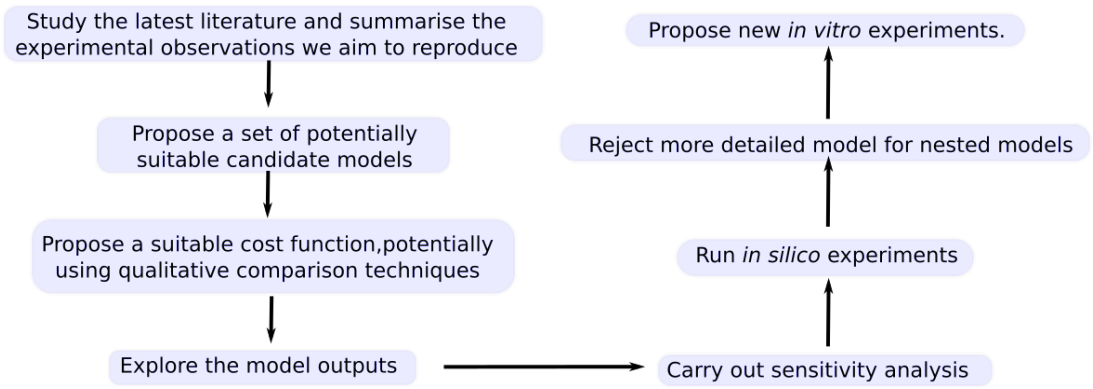


FIGURE 4.10: Our framework for studying dynamics of signalling pathways as applied to a reduced model of the canonical Wnt pathway in this chapter.

Study the latest biological results. Any model proposed to describe a real world system is going to involve some simplifications. By carrying out a detailed literature review, studying existing models and discussion with experts in the field we should be able to summarise the important experimental observations that may be relevant to our problem of interest.

Propose a set of candidate mathematical models. Instead of writing down just one mathematical model, we propose a set of candidate models that may be consistent with the observed experimental results. We note that there may be many more model structures that may also be able to describe the experimental observations.

Propose a suitable cost function. This will allow us to compare the mathematical model output with the experimental observations. If the experimental results are not quantitative, which is the case in many studies of signalling pathways, it might be suitable to use qualitative model comparison techniques such as satisfaction metrics.

Explore the model outputs. Use the CMA-ES optimisation algorithm to establish whether each candidate model can reproduce experimental observations. We remark that care must be taken if the candidate models have markedly different complexities.

Carry out sensitivity analysis. If the output of the biological system is known to be robust to certain perturbations (such as in the case of the canonical Wnt pathway (Goentoro and Kirschner, 2009)), we may use sensitivity analysis to reduce the number of candidate models further by studying their robustness to changes in parameter values.

Run *in silico* experiments. There may be other experimental observations beyond the initial observations that we may be able to use to analyse the candidate models. For example, experimentalists often stimulate cells *in vitro* using stimuli other than Wnt3A. We can perform *in silico* experiments on the candidate models and parameter sets found earlier and compare the results with analogous ones from *in vitro* experiments. This step allows us to further refine the set of suitable candidate models.

Reject more detailed models. If there are any nested models in our remaining candidate models, we will reject the complicated model.

Propose new *in vitro* experiments. We propose new experiments that may enable us to discriminate between the remaining candidate models.

Table 4.7 summarises the results of the steps above as applied to our twelve candidate models.

In the absence of suitable experimental data with which to discriminate between the remaining models, we invoke the principle of Occam's razor to select one of the remaining candidate models to study the canonical Wnt pathway further:

- When comparing candidate model structures H_{x1} and H_{x2}, we choose models H_{x1}, which have a simpler structure and fewer reactions.
- Between models H_{21} and H_{31}, we select model H_{21}, since it assumes there is only one Wnt driven reaction (phosphorylation of LRP6) rather than two (binding and release of Axin and LRP6).

We identify model H_{21} as the most suitable model for describing interactions between Axin and LRP6. In this model:

- Wnt drives phosphorylation of LRP6 by GSK3 rather than recruitment of Axin to LRP6. GSK3 is recruited to the membrane thanks to recruitment of Axin to LRP6.
- Recruitment of unphosphorylated Axin to pS1490 LRP6 is negligible.

Candidate Model	Wnt Dependent Reactions	Basal Axin/ LRP6 Binding	% optimisation runs with a good qualitative fit	% of good runs which are robust	% of good runs which match in silico experiments	Remaining robust parameter sets with good fits	Accepted as simplest
H_{11}	LRP6/Axin binding	-	4%	0%	0%	✗	
H_{12}	LRP6/Axin binding	✓	✗	-	-	✗	
H_{21}	Bounded LRP6 phosphorylation	-	14%	31%	50%	5,15	✓
H_{22}	Bounded LRP6 phosphorylation	✓	9%	80%	100%	1, 2, 3, 4, 5, 6, 8, 9	✓
H_{31}	LRP6/Axin binding and release	-	10%	18%	72%	1	✓
H_{32}	LRP6/Axin binding and release	✓	8%	11%	89%	8	✓
H_{41}	Bounded Axin dephosphorylation	-	✗	-	-	✗	
H_{42}	Bounded Axin dephosphorylation	✓	✗	-	-		
H_{51}	Bounded Axin dephosphorylation and Axin/LRP6 release	-	✗	-	-	✗	
H_{52}	Bounded Axin dephosphorylation and Axin/LRP6 release	✓	✗	-	-	✗	
H_{61}	Bounded LRP6 phosphorylation and Axin/LRP6 release	-	20%	41%	32%	0, 3, 4, 7	✗
H_{62}	Bounded LRP6 phosphorylation and Axin/LRP6 release	✓	16%	56%	100%	0, 1, 5, 6, 7, 8, 9, 12, 13, 14	✗

TABLE 4.7: Summary of model selection for the twelve candidate models. The second to last column contains the number for the parameter sets (from the original 112 sets under each candidate model) that were able to reproduce various experimental observations and were robust to perturbations in model parameter values. These are provided in Appendix C. The last column marks the candidate models we reject (H_{61} and H_{62}), since simpler nested candidate models are accepted (H_{21} and H_{22}).

4.4.2 Simplifying the model

As summarised in the last section, our study suggests that LRP6 phosphorylation is the most likely Wnt driven reaction in our models of the canonical Wnt pathway. We established that several model structures are consistent with the observed experimental results; however, for simplicity we consider the model with fewest reactions. In particular we assume pS1490 LRP6 binds to pS497/500 Axin only and focus on candidate model H_{21}. In this section we describe a simplified version of this candidate model.

Figure 4.11 displays the schematic of our simplified model. We remark that in all candidate models considered so far, we assume that Axin is required for LRP6 phosphorylation at the S1490 (Zeng et al., 2008). In particular, in model H_{21}, Axin is recruited to LRP6 via three reactions:

- via Reactions R_{3A} and R_{3B} to **unphosphorylated** LRP6,
- via Reaction R_5 to **phosphorylated** LRP6.

For our simplified model, we now ignore the Wnt-independent recruitment of Axin to LRP6 (reactions R_{3A} and R_{3B}) and assume LRP6 is phosphorylated upon Wnt stimulation without recruitment of Axin.

Our original model assumes Axin and LRP6 form 4 different complexes depending on whether either protein is phosphorylated or unphosphorylated:

- $C_0 \equiv [A_u : L_u]$
- $C_1 \equiv [A_p : L_u]$
- $C_2 \equiv [A_u : L_p]$
- $C_3 \equiv [A_p : L_p]$

We now ignore complexes C_0 and C_1 since we no longer assume Axin is required for LRP6 phosphorylation. Moreover, in the absence of any experimental data suggesting an important role for dephosphorylated Axin in complex with LRP6, we also ignore complex C_2 and assume that Axin is quickly released from LRP6 after its dephosphorylation upon Wnt stimulation.

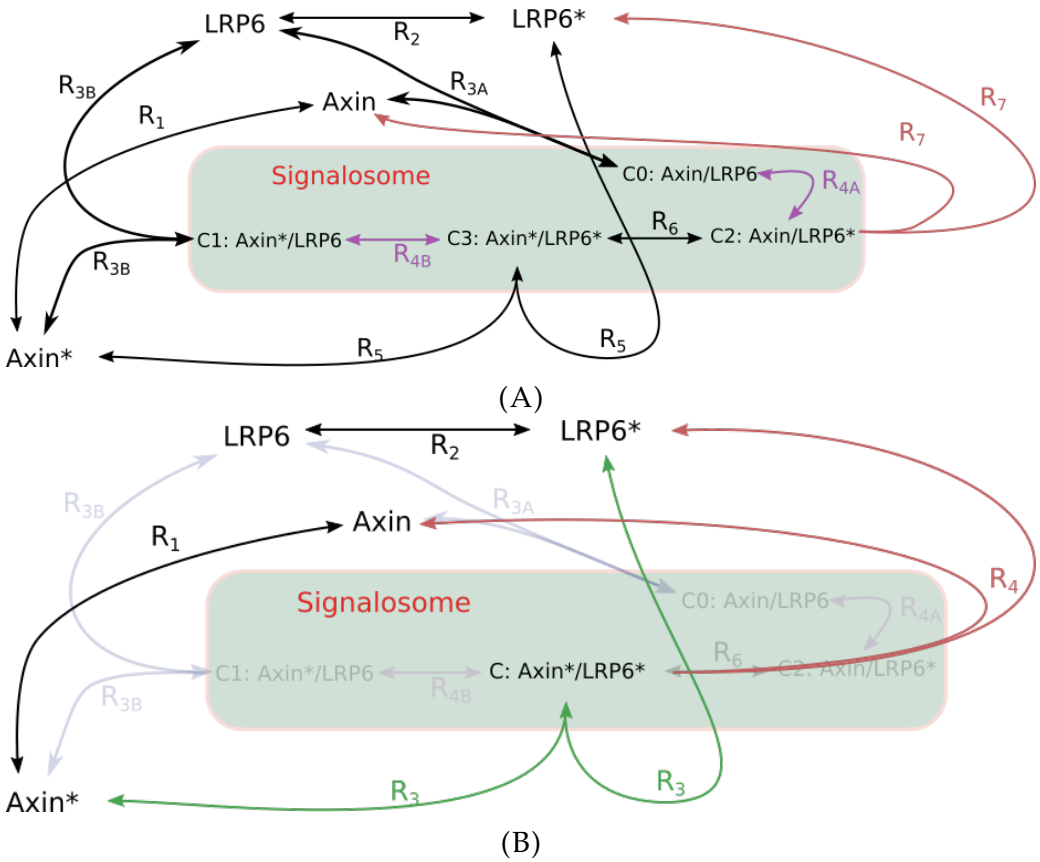


FIGURE 4.11: Schematic of candidate model (A) H_{21} and (B) S_1. The faded out reactions and species in Figure (B) are presented to reflect the simplifications from the original candidate model.

Under these assumptions the reactions involved in our model of the canonical Wnt pathway may be simplified to the following:

$$R_1\text{:}\quad \mathrm{A_u} \underset{k_{-1}}{\overset{k_1}{\rightleftharpoons}} \mathrm{A_p}, \tag{4.28}$$

$$R_2\text{:}\quad \mathrm{L_u} \underset{k_{-2}}{\overset{k_2(w)}{\rightleftharpoons}} \mathrm{L_p}, \tag{4.29}$$

$$R_3\text{:}\quad \mathrm{A_p} + \mathrm{L_p} \underset{k_{-3}}{\overset{k_3}{\rightleftharpoons}} \mathrm{C}, \tag{4.30}$$

$$R_4\text{:}\quad \mathrm{C} \xrightarrow{k_{-4}} \mathrm{A_u} + \mathrm{L_p}. \tag{4.31}$$

We represent our model via the following system of ODEs:

$$\frac{\mathrm{d}A_u}{\mathrm{d}t} = -k_1 A_u + k_{-1} A_p + k_{-4} C \tag{4.32}$$

$$\frac{\mathrm{d}A_p}{\mathrm{d}t} = k_1 A_u - k_{-1} A_p - k_3 A_p L_p + k_{-3} C \tag{4.33}$$

$$\frac{\mathrm{d}L_u}{\mathrm{d}t} = -k_2(w) L_u + k_{-2} L_p \tag{4.34}$$

$$\frac{\mathrm{d}L_p}{\mathrm{d}t} = k_2(w) L_u - k_{-2} L_p - k_3 A_p L_p + (k_{-3} + k_4) C \tag{4.35}$$

$$\frac{\mathrm{d}C}{\mathrm{d}t} = k_3 A_p L_p - (k_{-3} + k_{-4}) C. \tag{4.36}$$

We call this candidate model, model S_1.

In the new S_1 model, the rate of LRP6 phosphorylation $k_2(w)$ is altered by Wnt, changing as a function of time upon Wnt stimulation as described in Equation (4.24). Tables 4.8 and 4.9 summarise the dependent variables and parameters in candidate model S_1. Using the same methodology as before, we can also deduce conservation of Axin and LRP6, which enables us to reduce the number of ODEs to 3:

$$A_{\text{tot}} = A_u + A_p + C, \tag{4.37}$$

$$L_{\text{tot}} = L_u + L_p + C. \tag{4.38}$$

Dependent variable	Description	Initial Value (nM)
A_u	Concentration of Axin not phosphorylated at S497/S500	0
A_p	Concentration of Axin phosphorylated at S497/S500	Variable
L_u	Concentration of LRP6 not phosphorylated at S1490	15
L_p	Concentration of LRP6 phosphorylated at S1490	2
C	Concentration of Complex of $\mathrm{L_p}$ and $\mathrm{A_p}$	0

TABLE 4.8: Dependent variables used in the candidate model S_1, and their initial values in the "Wnt-off" simulation (see Section 4.2.4).

Parameter	Description	Unit
$k_{\pm 1}$	Rate of Axin phosphorylation/dephosphorylation (Wnt independent)	min^{-1}
$k_{\pm 2}$	Rate of LRP6 phosphorylation/dephosphorylation	min^{-1}
$k_{\pm 3}$	Rate of association/dissociation of pS497/500 Axin and pS1490 LRP6	$\mathrm{min}^{-1}\mathrm{nM}^{-1}$
k_{-4}	Rate of release of unphosphorylated Axin from Axin/LRP6 complex	min^{-1}
A_{tot}, L_{tot}	Total Axin and LRP6	nM
w	Wnt multiplier (see Section 4.2.4)	-
τ	Time constant (see Section 4.2.4)	-

TABLE 4.9: Parameters used in the simplified mathematical models of the canonical Wnt pathway.

4.4.3 Steady state analysis

Unlike the twelve candidate models introduced in the first part of this chapter, we can determine the steady states of candidate model S_1 by setting $\frac{\mathrm{d}}{\mathrm{d}t} = 0$ in Equations (4.32)-(4.36).

We can use Equations (4.34), (4.36) and (4.38) to write:

$$L_u = \frac{k_{-2}}{k_2} L_p \tag{4.39}$$

$$C = L_{\mathrm{tot}} - (1 + \frac{k_{-2}}{k_2} L_p), \tag{4.40}$$

$$k_3 A_p L_p = (k_{-3} + k_{-4})\big(L_{\mathrm{tot}} - (1 + \frac{k_{-2}}{k_2})L_p\big),$$

$$\implies A_p = \frac{k_{-3} + k_{-4}}{k_3}\Big(\frac{L_{\mathrm{tot}} - (1 + \frac{k_{-2}}{k_2})L_p}{L_p}\Big). \tag{4.41}$$

We can use conservation of Axin in Equation (4.37) to eliminate A_u from Equation (4.32). We can use this alongside Equation (4.40) to derive

$$A_p = \frac{1}{k_1 + k_{-1}}\Big((k_1 + k_{-4})\big(1 + \frac{k_{-2}}{k_2}\big)L_p + k_1 A_{\mathrm{tot}} - (k_1 + k_{-4})L_{\mathrm{tot}}\Big). \tag{4.42}$$

Notice Equations (4.41) and (4.42) describe a hyperbola and a straight line in the (L_p, Ap) plane. The intersection of these two lines represents the steady states of the system. Figure 4.12 displays these equations for an example set of parameter values. The hyperbola always has a discontinuity at $L_p = 0$, while the line always has a positive gradient. We can deduce that there can be at most one positive steady state for the system, confirming model S_1 cannot admit bistability.

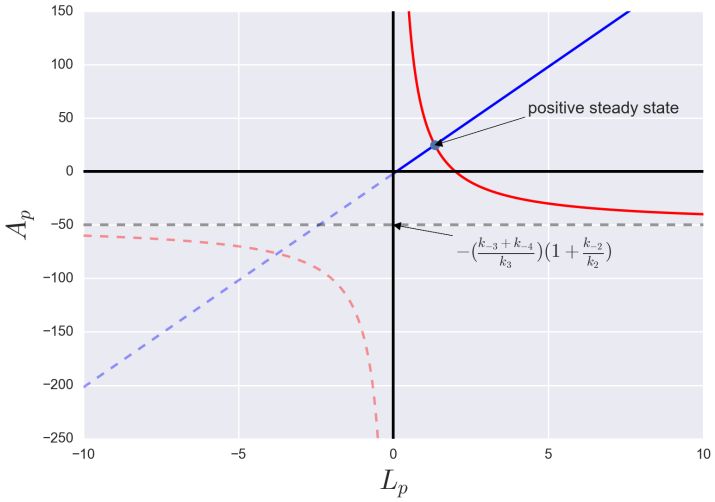


FIGURE 4.12: Assuming positive parameter values, there can only be one or zero positive intersection of the hyperbola described by Equation (4.41) and the line described by Equation (4.42) in the positive quadrant. If one does exist, it is the steady state of candidate model S_1.

4.4.4 Target model output

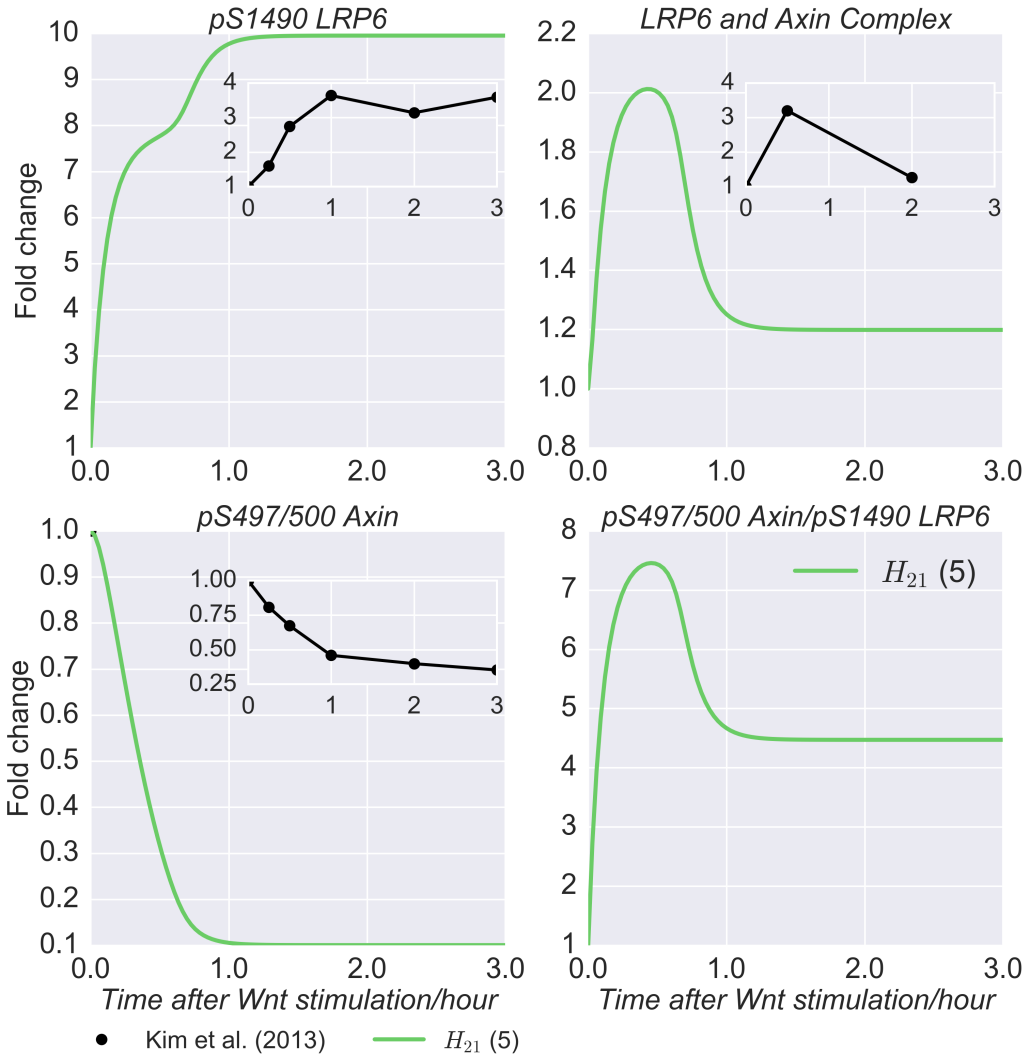


FIGURE 4.13: Typical output of candidate model H_{21} reproducing experimental results of Kim et al. (2013). We fit candidate model S_1 qualitatively to these outputs for total pS497/500 Axin ($A_p + C_1 + C_3$), pS1490 LRP6 ($L_p + C_2 + C_3$), and pS497/500 Axin/pS1490 LRP6 complex (C_3)

We explore the model output for candidate model S_1 to investigate whether it can reproduce the results of Kim et al. (2013). In the first part of this chapter we focused on the changes in levels of pS497/500 Axin, pS1490 LRP6 and complex of Axin and LRP6. Since our simplified model considers only pS497/500 Axin in complex with pS1490 LRP6, we replace the Axin/LRP6 complex output in our original cost function with pS497/500 Axin/pS1490 LRP6. Since Kim et al. (2013) did not measure the levels of pS497/500 Axin in complex with pS1490 LRP6, we fit the S_1 model to the output for the pS497/500 Axin/pS1490 LRP6 complex from the original candidate model H_{21}. Figure 4.13 displays the typical output of the H_{21} model. For all parameter sets found for model H_{21}, upon Wnt stimulation levels of pS497/500 Axin/pS1490 LRP6 complex increase before dropping to a level higher than the "Wnt-off" levels. We require the candidate model S_1 to produce similar qualitative behaviour. Upon Wnt stimulation:

- Levels of pS497/500 Axin ($A_p + C$) drop monotonically,
- Levels of pS1490 LRP6 ($L_p + C$) increase monotonically,

- Levels of pS497/500 Axin in complex with pS1490 LRP6 (C) increase within half an hour before dropping to a level which is higher than the original Wnt off level.

Our cost function hence differs from the original cost vector described in Table B.1 in Appendix B in one term. We now require levels of Axin/LRP6 complex to reach a level higher than the "Wnt-off" value.

4.4.5 Exploring the model output

We applied CMA-ES to the candidate model S_1 of the canonical Wnt pathway. We initiate the algorithm again at 112 random parameter vector values $\boldsymbol{\theta}$. The parameter vector $\boldsymbol{\theta}$ has ten elements including w, τ, phosphorylation and dephosphorylation rates $k_{\pm 1}$ and $k_{\pm 2}$, association rate k_3, dissociation rates K_3 and K_4, and total Axin A_{tot}. We use the range and values as defined in Table 4.5

The algorithm found six sets of parameter values that could describe the experimental observations. Figure 4.14 displays the model outputs for these parameter sets.

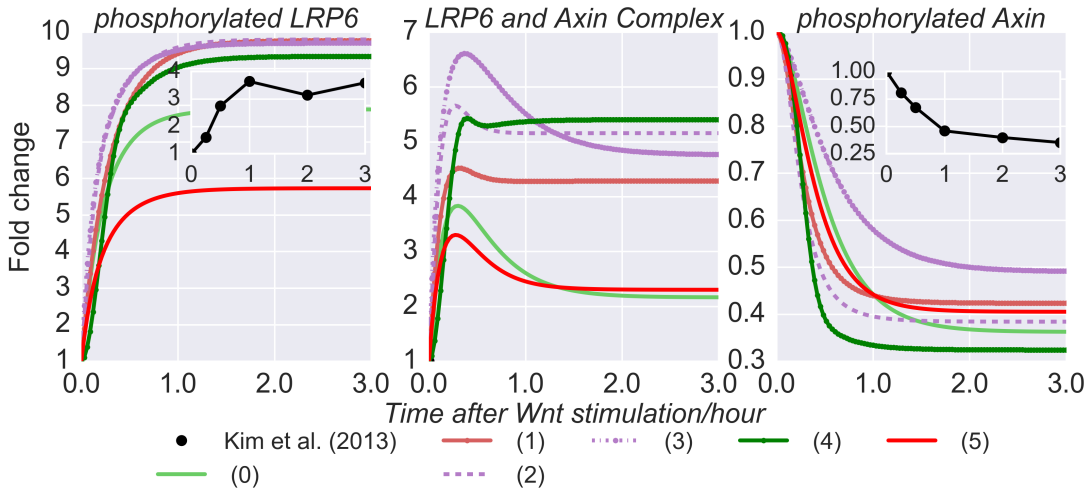


FIGURE 4.14: Typical output of candidate model S_1 fitted to a combination of experimental results by Kim et al. (2013) and output from candidate model H_{21}. Since Kim et al. (2013) do not measure the level of pS497/S500 Axin in complex with pS1490 LRP6, we fit this quantity in model S_1 to the output from our original reduced model H_{21}. The numbers in the figure legend corresponds to the number of the parameter set. These are provided in Appendix C.

4.4.6 Further model analysis

We performed *in silico* experiments and sensitivity analysis of candidate model S_1 to investigate its suitability in describing the observations by Kim et al. (2013). Figure 4.16A displays the sensitivity of fold changes in total levels of pS497/500 Axin upon Wnt stimulation to changes in model parameters. For all six parameter sets, this is below 0.5, meaning a 1% change in each rate parameter on average, affects the fold change in levels of pS497/500 Axin by less than 0.5%. We conclude that the model is robust for the parameter sets that are qualitatively consistent with the experimental observations.

Similarly to the study by Kim et al. (2013), where they measured the cell's response to PP1 inhibitor, Tautomycin (TM), we use the parameter sets found earlier for model S_1 to run similar *in silico* experiments to study the response of each candidate model and parameter set to a combination of TM and Wnt stimulation. Similarly to

Section 4.3.2, we assume TM reduces the rate of Wnt-dependent dephosphorylation of Axin. Since S_1 does not have a reaction corresponding directly to Axin dephosphorylation upon Wnt stimulation, we assume release of Axin from LRP6 (k_{-4}) is slowed down upon TM stimulation instead by $90\% \pm 10\%$ on a relative basis (i.e. 81%, 90% or 99%).

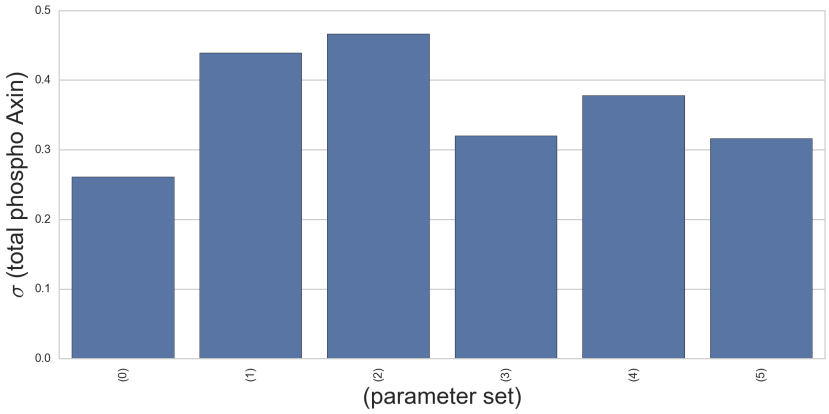
We display the results of the *in silico* experiments in Figures 4.16B, 4.16C, and 4.16D. We note that several set of parameter sets found for candidate model S_1 are able to describe these further *in vitro* experimental observations by Kim et al. (2013).

The results of these analyses suggest that candidate model S_1 is consistent with the experimental observations concerning the interaction of LRP6 and Axin in the canonical Wnt pathway.

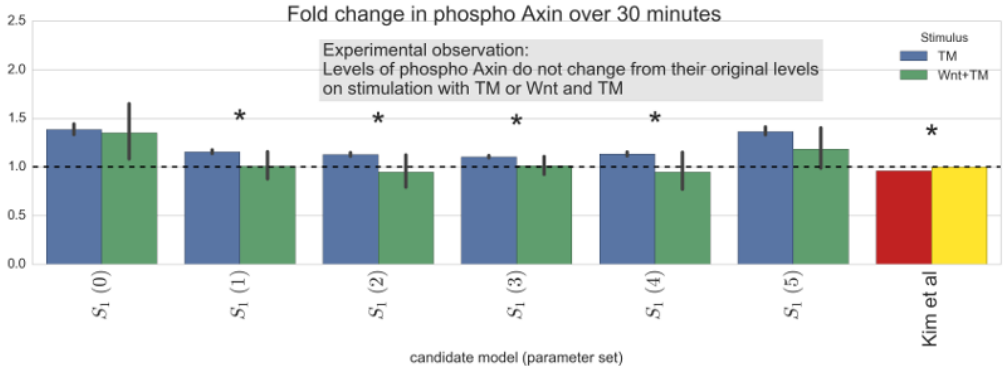
4.4.7 Final remarks about the simplified candidate model S_1

In this section, we showed that a simplified version of candidate model H_{21}, namely S_1, is able to reproduce various features of this candidate model. We note that, similarly to model H_{21}, in model S_1 the only Wnt-driven reaction is LRP6 phosphorylation. Candidate model H_{21} is a simplified version of candidate model H_{61}, which contains two Wnt-driven reactions, LRP6 phosphorylation and release of Axin from LRP6. Equivalently, if in model S_1 we assume that release of Axin from LRP6 (R_4) is also Wnt-dependent, this will describe a simplified version of candidate model H_{61}. We will call this model S_2 for future reference. Since S_1 and S_2 are nested models, with S_2 a more detailed version of S_1, it will also be able to reproduce the experimental observations by Kim et al. (2013).

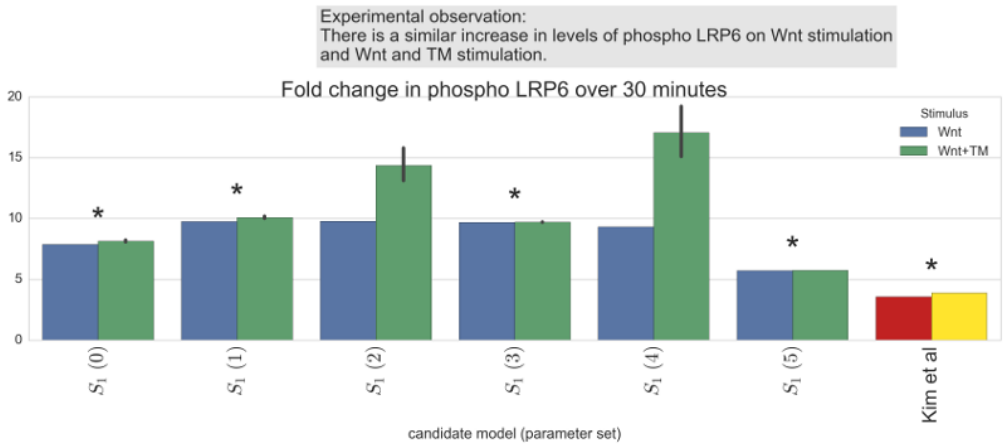
FIGURE 4.15: (Next page) Further analysis of candidate model S_1. (A) Standard deviation of control coefficients corresponding to fold change in total levels of pS497/500 Axin for various parameter sets. A lower standard deviation corresponds to a more robust system against perturbations in model rate parameters. Candidate model S_1 is robust for all parameter sets found that fit the experimental observation. (B,C and D) *in silico* experiments suggest that the model is able to describe further *in vitro* experiments by Kim et al. (2013). The final bars displayed in different colours represent a quantification of these equivalent *in vitro* experiments. We assume that stimulation with TM reduces rate of Axin dephosphorylation due to Wnt stimulation by $90\% \pm 10\%$ (see main text for further details). Black lines above each bar represent a one standard deviation confidence interval.


σ (total phospho Axin)
0.0
0.1
0.2
0.3
0.4
0.5
(0)
(1)
(2)
(3)
(4)
(5)
(parameter set)

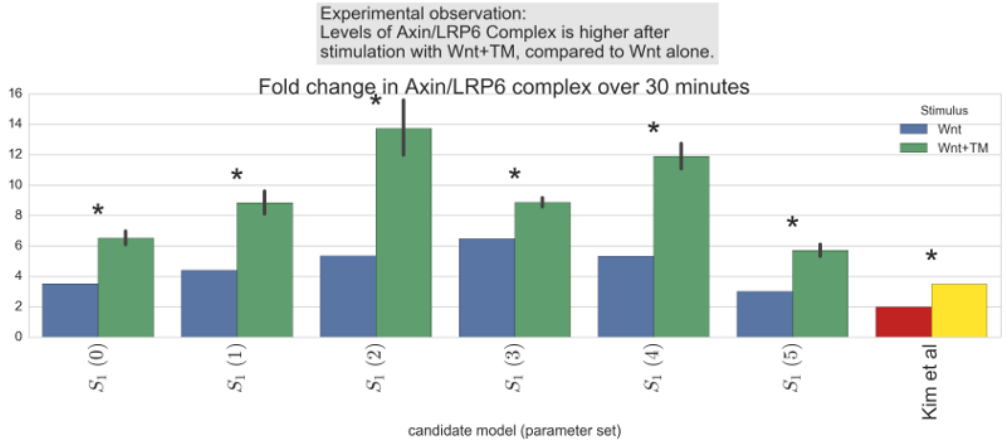
(A)


Fold change in phospho Axin over 30 minutes
Experimental observation:
Levels of phospho Axin do not change from their original levels on stimulation with TM or Wnt and TM
Stimulus
TM
Wnt+TM
candidate model (parameter set)
Kim et al

(B)


Experimental observation:
There is a similar increase in levels of phospho LRP6 on Wnt stimulation and Wnt and TM stimulation.
Fold change in phospho LRP6 over 30 minutes
Stimulus
Wnt
Wnt+TM
candidate model (parameter set)
Kim et al

(C)


Experimental observation:
Levels of Axin/LRP6 Complex is higher after stimulation with Wnt+TM, compared to Wnt alone.
Fold change in Axin/LRP6 complex over 30 minutes
Stimulus
Wnt
Wnt+TM
candidate model (parameter set)
Kim et al

(D)

4.5 Discussion

Various mathematical models of the canonical Wnt pathway have been proposed since the first model was introduced by Lee et al. (2003). Whereas many of these models have included some description of the pathway from Wnt stimulation to degradation of β-catenin, we have taken an alternative approach by focusing on the cell's first response to Wnt stimulation.

Instead of considering one mathematical model that may be suitable, we proposed a set of candidate models that may enable us to reject alternative hypotheses that have been proposed. For example, Zeng et al. (2008) proposed that Axin is required for LRP6 phosphorylation at PPPSP motifs by GSK3, and hence Axin recruitment to LRP6 might be an important Wnt driven biochemical reaction. On the other hand, other studies have suggested LRP6 phosphorylation is one of the first Wnt driven steps and in fact provides a docking site for Axin (MacDonald et al., 2008).

Starting from twelve candidate models, we reduced the number of suitable models to four. We proposed new tractable *in vitro* experiments that may enable us to discriminate between these remaining candidate models. We established that by measuring levels of Axin in complex with pS1490 LRP6 upon Wnt stimulation we can establish whether the primary Wnt driven reaction is LRP6 phosphorylation by GSK3 or recruitment of Axin to LRP6 and its release from LRP6.

In the absence of suitable experimental data, we established that LRP6 phosphorylation is the most likely Wnt driven reaction. If Axin recruitment was a Wnt driven reaction, we showed that its rate of release from LRP6 would also likely need to increase upon Wnt stimulation. Our investigations also suggested that LRP6 phosphorylation at S1490 residue (or the other equivalent 4 residues on the PPPSP motifs) does not necessarily recruit a substantial quantity of dephosphorylated Axin (see Summary in Section 4.4.1).

Having established suitable candidate mathematical models for the interaction between Axin and LRP6, we aim to extend these candidate models to incorporate β-catenin and a more detailed description of the destruction complex in Chapter 6. This increases the experimental data that the candidate models need to reproduce and the dimensionality of the models' parameter space. In an effort keep the problem of model selection computationally tractable, we introduced a simpler mathematical model that was able to replicate various experimental observations. This simplification reduced the average number of model simulations required for model selection using the CMA-ES technique from 3.6M to 630k (see Figure 6.20 in Chapter 6). Without availability of suitable experimental data, namely changes in levels of pS497/500 Axin in complex with pS1490 LRP6, we fitted this model using data generated from one of our original candidate models. We note that without our initial ground work on the twelve candidate models this step would not have been possible.

In this chapter we also used qualitative cost functions for model selection. In doing so, we demonstrated their relevance for fitting models to semi-quantitative experimental data, such as co-IP's and Western blots.

Mathematical models of signalling pathways are often fitted by minimisation of residual distance between model output and quantified Western blot results. This means a decision has to be made on 'closeness of fit'. In the same way as we may use a fit by eye to confirm whether a model fit looks reasonable, we use satisfaction

metrics to measure the goodness of fit of a model to experimental data. This means a model either fits (cost $= 0$), or does not (cost $\neq 0$).

We explored the model outputs using CMA-ES, a numerical optimisation algorithm over a region of parameter space that we consider to be biologically relevant. We note that the search space is still very wide for most parameter values in our mathematical models. Consequently values found via our optimisation algorithm may not be biologically appropriate with respect to the Wnt pathway and our proteins of interest. Further *in vitro* and *in vivo* experiments should be carried out to ensure model outputs are consistent under further scrutiny.

We note that there is not enough information in the experimental studies we have used here to allow us to identify suitable parameter values for our mathematical models of the canonical Wnt pathway. Qualitative cost functions and satisfaction metrics also add further complications to parameter identifiability as the acceptable model output, where the requirements are satisfied, can be very wide, making the space of suitable model parameters non-unique. However, our framework does enable us to generate parameter sets that we may use to perform further analysis, such as *in silico* experiments.

We build on the work in this chapter in the next two chapters. In Chapter 5 we detail the *in vitro* experiments we carried out to discriminate between our original candidate models that were able to reproduce experimental observations by Kim et al. (2013) (H_{21}, H_{22}, H_{31}, H_{32}).

In Chapter 6 we extend the simplified candidate models S_1 and S_2 described in the schematic in Figure 4.11. We introduce β-catenin and a more detailed description of the destruction complex in order to investigate whether the new extended model may fit experimental observations from different studies.

Chapter 5

Experimental work

5.1 Introduction

The primary aim of my D.Phil. study has been to use a combination of mathematical modelling and laboratory experiments to increase our understanding of the canonical Wnt pathway. In this chapter we summarise the experimental work that I carried out in the lab. I spent two periods in the lab. During the first six-month period, I learnt cell culture work and immunofluorescence. I spent another six months in the end of my second year/start of the final year, where I carried out co-immunoprecipitation experiments.

We gave a detailed description of the canonical Wnt pathway in Chapter 2, and in particular described that Wnt stimulation leads to deactivation of the destruction complex. The way in which the destruction complex becomes inactivated is poorly understood. Deactivation of the destruction complex drives an increase in levels of β-catenin, which translocates to the nucleus, leading to transcription of Wnt-target genes.

There are now several models proposed that describe how Wnt stimulation leads to deactivation of the destruction complex. Some studies have focussed on the interactions between the scaffolding protein Axin and the LRP6 co-receptor and the role that their conformational state plays in regulating the dynamics of the pathway. We note that upon Wnt stimulation, Axin is recruited to LRP6 and dephosphorylated at S497/S500. This reduces its binding affinity for β-catenin (Kim et al., 2013). LRP6 is phosphorylated at several sites upon Wnt stimulation. Of particular interest is phosphorylation of several residues on five PPPSP motifs, which have been observed to play important roles in deactivation of the destruction complex. First phosphorylated PPPSP petptides directly inhibit GSK3-phosphorylation of β-catenin (Wu et al., 2009), while LRP6 phosphorylated by GSK3 at S1490 on the PPPSP motif A binds preferentially to phosphorylated Axin (Kim et al., 2013). We refer the reader to the literature review in Chapter 2 for more details.

In the last chapter, we used our understanding of the biological literature to propose twelve candidate mathematical models for the first steps following Wnt stimulation. We focused on results by Kim et al. (2013), which showed how upon Wnt stimulation levels of Axin phosphorylated at S497/S500 (pS497/S500 Axin), LRP6 phosphorylated at S1490 (pS1490 LRP6) and the Axin/LRP6 complex change over time (see Figure 5.2).

Each candidate model has 8 species including pS497/500 Axin, pS1490 LRP6, their unphosphorylated analogues, and the four complexes that these four species may form. Figure 5.1 displays a simplified schematic of these candidate models. Table 5.1 summarises the structure of the candidate mathematical models and the model selection results.

The twelve mathematical candidate models differ in two ways:

- the biochemical reactions that are altered upon Wnt stimulation in the candidate

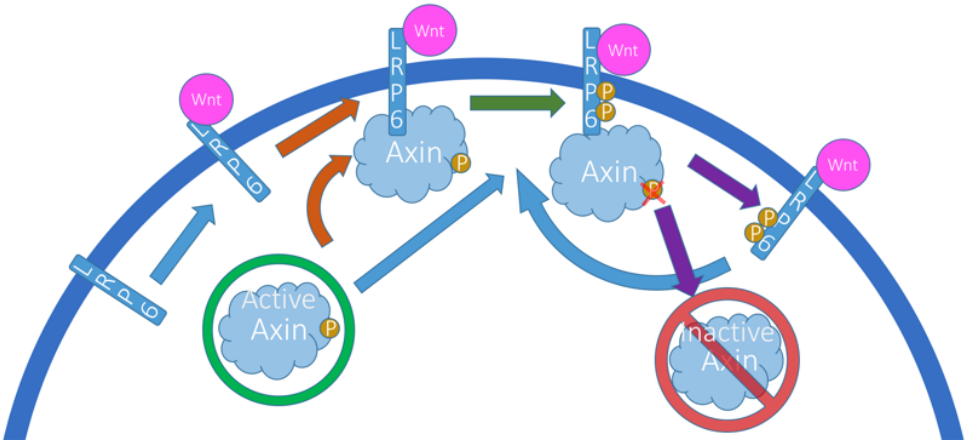


FIGURE 5.1: A simplified schematic of our candidate models illustrating how Axin and LRP6 interact. We do not show the recruitment of unphosphorylated Axin to LRP6 (for a more detailed and accurate schematic see Figure 4.2 in Chapter 4).

models vary. For example, Wnt stimulation may increase the rate of LRP6 phosphorylation or it may increase the rate of recruitment of Axin to LRP6, which may in turn increase LRP6 phosphorylation.

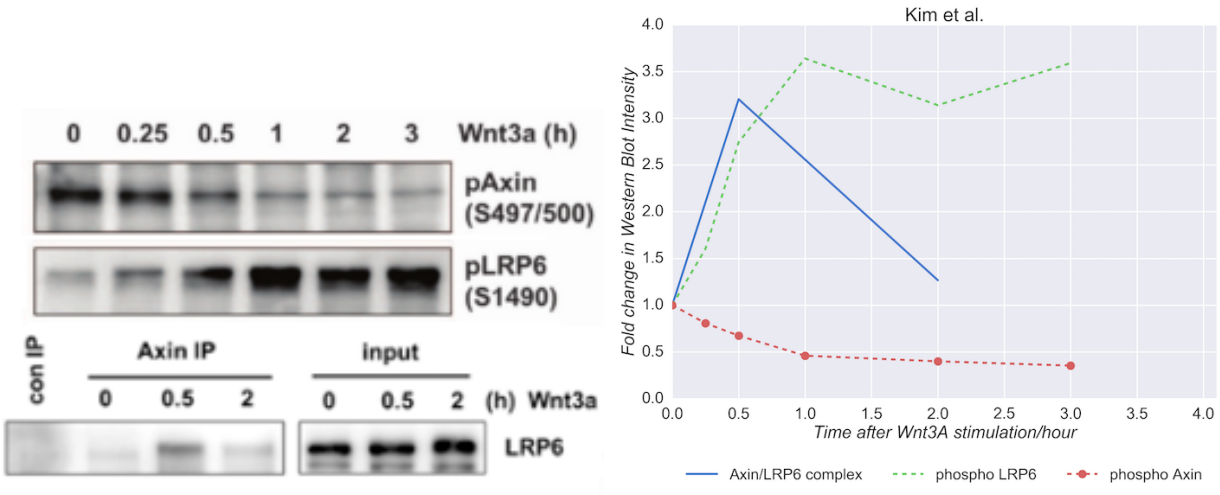
- the biochemical reactions included in each candidate model also vary. For some models phosphorylated LRP6 recruits Axin in all conformational states whereas in others it only recruits phosphorylated Axin.

We refer the readers to Section 4.2.2 of Chapter 4 for justification of the structure of each candidate model.

Candidate Model	Wnt Dependent Reactions	Basal Axin/LRP6 Binding	Accepted model?
H_{11}	LRP6/Axin binding	✗	✗
H_{12}	LRP6/Axin binding	✓	✗
H_{21}	LRP6 phosphorylation	✗	✓
H_{22}	LRP6 phosphorylation	✓	✓
H_{31}	LRP6/Axin binding and release	✗	✓
H_{32}	LRP6/Axin binding and release	✓	✓
H_{41}	Axin dephosphorylation	✗	✗
H_{42}	Axin dephosphorylation	✓	✗
H_{51}	Axin dephosphorylation and Axin/LRP6 release	✗	✗
H_{52}	Axin dephosphorylation and Axin/LRP6 release	✓	✗
H_{61}	LRP6 phosphorylation and Axin/LRP6 release	✗	✗
H_{62}	LRP6 phosphorylation and Axin/LRP6 release	✓	✗

TABLE 5.1: The twelve candidate models proposed in Chapter 4, and whether they are accepted or reject under our framework. We proposed new *in vitro* experiments (Figure 5.3) that may discriminate between these remaining four candidate models.

Using our framework, we reduced the number of suitable candidate models from twelve to four (see Table 5.1 or the Results section in Chapter 4). The four remaining candidate models (H_{21}, H_{22}, H_{31} and H_{32}) were able to reproduce experimental



(A) (B)

FIGURE 5.2: Kim et al. (2013) stimulate human cell lines HEK293T and L-Cells with Wnt conditoned media or Wnt3A ligands and use Western blots and co-immunoprecipitation studies to measure changes in levels of components of the Wnt signalling pathway. (A) Actual blots data in L-cells reproduced with permission. (B) Quantification of these results.

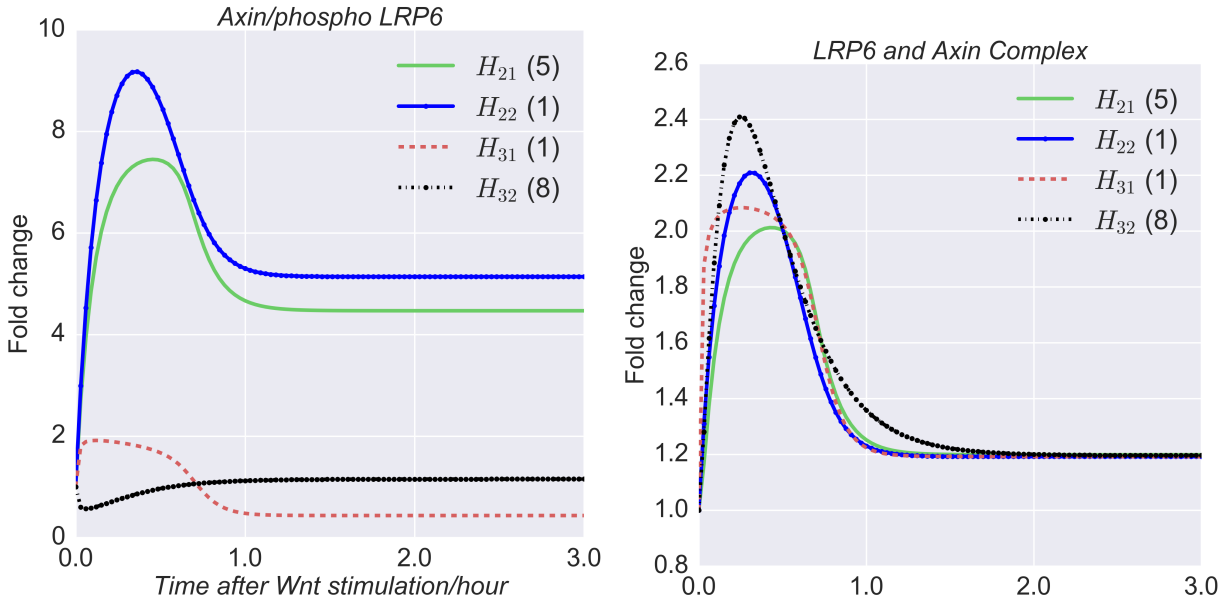
observations by Kim et al. (2013), including response to stimulations by Wnt and/or phosphatase inhibitor, Tautomycin.

By studying the output of these four candidate models, we identified a new *in vitro* experiment, where we measure levels of pS1490 LRP6 in complex with Axin using a co-IP experiment, that we predict could enable us to discriminate between the remaining candidate models (see Figure 5.3). An increase to a higher steady state level would imply candidate models H_{21} and H_{22} may be appropriate, whereas a reduction or no change would suggest candidate models H_{31} or H_{32} respectively may be appropriate for describing the observed dynamics.

We emphasise that this experiment would determine which reaction is altered in our models upon Wnt stimulation; in candidate models H_{2y}, $(y = 1, 2)$, LRP6 phosphorylation is the Wnt driven reaction, whereas in candidate models H_{3y}, $(y = 1, 2)$, Axin/LRP6 association and disassociation reactions are altered by Wnt.

We note that if there is an increase in levels of Axin in complex with pS1490 LRP6, then we cannot discriminate between candidate models H_{21} and H_{22}. In this case, we would have to study the models further to propose new experiments. We note also that changes in levels of Axin/pS1490 LRP6 complex should be measured alongside levels of Axin/LRP6 since different studies (e.g. Li et al. (2012) and Azzolin et al. (2014)) have observed qualitatively different behaviours for levels of Axin/LRP6 complex to the experimental data we used by Kim et al. (2013). Our model selection is valid only if we are able to observe the same results as our candidate model output for Axin/LRP6 and Axin/pS1490 LRP6 complexes.

The rest of this Chapter is structured as follows. In Section 5.2, we provide the materials and methods used in carrying out our experiments during this work. We include the immunofluorescence protocol used to produce some of the figures in other chapters. In Section 5.3, we provide our preliminary results. Finally, we discuss our results and outline directions for future work.



(A) (B)

FIGURE 5.3: (A) Measuring changes in levels of Axin/pS1490 LRP6 upon Wnt stimulation could discriminate between the remaining candidate models. However, it cannot discriminate between candidate models H_{21} and H_{22}. (B) The dynamics of the Axin/LRP6 complex associated with the four candidate models is consistent with observations by Kim et al. (2013).

5.2 Materials and Methods

All chemicals and materials were used according to manufacturers' guidelines. Most were from Sigma-Aldrich or Fisher Scientific, and all culture media and supplements purchased from Gibco. All concentrations are given as volume/volume unless otherwise stated. In Table 5.2 we list the antibodies and the concentrations used in our experiments.

5.2.1 Cell culture

All cell lines were maintained in a humidified incubator in 5% CO_2 at 37°C and cultured in Dulbeccos modified Eagle's medium (DMEM) with 10% Fetal bovine serum (FBS), 100Units/ml of Pen/Strep, and 2mM of Glutamine. The cells were passaged as necessary with 1x PBS and 0.25% Trypsin-EDTA.

5.2.2 Ligands, inhibitors and conditioned media

All stimulants were diluted to the appropriate concentration in 10% FBS media. Recombinant Human Wnt3A ligands were purchased from R&D systems and suspended in 0.1% (mass/volume) Bovine serum albumin (BSA) as per the manufacturer's instructions. A concentration of 100 ng/ml was used for all experiments. We used 0.75ml of media per well in 12-well plates or 7ml of media per 10cm dish. 0.1% BSA was used as Control. MG132, a proteasomal inhibitor, was similarly diluted to appropriate concentrations of 5, 10 or 20 µM.

Wnt3A conditioned media and control media were produced using L-Wnt3a cells (ATCC 2647) and control L-cells (ATCC CRL-2648) according to the provided guidelines. They were aliquoted in 10 ml Falcon tubes and kept at -20°C for up to 6 months.

Type	Name	Concentratio	Manufacturer	Catalogue Number
Primary (IF, WB)	Mouse β-catenin (G-10)	1:200 (IF), 1:1000 (WB)	Santa Cruz Technology	SC-376959
Primary (IF, WB)	Rabbit β-catenin (H-102)	1:200 (IF), 1:1000 (WB)	Santa Cruz Technology	SC-7199
Primary (IF)	Rabbit E-cadherin	1:100	Cell Signalling	3195
Primary (IF)	mouse YAP (63.7)	1:100	Santa Cruz Technology	SC-101199
Primary (IF, WB)	Non-phospho (active) B-catenin Ser33/37/Thr41	1:200 (IF), 1:1000 (WB)	Cell Signalling	D13A1
Primary (WB)	Phospho-β-catenin (Ser33/37/Thr41)	1:1000	Cell Signalling	9561
Primary (WB)	Phospho-LRP6 (Ser1490)	1:1000	Cell Signalling	2568
Primary (WB)	LRP6	1:1000	Cell Signalling	3395
Primary (WB, IP)	Axin	1:100 (IP), 1:1000 (WB)	Cell Signalling	2087
Primary (IP)	Axin-1, clone A5	1:100	Merck Millipore	05-1579
Secondary	Alexa fluor goat anti-mouse 488 nm (Green)	1:500	Invitrogen, Life Technologies	A-11001
Secondary	Alexa fluor goat anti-rabbit 488 nm (Green)	1:500	Invitrogen, Life Technologies	A-11008
Secondary	Alexa fluor goat anti-mouse 594 nm (Red)	1:500	Invitrogen, Life Technologies	A-11005
Secondary	Alexa fluor goat anti-rabbit 594 nm (Red)	1:500	Invitrogen, Life Technologies	A-11012
Secondary (WB)	Goat anti-mouse 680 nm	1:5000	Licor	926-32210
Secondary (WB)	Goat anti-rabbit 800 nm	1:5000	Licor	926-32221

TABLE 5.2: Antibodies used in our immunofluorescence (IF), Western blots (WB) and immunoprecipitation (IP) experiments and the specific concentrations we used.

5.2.3 Immunofluorescence

Cells were plated on glass coverslips (Fisher) in 12-well plates. Unless otherwise stated, RKO, Caco-2 and HEK293T cells were plated at 50,000-100,000 cells per well, and experiments started when cells had reached more than $60-70\%$ confluency. Coverslips for HEK293T experiments were pre-coated with Fibronectin at a concentration of 1 μ/cm^2 to improve adhesion.

Cells were washed with 1x PBS before being fixed by 0.5ml of 4% Paraformaldehyde (PFA) in 1x PBS for 15 minutes, and permeabilised with 0.2% Titon-x solution in 1x PBS for 5 minutes and blocked for 1 hour in 0.2% Fish Skin Gelatin (FSG). Each coverslip was incubated in 50ml of appropriate dilution of primary antibody for 3-4 hours at room temperature (or overnight at 4°C), before they were incubated with secondary antibodies for 2-3 hours. Cells were mounted onto slides with Prolong Gold anti-fade reagent with DAPI (Life Technologies), and fixed with nail varnish. Cells were washed with 1x PBS at least twice between each of the steps described above. All images were taken using a Nikon 90I widefield microscope with most images taken using a 100x oil lens using NIS Elements software.

Buffer	Content
5% skimmed milk blocking solution	5% (w/v) skimmed milk powder in 1x PBST
PBS (pH 7.4)	137 mM NaCl, 2.7 mM KCl, 10mM Na_2HPO_4, 1.76 mM KH_2PO_4
PBST	PBS, 0.1% Tween20
Transfer buffer	25 mM Tris, 190 mM Glycine, 20% Methanol
2x SDS-PAGE Sample Buffer	40% (v/v) NuPAGE LDS sample buffer, 40% (v/v) Nuclease-Free Water, 0.2Molar DTT

TABLE 5.3: The content of buffers used in our experiments which were mixed in the lab.

5.2.4 Protein complex immunoprecipitation (Co-IP)

Figure 5.4 summarises the protocol we used to carry out co-IP's. The protocol, including the antibodies and lysis buffer used in is based on the Materials and Methods by Kim et al. (2013), For steps that were not detailed, we used and optimized protocols used commonly in our laboratory (the cell signalling group in the Department of Oncology, University of Oxford).

	Stock concentration	Kim et al. (2013)	Volume for 50 ml of lysis buffer
HEPES (7.4 pH)	1 mM	50 mM	2.5 ml
NaCl	5 mM	150 mM	150 µl
EDTA	500 mM	1.5 mM	1.5 ml%
Triton X-100	100%	1%	0.5 ml
Glycerol	50%	10%	10 ml
DTT	1 M	0.5 mM	25 µl
Protease inhibitor cocktail tablets (EDTA-free) (Roche)		1 tablet per 50ml	1
Phosphatase inhibitor cocktail tablets (Roche)		1 tablet per 10ml	5
Distilled water			35.3 ml

TABLE 5.4: Lysis buffer used in the co-IP studies, produced according to the protocol by Kim et al. (2013).

We ran our IPs using Sepharose beads and Dyna magnetic beads, using protein G for mouse antibodies and protein A for rabbit antibodies. We focus here on description of the experiments with magnetic beads as using Sepharose beads we achieved similar

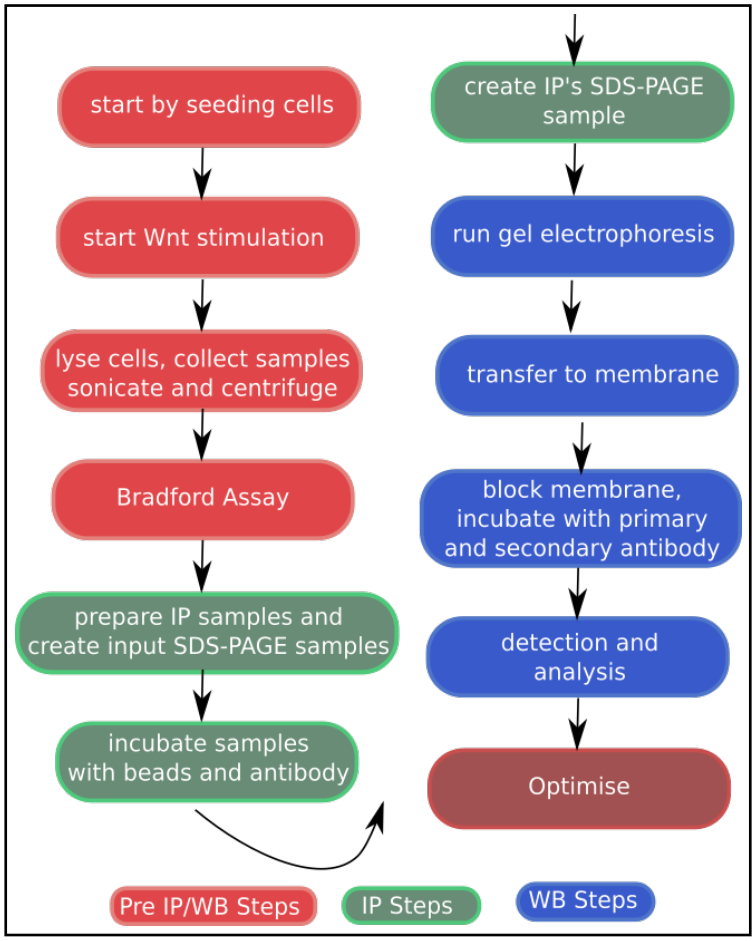


FIGURE 5.4: Summary of steps involved in a co-immunoprecipitation study. We have broken down the steps into (1) pre IP steps, which are similar for other procedures such as simple Western blots, (2) actual IP steps, and (3) Western blot steps. We have displayed these steps in the order we carry them out during a typical experiment.

results. We used 20 µl of magnetic beads per IP, ensuring the beads container was vortexed before collecting the appropriate amount.

The beads were washed 3 times using 5 times the volume of beads with lysis buffer and re-suspended in 20 µl of lysis buffer per IP. We used 1.5 mg/ml of antibody (or the recommended dilution antibodies from Cell Signalling where the antibody concentration is not provided). The total volume of the lysate was used to calculate the volume of antibody required. We used 0.5µl of IGG mouse/rabbit IGG for the control IP's. The beads were kept on ice or at 4°C until needed.

40ml of lysis buffer (Table 5.4) was made the day before sample collection and kept at 4°C. Protease and phosphotase inhibitors were added on the day of the experiment.

Media (control, Wnt conditioned media or media plus Wnt3A ligands) were pre-warmed to 37°C, and any extra ligands or inhibitors were added. We used one 10cm dish per sample and started the experiment when cells had reached 60%-70% confluency. The media in each dish was changed to the experiment's media and placed back in the incubator. The times for media changes were staggered for each dish to ensure that the cells were lysed and collected at similar times.

In order to minimise the break up of protein complexes all samples were kept on

ice and PBS and the eppendorf tubes used for sample collection were all pre-chilled and kept on ice. When the allocated stimulation time was reached, the dishes were moved to an ice tray. The media was aspirated, and the dish washed once and the cells were lysed using 750 µl of lysis buffer.

The lysates was removed using cell scrappers and added to pre-chilled eppendorf tubes and rotated for 15 minutes at 4°C. Each sample was then sonicated twice before being spun at 4°C at 13200 rpm for 30 minutes. Once the centrifuge was completed the supernatants were moved to new tubes and the pelletes discarded.

In order to load the same quantity of proteins when carrying out gel electrophoresis we used the Bradford assay (Bradford, 1976). The Bradford assay uses the change in colour of Coomassie Brilliant Blue G-250 dye, which changes from 465 nm (brown) to 595 nm (blue) depending on whether it is bound to a protein or not.

A standard curve was created using BSA diluted in PBS at different concentrations: 0, 0.125, 0.1875, 0.25, 0.375, 0.5, 0.75 and 1 mg/ml. BSA standards were created once by using BSA Standard Ampules (2 mg/mL) and kept at -20°C.

Protein samples were diluted 1:10 in 18µl of PBS. 5µl of each sample and the BSA standards were loaded twice on Sterlin 96-well plates alongside 245 µl of Bradford reagent. Absorption at 595 nm wavelength was measured using a spectrophotometer.

We calculated the average absorption for each sample and the BSA standards. Using a simple linear regression analysis on the BSA standard curve we calculated a line of best fit for protein concentration versus light absorption at 595 nm wavelength. This enabled us to calculate the protein concentration in each sample.

Once total protein concentrations were known for each sample, we diluted all samples to the lowest calculated concentration in order to ensure the IP and gel electrophoresis were carried out at the same total protein levels. We collected a total volume of 350-500 µl ("IP Volume") of lysate for the sample with the lowest protein concentration, while ensuring a total protein level of 1-1.5mg in the samples. Samples with higher protein concentrations were diluted using the lysis buffer to reach the same concentration at "IP Volume".

For each sample, one tenth (35-50µl) of these normalised cell lysates was mixed with equal volume of 2x dye to create the inputs for SDS-PAGE. These were kept in eppendorf tubes at -20°C to be run alongside the IP's.

Cell lysates were incubated with an appropriate concentration of antibody or IGG overnight at 4°C. This mix was then added to pre-washed beads for 1 hour with mixing at room temperature. The beads were washed 4 times with 1ml of lysis buffer. 1x SDS dye was added to the beads to create the IP SDS-PAGE samples. These samples were also kept at -20°C.

5.2.5 Western blot

Levels of the proteins of interest in the samples collected in the co-IP study were studied using Western blot analysis. First gel electrophoresis was used to separate out the proteins in our samples according to their size. The SDS added to the samples negatively charges the proteins and breaks up all the secondary and other structures such that the proteins can move through the gel from negative to positive.

The samples were boiled using a heat block for 30 minutes to denature the proteins further and, for the IP's eluting the proteins from the beads. We then spun down each sample for 30-45 seconds to facilitate loading.

Since LRP6 is more than 200 kDa whereas β-catenin is less than 100 kDa, we used NuPAGE 3-8% Tris-Acetate pre-cast gels. The gels were loaded into BioRad mini-Protean TetraCell gel tanks filled with pre-chilled 1x Tris-Acetate buffer. We loaded 15-20µl of sample in each well. We used 7.5µl of HiMark pre-stained protein ladder. The gels were run at a constant voltage of 120 V until the sample front was almost run off the bottom of the gel.

The proteins separated on the gels were transferred to Immobilon membranes from Millipore. Membranes were activated using 100% methanol and the transfer was performed in the BioRad mini gel blotting system at a fixed current of 350mA for 3 hours at 4°C.

The transfer was checked using Ponceau S staining solution to ensure good transfer in particular at higher molecular weights. The membranes were then washed three times for a total of 20 minutes on a shaker, before being blocked for 30 minutes in a fresh mixed solution of 5% (mass/volume) skimmed milk in PBST or 2.5% or (mass/volume) BSA in PBST, depending on the antibody.

The blocked membranes were then placed in Falcon tubes with the appropriate dilution of primary antibody in 3ml of milk/BSA solution, and were left on a roller at 4°C overnight. The membranes were again washed three times for a total of 20 minutes, before secondary antibody conjugated to Horseradish Peroxidase (HRP) was applied at a dilution of 1:5000 in 5ml of milk for 1-3 hours at room temperature.

After another set of PBST washes, the membranes were incubated for 1 minute at room temperature in Pierce ECL Western Blotting Substrate. Finally, Fuji X-ray films were exposed to the membranes in the dark room for a period of a few seconds (for GAPDH primary) to 30 minutes (when probing for pS1490 LRP6 in co-IP samples) depending on the protein of interest, before the film was developed. In some cases, the membranes were washed with PBST and re-incubated with the Millipore Immobilon ECL, which can provide a stronger signal. To run the membrane for another primary antibody, the membrane was re-blocked in milk/BSA in PBST solution with addition of sodium azide to deactivate the secondary antibody.

Protocol optimisation. Since the materials and methods of papers investigating the interaction between Axin and LRP6 in recent years were not detailed, I spent a large amount of time optimising the procedure described above. Table 5.5 describes some of the optimisation steps I carried out in order to improve the experimental results.

Step	Details	Results summary	Conclusion
Wnt Conditioned Media (CM) /Ligands	What is a suitable concentration for Wnt ligands/CM to ensure good pathway activity?	Pathway activation as measured by LRP6 phosphorylation was comparable using 100% CM and 100ng/ml ligands. We noticed a substantial drop in activity after 4 months of keeping CM at -20°C.	Use 100% CM or 100ng/ml ligands. Regularly check both for activity using TOP/Flash, pLRP6 levels or β-catenin levels.
IP beads	Is there an advantage in using magnetic or sepharose IP beads?	Many papers studying the interaction of Axin/LRP6 have used Sepharose beads. We confirmed with one of the authors that they have not tried magnetic beads. We tried sepharose beads once and saw no improvement compared to magnetic beads.	Further investigation with Sepharose beads might be required as they are more commonly used.
Incubation with antibody and beads	Should we incubate our samples with the antibody and beads at the same time or seperately?	We achieved slightly better blots by incubating our samples with antibody overnight at 4°C and then with the beads at room temperature for 1 hour with mixing.	Further optimisation required.
Membrane transfer	What is the most appropriate electroblotting procedure when working with heavy proteins such as LRP6?	We had a better transfer of heavy proteins, in particular LRP6 using a fixed current of 350mA for 3 hours (at 4°C), rather than using a fixed voltage of 100 V for 80 min.	Use the fixed current method.
Membrane	What is the most suitable blocking buffer and detection procedure when blotting for LRP6?	We detected no signal for LRP6 in the Axin IP samples using milk but detected a faint signal when using BSA, however the resulting blots were dirtier.	Further optimisation is required here, in particular experimenting with exact washing and blocking procedure.

TABLE 5.5: Summary of the steps we optimised during our investigation of the interactions between Axin and LRP6.

5.3 Results

The results from Chapter 4 lead us to the conclude that for the conditions used by Kim et al. (2013), measuring changes in levels of pS1490 LRP6 in complex with Axin upon Wnt stimulation, might enable us to discriminate between our candidate models (see Figure 5.3). In particular it could reveal which reactions are most markedly Wnt driven; association and dissociation of Axin to LRP6 (models H_{31} and H_{32}) or LRP6 phosphorylation (models H_{21} and H_{22}).

Figure 5.5 summarises the results of our co-IP experiments. Unfortunately, our results are inconclusive and further experiments are needed to discriminate between the candidate models.

As reported in other studies, we observe an increase in levels of pS1490 LRP6 (see input columns in Figures 5.5A, 5.5B and 5.5C). We remark that the GAPDH blots are likely saturated, making it difficult to accurately quantify and validate the total

protein levels in our samples. However, levels of Axin remain unchanged. This is a good second control as levels of Axin are not expected to change significantly in the first few hours of Wnt stimulation.

Kim et al. (2013) observed an initial increase in levels of LRP6 in Axin IP upon Wnt stimulation, followed by a return to the original levels. We make a similar observation in Figure 5.5C, however, we believe the Axin blot is saturated in this experiment and hence we have some concerns about the quality of these results.

Figure 5.5 also shows how levels of Axin with pS1490 LRP6 change. These blots suggest that levels of Axin in complex with pS1490 LRP6 are higher after 2 hours of Wnt stimulation compared to the levels with no Wnt stimulation (see Figures 5.5A and 5.5C). These results are consistent with the candidate models H_{21} and H_{22} and suggest that Wnt increases rate of phosphorylation of LRP6 at S1490, which in turn drives recruitment of pS497/500 Axin to the membrane.

We spent several months trying to optimise the experimental procedure described in the last section as detailed in Table 5.5. However, the protocol needs to be optimised further to improve the quality of these results.

Lack of IGG. By the end of my six months in the laboratory, I was focusing solely on optimising the protocol for the IP, and hence did not run Western blots on the IGG samples. The only control I have is hence from earlier experiments, where we confirmed that the IGG lanes were empty.

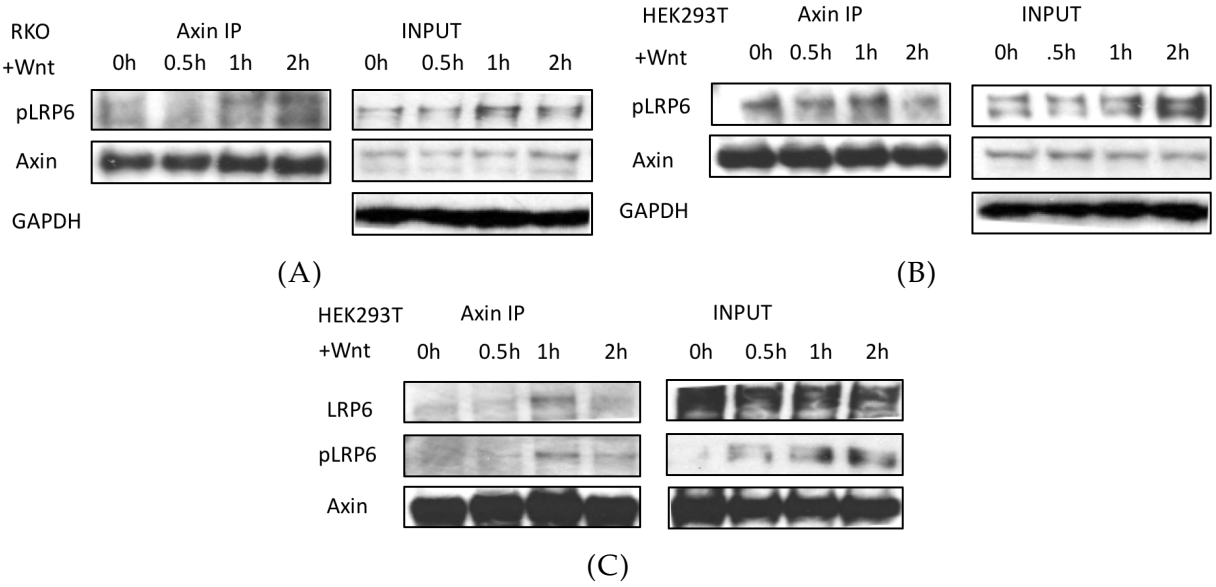


FIGURE 5.5: Preliminary results measuring the interaction between Axin and pS1490 LRP6 upon Wnt stimulation in (A) RKO cells, and (B,C) in HEK293T cells. These preliminary results suggest that levels of Axin in complex with pS1490 LRP6 may increase after 2 hours of Wnt stimulation. These experiments will have to be repeated and the protocols have to be optimized further.

5.4 Discussion

In this chapter we detailed our attempts to measure the interaction between two core components of the canonical Wnt pathway; Axin and LRP6. Our protocol was based

on the Materials and Methods section of Kim et al. (2013). We aimed to reproduce their observations, before studying the interaction between Axin and pS1490 LRP6. This would have enabled us to discriminate between the candidate models H_{xy} as proposed in Chapter 4.

In summary, our preliminary results hint that levels of Axin/LRP6 complex increase quickly after Wnt stimulation before returning to their original levels within 2 hours (in line with results of Kim et al. (2013)), while levels of Axin/pS1490 LRP6 may stay higher than the non-stimulated levels. These results suggest that H_{21} and H_{22} may be best in describing the dynamics of the interactions between Axin and LRP6. However, further work is required to completely validate these results.

Candidate models H_{21} and H_{22} assume that the primary Wnt driven reaction is phosphorylation of LRP6, rather than recruitment of Axin to LRP6. We remark that candidate model H_{21} is in fact the simplest candidate model that could reproduce the experimental observation by Kim et al. (2013). In Chapter 4, we invoked the principle of Occam's razor to select candidate model H_{21} as the model we will take forward to study further. Our results in this chapter, although inconclusive, provide further support for this decision.

My struggle to reproduce the results by Kim et al. (2013) in the laboratory highlight the problem of reproducibility in science that has been discussed in the past (Kaiser, 2017; Baker, 2016). We have confidence that with more time in the laboratory and more guidance it will be possible to complete these experiments.

Frustratingly, I lost several months since the paper by Kim et al. (2013) had not provided the correct antibody used for the Axin IP's. Moreover, incomplete materials and methods in different experimental papers meant I spent time optimising protocols which had already been optimised in other labs. We discuss these issues further in Chapter 7 of this thesis.

Although our results have been inconclusive, we hope that the detailed protocols described here will assist future scientists studying the interactions between Axin and LRP6.

In the next chapter, we extend our mathematical models of the Wnt pathway beyond the interaction between Axin and LRP6. We extend the simplified models S_1 and S_2 and look beyond the results by Kim et al. (2013) and consider whether a single mathematical model can reconcile the different experimental results in the literature.

Chapter 6

A new model of the Wnt pathway

6.1 Introduction

In Chapter 2 we described the state-of-the-art biological literature with regards to interactions between core components of the Wnt pathway and the post translational modifications that these go through upon Wnt stimulation. We summarised the latest verbal models of the Wnt pathway, which had been proposed to explain different experimental observations (see Section 2.2.1). We introduced some of the hypotheses with regards to how Wnt signalling leads to deactivation of the destruction complex (see Figure 2.5).

Li et al. (2012) suggested that the release of β-TrCP from the destruction complex upon Wnt stimulation prevents it from marking β-catenin for degradation. In a similar fashion, Azzolin et al. (2014) proposed that LRP6 replaces YAP and β-TrCP in the destruction complex, and thereby prevent it from ubiquitinating β-catenin. Kim et al. (2013) and Hernández et al. (2012) argued that the ubiquitination step of the destruction complex is unchanged upon Wnt stimulation. Instead Kim et al. (2013) proposed that Wnt stimulation leads to dephosphorylation of Axin, which prevents it from recruiting β-catenin. Hernández et al. (2012), Wu et al. (2009), and Piao et al. (2008) and several other studies have proposed that Wnt reduces the rates of phosphorylation of β-catenin by CK1 and GSK3, but do not explicitly model how this may occur.

It is a main aim of this thesis to use mathematical modelling to investigate whether a single model can reconcile the observations that have led to different models. Lee et al. (2003) proposed the first mathematical model of the Wnt pathway, and since then many alternatives have been proposed over the past fourteen years (please see our summary in Chapter 2 or a more detailed review by Lloyd-Lewis et al. (2013)). To our knowledge, none of these models consider the interactions between Axin and LRP6 and how these alter the destruction complex. Our goal is hence to develop a new model of the Wnt pathway that studies these interactions.

In order to keep the problem computationally tractable, in Chapter 4, we focused on the cell's initial response to Wnt stimulation and recruitment of the Axin scaffolding protein to the receptors at the cell membrane. We proposed a set of candidate models and studied which may best describe various experimental observations. Our analysis revealed that the simplest of our candidate models, which is consistent with the experimental data considered, is one where Axin is recruited to LRP6 even in the absence of Wnt. Axin facilitates phosphorylation of LRP6 upon Wnt stimulation, which amplifies the recruitment of Axin to LRP6, thereby enhancing Axin dephosphorylation.

After establishing this model of the Wnt pathway (namely candidate model H_{21}), we ended Chapter 4 by simplifying this model further (to develop candidate models S_1 and S_2) and showing that they were could reproduce experimental observations by Kim et al. (2013). Our candidate models in Chapter 4 did not model β-catenin. In this chapter, we extend these candidate models to include β-catenin and a more detailed explanation of the destruction complex. We aim to use our candidate mathematical

models to analyse existing competing verbal models proposed in the literature (Li et al., 2012; Kim et al., 2013; Azzolin et al., 2014).

In order to ensure that model selection is computationally tractable, we extend the candidate models in two steps. In the next section we describe the first extension to models S_1 and S_2. We introduce a set of candidate models that account for synthesis and degradation of β-catenin. We study these candidate models analytically and use the framework developed in Chapter 4 to establish whether they can reproduce the experimental observations by Kim et al. (2013).

After identifying the most suitable candidate models from this first extension using our model selection framework, we then introduce further details about the destruction complex and propose a new set of candidate models. This final extension enables us to explore whether these candidate models can reproduce the experimental observations from three different studies: Kim et al. (2013), Li et al. (2012) and Azzolin et al. (2014). Once we have established suitable candidate models and feasible parameter sets, we use *in silico* experiments to study the models further to learn more about the dynamics of the pathway.

6.2 Extension 1: Introducing the destruction complex

6.2.1 Introduction

The candidate mathematical models in Chapter 4 focused on the interaction between Axin and LRP6 and whether they can reproduce observations by Kim et al. (2013). Kim et al. (2013) also measured levels of β-catenin in complex with Axin. In this section, we incorporate this additional constraint into new candidate models.

Since β-catenin is observed to have higher affinity for pS497/500 Axin compared to its unphosphorylated counterpart (Jho et al., 1999; Kim et al., 2013), in this first extension we assume that β-catenin binds only to pS497/500 Axin. We do not explicitly model other components of the destruction complex. We neglect modifications β-catenin is observed to go through, and simply assume it is degraded once it is released from Axin.

6.2.2 Methods

Figure 6.1 summarises the framework we used in Chapter 4. We now use this framework to study a more complete model of the Wnt pathway.

We start this section by describing the biochemical reactions included, and detailing the candidate models and associated mathematical equations. We then summarise the experimental observations by Kim et al. (2013) we aim to reproduce. Next, we carry out a steady state analysis of the system of ODEs describing the temporal dynamics of the models. Finally, we quickly touch on the setup for the CMA-ES optimisation algorithm we use to perform model selection.

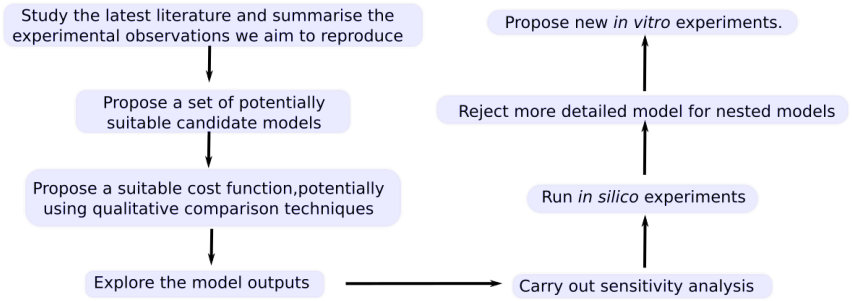


FIGURE 6.1: The framework we use for studying dynamics of signalling pathways. We applied this framework to study the interaction of Axin and LRP6 upon Wnt stimulation in Chapter 4. We again recruit this framework as we extend our mathematical model of the Wnt pathway further to include β-catenin and the destruction complex.

6.2.2.1 Qualitative description of our mathematical models

We base our candidate models on models S_1 and S_2 from Section 4.4 (see Reactions (4.28)-(4.31)). These models comprise of 5 ODEs describing the evolution of pS1490 LRP6, pS495/500 Axin, their unphosphorylated counterparts, and the complex of pS1490 LRP6 and pS497/500 Axin (see Equations (4.32)-(4.36).

In Figure 6.2 we indicate the new candidate models. The models now have up to eight species: five of these also appear in candidate models S_1 and S_2. The new species represent free β-catenin (B), the destruction complex/β-catenin complex ($D \equiv [A_p : B]$) and the destruction complex and β-catenin complex recruited to LRP6 ($E \equiv [A_p : L_p : B]$). Table 6.1 summarises these dependent variables.

Dependent Variable	Description
A_u	Concentration of Axin not phosphorylated at S497/S500
A_p	Concentration of Axin phosphorylated at S497/S500
L_u	Concentration of LRP6 not phosphorylated at S1490
L_p	Concentration of LRP6 phosphorylated at S1490
B	Concentration of β-catenin
$C \equiv [A_p : L_p]$	Concentration of Complex of L_p and A_p
$D \equiv [A_p : B]$	Concentration of Complex of B and A_p
$E \equiv [A_p : L_p : B]$	Concentration of Complex of B, A_p and L_p

TABLE 6.1: Dependent variables in our candidate mathematical models in first Extension introduced in this chapter.

The reactions included are:

$$R_1: \quad \mathrm{A_u} \underset{k_{-1}}{\overset{k_1}{\rightleftharpoons}} \mathrm{A_p}, \tag{6.1}$$

$$R_2: \quad \mathrm{L_u} \underset{k_{-2}}{\overset{k_2(w)}{\rightleftharpoons}} \mathrm{L_p}, \tag{6.2}$$

$$R_{3A}: \quad \mathrm{A_p} + \mathrm{L_p} \underset{k_{-3}}{\overset{k_3}{\rightleftharpoons}} \mathrm{C}, \tag{6.3}$$

$$R_{4A}: \quad \mathrm{C} \xrightarrow{k_{-4}(w)} \mathrm{A_u} + \mathrm{L_p}, \tag{6.4}$$

$$R_s: \quad \emptyset \xrightarrow{s} \mathrm{B}, \tag{6.5}$$

$$R_5: \quad \mathrm{A_p} + \mathrm{B} \underset{k_{-5}}{\overset{k_5}{\rightleftharpoons}} \mathrm{D}, \tag{6.6}$$

$$R_d: \quad \mathrm{D} \xrightarrow{d} \mathrm{A_p} + \emptyset, \tag{6.7}$$

$$R_{3B}: \quad \mathrm{D} + \mathrm{L_p} \underset{k^*_{-3}}{\overset{k^*_3}{\rightleftharpoons}} \mathrm{E}, \tag{6.8}$$

$$R_{4B}: \quad \mathrm{E} \xrightarrow{k^*_{-4}(w)} \mathrm{A_u} + \mathrm{L_p} + \mathrm{B}. \tag{6.9}$$

The colour of each reaction matches that used in the model schematics in Figure 6.2. Reactions R_1, R_2, R_{3A} and R_{4A} appeared in models S_1 and S_2 (see Chapter 4 for details). We now provide the motivation behind the new reactions R_s, R_d, R_{3B}, R_{4B} and R_5.

Reaction R_s. CTNNB1 (the β-catenin gene) mRNA levels have been observed to remain unchanged during Wnt stimulation (Hernández et al., 2012), we hence assume that β-catenin is synthesised at a fixed rate, s.

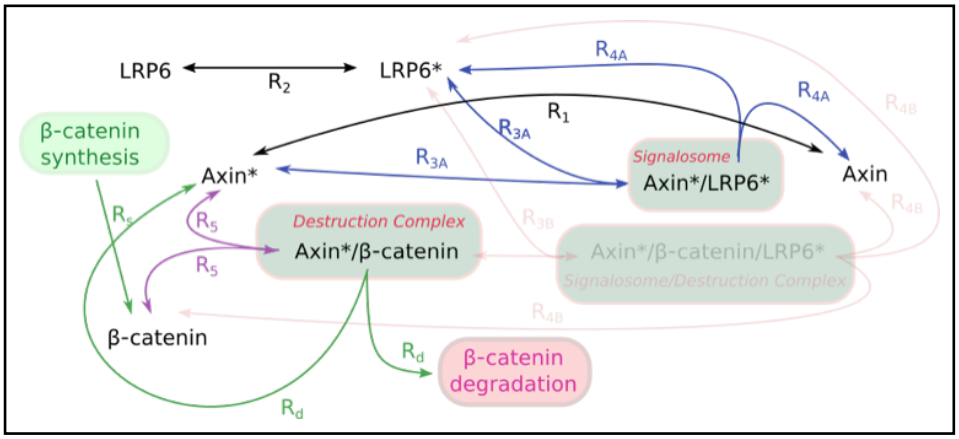
Reaction R_5. β-catenin is degraded via recruitment to the destruction complex and in particular to Axin (Valenta et al., 2012; Stamos and Weis, 2013; MacDonald and He, 2012). This reaction represents the reversible binding of β-catenin to the destruction complex.

Reaction R_d. This reaction represents the degradation of β-catenin after recruitment to the destruction complex. This releases pS497/500 Axin (A_p), which can then recruit further β-catenin.

Reaction R_{3B}. β-catenin is observed in complex with LRP6 upon Wnt stimulation (Hendriksen et al., 2008), we assume that the destruction complex D may be recruited to LRP6 upon Wnt stimulation (Reaction R_{3B}), leading to dephosphorylation of Axin and its release alongside β-catenin back into the cytoplasm.

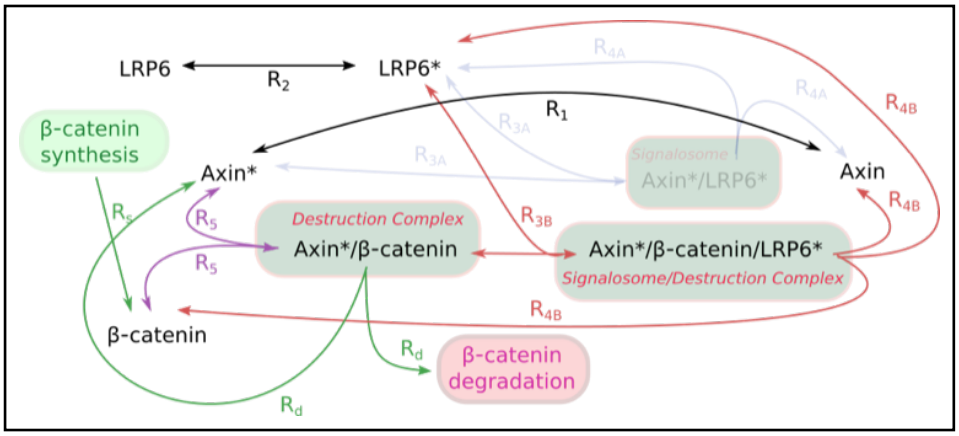
Reaction R_{4B}. LRP6 phosphorylated at PPPSP motifs can inhibit phosphorylation of β-catenin by GSK3 (Piao et al., 2008; Wu et al., 2009; Cselenyi et al., 2008). Hence we assume that the destruction complex cannot continue degrading β-catenin while in complex with LRP6 in complex E. We note that Reaction R_{4B} is one where a trispecies complex of Axin, LRP6 and β-catenin is broken down into its constitutive parts in one

Candidate models M_{x1}: we introduce a simple extension to model S_1 and S_2 in Chapter 4 (see Figure 4.11): A_p may be recruited to L_p as before, or form a complex with B, leading to degradation of B.



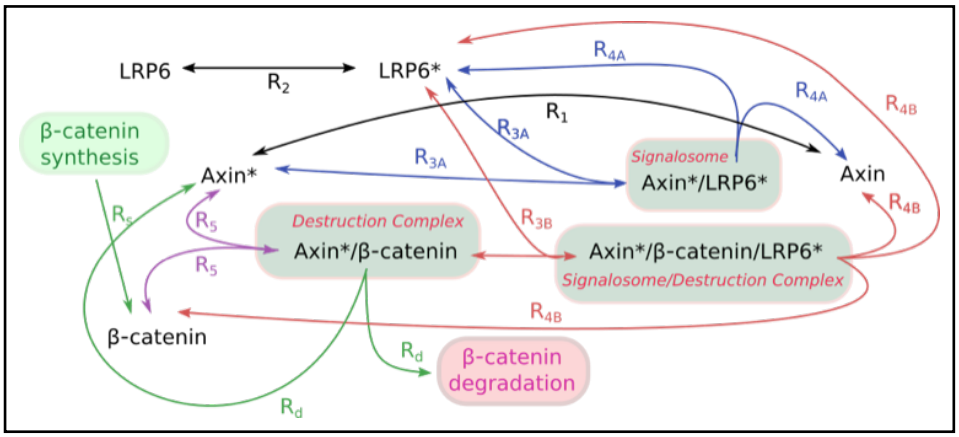
(A)

Candidate models M_{x2}: A_p is not recruited to LRP6. Instead, D is the only Axin complex that can form a complex with LRP6.



(B)

Candidate models M_{x3}: A_p or D may be recruited to L_p and released from it at exactly the same rate, i.e. all forms of the destruction complex are recruited to the membrane upon Wnt stimulation.



(C)

FIGURE 6.2: Schematics of the candidate models of the canonical Wnt pathway incorporating degradation of β-catenin via the destruction complex (A) M_{x1}, (B) M_{x2}, and (C) M_{x3} (See Section 6.2.2.2 for details).

step. This is a simplification of a more detailed model which may include an intermediate step leading to Axin dephosphorylation and release of β-catenin before a second step in which Axin is released from LRP6.

We remark that we ignore some components of the destruction complex and, particularly, the GSK3 and CK1 kinases and APC. We do this for simplicity and because recent studies have suggested that levels of these proteins in complex with Axin do not change in the first few hours after Wnt stimulation (Li et al., 2012; Kim et al., 2013).

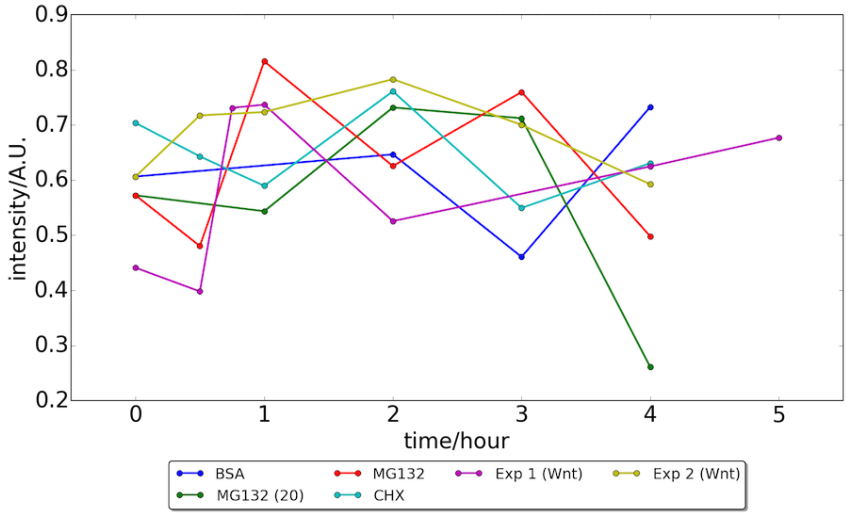


FIGURE 6.3: We stimulated RKO cells with various stimuli including Wnt, CHX and MG132 and measured the intensity of β-catenin in the nucleus versus the cytoplasm. We failed to detect any significant changes in this ratio in the first few hours after stimulation.

The mechanism of entry of β-catenin into the nucleus is not very well understood, however an increase in levels of cytoplasmic β-catenin generally leads to its translocation into the nucleus (Valenta et al., 2012). Our own data suggests that the ratio of nuclear β-catenin and cytoplasmic β-catenin is independent of Wnt stimulation and rates of degradation and synthesis of β-catenin (Figure 6.3). Therefore we ignore the nuclear compartment and, as in Chapter 4, assume that all reactions take place in a single well-mixed compartment.

Modelling the effect of Wnt. As detailed in Chapter 4, we follow Lee et al. (2003) and introduce the effect of Wnt via an externally prescribed function of time that acts on certain reactions. We assume a "Wnt-off" value for a Wnt-dependent rate parameter corresponding to the activity of the pathway in the absence of a Wnt stimulus. Upon Wnt stimulation, we assume that an exponential function with a time constant of between 1 and 20 minutes changes this rate parameter from the "Wnt-off" value to a new "Wnt-on" value.

6.2.2.2 Candidate models

We consider several candidate models and study whether they are consistent with the experimental observations by Kim et al. (2013). We use notation M_{xy} where x and y are positive integers to refer to different candidate models.

Subscript $x = 1, 2$, determines which rates are altered by Wnt stimulation, whereas subscript $y = 1, 2, 3$ determines how the destruction complex is recruited to LRP6:

- **x=1:** LRP6 phosphorylation (k_2).
- **x=2:** LRP6 phosphorylation (k_2) and release of Axin from LRP6 (k_{-4}, k^*_{-4}),
- **y=1:** LRP6 recruits only Axin without β-catenin, i.e. it recruits only A_p and hence rates for reactions R_{3B} and R_{4B} are zero: $k^*_{\pm 3} = k^*_{-4} = 0$ (see Figure 6.2A).
- **y=2:** LRP6 recruits only Axin with β-catenin, i.e. it recruits only D, and hence rates for reactions R_{3A} and R_{4A} are zero: $k_{\pm 3} = k_{-4} = 0$ (see Figure 6.2B).
- **y=3:** LRP6 recruits A_p and D at the same rate: $k_{\pm 3} = k^*_{\pm 3}$, $k_{-4} = k^*_{-4}$ (see Figure 6.2C).

Figure 6.2 illustrates the three different cases described by subscript y. Table 6.2 summarises all six candidate models under consideration.

We remark that assumptions under subscript $x = 1, 2$ correspond to assumptions in candidate models S_1 and S_2 respectively. We also note that we assume only reactions that involve LRP6 may be altered by Wnt. We do so since Wnt ligands bind to the extracellular domain of LRP6, and can lead to modifications in this protein, which in turn may change the rates of the reactions involving LRP6.

Candidate Model	Wnt Dependent Reactions	A_p binds to L_p	D binds to L_p	A_p and D bind to L_p at the same rate	Dependent Variables	Rate Parameters
M_{11}	LRP6 phosphorylation	✓	✗	-	7	11
M_{12}	LRP6 phosphorylation	✗	✓	-	7	11
M_{13}	LRP6 phosphorylation	✓	✓	✓	8	11
M_{21}	LRP6 phosphorylation and Axin/LRP6 release	✓	✗	-	7	11
M_{22}	LRP6 phosphorylation and Axin/LRP6 release	✗	✓	-	7	11
M_{23}	LRP6 phosphorylation and Axin/LRP6 release	✓	✓	✓	8	11

TABLE 6.2: Candidate models for our first extension to the model proposed in Chapter 4.

We do not consider a model in which rate of recruitment of Axin to LRP6 depends on whether or not Axin is in complex with β-catenin as we are not aware of any experimental observations that suggest this may be the case.

6.2.2.3 Mathematical representation of our candidate models

If we assume mass-action kinetics for all reactions, we may use the principles of mass balance to derive the following time dependent system of ODEs to represent the different candidate models:

$$\frac{\mathrm{d}B}{\mathrm{d}t} = r_s - + r_{4b} - r_5, \tag{6.10}$$

$$\frac{\mathrm{d}A_u}{\mathrm{d}t} = -r_1 + r_{4a} + r_{4b}, \tag{6.11}$$

$$\frac{\mathrm{d}A_p}{\mathrm{d}t} = r_d + r_1 - r_{3a} - r_5, \tag{6.12}$$

$$\frac{\mathrm{d}L_u}{\mathrm{d}t} = -r_2, \tag{6.13}$$

$$\frac{\mathrm{d}L_p}{\mathrm{d}t} = r_2 - r_{3a} - r_{3b} + r_{4a} + r_{4b}, \tag{6.14}$$

$$\frac{\mathrm{d}C}{\mathrm{d}t} = +r_{3a} - r_{4a}, \tag{6.15}$$

$$\frac{\mathrm{d}D}{\mathrm{d}t} = -r_d - r_{3b} - r_5, \tag{6.16}$$

$$\frac{\mathrm{d}E}{\mathrm{d}t} = +r_{3b} - r_{4b}, \tag{6.17}$$

where

$$\begin{aligned}
R_1 &: & r_1 &= k_1 A_u - k_{-1} A_p, \\
R_2 &: & r_2 &= k_2(w) L_u - k_{-2} L_p, \\
R_{3A} &: & r_{3a} &= k_3 A_p L_p - k_{-3} C, \\
R_{3B} &: & r_{3b} &= k_3^* D L_p - k_{-3}^* E, \\
R_{4A} &: & r_{4a} &= k_{-4}(w) C, \\
R_{4B} &: & r_{4b} &= k_{-4}^*(w) E, \\
R_s &: & r_s &= s, \\
R_d &: & r_d &= dD, \\
R_5 &: & r_5 &= k_5 A_p B - k_{-5} D.
\end{aligned}$$

Table 6.1 summarises all the dependent variables. We impose initial conditions in the "Wnt-off" simulation for which all dependent variables are zero except $L_u(t=0) = L_{\text{tot}}$ and $A_p(t=0) = A_{\text{tot}}$, where L_{tot} and A_{tot} represent the total levels of LRP6 and Axin.

Summing up the relevant combinations of Equations (6.11)-(6.17) yields the following identities, which represent the conservation of total levels of Axin and LRP6:

$$A_{\text{tot}} = A_u + A_p + C + D + E, \tag{6.18}$$

$$L_{\text{tot}} = L_u + L_p + C + E. \tag{6.19}$$

These equations may be used to reduce the number of species in our candidate models by two. Tables 6.1 and 6.3 summarise the dependent variables and parameters used in our candidate models.

parameter	Description	Unit
$k_{\pm 1}$	Rate of Axin phosphorylation/dephosphorylation	min^{-1}
$k_{\pm 2}$	Rate of LRP6 phosphorylation/dephosphorylation	min^{-1}
$k_{\pm 3}$	Rate of association/dissociation of Axin and LRP6	$\mathrm{min}^{-1}\mathrm{nM}^{-1}$
$k^*_{\pm 3}$	Rate of association/dissociation of Axin/β-catenin complex and LRP6	$\mathrm{min}^{-1}\mathrm{nM}^{-1}$
k_{-4}	Rate of release of unphosphorylated Axin from Axin/LRP6 complex	min^{-1}
k^*_{-4}	Rate of release of unphosphorylated Axin and β-catenin from Axin/LRP6/β-catenin complex	min^{-1}
s	Rate of synthesis of β-catenin	nMmin^{-1}
d	Rate of degradation of β-catenin via the destruction complex	min^{-1}
$k_{\pm 5}$	Rate of association/dissociation of β-catenin and phosphorylated Axin	$\mathrm{min}^{-1}\mathrm{nM}^{-1}$
A_{tot}, L_{tot}	Total Axin and LRP6	nM
w_2, w_{-4}	Wnt multiplier	-
τ	Time constant	-

TABLE 6.3: Parameters used in our mathematical models M_{xy} ($x = 1, 2$; $y = 1, 2, 3$). Note under candidate models M_{x1}, $k^*_{\pm 3} = k^*_{-4} = 0$; under candidate models M_{x2}, $k_{\pm 3} = k_{-4} = 0$; and under candidate models M_{x3}, $k_{\pm 3} = k^*_{\pm 3}$, $k_{-4} = k^*_{-4}$

6.2.2.4 Implementation of the mathematical model

As described in Section 4.2.4, we use the Python packages PySB (Lopez et al., 2014) and SciPy, to solve the candidate mathematical models numerically.

6.2.2.5 Experimental observations

As in Chapter 4 we focus on establishing whether the candidate mathematical models can reproduce the experimental observations by Kim et al. (2013). Figure 6.4 displays in quantitative form the data we aim to reproduce (see method in Appendix A). For completeness, the original Western blot data for L-cells are displayed in Figure 6.5. The data for HEK293T cells yielded similar qualitative outputs except for the levels of Axin/β-catenin complex. In L-cells the levels of this complex dropped after 30 minutes before increasing, whereas in HEK293T cells these levels increased monotonically.

As in Chapter 4, we employ satisfaction metrics when comparing the output from the candidate models to the experimental observations. The qualitative behaviours we would aim to replicate using the candidate mathematical models M_{xy} ($x = 1, 2$; $y = 1, 2, 3$) are that in response to Wnt stimulation:

1. Levels of pS497/500 Axin decrease monotonically,
2. Levels of pS1490 LRP6 increase monotonically,
3. Levels of β-catenin increase monotonically,
4. β-catenin levels have attained a new steady state level at four hours.
5. Levels of Axin/LRP6 complex are biphasic, increasing to a maximum value within half an hour before falling to levels that are higher than non-stimulated levels.

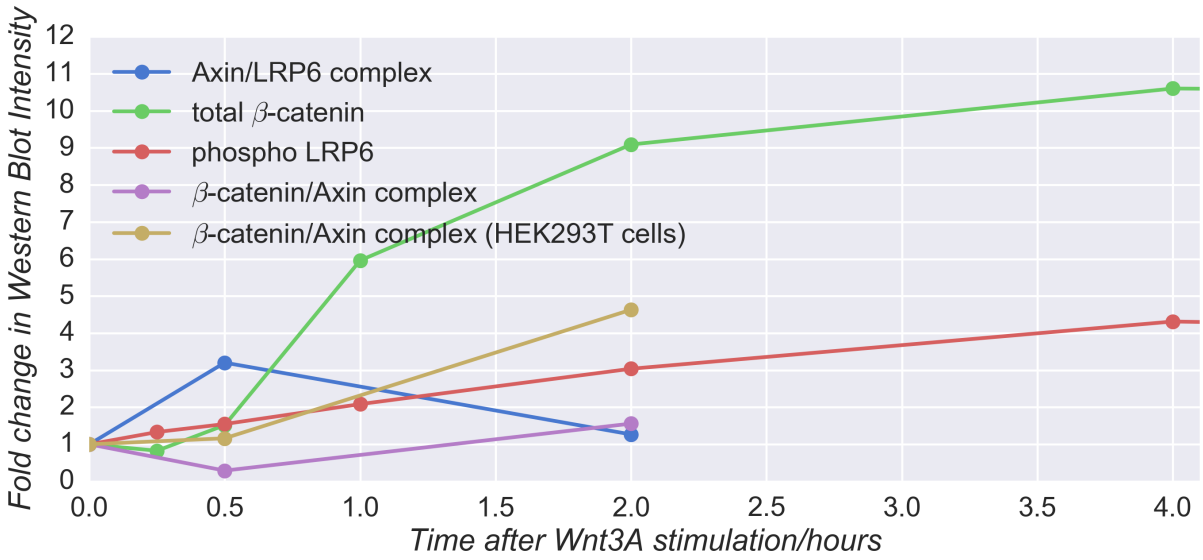


FIGURE 6.4: Quantification of typical blots from studies by Kim et al. (2013). All results are from L-cells, apart from one, which is from HEK293T cells. The authors observe qualitatively similar results in HEK293T cells in all experiments apart from changes in levels of Axin/β-catenin complex.

6. levels of Axin/β-catenin complex do not increase rapidly in the first half hour before increasing to levels above the original non-stimulated levels.

A_p binds to L_p	D binds to L_p	Total pS497/500 Axin	Total pS1490 LRP6	Total Axin/ β-catenin	Total β-catenin
✓	✗	$A_p + C + D$	$L_p + C$	D	$B + D$
✗	✓	$A_p + D + E$	$L_p + E$	$D + E$	$B + D + E$
✓	✓	$A_p + C + D + E$	$L_p + C + E$	$D + E$	$B + D + E$

TABLE 6.4: Summary of the different combination of dependent variables that are used when comparing the behaviour of model outputs to the results by Kim et al. (2013).

We note that for the candidate models, different combinations of model dependent variables need to be compared with the experimental observations. Table 6.4 summarises these combinations. We remark also that the qualitative behaviour we require for the Axin/LRP6 complex in (5) is different to the Axin/LRP6 interaction observed by Kim et al. (2013). Since in these models we ignore several Axin/LRP6 complex combinations, unlike models H_{xy}, and because Kim et al. (2013) do not measure the levels of the pS497/500 Axin/pS1490 LRP6 complex, similar to models S_x, we compare this model output qualitatively to the model output from candidate model H_{21} (see Section 4.4 for further details).

6.2.2.6 Steady state analysis

We can study the candidate models analytically and solve for steady states. Summing Equations (6.10), (6.16) and (6.17), we deduce that

$$\frac{\mathrm{d}(\text{total } \beta\text{-catenin})}{\mathrm{d}t} = \frac{\mathrm{d}(B + D + E)}{\mathrm{d}t} = s - dD. \tag{6.20}$$

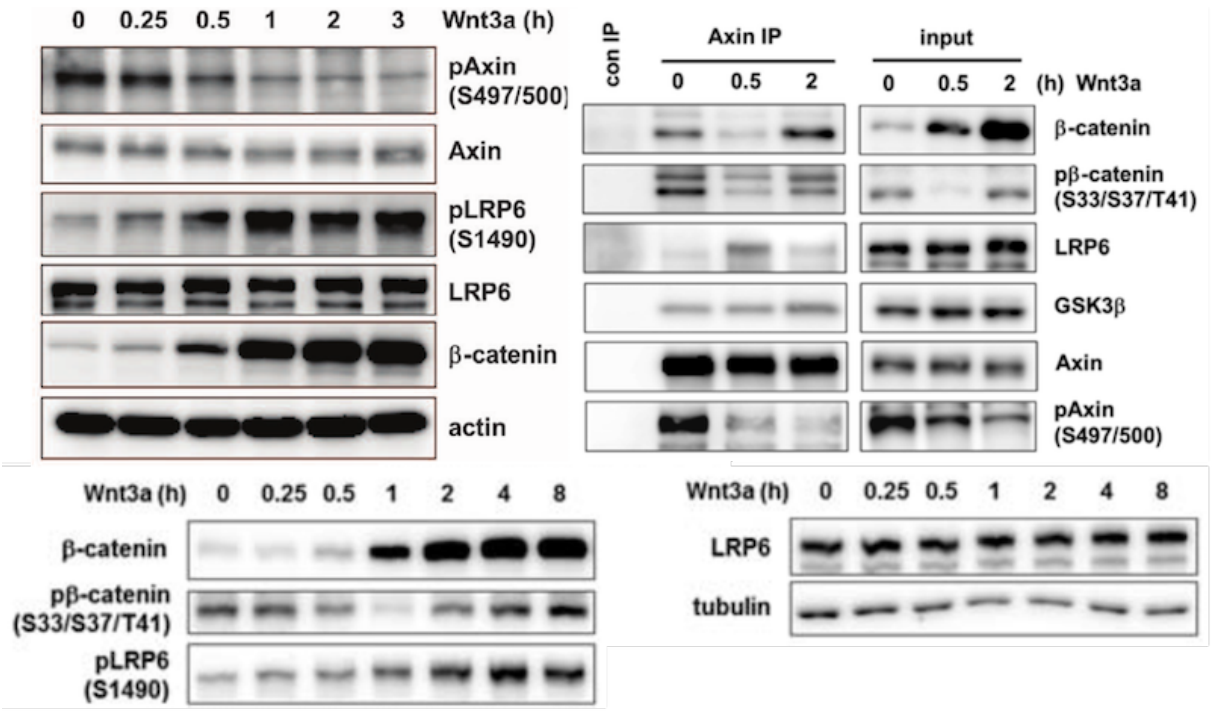


FIGURE 6.5: Kim et al. (2013) study interactions between some of the core components of the canonical Wnt pathway using co-immunoprecipitation and Western blots. They create an antibody specifically for Axin phosphorylated at S497/S500 and study these interactions in L cells and HEK293T cells. The results displayed here were generated from L cells

Setting $\frac{\mathrm{d}}{\mathrm{d}t} = 0$ in Equation (6.20) for steady state, we deduce that the steady state for D is given by

$$D = \frac{s}{d}. \tag{6.21}$$

We can use this and Equation (6.17) to write E in terms of L_p to obtain

$$E = \frac{k_3^* D L_p}{(k_{-3}^* + k_{-4}^*)} = \frac{k_3^* s L_p}{d(k_{-3}^* + k_{-4}^*)}. \tag{6.22}$$

Similarly, Equation (6.13) supplies

$$L_u = \frac{k_{-2}}{k_2} L_p. \tag{6.23}$$

We can substitute Equations (6.22) and (6.23) into Equation (6.19) yields

$$C = L_{\text{tot}} - k_2^* L_p, \tag{6.24}$$

where

$$k_2^* = 1 + \frac{k_{-2}}{k_2} + \frac{k_3^* s}{d(k_{-3}^* + k_{-4}^*)} > 1. \tag{6.25}$$

Substituting Equation (6.24) into Equation (6.15) gives

$$A_p = \Big(\frac{k_{-3} + k_{-4}}{k_3}\Big)\Big(\frac{L_{\text{tot}} - k_2^* L_p}{L_p}\Big). \tag{6.26}$$

Finally, we can use Equation (6.11) to eliminate A_u from Equation (6.18) to obtain

$$A_p = \frac{1}{k_1 + k_{-1}}\left(k_1\big(A_{\text{tot}} - \frac{s}{d}\big) - (k_1 + k_{-4})L_{\text{tot}}\right) - \frac{1}{k_1 + k_{-1}}\left((k_1 + k^*_{-4})\frac{k^*_3 s}{d(k^*_{-3} + k^*_{-4})} - (k_1 + k_{-4})k^*_2\right)L_p. \tag{6.27}$$

The intersections in (L_p, A_p) space of the hyperbola and line described by Equations (6.26) and (6.27) describe the steady state solutions of our candidate models. We note that there is a discontinuity in Equation (6.26) at $L_p = 0$ and since $k^*_2 > 1$, Equation (6.26) describes a strictly decreasing function of A_p for $L_p > 0$. Moreover, Equation (6.27) is a monotonically increasing or decreasing function of L_p. There is hence a maximum of one positive steady state possible for our candidate models, confirming that bistability is not possible for any of the models.

It may be possible to use the expression for the steady state solutions to identify regions of parameter space in which the model outputs are biologically relevant and consistent with the experimental observations. Where steady state solutions are inconsistent with the experimental observations, such an analysis enables us to reject a candidate model outright. In other cases, it might enable us to reduce the search space when running the CMA-ES optimisation algorithm. We remark that we refrain from carrying out any significant such analysis as this will slow down the candidate model development procedure. For us, the efficient prototyping of new candidate models using PySB package and exploration of the model parameter space using SciPy and CMA-ES outweighs its potential disadvantage of requiring longer computational time due to a larger parameter space.

6.2.2.7 Model selection

We solve the model ODEs numerically in the "Wnt-off" conditions until the system reaches steady state, before switching the parameter values to the "Wnt-on" value and solving the ODEs again numerically. We check that the "Wnt-off" steady state matches the value found in Section 6.2.2.6. As in Chapter 4, we assume that if Wnt acts on reaction rate k_i, then it increases it by a factor of w upon Wnt stimulation, that is

$$k_i^{\text{on}}(t) = k_i\Big(1 + (w-1)\big(1 - e^{(-t/\tau)}\big)\Big), \tag{6.28}$$

where w is the Wnt multiplier, and τ is the exponential time constant, meaning $\tau \log 2$ is the half life of the exponential growth describing the change in k_i.

We compare model output to experimental observations described in Section 6.2.2.5 via a cost function based on satisfaction metrics (see Section 3.5.2). In Section B.2 of Appendix B, we detail the elements of the cost vector. The final cost value is then given by

$$J = \sum_{i=0}^{8} w_i J_i^2, \tag{6.29}$$

where J_i and w_i correspond to the cost elements and their associated weights.

We explore the candidate model outputs using the CMA-ES optimisation algorithm. As summarised in Table 6.2, each candidate model has eleven rate parameters.

Param	Description	Unit	Value	Details
L_{tot}	Total LRP6 concentration	nM	17	Bafico et al. (2001) calculate 2500-5000 molecules/cell in NIH3T3 cells. Average number of receptors per cell (3750) is converted to a concentration level using a membrane volume of 0.37pL for HEK293T cells (Tan et al., 2012).
A_{tot}	Total Axin concentration	nM	0.001-200	150 (HEK293T), 110 (MDCK), 30 (Caco-2), 30 (SW480), 20 (SW480APC) (Tan et al., 2012), 0.02 (Xenopus egg extracts) (Lee et al., 2003).
	Phosphorylation, dephosphorylation rates	min^{-1}	10^{-4}-10^{4}	Upper bound chosen to be one order of magnitude above highest measured by Rose and Dube (1976), and the lower bound chosen one order of magnitude below the lowest values found in mathematical models of the Wnt pathway.
	Association rates	$\text{nM}^{-1}\,\text{min}^{-1}$	10^{-5}-10^{6}	Northrup and Erickson (1992) argue that typical values for association rates are of order of $10^6\text{M}^{-1}\text{s}^{-1} = 10^6 \times 60 \times 10^{-9}\text{nM}^{-1}\,\text{min}^{-1} = 0.06\text{nM}^{-1}\,\text{min}^{-1}$. There is a large range of fitted parameter values in the relevant literature. We select upper and lower bounds that are one order of magnitude beyond the highest and lowest values fitted.
	Dissociation constants	nM	0.01-10^{4}	Upper and lower bounds chosen one order of magnitude beyond the values found in the relevant references (Lee et al., 2003; Wei et al., 2007). Other mathematical models of the Wnt pathway have found lower fitted rate constants, however we do not use these values as they are not backed by any experimental observations.
w_i^*	Wnt multipliers		0.01-100	Upon Wnt stimulation, Hernández et al. (2012) see up to a ten fold increase in the inhibition of the rate of phosphorylation of β-catenin. We use a range which is one order of magnitude beyond this value. Unlike Chapter 4, we consider both an increase and decrease (see the discussion in Section 6.4.)
d	β-catenin degradation	min^{-1}	10^{-4}-10^{4}	Calculated using a flux of 25 $\text{nMh}^{-1} \approx 0.4\text{nM}\,\text{min}^{-1}$ (Lee et al., 2003), and the range for A_{tot} given above. We allow values one order of magnitude above and below these.
s	β-catenin synthesis	$\frac{\text{nM}}{\text{min}}$	0.01-10	Calculated using a flux of $25\text{nMh}^{-1} \approx 0.4\text{nM}\,\text{min}^{-1}$ (Lee et al., 2003), we assume upper and lower bounds one order of magnitude beyond these levels.
τ	Activation time constant		1-20	Exponential time constant used to calculate the speed of fold change in the rate of Wnt driven reaction, in line with values observed by Hernández et al. (2012).

TABLE 6.5: Range of parameter values used to explore the output of each candidate mathematical model. The upper and lower ranges for the rate constants are taken from a combination of measurements from biological experiments or values used in other mathematical models of the Wnt pathway.

Depending on the candidate model there are one or two Wnt multipliers, one time constant τ and two parameters for total levels of Axin and LRP6 (A_{tot} and L_{tot}).

As we explore the model parameter space, we assume that total levels of LRP6 are fixed. However, since a wide range of values for levels of Axin are reported in the literature, we allow total levels of Axin to vary. The elements of our parameter vector $\boldsymbol{\theta}$ are:

- Phosphorylation and dephosphorylation rates ($k_{\pm 1}$, $k_{\pm 2}$),
- Association rates (k_3, k_5),
- Dissociation constants ($K_3 = k_{-3}/k_3$, $K_4 = k_{-4}/k_3$, $K_5 = k_{-5}/k_5$),
- Rate of β-catenin synthesis and degradation (s, d),
- Time constant τ for the exponential change in Wnt dependent reaction rates,
- A subset of Wnt multipliers w_2 and w_{-4}, depending on the candidate model,
- Total Axin levels A_{tot}.

We represent the ranges for the model parameters in Table 6.5.

6.2.2.8 Parameter values for the multi-start CMA-ES technique

In order to gain confidence that we are exploring the high dimensional parameter space sufficiently, we again apply the multi-start CMA-ES technique to synthetic model outputs generated using each candidate model. For each candidate model, M_{12}, M_{13}, M_{22} and M_{23}, we generated eight random vectors from the parameter space defined in Table 6.5 and used these to generate $4 \times 8 = 32$ synthetic model outputs. We ignore candidate models M_{x1} as we can reject these using steady state analysis - see Section 6.2.3.

We solve each model numerically as described earlier and use a sum of squared errors distance function at 10 equidistant time points to compare the model outputs with the true synthetic output. We accept any fits with a cost less than 0.001. For consistency with the problem of interest, we use levels of pS497/500 Axin, pS1490 LRP6, Axin/LRP6 complex and Axin/β-catenin complex when measuring the distance between the target data and model output.

We ran the CMA-ES technique with the same number of random starts (112) in log-space as before, however, we doubled the number of particles used in the CMA-ES technique from the default value of $4 + 3\log(n_H)$, where n_H is the dimensionality of the parameter space. In all cases we confirmed that we are able to recover a set of parameter values that reproduce the synthetic target outputs. We hence use these parameter values on our real cost function.

6.2.3 Results

We have proposed a set of candidate models and investigated whether any of these models can reproduce the experimental observations by Kim et al. (2013). By carrying out steady state analyses and exploring the output of the models numerically using the CMA-ES technique, we have established whether we can find a feasible set of parameter values for each model. Table 6.6 summarises these results.

First we reject candidate models M_{11} and M_{21} on the basis of the steady state analysis in Section 6.2.2.6. Kim et al. (2013) observe an increase in levels of Axin/β-catenin complex (see Figure 6.4). The total levels of β-catenin/Axin complex in candidate models M_{11} and M_{21} is represented by D (see Table 6.4), which has a steady state value that

is independent of Wnt (see equation (6.21). Consequently, we can dismiss candidate models M_{11} and M_{21}.

Candidate Model	Wnt Dependent Reactions	A_p binds to L_p	D binds to L_p	A_p and D bind to L_p at the same rate	% optimisation runs with good qualitative fit	Method
M_{11}	LRP6 phosphorylation	✓	✗	-	✗	Steady state analysis
M_{12}	LRP6 phosphorylation	✗	✓	-	✗	Numerical
M_{13}	LRP6 phosphorylation	✓	✓	✓	3.5%	Numerical
M_{21}	LRP6 phosphorylation and Axin/LRP6 release	✓	✗	-	✗	Steady state analysis
M_{22}	LRP6 phosphorylation and Axin/LRP6 release	✗	✓	-	✗	Numerical
M_{23}	LRP6 phosphorylation and Axin/LRP6 release	✓	✓	✓	4.4%	Numerical

TABLE 6.6: Candidate models of the canonical Wnt pathway considered in this section and whether or not they match experimental observations by Kim et al. (2013). We also name the method used to establish whether they can reproduce the experimental observations.

For the other candidate models, we use the multi-start CMA-ES algorithm to establish if they can reproduce observations by Kim et al. (2013). We failed to find any such fits for candidate models M_{12} and M_{22}, but we could find suitable parameter values for candidate models M_{13} and M_{23}. We find 4 feasible parameter sets for candidate model M_{13}, and 5 feasible parameter sets for model M_{23} (these parameter values are presented in Appendix D). Figure 6.6 displays the model outputs for some of the parameter sets found.

We note that M_{13} and M_{23} are nested, with M_{13} a simpler version of candidate model M_{23}. Assuming both models pass further tests as defined by our model selection framework, we preferentially select candidate model M_{13} as it has only one Wnt dependent reaction rather than two. However, we note that we extend both of these models in the next section where continue our analysis of the Wnt pathway.

6.2.3.1 Sensitivity analysis

We have established that model M_{13} is the simplest candidate model that reproduces the experimental observations of Kim et al. (2013). As described in Chapter 4, Goentoro and Kirschner (2009) show that the fold change in total levels of β-catenin upon Wnt stimulation is robust to perturbation in Wnt pathway machinery in the first few hours after Wnt stimulation.

As in Chapter 4, we recruit control coefficients to calculate the robustness of fold change in total levels of β-catenin for different candidate model and parameter sets. For each candidate model and feasible parameter set, we perturb each reaction rate locally and measure the fold change in total levels of β-catenin upon Wnt stimulation

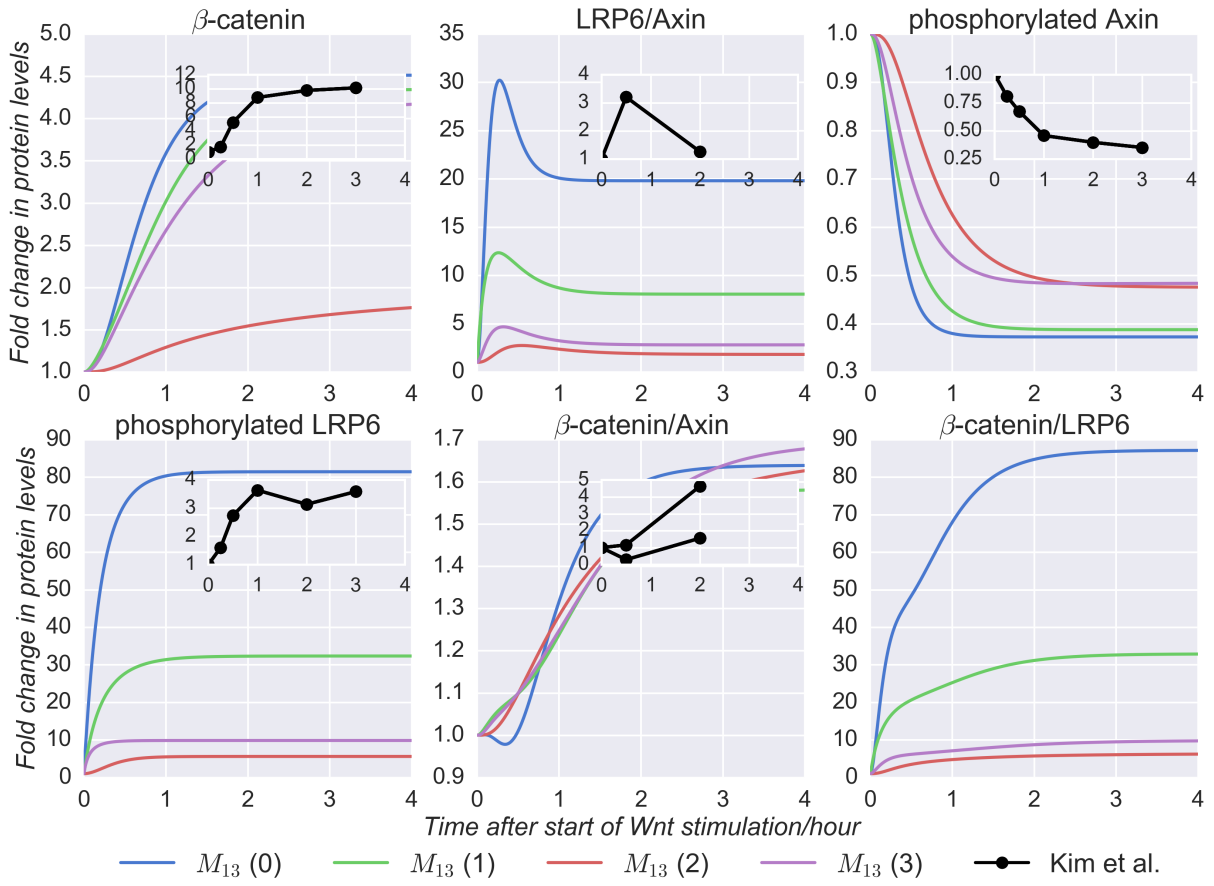


FIGURE 6.6: Typical output of candidate models M_{13} and M_{23} for some feasible parameter sets found as suitable fits to experimental results by Kim et al. (2013). The inset in each plot shows the equivalent experimental observation by Kim et al. (2013).

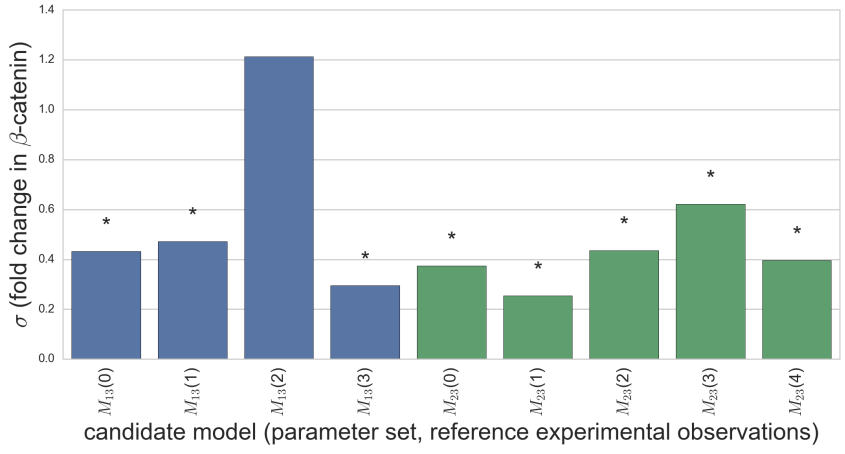


FIGURE 6.7: Standard deviation of control coefficients corresponding to fold change in total levels of β-catenin for the candidate models and parameter sets. Each bar corresponds to one candidate model and parameter set combination. Lower values of the standard deviation corresponds to a system that is more robust to perturbations in the values of rate parameters. * above the bar marks models and parameter combinations with a standard deviation of less than 1.

over 4 hours. We use the standard deviation σ^X of all control coefficients, where X is a model output, to calculate a measure of system robustness to variation in all model parameters. A high value of σ^X indicates that the given model output $X = B + D + E$ is on average very sensitive to changes in reaction rates. Figure 6.7 shows how the standard deviation of control coefficients, σ^X for the two remaining candidate models M_{13} and M_{23} and feasible parameter sets. We observe that for several parameter sets fold changes in β-catenin are robust to local variations in rate parameters.

6.2.3.2 *in silico* experiments

In addition to studying the cell's response to Wnt, Kim et al. (2013) also studied its response to various other stimuli. We analyse the candidate models and feasible parameter sets to investigate whether they can reproduce other experimental observations by Kim et al. (2013) (see Section 4.3.2 of Chapter 4 for a detailed description).

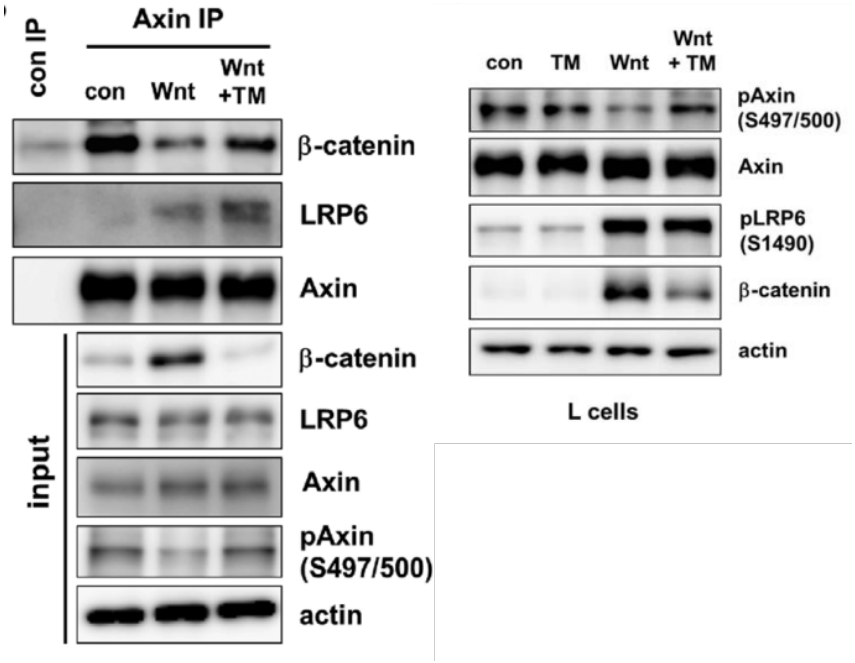


FIGURE 6.8: Kim et al. (2013) stimulate L cells with Wnt and/or the PP1 inhibitor, Tautomycin (TM). They measure levels of various proteins in complex with Axin after 30 minutes (left), and levels of various proteins after 2 hours (right) *in vitro*. We present the results from similar *in silico* experiments performed on each candidate model in Figure 6.9.

In particular, Kim et al. (2013) stimulated L cells with the PP1 inhibitor, Tautomycin (TM), and/or Wnt. Their results are presented in Figure 6.8 and can be summarised as follows

- Levels of the Axin/LRP6 complex are higher after stimulation with Wnt and TM, compared to Wnt alone.
- Unlike with Wnt stimulation alone, levels of pS497/500 Axin do not fall upon stimulation with TM, or Wnt and TM combined.
- The increase in levels of pS1490 LRP6 on stimulation with Wnt is similar to that for stimulation with Wnt and TM.
- Levels of β-catenin do not increase upon stimulation with Wnt and TM, whereas they increase with Wnt alone.

- Levels of β-catenin in complex with Axin after stimulation with Wnt and TM are higher than levels after stimulation with Wnt alone.

We do not re-run the CMA-ES optimisation algorithm to study whether the candidate models can describe these new experimental observations. Instead, we start with the feasible parameter sets found earlier and assume that stimulation with the phosphatase inhibitor TM reduces the rate of Wnt-driven Axin dephosphorylation by $90\% \pm 10\%$ on a relative basis. Since we do not explicitly model dephosphorylation of Axin after recruitment to LRP6, we assume that TM reduces the rate of release of Axin from LRP6 (i.e. rate parameter k_{-4}). Figure 6.9 summarise the results of these *in silico* experiments.

Three parameter sets under candidate models M_{13} and two under candidate model M_{23} are able to reproduce the experimental observations by Kim et al. (2013) involving Wnt and TM.

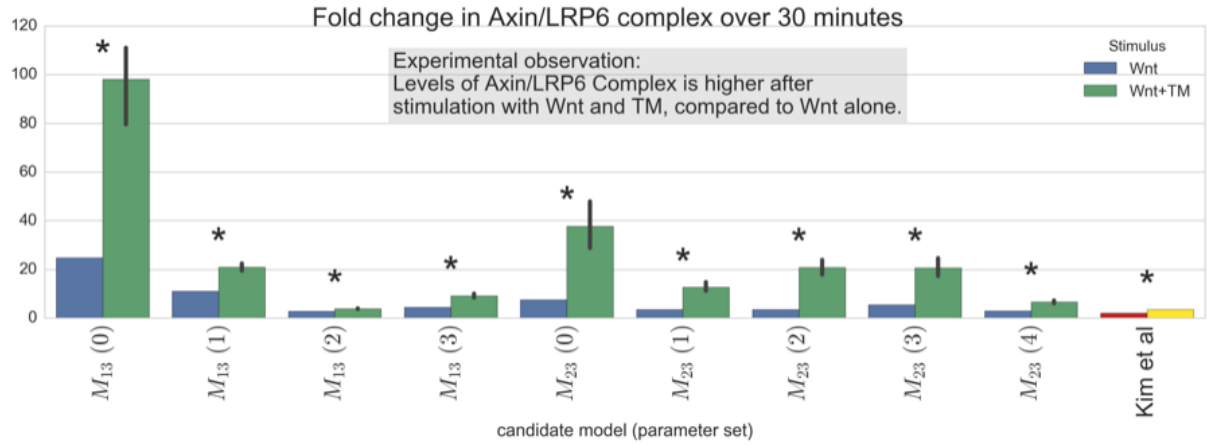
6.2.3.3 Summary so far

In this section we have proposed a set of candidate models to help us understand how Wnt stimulation leads to the observed dynamics involving some of the core components of the Wnt pathway including Axin, LRP6 and β-catenin. Using the framework introduced in Chapter 4 applied to *in vitro* experiments by Kim et al. (2013), we were able to reduce the number of candidate models from 6 to 2.

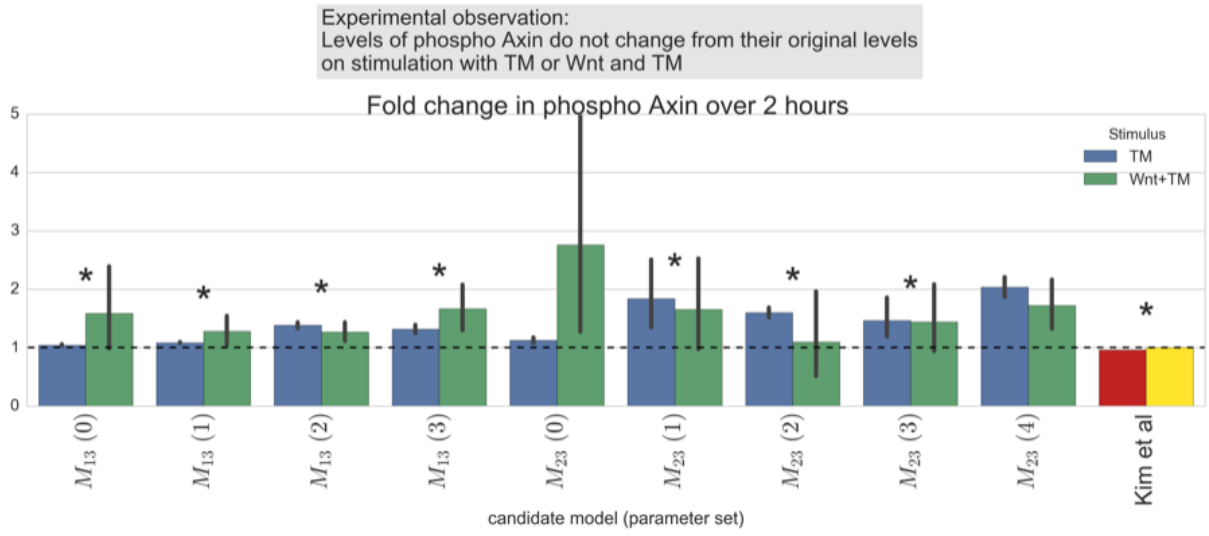
We were able to find several feasible set of parameter values for each candidate model using the CMA-ES technique. We confirmed that fold change in levels of β-catenin was robust to changes in rate parameters for all but one of these parameter sets. By carrying out further *in silico* experiments, we showed that these two candidate models can describe further *in vitro* observations. These results combined confirmed the suitability of these candidate models. Since candidate models M_{13} and M_{23} have the same biochemical reactions, with the latter model having one extra Wnt dependent reaction rate (k_{-4}), we reject candidate model M_{23} and select M_{13} as the most suitable candidate model.

Our results suggest that recruitment of Axin with and without β-catenin and accumulation of β-catenin at the cell membrane in the LRP6 signalosome (as in candidate models M_{13} and M_{23}) is important in describing the observing the dynamics between LRP6, Axin and β-catenin. According to candidate model M_{13}, an increase in the rate of LRP6 phosphorylation upon Wnt stimulation is sufficient to describe these observed dynamics.

So far we have focused on using our candidate models to reproduce the experimental observations by Kim et al. (2013). In the next section, we will extend our candidate models further by including more details about the destruction complex in each candidate model. This enables us to compare our candidate models with experimental observations reported by Li et al. (2012) and Azzolin et al. (2014). In particular we aim to determine wherther one unifying mathematical model of the canonical Wnt pathway can describe all of the different experimental observations.

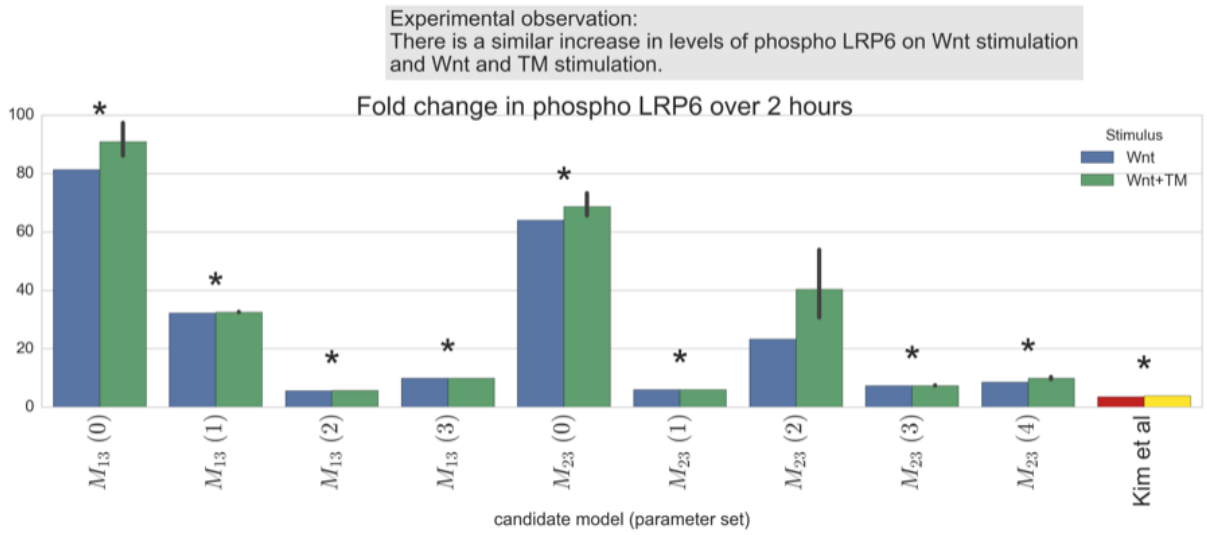


(A)

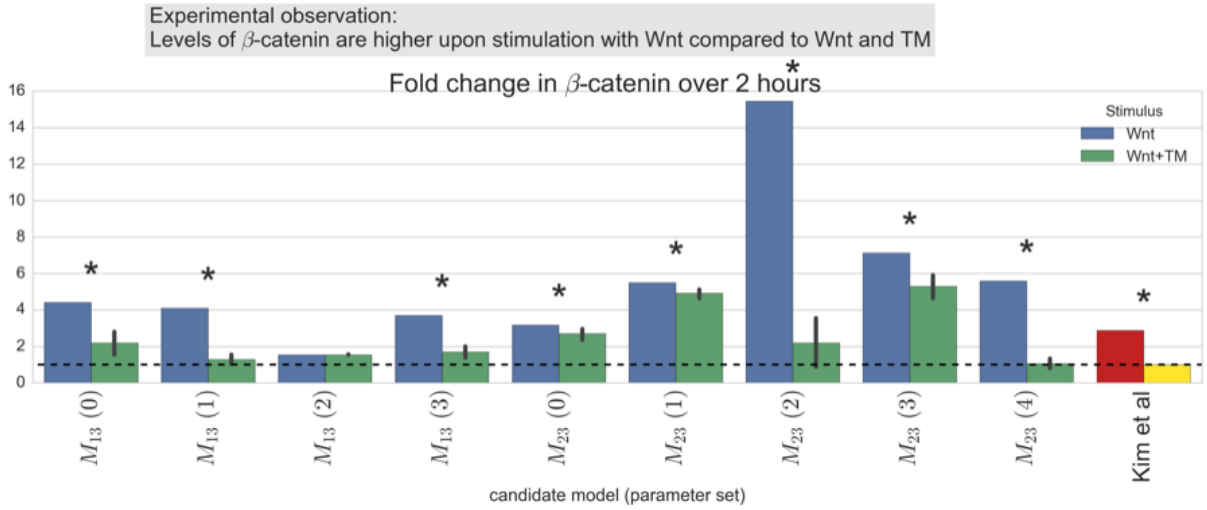


(B)

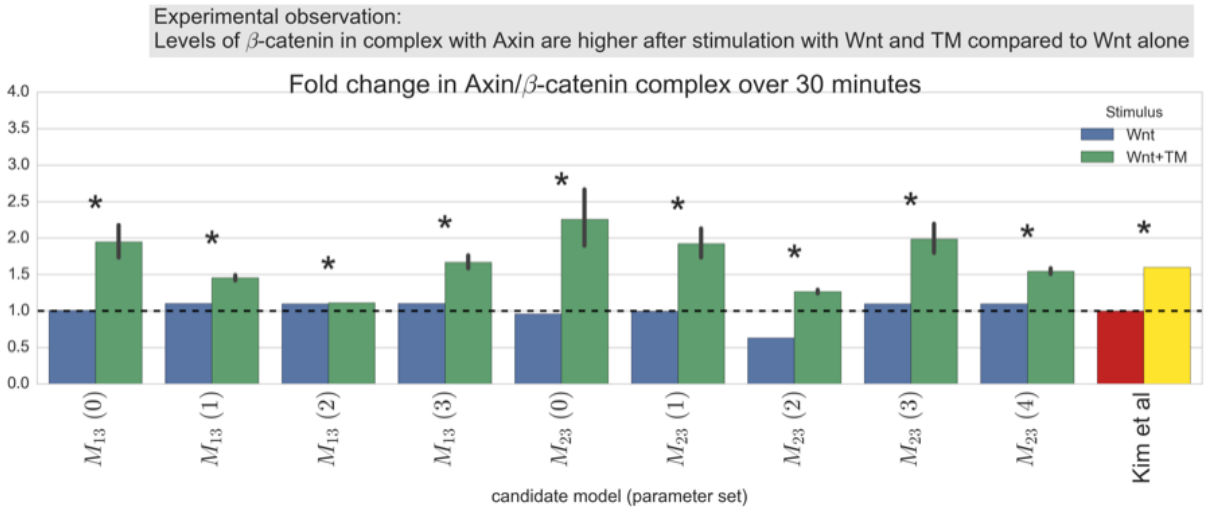
FIGURE 6.9: Results of *in silico* experiments using candidate models M_{13} and M_{23}. The bars displayed on right hand side depict quantification of the equivalent *in vitro* experiments by Kim et al. (2013). Starting from a "Wnt-off" steady state, we solve each model numerically using the parameter values found earlier. We assume that stimulation with the phosphatase inhibitor TM reduces the reaction rate k_{-4} by $90\% \pm 10\%$ on a relative basis. Black lines above each bar represent a one standard deviation confidence interval. We perturb our candidate models with TM alone, with Wnt alone, or with Wnt and TM for 30 minutes or 2 hours, before measuring the fold change in protein concentrations. * above each bar marks model and parameter sets that are consistent with *in vitro* experimental observations (Figure continues onto the next page).


Experimental observation:
There is a similar increase in levels of phospho LRP6 on Wnt stimulation and Wnt and TM stimulation.
Fold change in phospho LRP6 over 2 hours
Stimulus
Wnt
Wnt+TM
100
80
60
40
20
0
M_{13} (0)
M_{13} (1)
M_{13} (2)
M_{13} (3)
M_{23} (0)
M_{23} (1)
M_{23} (2)
M_{23} (3)
M_{23} (4)
Kim et al
candidate model (parameter set)

(C)


Experimental observation:
Levels of β-catenin are higher upon stimulation with Wnt compared to Wnt and TM
Fold change in β-catenin over 2 hours
Stimulus
Wnt
Wnt+TM
16
14
12
10
8
6
4
2
0
M_{13} (0)
M_{13} (1)
M_{13} (2)
M_{13} (3)
M_{23} (0)
M_{23} (1)
M_{23} (2)
M_{23} (3)
M_{23} (4)
Kim et al
candidate model (parameter set)

(D)


Experimental observation:
Levels of β-catenin in complex with Axin are higher after stimulation with Wnt and TM compared to Wnt alone
Fold change in Axin/β-catenin complex over 30 minutes
Stimulus
Wnt
Wnt+TM
4.0
3.5
3.0
2.5
2.0
1.5
1.0
0.5
0.0
M_{13} (0)
M_{13} (1)
M_{13} (2)
M_{13} (3)
M_{23} (0)
M_{23} (1)
M_{23} (2)
M_{23} (3)
M_{23} (4)
Kim et al
candidate model (parameter set)

(E)

6.3 Extension 2: β-catenin modifications in the destruction complex

6.3.1 Introduction

As summarised in Section 6.2.3.3, we established using our framework that the most suitable model for reproducing the observations by Kim et al. (2013) is model M_{13} where

- pS497/500 Axin is recruited to pS1490 LRP6 independently of whether or not it is in complex with β-catenin,
- The rate of recruitment and release of Axin to LRP6 are independent of whether or not β-catenin is in complex with phosphorylated Axin,
- Wnt acts on only one reaction in the model; it increases the rate of phosphorylation of LRP6.

We now extend the candidate models from the last section to include the steps that β-catenin goes through following recruitment to the destruction complex. This will enable us to compare the candidate models against experimental observations by Azzolin et al. (2014), Li et al. (2012), and Kim et al. (2013).

In the next section we describe the new candidate models we study and introduce the three sets of experimental observations we aim to reproduce. We then explain the parameter value and cost function used for the CMA-ES technique. In the Results section we give the results of model selection. Finally, we use our new candidate models to carry out further *in silico* experiments. We compare the results of these experiments with *in vitro* experiments to provide further information about the Wnt pathway.

6.3.2 Methods

Rather than repeating the details of our model selection framework here, we simply provide the new qualitative and mathematical description of our new candidate models, the new experimental observations and explain any aspects that are different from Section 6.2.2 (see Sections 4.2 and 6.2.2 for further details).

6.3.2.1 Qualitative description of our mathematical models

β-catenin undergoes three well characterised modifications after recruitment to the destruction complex. It is phosphorylated by CK1 at the S45 residue. This primes it for phosphorylation at the T41, S33 and S37 residues by GSK3. β-catenin phosphorylated at S33 and S37 is recognised by the β-TrCP subunit of Skp1/Cul1/F-box/β-TrCP E3 ubiquitin ligase, which marks it for ubiquitination and degradation.

In this extension, we ignore phosphorylation of β-catenin by CK1. We include the GSK3 phosphorylation step only as it is observed that LRP6 phosphorylated at PPPSP motifs can directly inhibit GSK3 activity.

Our candidate models now contain up to ten species. Eight of these species were introduced in models M_{xy}: A_u, A_p, L_u, L_p, B, C, D and E. The new species are D_p, which corresponds to the complex of pS497/500 Axin and pS33/S37/T41 β-catenin, and E_p, which is the complex of pS1490 LRP6, pS497/500 Axin and pS33/S37/T41 β-catenin. Table 6.7 summarises the ten dependent variables.

We do not explicitly model ubiquitination of β-catenin in our models and simply assume instead that β-catenin may be degraded after phosphorylation by GSK3 while in complex with Axin (Li et al., 2012). Since in the last section we established that the most suitable candidate models were ones where both A_p and D are recruited to L_p, we assume A_p, D and D_p may be recruited to pS1490 LRP6. We also investigate whether simpler models where only A_p and D bind to L_p can reproduce the experimental observations.

The reactions describing the new candidate models are:

$$R_1: \quad \mathrm{A_u} \underset{k_{-1}}{\overset{k_1}{\rightleftharpoons}} \mathrm{A_p}, \tag{6.30}$$

$$R_2: \quad \mathrm{L_u} \underset{k_{-2}}{\overset{k_2(w)}{\rightleftharpoons}} \mathrm{L_p}, \tag{6.31}$$

$$R_{3A}: \quad \mathrm{A_p} + \mathrm{L_p} \underset{k_{-3}}{\overset{k_3}{\rightleftharpoons}} \mathrm{C}, \tag{6.32}$$

$$R_{4A}: \quad \mathrm{C} \xrightarrow{k_{-4}(w)} \mathrm{A_u} + \mathrm{L_p}, \tag{6.33}$$

$$R_s: \quad \emptyset \xrightarrow{s} \mathrm{B}, \tag{6.34}$$

$$R_5: \quad \mathrm{A_p} + \mathrm{B} \underset{k_{-5}}{\overset{k_5}{\rightleftharpoons}} \mathrm{D}, \tag{6.35}$$

$$R_6: \quad \mathrm{D} \underset{k_{-6}}{\overset{k_6}{\rightleftharpoons}} \mathrm{D_p}, \tag{6.36}$$

$$R_d: \quad \mathrm{D_p} \xrightarrow{d} \mathrm{A_p} + \emptyset, \tag{6.37}$$

$$R_{3B}: \quad \mathrm{D} + \mathrm{L_p} \underset{k_{-3}}{\overset{k_3}{\rightleftharpoons}} \mathrm{E}, \tag{6.38}$$

$$R_{4B}: \quad \mathrm{E} \xrightarrow{k_{-4}(w)} \mathrm{A_u} + \mathrm{L_p} + \mathrm{B}, \tag{6.39}$$

$$R_{3C}: \quad \mathrm{D_p} + \mathrm{L_p} \underset{k^*_{-3}}{\overset{k^*_3}{\rightleftharpoons}} \mathrm{E_p}, \tag{6.40}$$

and finally

$$R_{4C}: \quad \mathrm{E_p} \xrightarrow{k^*_{-4}(w)} \mathrm{A_u} + \mathrm{L_p} + \mathrm{B}, \tag{6.41}$$

or

$$R'_{4C}: \quad \mathrm{E_p} \xrightarrow{k^{**}_{-4}(w)} \mathrm{A_u} + \mathrm{L_p} + \emptyset. \tag{6.42}$$

It has been observed that pS33/S37/T41 β-catenin not protected by the destruction complex component APC is quickly dephosphorylated (Su et al., 2008). However, pS33/S37/T41 β-catenin may also be degraded if it has been ubiquitinated (Stamos and Weis, 2013). So under different candidate models whether pS33/S37/T41 β-catenin in the LRP6 signalosome is (1) degraded or (2) dephosphorylated upon its release. These two hypotheses are captured by Reactions R_{4C} and R'_{4C}.

6.3.2.2 Candidate models

We use notation N_{xy} where x and y are positive integers to refer to different candidate models. The subscript $x = 1, 2$ indicates which reactions are altered by Wnt, whereas subscript $y = 1, 2, 3$ indicates different candidate structures (see Figure 6.10):

- **x=1:** LRP6 phosphorylation (k_2),

Dependent Variable	Description
A_u	Concentration of Axin not phosphorylated at S497/S500
A_p	Concentration of Axin phosphorylated at S497/S500
L_u	Concentration of LRP6 not phosphorylated at S1490
L_p	Concentration of LRP6 phosphorylated at S1490
B	Concentration of β-catenin
B_p	Concentration of pS33/S37/T41 β-catenin (NOTE: appears only in complex with A_p and not as an independently.)
$C \equiv [A_p : L_p]$	Concentration of Complex of L_p and A_p
$D \equiv [A_p : B]$	Concentration of Complex of B and A_p
$D_p \equiv [A_p : B_p]$	Concentration of Complex of A_p and B_p
$E \equiv [A_p : L_p : B]$	Concentration of Complex of B, A_p and L_p
$E_p \equiv [A_p : L_p : B_p]$	Concentration of Complex of A_p and L_p and B_p

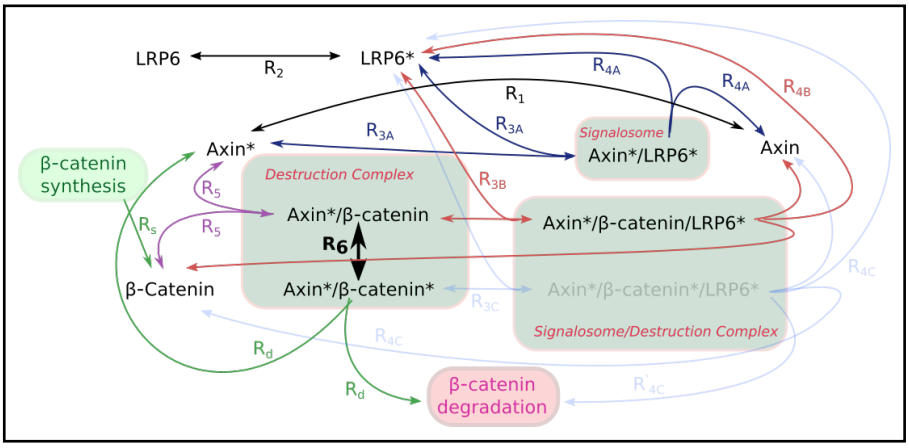
TABLE 6.7: Dependent variables used in our candidate mathematical models.

- **x=2:** LRP6 phosphorylation (k_2) and release of Axin from LRP6 (k_{-4}, k^*_{-4}),
- **y=1:** LRP6 recruits A_p and D only, i.e. D_p is not recruited to LRP6: $k^*_{\pm 3} = k^*_{-4} = k^{**}_{-4} = 0$ (see Figure 6.10A).
- **y=2:** LRP6 recruits the destruction complex in all forms (A_p, D and D_p) and at the same rate. When E_p breaks into its constituent parts via Reaction R_{4C}, pS33/S37/T41 β-catenin is quickly dephosphorylated: $k^*_{\pm 3} = k_{\pm 3}$, $k^*_{-4} = k_{-4}$, $k^{**}_{-4} = 0$ (see Figure 6.10B).
- **y=3:** LRP6 recruits the destruction complex in all forms (A_p, D and D_p) and at the same rate. When E_p breaks into its constituent parts via Reaction R'_{4C}, pS33/S37/T41 β-catenin is degraded: $k^*_{\pm 3} = k_{\pm 3}$, $k^*_{-4} = 0$, $k^{**}_{-4} = k_{-4}$ (see Figure 6.10C).

Candidate Model	Wnt Dependent Reactions	A_p binds to L_p	D binds to L_p	D_p binds to L_p	Fate of pS33/S37/T41 β-catenin upon release from LRP6	Dependent Variables	Rate Parameters
N_{11}	LRP6 phosphorylation	✓	✓	✗	-	9	13
N_{12}	LRP6 phosphorylation	✓	✓	✓	dephosphorylated	10	13
N_{13}	LRP6 phosphorylation	✓	✓	✓	degraded	10	13
N_{21}	LRP6 phosphorylation and Axin/LRP6 release	✓	✓	✗	-	9	13
N_{22}	LRP6 phosphorylation and Axin/LRP6 release	✓	✓	✓	dephosphorylated	10	13
N_{23}	LRP6 phosphorylation and Axin/LRP6 release	✓	✓	✓	degraded	10	13

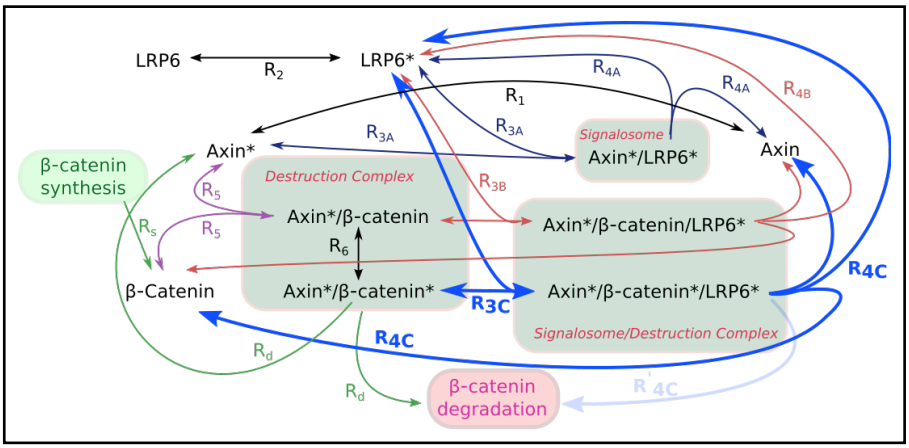
TABLE 6.8: Summary of the differences between candidate models N_{xy}.

Candidate models N_{x1}: An extension to the candidate models M_{x3} (Figure 6.2C), the destruction complex now includes phosphorylation of β-catenin via Reaction R_6.



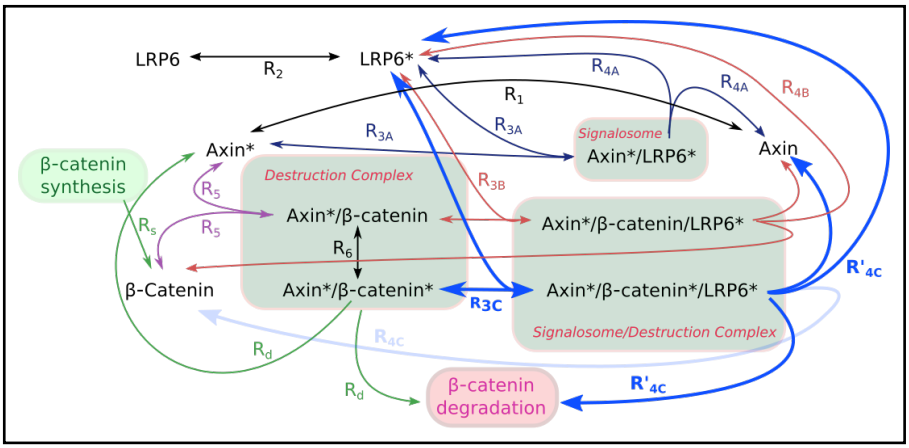
(A)

Candidate models N_{x2}: D_p may also be recruited to LRP6. Upon break up of the signalosome E_p, pS33/S37/T41 β-catenin is quickly dephosphorylated.



(B)

Candidate models N_{x3}: D_p may also be recruited to LRP6. Upon break up of the signalosome E_p, pS33/S37/T41 β-catenin is degraded.



(C)

FIGURE 6.10: Series of schematics showing the structure of different candidate mathematical models of the canonical Wnt pathway: (A) N_{x1}, (B) N_{x2}, and (C) N_{x3} (see Section 6.3.2.2 for details).

6.3.2.3 Mathematical representation of our candidate models

As before, we can derive a time dependent system of ODEs to represent our candidate models:

$$\frac{\mathrm{d}B}{\mathrm{d}t} = r_s - r_{4b} + \hat{r_{4c}} - r_5, \tag{6.43}$$

$$\frac{\mathrm{d}A_u}{\mathrm{d}t} = -r_1 + r_{4a} + r_{4b} + r_{4c}, \tag{6.44}$$

$$\frac{\mathrm{d}A_p}{\mathrm{d}t} = r_d + r_1 - r_{3a} - r_5, \tag{6.45}$$

$$\frac{\mathrm{d}L_u}{\mathrm{d}t} = -r_2, \tag{6.46}$$

$$\frac{\mathrm{d}L_p}{\mathrm{d}t} = r_2 - r_{3a} - r_{3b} - r_{3c} + r_{4a} + r_{4b} + r_{4c} \tag{6.47}$$

$$\frac{\mathrm{d}C}{\mathrm{d}t} = +r_{3a} - r_{4a}, \tag{6.48}$$

$$\frac{\mathrm{d}D}{\mathrm{d}t} = -r_{3b} + r_5 - r_6, \tag{6.49}$$

$$\frac{\mathrm{d}D_p}{\mathrm{d}t} = -r_d - r_{3c} + r_6, \tag{6.50}$$

$$\frac{\mathrm{d}E}{\mathrm{d}t} = +r_{3b} - r_{4b}, \tag{6.51}$$

$$\frac{\mathrm{d}E_p}{\mathrm{d}t} = +r_{3c} - r_{4c}, \tag{6.52}$$

where

$$\begin{aligned}
R_1 &: \quad r_1 = k_1 A_u - k_{-1} A_p, \\
R_2 &: \quad r_2 = k_2(w) L_u - k_{-2} L_p, \\
R_{3A} &: \quad r_{3a} = k_3 A_p L_p - k_{-3} C, \\
R_{3B} &: \quad r_{3b} = k_3 D L_p - k_{-3} E, \\
R_{3C} &: \quad r_{3c} = \begin{cases} 0 & \text{for } N_{x1}, \\ = k_3^* D_p L_p - k_{-3}^* E_p & \text{for } N_{x2} \text{ and } N_{x3}, \end{cases} \\
R_{4A} &: \quad r_{4a} = k_{-4}(w) C, \\
R_{4B} &: \quad r_{4b} = k_{-4}(w) E, \\
R_{4C} &: \quad r_{4c} = \begin{cases} 0 & \text{for } N_{x1}, \\ k_{-4}^*(w) E_p & \text{for } N_{x2} \text{ and } N_{x3}, \end{cases} \\
R'_{4C} &: \quad \hat{r_{4c}} = \begin{cases} 0 & \text{for } N_{x1}, N_{x3}, \\ k_{-4}^{**}(w) E_p & \text{for } N_{x2}, \end{cases} \\
R_s &: \quad r_s = s, \\
R_d &: \quad r_d = d D_p, \\
R_5 &: \quad r_5 = k_5 A_p B - k_{-5} D, \\
R_6 &: \quad r_6 = k_6 D - k_{-6} D_p.
\end{aligned}$$

As before, we impose initial conditions in the "Wnt-off" simulation for which all dependent variables are zero except $L_u(t=0) = L_{\text{tot}}$ and $A_p(t=0) = A_{\text{tot}}$, where L_{tot} and A_{tot} represent the total levels of LRP6 and Axin.

parameter	Description	Unit
$k_{\pm 1}$	Rate of Axin phosphorylation/dephosphorylation	min^{-1}
$k_{\pm 2}$	Rate of LRP6 phosphorylation/dephosphorylation	min^{-1}
$k_{\pm 3}$	Rate of association/dissociation of Axin and LRP6	$\mathrm{min}^{-1}\mathrm{nM}^{-1}$
$k^*_{\pm 3}$	Rate of association/dissociation of Axin/pS33/S37/T41 β-catenin complex and LRP6	$\mathrm{min}^{-1}\mathrm{nM}^{-1}$
k_{-4}	Rate of release of unphosphorylated Axin from Axin/LRP6 complex	min^{-1}
k^*_{-4}, k^{**}_{-4}	Rate of release of unphosphorylated Axin from Axin/LRP6/pS33/S37/T41 β-catenin complex	min^{-1}
s	Rate of synthesis of β-catenin	nMmin^{-1}
d	Rate of degradation of β-catenin via the destruction complex	min^{-1}
$k_{\pm 5}$	Rate of association/dissociation of β-catenin and phosphorylated Axin	$\mathrm{min}^{-1}\mathrm{nM}^{-1}$
$k_{\pm 6}$	Rate of phosphorylation/dephosphorylation of β-catenin	min^{-1}
A_{tot}, L_{tot}	Total Axin and LRP6	nM
w_3, w_{-4}	Wnt multiplier	-
τ	Time constant	-

TABLE 6.9: Parameters used in our mathematical models N_{xy}. We note that parameter values $k^*_{\pm i}$ and $k^{**}_{\pm i}$ are either zero or fixed at the same values as the non-*'ed values.

Summing up the appropriate combinations of Equations (6.44)-(6.52) yields the following identities for conservation of total levels of Axin and LRP6:

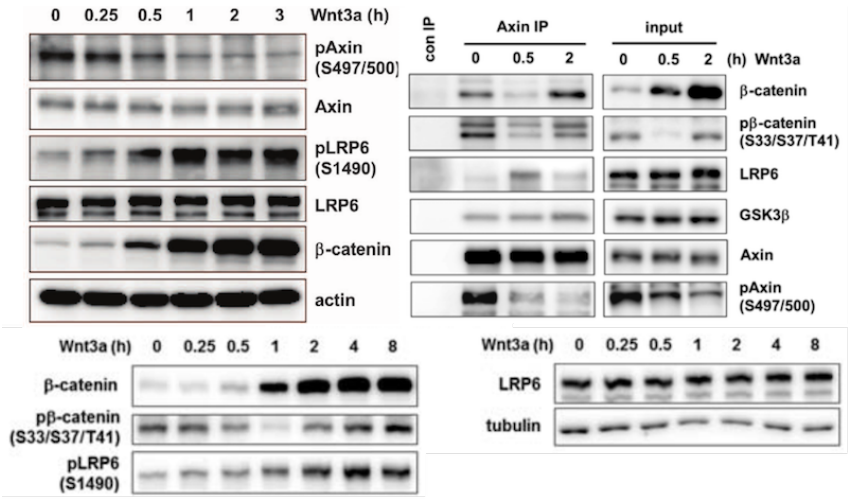
$$A_{\mathrm{tot}} = A_u + A_p + C + D + D_p + E + E_p, \tag{6.53}$$
$$L_{\mathrm{tot}} = L_u + L_p + C + E + E_p, \tag{6.54}$$

which may be used to reduce the number of species in our candidate models by two. We also represent the effect of Wnt in our models in the same form as before using a time-dependent function (see Section 4.2.1.1 in Chapter 4). Tables 6.7 and 6.9 summarise the dependent variables and parameters used in our candidate models.

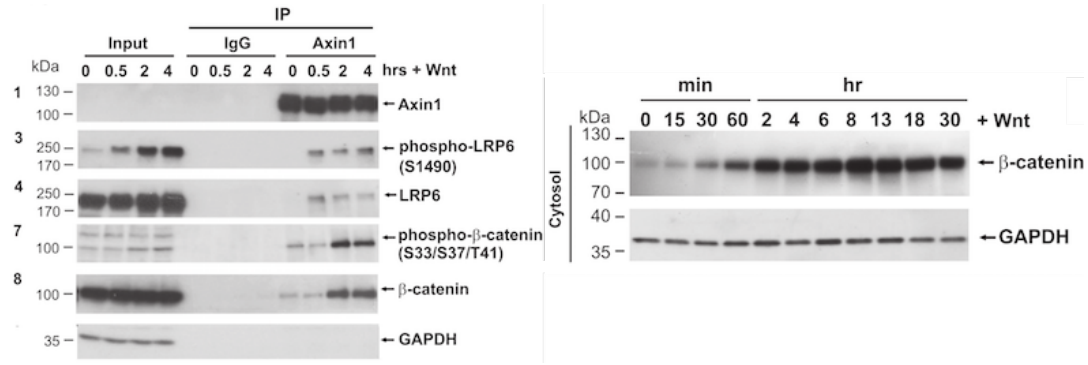
6.3.2.4 Experimental observations

With a set of candidate models that provide a more detailed description of the Wnt pathway we may investigate whether a single model can reproduce the observations of Kim et al. (2013), Li et al. (2012) and Azzolin et al. (2014). In Figure 6.12 we present the quantification of Western blots from these three studies (the actual blots are displayed in Figure 6.11). For example, we note very different behaviours for how the levels of β-catenin in complex with Axin change upon Wnt stimulation. The differences between these observations have led the authors to propose different verbal models of the Wnt pathway. Table 6.11 summarises the equivalent model output that should be compared with the experimental observations.

Notes on results of Kim et al. (2013). Apart from differences in the changes in levels of β-catenin/Axin complex upon Wnt stimulation for different cell lines, the Kim et al. (2013) results are consistent across different cell lines. The other difference of note



(A) Kim et al. (2013)



(B) Li et al. (2012)



(C) Azzolin et al. (2014)

FIGURE 6.11: Western blots from (A) Kim et al. (2013), (B) Li et al. (2012) and (C) Azzolin et al. (2014), to which we fit our candidate model. Table 6.10 summarises the results we extract from these blots qualitatively. Actin, Tubulin and GAPDH are used as loading control and we adjust the quantification results based on the levels of these proteins. We also note that we do not explicitly model GSK3, β-TrCP, YAP or TAZ in our candidate models. All reproduced with permission.

	Kim et al. (2013)	**Li et al. (2012)**	**Azzolin et al. (2014)**
Cell line	HEK293T, L-cells, RKO	HEK293T	HEK293T, P19
LRP6 phosphorylated at S1490	Levels increase monotonically.	Levels increase monotonically.	-
Axin phosphorylated at S497/S500	Levels fall monotonically.	-	-
Axin/LRP6 Complex	Increase within half an hour, before dropping to original levels within 2 hours.	Increase within half an hour before dropping to levels higher than original level.	Increase monotonically.
Axin/pS1490 LRP6 complex	-	Increases [see comment in text].	-
Axin/β-catenin complex	Increase monotonically in HEK293T cells or drop in the first half hour before increasing to levels above the original levels in L-cells.	Drop in the first half hour before increasing to levels above the original levels.	Either drop monotonically (P19 cells), or stay the same or increase (HEK293T cells) [see comment in text].
Axin/active β-catenin complex	-	-	fall.
Axin/β-catenin phosphorylated at T41/S33/S37	Fall before returning to original levels.	Fall in the first half hour before increasing to levels above the original levels.	-
β-catenin	Increase monotonically.	Increase monotonically [see comment in text].	Increase monotonically.

TABLE 6.10: Summary of the experimental observations used to explore our candidate mathematical models of the canonical Wnt pathway.

Candidate Model	N_{x1}	N_{x2}, N_{x3}
Total pS497/500 Axin	$A_p + C + D + D_p + E$	$A_p + C + D + D_p + E + E_p$
Total pS1490 LRP6	$L_p + C + E$	$L_p + E + E_p$
Total Axin/ β-catenin	$D + D_p + E$	$D + D_p + E + E_p$
Total β-catenin	$B + D + D_p + E$	$B + D + D_p + E + E_p$
Total active β-catenin	$D + E$	$D + E$
total pS33/S37/T41 β-catenin	D_p	$D_p + E_p$

TABLE 6.11: Summary of the combinations of dependent variables needed for comparison of the candidate model outputs to experimental observations.

between results across different cell lines was how quickly the cells respond to Wnt stimulation (Figure S5 in the original paper).

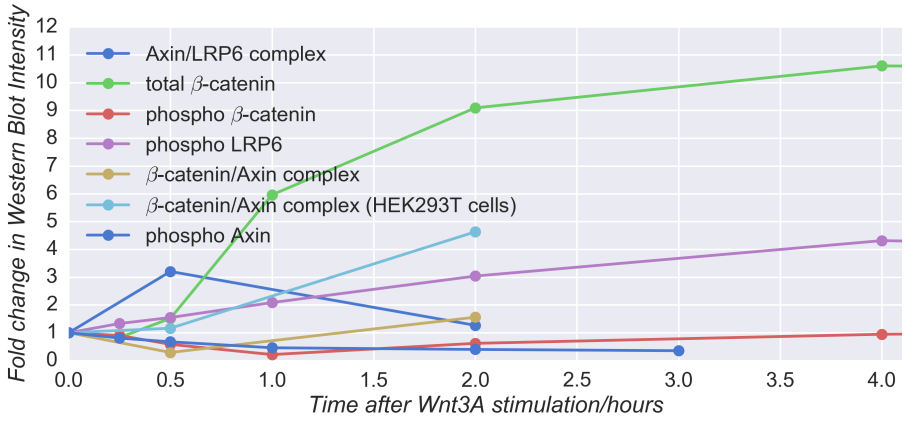
Notes on the results of Li et al. (2012). The authors measured levels of Axin/LRP6 and Axin/pS1490 LRP6 after Wnt stimulation. Since in our candidate models N_{xy} we ignore all Axin/LRP6 complexes apart from pS497/500 Axin/pS1490 LRP6 complex, we ignore the Axin/LRP6 results and base our fitting on Axin/pS1490 LRP6 complex levels only.

Another issue with Li et al. (2012) results is the absence of protein in the inputs of some of the co-IP's (e.g. Figure 2A in the original paper). Moreover, a slight drop in the levels of β-catenin is observed after 15 minutes of Wnt stimulation (Figure 1A in the original paper), however, we speculate that this may be due to limitations of Western blots rather than a real phenomenon.

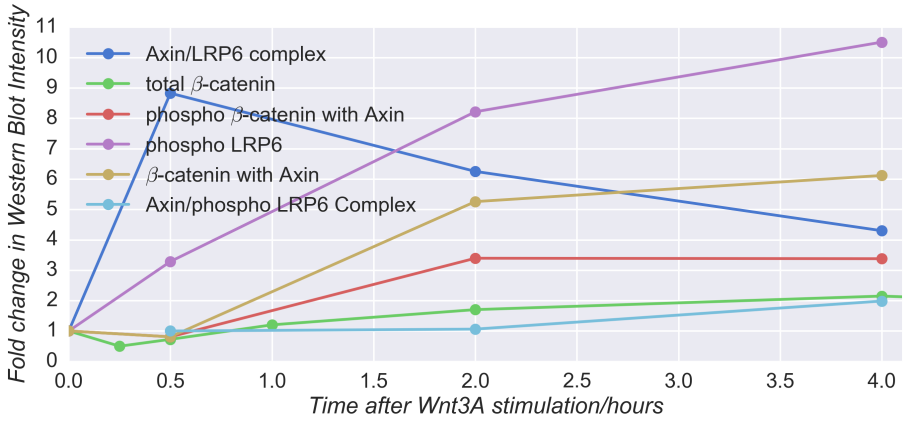
Notes on the results of Azzolin et al. (2014). Interestingly, the authors observe that β-catenin in complex with Axin:

- increases in HEK293T cells (Figure 5 in the original paper),
- stays the same in HEK293T cells (Figure 4 in the original paper),
- falls in P19 cells (Figure S2 in the original paper).

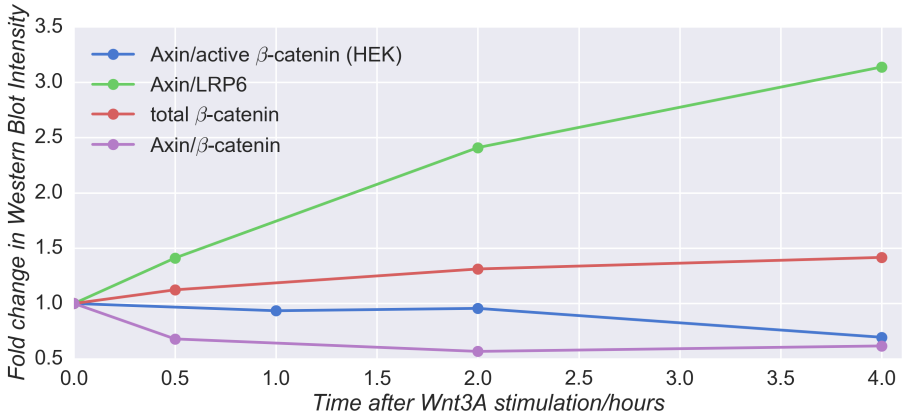
They observe a fall in levels of active β-catenin (i.e. β-catenin not phosphorylated at T41/S33/S37 by GSK3) in complex with Axin in both HEK293T cells (Figure 4 in the original paper) and P19 cells (Figure S2 in the original paper). The authors do not comment on these differences as these particular results are not relevant to their conclusions. For our study we assume that total levels of β-catenin in complex with Axin drop in line with levels of active β-catenin in complex with Axin.



(A) Kim et al. (2013)



(B) Li et al. (2012)



(C) Azzolin et al. (2014)

FIGURE 6.12: Quantification of typical blots from: (A) Kim et al. (2013) in L-cells (B) Li et al. (2012) in HEK293T cells and (C) Azzolin et al. (2014) in P19 cells. Table 6.10 summarises these observations. Since Li et al. (2012) detect little Axin in complex with pS1490 LRP6 at time $t = 0$, we normalise these levels from the second time point.

6.3.2.5 Steady state analysis

We can determine explicit steady state solutions for all candidate models to investigate whether our models can exhibit bistability. Below we describe this analysis for each of the model structures N_{xy}.

Steady state solution for candidate models N_{x1}. We proceed as in Section 6.2.2.6 by first calculating the time rate of change of total levels of β-catenin, and eliminating different dependent variables to re-write all dependent variables in terms of L_p and model parameters. In this way, we deduce

$$D_p = \frac{s}{d}, \tag{6.55}$$

$$L_u = \frac{k_{-2}}{k_2} L_p, \tag{6.56}$$

$$D = \left(\frac{d + k_{-6}}{k_6}\right) \frac{s}{d}, \tag{6.57}$$

$$E = \frac{k_3}{k_{-3} + k_{-4}} \left(\frac{d + k_{-6}}{k_6}\right) \frac{s}{d} L_p, \tag{6.58}$$

$$C = L_{\text{tot}} - k_2^* L_p, \tag{6.59}$$

$$A_p = \frac{(L_{\text{tot}} - k_2^* L_p)(k_{-3} + k_{-4})}{k_3 L_p}, \tag{6.60}$$

where

$$k_2^* = 1 + \frac{k_{-2}}{k_2} + \frac{k_3}{k_{-3} + k_{-4}} \left(\frac{d + k_{-6}}{k_6}\right) \frac{s}{d}. \tag{6.61}$$

By eliminating A_u from Equation (6.53) using Equation (6.44), we can write a second equation for A_p in terms of L_p

$$A_p = \frac{k_1}{k_1 + k_{-1}} \left(A_{\text{tot}}^* + \left(k_2^* - \frac{k_3 D}{k_{-3} + k_{-4}}\right) \left(1 + \frac{k_{-4}}{k_1}\right) L_p\right), \tag{6.62}$$

where

$$A_{\text{tot}}^* = A_{\text{tot}} - \left(1 + \left(\frac{d + k_{-6}}{k_6}\right) + 1\right) \frac{s}{d} - \left(1 + \frac{k_{-4}}{k_4}\right) L_{\text{tot}}. \tag{6.63}$$

The intersections of these two equations in (A_p, L_p) space describe the steady state solution of candidate models N_{x1}. In the same fashion as in Section 6.2.2.6, since Equations 6.60 and 6.62 describe two monotonic functions of L_p, we can conclude that biologically appropriate bistability (where all dependant variables have a positive value) is not possible.

Steady state solution for candidate models N_{x2}. Following a similar procedure we can derive a pair of simultaneous equations for A_p in terms of L_p

$$A_p = \frac{k_1}{k_1 + k_{-1}} \Bigg(\left(\left(\frac{k_{-2}}{k_2} + 1\right) \left(\frac{k_{-4}}{k_4} + 1\right) - \frac{k_3 k_{-4} s}{d k_6 (k_{-3} + k_{-4})} \right) L_p + A_{\text{tot}} - \frac{s}{d} - \left(1 + \frac{k_{-4}}{k_1}\right) L_{\text{tot}} - \frac{s(d + k_{-6})}{d k_6} \Bigg), \tag{6.64}$$

$$A_p = \frac{k_3 k_{-4} s}{d k_6 (k_{-3} + k_{-4}) L_{\text{tot}}} (c - b L_p - L_p^2), \tag{6.65}$$

where

$$b = \frac{(k_{-3}+k_{-4})(dk_2k_6(k_{-3}+k_{-4}) + dk_6k_{-2}k_{-4} + dk_2k_3s + k_2k_3s(k_6+k_{-6}))}{k_2k_3^2k_{-4}s}, \tag{6.66}$$

$$c = \frac{dk_6(k_{-3}+k_{-4})^2}{k_3^2k_{-4}s}L_{\text{tot}}. \tag{6.67}$$

The solution of this pair of equations is the steady state solutions of our candidate models N_{x2}. Since both b and c are positive for all model parameter values, we conclude that the quadratic $c - bL_p - L_p^2$ in Equation (6.65) has one positive and one negative root in L_p. Hence there is a maximum of one positive intersection for the line defined in Equation (6.64) and the hyperbola in Equation (6.65) in the positive quadrant in (A_p, L_p) space. We conclude that bistability is not possible for this set of candidate models.

Steady state solution for candidate models N_{x3}. Finally using a similar procedure to candidate models N_{x1} and N_{x2}, by setting $\frac{\mathrm{d}}{\mathrm{d}t} = 0$ in Equations (6.44)-(6.52) we can eliminate all dependent variables bar A_p and L_p to write two equations for A_p in terms of L_p and model parameter values

$$A_p = \frac{k_1}{k_{-1}}A_{\text{tot}} + \frac{1}{k_{-1}k_2L_p}\big((k_2+k_{-2})L_p - k_2L_{\text{tot}}\big)\big((k_1+k_{-4})L_p + (k_{-3}+k_{-4})\frac{k_1}{k_3}\big) \tag{6.68}$$

$$A_p = \frac{(k_{-3}+k_{-4})(k_2L_{\text{tot}} - (k_2+k_{-2})L_p)}{k_2k_3L_p} - \frac{s}{k_6} - \frac{s(k_{-3}+k_{-4})(k_6+k_{-6})}{k_6(d(k_{-3}+k_{-4}) + k_3k_{-4}k_6L_p)}. \tag{6.69}$$

The intersection points of these two lines represent the steady state solution of our system of ODEs for candidate models N_{x3}. Grouping similar terms together, we note that we can re-write these two equations in the following forms

$$A_p = C_1 + C_2L_p - \frac{C_3}{L_p}, \tag{6.70}$$

$$A_p = \frac{D_1}{L_p} - D_2 - \frac{D_3}{D_4+L_p}. \tag{6.71}$$

Assuming that all our model parameters are positive, then C_2, C_3, D_1, D_2, D_3 and D_4 are also positive (we note C_1 may not be). We remark that both these equations are continuous for $L_p > 0$. We can differentiate Equation (6.70) with respect to L_p to get

$$\frac{\mathrm{d}A_p}{\mathrm{d}L_p} = C_2 + \frac{C_3}{L_p^2} > 0. \tag{6.72}$$

Hence Equation (6.70) describes a monotonically increasing function of L_p. Differentiating Equation (6.71) with respect to L_p

$$\frac{\mathrm{d}A_p}{\mathrm{d}L_p} = -\frac{D_1}{L_p^2} + \frac{D_3}{(D_4+L_p)^2}. \tag{6.73}$$

Setting $\frac{\mathrm{d}A_p}{\mathrm{d}L_p} = 0$ in Equation (6.73) and re-arranging the terms while assuming $L_p \neq 0$, we have

$$(D_4+L_p)^2 = \frac{D_3}{D_1}L_p^2. \tag{6.74}$$

The solution of Equation (6.74) represents the turning points for the function described in Equation (6.71). We note that since both sides of this equation are complete squares and D_1, D_3 and $D_4 > 0$, there is a maximum of one positive root for this equation. $\frac{\mathrm{d}A_p}{\mathrm{d}L_p}$ also reaches zero while $A_p \to -D_2 < 0$ as $L_p \to \infty$. Moreover $A_p \to +\infty$ as $L_p \to +0$. Notice this means A_p is either a monotonically decreasing function of L_p for $L_p > 0$ or it has one turning point, at wich $L_p < -D_2$. Hence both Equations (6.68) and (6.69) describe monotonic functions for positive values of A_p and $L_p > 0$ with a maximum of one possible point of intersection. We again conclude that bistability is not possible for candidate models N_{x3}.

In summary, none of our candidate models can exhibit bistability.

6.3.2.6 Model selection

We explored the candidate model outputs in the same manner described for in Section 6.2.2.7 for Extension 1. There are now two additional parameter values; rate of phosphorylation and dephosphorylation of β-catenin ($k_{\pm 5}$). Our candidate models now have thirteen rate parameters, 2 parameters for total levels of Axin and LRP6, a time constant and up to two Wnt multipliers.

6.3.2.7 Parameter values for the multi-start CMA-ES technique

Similarly to Sections 4.2.5.1 and 6.2.2.8, we use synthetically generated model outputs to determine the appropriate parameter values for the CMA-ES technique. We generated eight random vectors for each of the six candidate models to produce $48 = 6 \times 8$ synthetic targets. Using the same methodology as before we run the multi-start CMA-ES technique on these model outputs. For consistency with the original problem, we included pS497/500 Axin, pS1490 LRP6, Axin/LRP6 complex, Axin/β-catenin complex, Axin/active β-catenin and Axin/pS33/S37/T41 β-catenin.

We found that a combination of increasing the number of random starts in log-space to 320 and doubling the population of particles similarly to Extension 1 from their default value enabled us to recover suitable parameter sets for all synthetic datasets. In all but 5 of the 48 cases, fewer than 35 random starting points were sufficient to find a feasible parameter value, while two sets of synthetic targets required 160 and 310 starting points.

6.3.3 Results

So far in this section we have proposed a set of candidate models that include the interplay between Axin, LRP6 and β-catenin. We have included each of these proteins in two different conformational states and considered whether we can explain seemingly contradictory experimental observations using a single mathematical model.

We explored the outputs for each model numerically using different cost functions corresponding to each set of experimental results. Table 6.12 summarises these results. We remark that the parameter sets found for each cost function are independent.

The first important observation we make is that again only one Wnt dependent reaction, namely LRP6 phosphorylation, is needed to describe the experimental observations by Kim et al. (2013), Li et al. (2012) and Azzolin et al. (2014). Moreover, all

Candidate Model	Wnt Dependent Reactions	A_p binds to L_p	D binds to L_p	D_p binds to L_p	What happens to pS33/S37/T41 β-catenin upon release from LRP6	% runs fitting Kim et al. (2013)	% runs fitting Li et al. (2012)	% runs fitting Azzolin et al. (2014)	Accepted
N_{11}	LRP6 phosphorylation	✓	✓	✗	-	2%	✗	✗	✗
N_{12}	LRP6 phosphorylation	✓	✓	✓	dephosphorylated	0.3%	49%	✗	✗
N_{13}	LRP6 phosphorylation	✓	✓	✓	degraded	1%	34%	59%	✓
N_{21}	LRP6 phosphorylation and Axin/LRP6 release	✓	✓	✗	-	7%	0.3%	✗	✗
N_{22}	LRP6 phosphorylation and Axin/LRP6 release	✓	✓	✓	dephosphorylated	3%	70%	✗	✗
N_{23}	LRP6 phosphorylation and Axin/LRP6 release	✓	✓	✓	degraded	2%	51%	40%	✗

TABLE 6.12: Model selection results for candidate models N_{xy}. Model outputs were explored numerically using the cost functions corresponding to each set of experimental results. The final column marks if the particular model is accepted or rejected after all the steps of our framework has been completed.

forms of active destruction complex (A_p, D and D_p) are required to bind to LRP6 in order to explain the observed dynamics.

Interestingly, since models N_{12} and N_{22} fail to reproduce some of the experimental observations, our results suggest that the majority of pS33/S37/T41 β-catenin in the LRP6 signalosome (i.e. in E_p) is degraded upon release. Since Li et al. (2012) observe that pS33/S37/T41 β-catenin is ubiquitinated while in complex with Axin, this suggests that the majority of pS33/S37/T41 β-catenin may in fact be ubiquitinated.

Figures 6.13, 6.14 and 6.15 display some typical model outputs for candidate model N_{13} for each set of experimental observations. The technique was able to only identify 2 suitable parameter vectors for observations by Kim et al. (2013), but it was able to find many more suitable fits for the other two observations. One reason behind this could simply be that we had fewer constraints for the latter two experimental observations (6 target model outputs versus 5 and 4). We provide some example parameter vectors for candidate model N_{13} for each set of experimental observations in Appendix C.

We note that candidate models N_{13} and N_{23} are nested with N_{13} the simpler model. Since we now have three rather than one set of experimental observations, for simplicity we restrict any further analysis of the candidate models to model N_{13} only. As we will later find (see Sections 6.3.3.1 and 6.3.3.2) this particular model in fact satisfies all other requirements, including robustness and further *in silico* experiments.

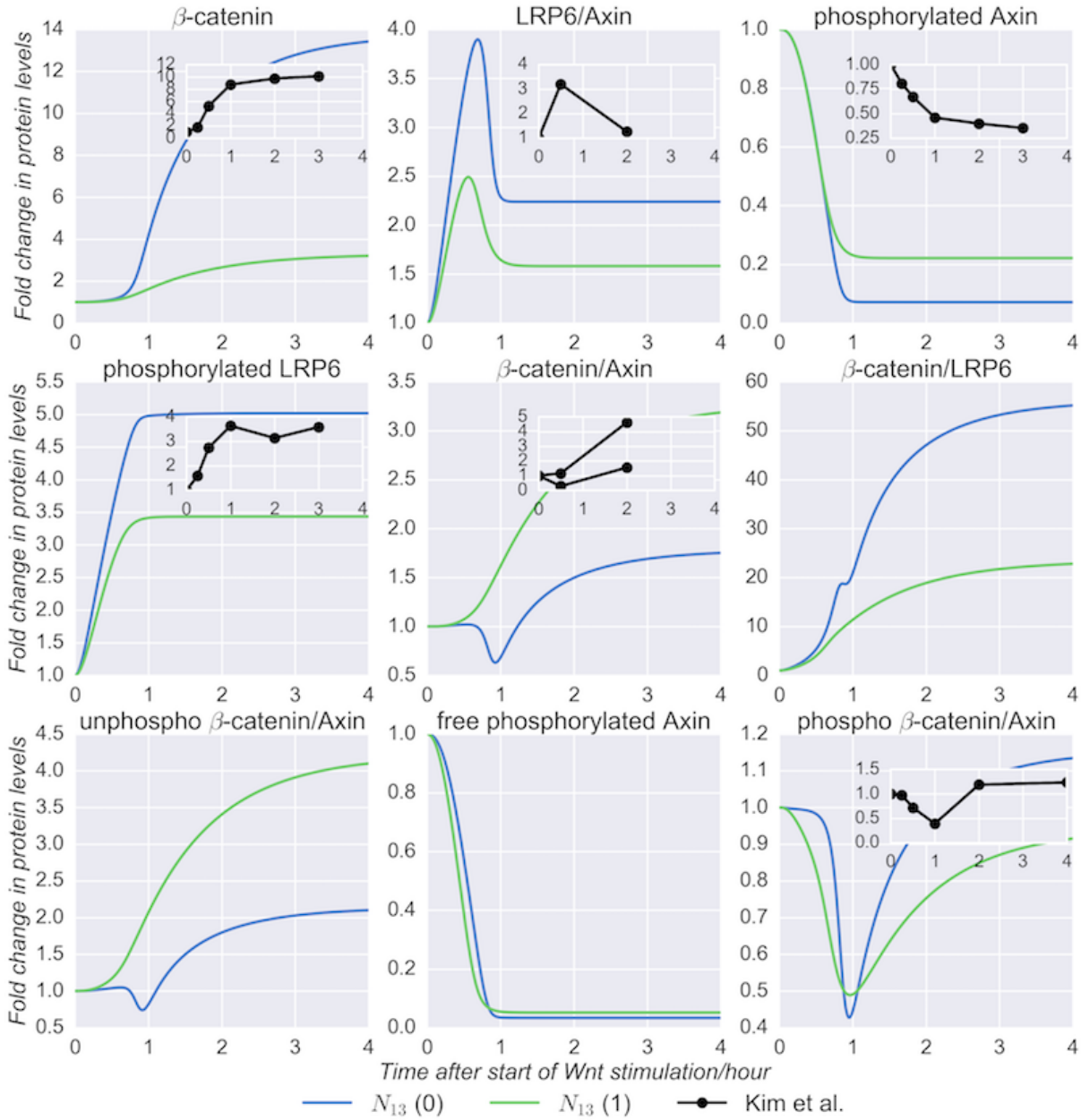


FIGURE 6.13: Output of candidate model N_{13} for the two feasible parameter sets found as suitable fits to experimental results by Kim et al. (2013). The inset in each plot shows the equivalent experimental observation by Kim et al. (2013). We note again that the qualitative behaviour required for Axin/LRP6 is different to the observations by Kim et al. (2013) (see Section 6.2.2.5). Interestingly, the CMA-ES technique has found two parameter sets where the change in levels of β-catenin/Axin complex are consistent with the observed results in L-cells (parameter set 0) and HEK293T cells (parameter set 1) (see Section 6.2.2.5). We also note that the model output for β-catenin/LRP6 complex ($E + E_p$ in terms of our dependent variables) for parameter set 0 has an unusual shape just before $t = 1$. We investigated the numerical solution and confirmed this output is not in error for the given parameter set. We remark that our cost function has no terms to disallow such behaviour, but such requirements could be incorporated if desired.

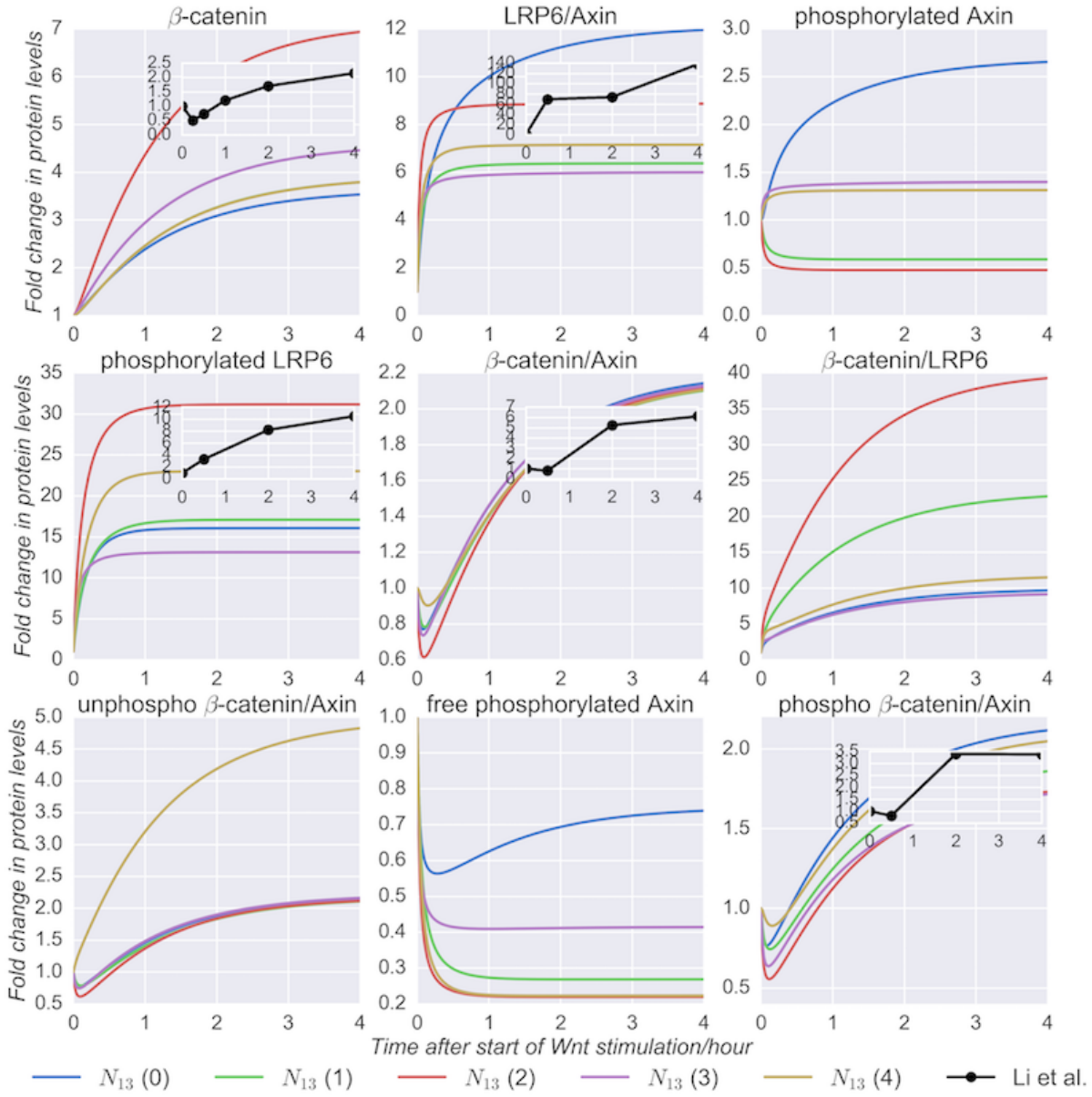


FIGURE 6.14: Output of candidate model N_{13} for five of the feasible parameter sets that reproduce the experimental results by Li et al. (2012). The inset in each plot shows the equivalent experimental observation by Li et al. (2012). 34% of all the multi-start optimisation runs were able to find a suitable parameter set.

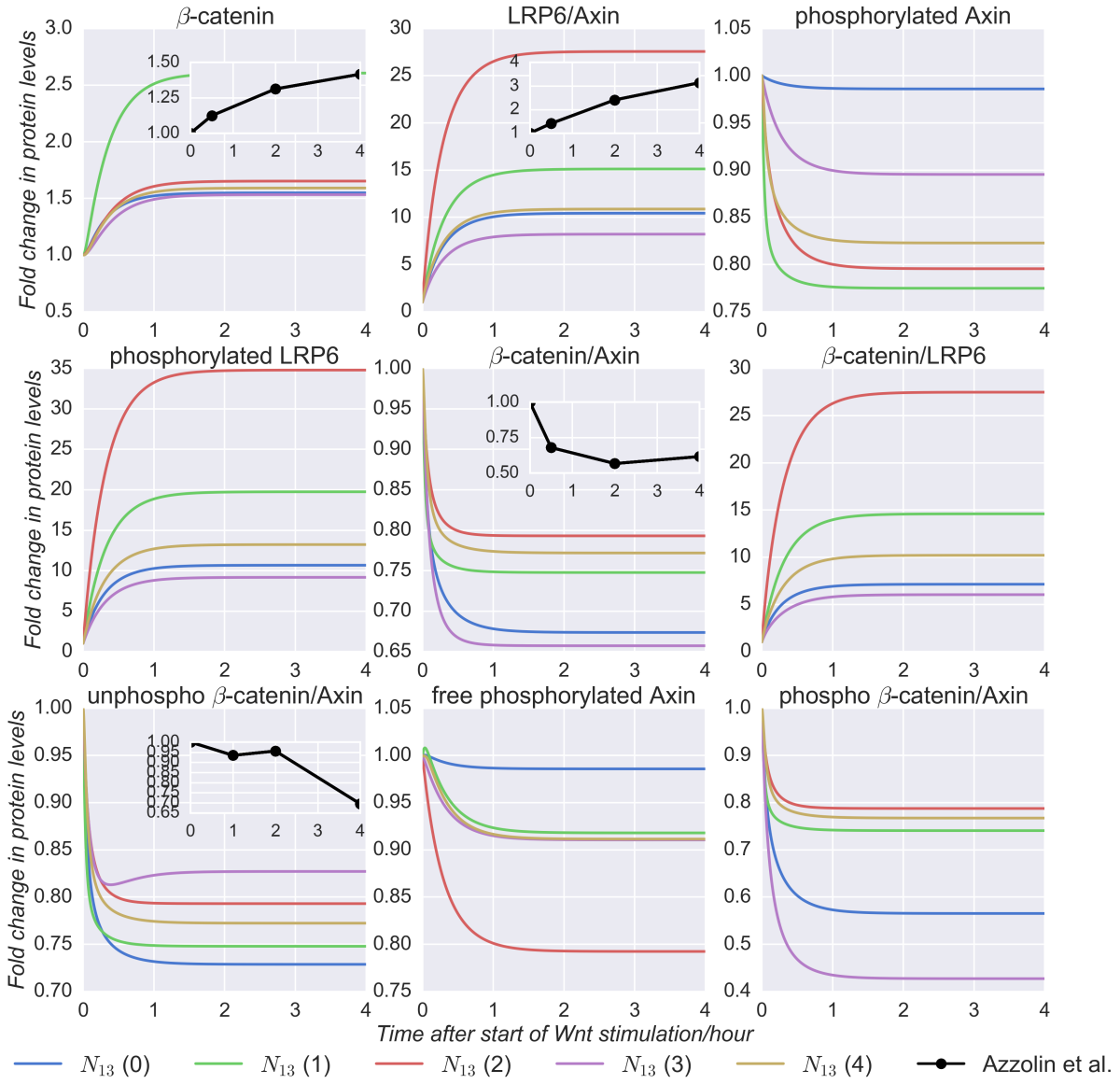


FIGURE 6.15: Output of candidate model N_{13} for five of the feasible parameter sets that reproduce the experimental results by Azzolin et al. (2014). The inset in each plot shows the equivalent experimental observation by Azzolin et al. (2014). 59% of all the multi-start optimisation runs were able to find a suitable parameter set.

6.3.3.1 Sensitivity analysis

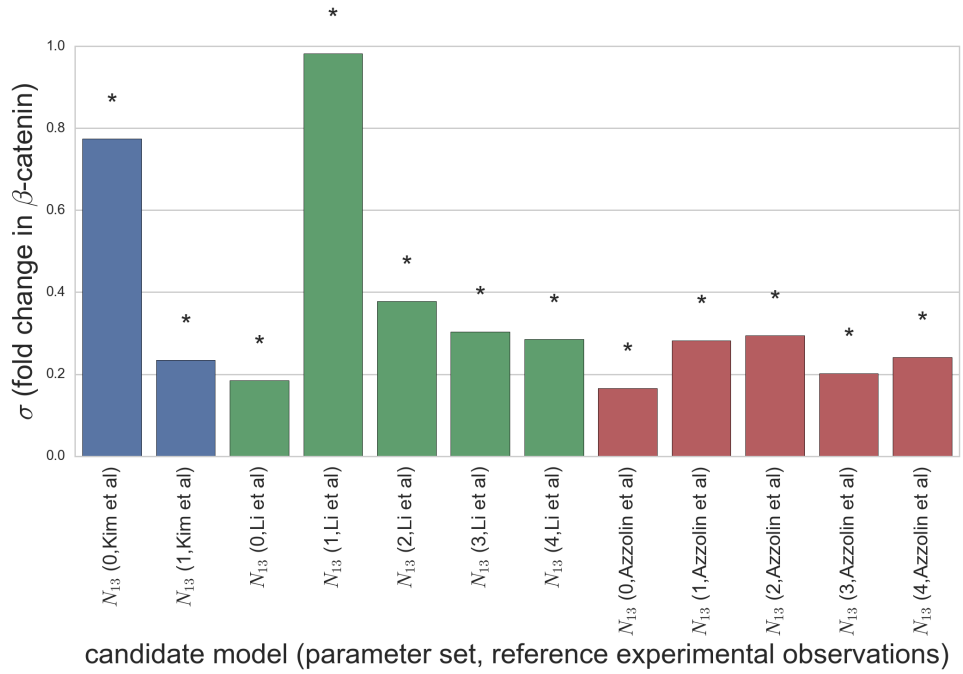


FIGURE 6.16: Standard deviation of control coefficients of fold change in levels of β-catenin for candidate model N_{13} for different parameter sets . * above the bar marks parameter sets that produce a robust model output. We show only 5 parameter sets for fits to results by Li et al. (2012) and Azzolin et al. (2014)

Using the same methodology as before, we study the robustness of fold change in levels of β-catenin with respect to local changes in model rate parameters. Figure 6.16 summarises the standard deviation (σ) of control coefficients for rate parameters under Model N_{13} for different feasible parameter sets found using the CMA-ES algorithm that reproduce the three sets of target experimental observations. We display only five of the feasible parameter sets that reproduce observations by Li et al. (2012) and Azzolin et al. (2014). All feasible parameter sets found in the last section for the experimental observations by Li et al. (2012) had a σ value of less than one. All but six feasible parameter sets found for Azzolin et al. (2014) were also similarly robust.

6.3.3.2 *in silico* experiments: Kim et al. (2013)

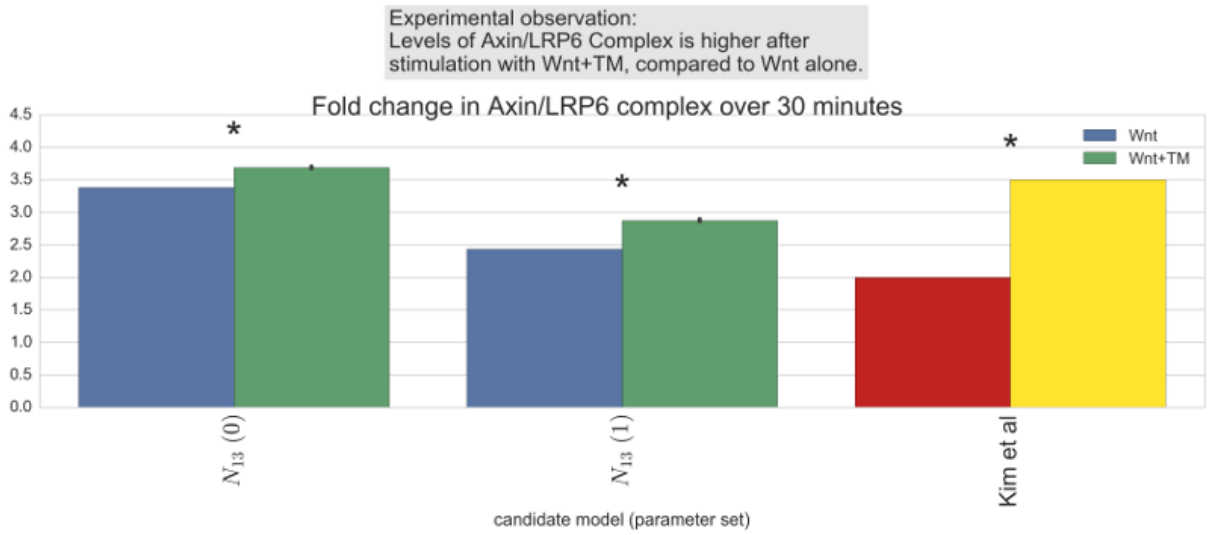
We found two suitable parameter sets for the candidate model N_{13} that reproduce the cell's response to Wnt stimulation as observed by Kim et al. (2013). We would like to study whether the model using these parameter sets can reproduce other experimental observations. We hence carry out *in silico* experiments using the same technique described in Section 6.2.3.2. We again perturb the model N_{13} for each feasible parameter set found earlier to reproduce stimulation of the system by the PP1 inhibitor, Tautomycin (TM) and/or Wnt, and compare the behaviour of various model outputs with *in vitro* experiments by Kim et al. (2013). We refer the reader to Section 6.2.3.2 for a more detailed description of the *in silico* experiments carried out here.

Figure 6.17 display the results of these experiments. The only results we would like to highlight are changes in levels of phosphorylated Axin and LRP6 upon stimulation with Wnt or Wnt and TM. All other results are consistent with the *in vitro* observations. For the two feasible parameter sets found:

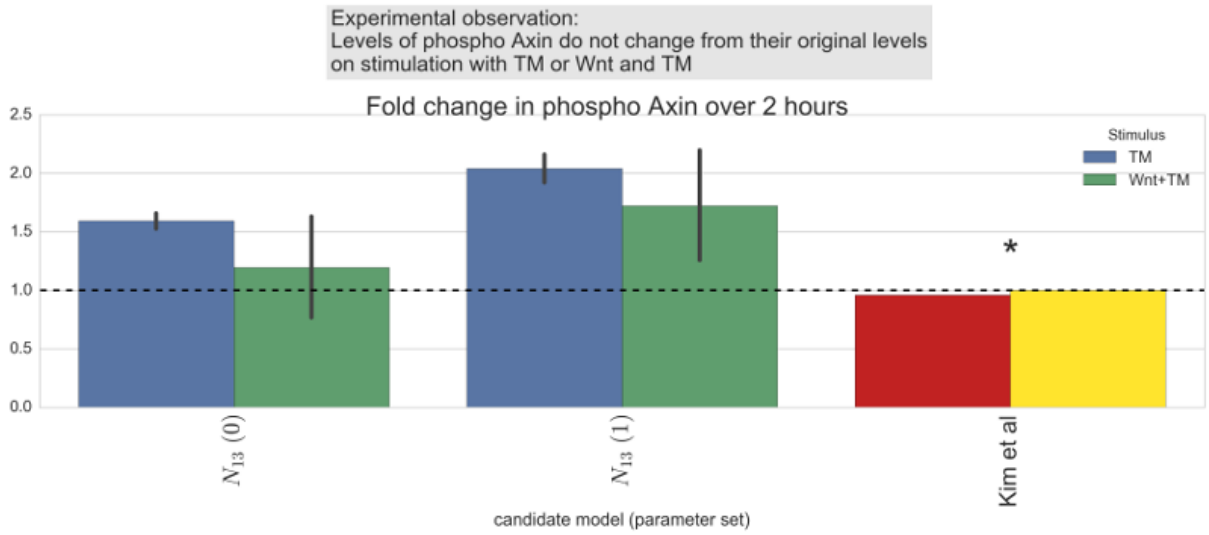
- **Figure 6.17C:** Levels of phosphorylated LRP6 increase under both stimulation with Wnt and TM, and Wnt alone. However, we find higher levels of phosphorylated LRP6 under stimulation with Wnt and TM, compared to Wnt alone; whereas the Kim et al. (2013) observe a similar increase,
- **Figure 6.17B:** Levels of phosphorylated Axin stay the same or increase under stimulation with Wnt and TM, and Wnt alone, whereas Kim et al. (2013) observe no increase.

We can hypothesise two reasons behind this difference:

1. This may be due to the semi-quantitative nature and possible saturation of the Western blot procedure, since Kim et al. (2013) would have only been looking to observe an increase in pS1490 LRP6 levels and no drop in levels of pS497/500 Axin, or
2. It may be due to the strength of TM stimulation; reducing levels of our *in silico* TM stimulation from 90% to 75% brings the results of *in silico* experiments in line with the *in vitro* observations. We avoid reducing these perturbation levels to stay consistent with other *in silico* experiments carried out so far in this thesis.

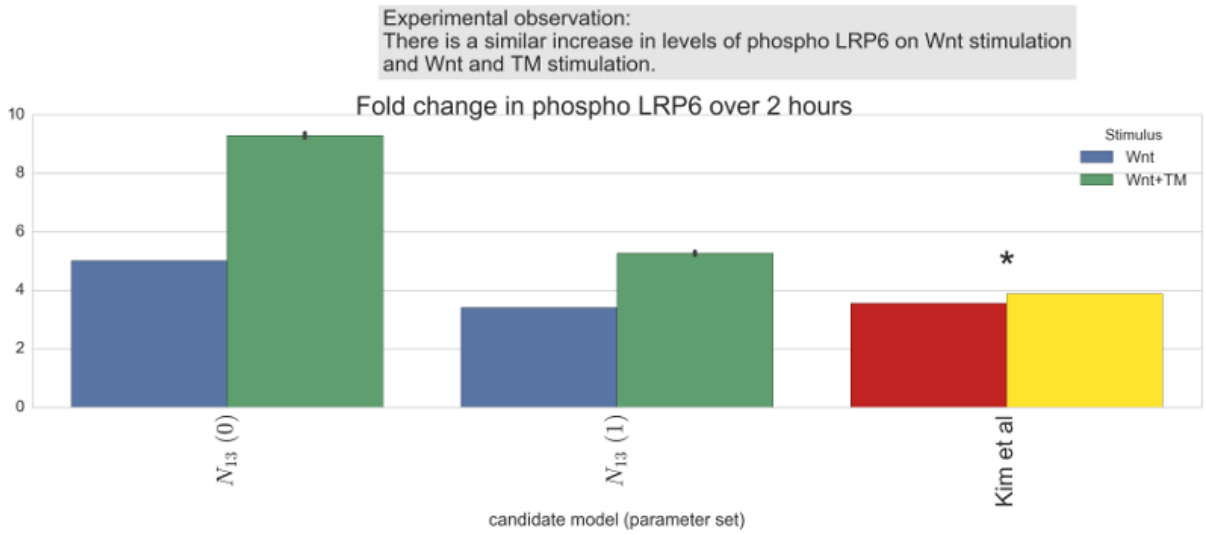


(A)

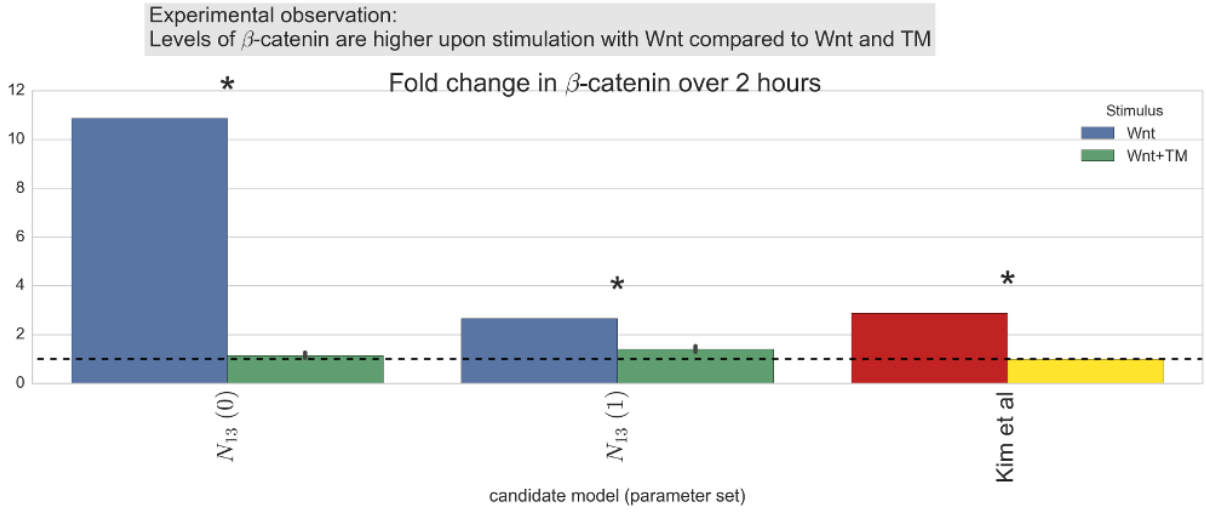


(B)

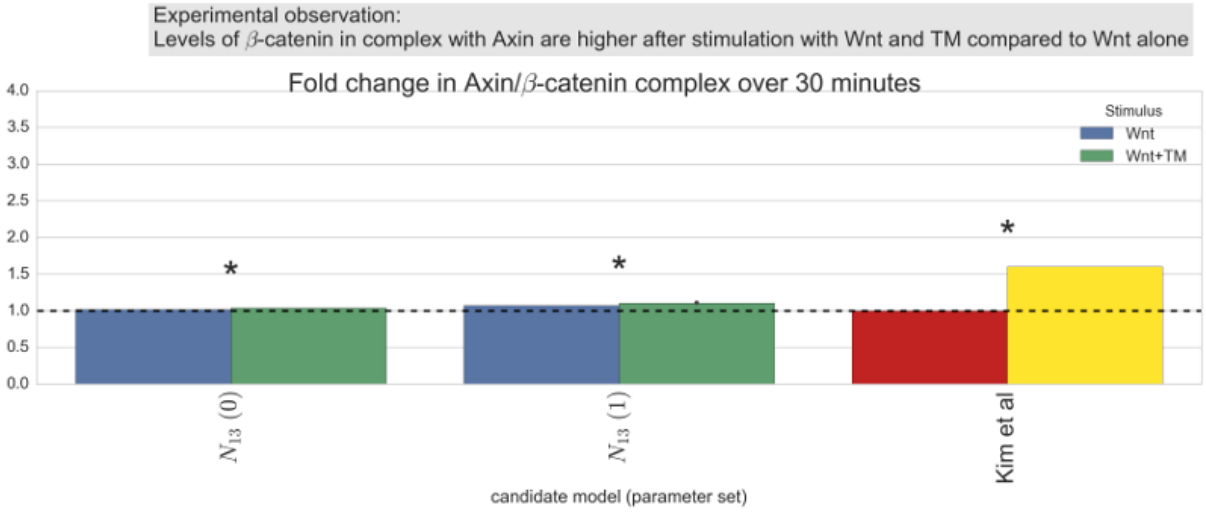
FIGURE 6.17: Results of *in silico* experiments using candidate model N_{13} and parameter sets found earlier that reproduce observations by Kim et al. (2013). The final bars, displayed in different colours, are quantification of the equivalent *in vitro* experiments by Kim et al. (2013). Starting from a "Wnt-off" steady state, we solve each model numerically using the parameter values found earlier with the assumption that phosphatase inhibitor TM exposure reduces the reaction rate k_{-4} by $90\% \pm 10\%$ on a relative basis. Black lines above each bar represent a one standard deviation confidence interval. We perturb our candidate models with TM alone, with Wnt alone, or with Wnt and TM for 30 minutes or 2 hours depending on the equivalent *in vitro* experiment, before measuring the fold change in protein concentrations. * above each bar marks model and parameter sets that are consistent with *in vitro* experimental observations (Figure continues onto the next page).


Experimental observation:
There is a similar increase in levels of phospho LRP6 on Wnt stimulation and Wnt and TM stimulation.
Fold change in phospho LRP6 over 2 hours
Stimulus
Wnt
Wnt+TM
10
8
6
4
2
0
*
N_{13} (0)
N_{13} (1)
Kim et al
candidate model (parameter set)

(C)


Experimental observation:
Levels of β-catenin are higher upon stimulation with Wnt compared to Wnt and TM
Fold change in β-catenin over 2 hours
Stimulus
Wnt
Wnt+TM
12
10
8
6
4
2
0
*
*
*
N_{13} (0)
N_{13} (1)
Kim et al
candidate model (parameter set)

(D)


Experimental observation:
Levels of β-catenin in complex with Axin are higher after stimulation with Wnt and TM compared to Wnt alone
Fold change in Axin/β-catenin complex over 30 minutes
Stimulus
Wnt
Wnt+TM
4.0
3.5
3.0
2.5
2.0
1.5
1.0
0.5
0.0
*
*
*
N_{13} (0)
N_{13} (1)
Kim et al
candidate model (parameter set)

(E)

6.3.3.3 *in silico* experiments: Li et al. (2012)

Li et al. (2012) carry out several experiments involving Wnt and MG132, a proteasome inhibitor that can inhibit proteasomal degradation of β-catenin via the destruction complex and lead to accumulation of β-catenin. They observe that levels of pS33/S37/T41 β-catenin are higher upon stimulation of HEK293T cells with MG132 alone compared to MG132 and Wnt combined (Figure 6.18).

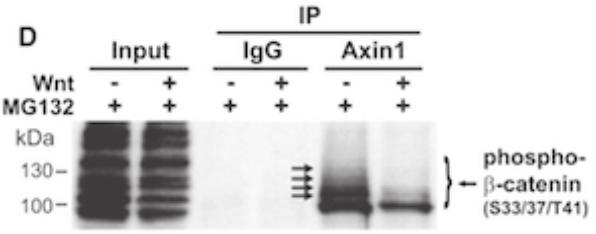


FIGURE 6.18: Li et al. (2012) observe lower levels of ubiquitinated β-catenin after stimulating HEK293T cells for 4 hours with MG132 and Wnt compared to with MG132 alone.

Using the candidate model N_{13} and the feasible parameter sets found earlier, we carry out *in silico* experiments on model N_{13}. We assumed MG132 reduces the rate of degradation of β-catenin (d in Reaction R_d) by 90%.

In our *in silico* experiments, we measured the levels of pS33/S37/T41 β-catenin (in complex with Axin) upon stimulation with MG132 alone, or Wnt and MG132 after 4 hours. For 63% of the feasible parameter sets found earlier, these levels were over 30% lower (and in 15% the levels were half as much) upon stimulation with Wnt plus MG132 compared to MG132 alone. For these parameter sets, our *in silico* results are consistent with results by Li et al. (2012) (see Figure 6.18).

As described in Chapter 2, Li et al. (2012) use their results (e.g. Figure 6.18) to propose a verbal model of the Wnt pathway where Wnt alters the ubiquitination step of the destruction complex. However, as we have demonstrated here, their results are consistent with our candidate model N_{13} where rate of ubiquitination of β-catenin is left unchanged.

We note that we do not change the rate of degradation of β-catenin via Reaction R'_{4C} and hence allow degradation of β-catenin via this reaction after MG132 stimulation. This is because in our candidate models we have combined Axin dephosphorylation, release of Axin from LRP6, and β-catenin degradation in this single reaction. Perturbing this reaction is not consistent with a simple MG132 stimulation.

6.3.3.4 *in silico* experiments: Azzolin et al. (2014)

Azzolin et al. (2014)'s primary focus was on the role of YAP, a Hippo pathway target, on canonical Wnt signalling. They carry out time course Axin1 co-IP's in cell lines with endogenous levels of YAP and with cell lines overexpressing YAP (see Figure 6.19). They observe that YAP overexpression

- stops the observed dissociation of β-TrCP from Axin,
- reduces association of Axin and LRP6, and
- reduces TOP-FLASH reporter assay activity.

TOP-FLASH reporter assay activity is used to measure activation of the Wnt pathway. We remark that we do not model Wnt-driven gene transcription in our candidate model explicitly and instead use levels of free β-catenin as a proxy for levels of Wnt pathway activity. We also note that we do not explicitly model β-TrCP.

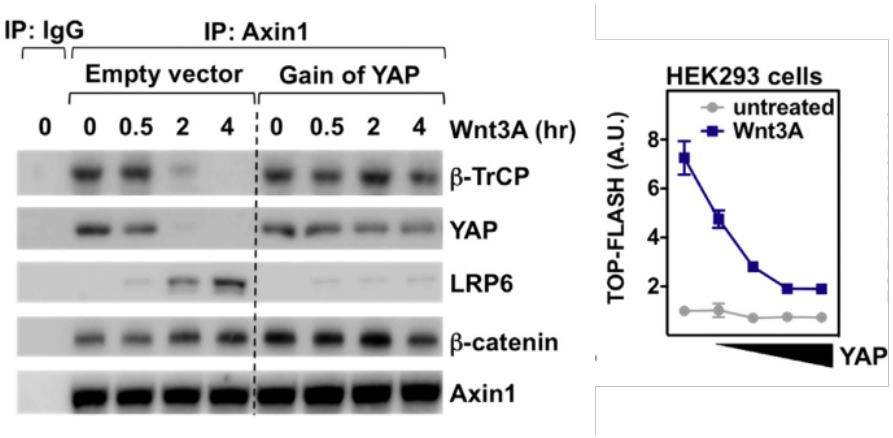


FIGURE 6.19: Azzolin et al. (2014) observe that in cells that overexpress YAP, there is reduced canonical Wnt pathway activity alongside lack of recruitment of Axin to LRP6 and increased association of β-TrCP and Axin.

The authors propose a verbal model where YAP allows LRP6 to replace β-TrCP from the destruction complex leading to deactivation in the final step of the destruction complex.

Since we do not explicitly model YAP in our candidate models, we investigated how YAP overexpression might change our mathematical model for the canonical Wnt pathway by exploring which reaction rates in our candidate models may be altered upon YAP overexpression. For example, if YAP is required for recruitment of Axin to LRP6, we may model YAP overexpression as an increase in the rate of recruitment of Axin to LRP6, k_3.

We run *in silico* experiments on candidate model N_{13} and the feasible parameter sets found earlier that reproduce experimental observations by Azzolin et al. (2014) to study if they may reproduce the changes observed upon YAP overexpression. We investigate whether changing a rate parameter due to YAP overexpression can:

- reduce levels of Axin/LRP6 complex,
- reduce levels of free β-catenin, which we assume as a proxy for TOP-FLASH report assay activity.

We assume YAP overexpression may increase or reduce a reaction rate ten-fold. In each experiment, we reduce a given reaction rate, we then solve the model numerically as before: we first solved the model in "Wnt-off" conditions until the system reaches state state. Taking the final "Wnt-off" simulation values as initial conditions for "Wnt-on" simulation, we switch to "Wnt-on" parameter values and run the simulation for another 4 hours. We look at the fold change in levels of Axin/LRP6 complex and fold change in levels of free β-catenin.

We found that

1. a reduction in LRP6 phosphorylation (k_2) (or increase in k_{-2}),
2. a reduction in Axin recruitment to LRP6 (k_3) (or increase in k_{-3}), or

3. a reduction in Wnt multiplier w_2

had a substantial impact in fold change in levels of free β-catenin, and complex formation between Axin and LRP6, in line with *in vitro* observations by Azzolin et al. (2014). Table 6.13 summarises these results.

Parameter shocked	Level of shock	% of feasible parameter sets showing 50% drop in Axin/LRP6 complex and in free β-catenin levels
k_2	Down 10-fold	22%
k_3	Down 10-fold	23%
w_2	Down 10-fold	24%

TABLE 6.13: Results of *in silico* experiments studying where YAP might act in model N_{13} of Wnt signalling. We shocked different model parameters up and down by 10 folds and investigated whether the model output is consistent with *in vitro* experiments by Azzolin et al. (2014). We found that for just over 20% of the feasible parameter sets found using the CMA-ES technique (see Table 6.12) reducing levels of k_2, k_3 or w_2 (or increasing the reverse reactions k_{-2} or k_{-3}) produces outputs consistent with the observed *in vitro* results.

This suggests that YAP might block LRP6 phosphorylation or recruitment of Axin to LRP6. In the first case, levels of LRP6 phosphorylated at S1490 are much lower in cells overexpressing YAP, whereas in the latter, this level is unchanged.

We also note that for all parameter sets where the *in silico* experiments were consistent with the *in vitro* YAP overexpression results, the levels of phosphorylated Axin fail to drop from their "Wnt-off" levels with YAP overexpression. This is in line with the behaviour the authors observe in levels of β-TrCP in complex with Axin upon Wnt stimulation. We hypothesise that Axin not phosphorylated at S497/S500 might have a lower affinity to β-TrCP, and hence release of β-TrCP from Axin upon Wnt stimulation might simply be due to dephosphorylation of Axin at S497/S500.

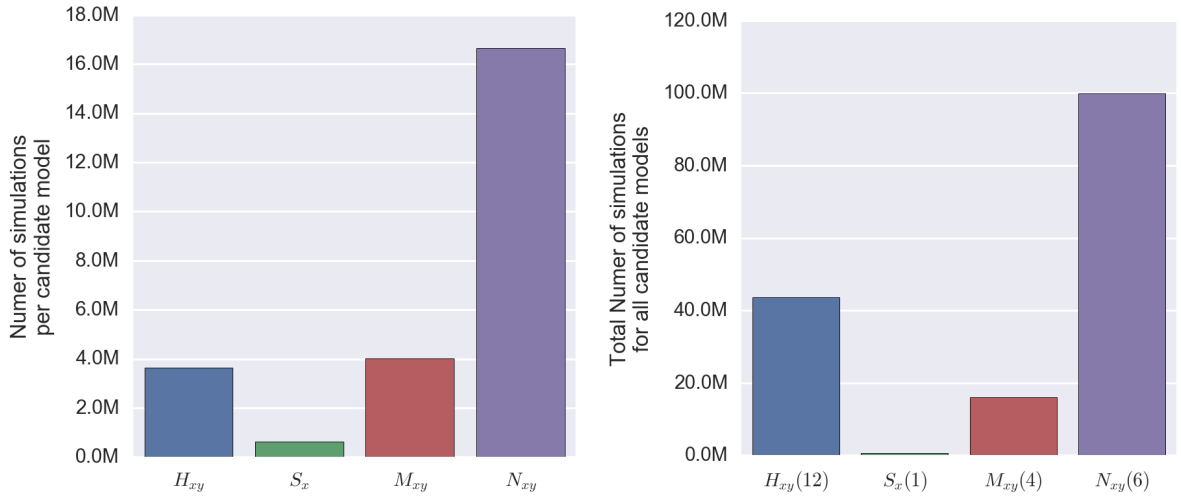
New *in vitro* experiments where we measure levels of Axin phosphorylated at S497/S500 residues and LRP6 phosphorylated at S1490 may shed further light on where exactly YAP acts in the canonical Wnt pathway, and whether β-TrCP may have higher affinity to phosphorylated Axin.

6.4 Discussion

Several recent studies have investigated the effect of Wnt stimulation on the interaction between Axin, LRP6 and β-catenin in different conformational states. Different results in these papers have led their authors to propose different verbals models of the Wnt pathway (see Section 2.2.1 in Chapter 2). The initial aim of this chapter was to investigate whether a unifying mathematical model could in fact describe these observations.

We proposed sets of candidate models and focused on model selection to study which potential pathway structures may be consistent with these observations. Proposing simpler models of the canonical Wnt pathway in Chapter 4 and the first part of this chapter, enabled us to keep the problem of model selection tractable. Figure 6.20 summarises the number of model simulations needed for model selection using the multi-start CMA-ES algorithm for different sets of candidate models studied in this chapter and Chapter 4. In order to investigate the increase in computational cost as we introduce more complexities into the candidate models, we include only those results that compare our model outputs to the experimental results of Kim et al. (2013).

Figure 6.20A displays the number of model simulations per candidate model, whereas Figure 6.20B displays the total number for all candidate models. Without the groundwork earlier in Chapter 4, where we only focused on the interaction between Axin and LRP6, exploring the possible structures for the interactions between Axin, LRP6 and β-catenin (as we did under models N_{xy}) would have been more computationally expensive.



(A) (B)

FIGURE 6.20: As we introduced further complexities in our candidate models of the Wnt pathway, model selection became more computationally intensive. These figures represent the number of model simulations required for fitting each set of candidate models to experimental results of Kim et al. (2013). (A) the average number of model simulations carried out by the multi-start CMA-ES algorithm per candidate model (B) the total number of model simulations when considering all candidate models. The number in the bracket indicates the number of candidates models that the CMA-ES technique was run for.

Unlike in Chapter 4, in this chapter, we allowed Wnt to reduce the rate of Wnt-dependent reactions by allowing the parameters w to vary between 0.01 and 100. However, a review of the feasible parameter values found reveals that for all candidate models, the rate of LRP6 phosphorylation increases upon Wnt stimulation ($w_2 > 1$ for all parameter sets found). For some parameter vectors in candidate models M_{23}, and N_{23}, the change in rate of release of Axin from LRP6 (w_{-4}) is found to be less than 1, however, these candidate models are a more complicated version of our preferred candidate models M_{13} and N_{13}, which also describe the experimental results. As such the result that levels of w_{-4} are below 1 for some parameter sets is not meaningful.

Nondimensionalization can be used to reduce the number of independent parameters in a mathematical model, reducing the dimensionality of the parameter vector when carrying out model selection. We note that we do not nondimensionalize the candidate mathematical models in order to speed up prototyping and testing new structures, even though exploring the parameter space of each model is slower without nondimensionalization.

Our final candidate model N_{13} was consistent with observations by three recent publications studying the interaction between Axin, LRP6 and β-catenin (Kim et al., 2013; Li et al., 2012; Azzolin et al., 2014). The model output was robust to parameter

perturbation, and the results of *in silico* experiments were consistent with observed *in vitro* results.

Studying the structure of our final candidate model N_{13} reveals several important features. First, a change in rate of LRP6 phosphorylation upon Wnt stimulation seems sufficient to describe various observed dynamics of the pathway in the first 4 hours after Wnt stimulation. Moreover, accumulation of β-catenin at the membrane and with LRP6 phosphorylated at PPPSP motifs seems important to describing the dynamics of the pathway. LRP6 phosphorylation plays an important role in slowing down the rate of β-catenin phosphorylation by GSK3, whereas it does not seem to hinder the degradation of pS33/S37/T41 β-catenin.

Recently crosstalk between the Hippo and Wnt pathways have been observed (Azzolin et al., 2012; Azzolin et al., 2014). We have used our mathematical model to study this crosstalk. We have investigated where the Hippo pathway target, YAP, might act in the canonical Wnt pathway. We found that observations by Azzolin et al. (2014) are consistent with our candidate models if we assume YAP either (1) increases the basal rate of LRP6 phosphorylation, or (2) increases the rate of recruitment of Axin to LRP6, or (3) increases how much Wnt stimulation increases rate of LRP6 phosphorylation. We proposed two new *in vitro* experiments which can help us discriminate between these three possibilities. Moreover, Azzolin et al. (2014) have observed that YAP overexpression stops dissociation of β-TrCP from Axin, whereas in our *in silico* study, we found that YAP overexpression stops dephosphorylation of Axin. This might suggest that dephosphorylation of Axin at S497/S500 leads to a reduced affinity of Axin to β-TrCP.

The ground work in Chapter 4 has enabled us to extend a simplified model for the recruitment of Axin to the membrane (candidate models S_1) to one that includes a more complete picture of the pathway (N_{13}), while keeping the problem of model selection computationally tractable. We note that in all of these models we ignore the experimental observation that Axin increases the rate of phosphorylation of LRP6 and do not explicitly model several species such as unphosphorylated Axin in complex with LRP6. We also note that due to lack of suitable experimental results, while studying the observations by Kim et al. (2013), we fit the output of our candidate models for the Axin/LRP6 complex to the output from the candidate model H_{21} from Chapter 4.

We also remark that we started this chapter by extending the final candidate models in Chapter 4. In particular, this means that we assumed that Wnt alters rate of LRP6 phosphorylation and release of Axin from LRP6 only. We ignored other possible candidate models where for example Wnt alters the rate of recruitment of Axin to LRP6, which was originally rejected in Chapter 4.

We also note that all model selection runs under different experimental observations by Kim et al. (2013), Li et al. (2012) and Azzolin et al. (2014), were independent. A next step in our work could be to start with a set of parameter values that are feasible under one set of experimental observations and explore how such a parameter vector might change to reproduce other experimental results. This could explain why different labs report markedly different results when studying the interactions between Axin, LRP6 and β-catenin. We discuss these next steps further in the next chapter.

Chapter 7

Discussion

7.1 Summary of the thesis

The elaborate biochemical networks underlying signalling pathways, the complicated interactions between their components, and crosstalk between different pathways, make studies of signalling pathways highly challenging. The qualitative and/or semi-quantitative nature of the associated experimental data, the challenge of reproducibility, and the sparsity of such data add to the challenge of identifying consistent models of these pathways. These challenges mean that experimental data and proposed models of signalling pathways can appear contradictory.

In this thesis, we have used the canonical Wnt pathway as a model system to propose a new computational framework that may be combined with qualitative experimental data to discriminate between competing verbal models of the pathway and to guide the design of new experiments. The framework combines qualitative comparison of quantitative model outputs with experimental data and *in silico* experiments to establish whether a given model is consistent with observed experimental results.

We used our framework to study the Wnt pathway in the first few hours after Wnt stimulation. We proposed and carried out new *in vitro* experiments to elucidate the interactions between two of the core components of the Wnt pathway; Axin and LRP6. We then applied our framework to a more detailed set of candidate mathematical models and established that under this framework, we can use existing experimental data to narrow down the list of suitable models to unify seemingly inconsistent experimental data with a single mathematical model.

In the next section, we summarise the findings in the earlier chapters of this thesis. We will then discuss our ideas for future work, before concluding with a few final remarks.

7.2 Summary of the work in each chapter

In Chapter 2, we presented a detailed literature review of the latest research on the canonical Wnt pathway. We introduced the core components of the Wnt pathway, and summarised competing hypotheses about how Wnt signalling leads to accumulation of β-catenin. We focused on the steps that lead to deactivation of the destruction complex. We also described the experimental procedures that are often used to study signalling pathways and how they can often produce semi-quantitative and/or qualitative experimental data.

In Chapter 3 we provided a brief introduction to mathematical model selection. We described model selection based on a well established technique, Approximate Bayesian Computation Sequential Monte Carlo (ABC SMC). We also introduced model selection using qualitative comparisons and the Covariance Matrix Adaptation Evolution Strategy (CMA-ES) optimisation algorithm. We compared the performance of the two techniques in various cases studies. We applied the techniques for model selection on simple biochemical reaction networks using qualitative cost functions. We

discussed the advantages and disadvantages of the two techniques and explained why we use the CMA-ES optimisation technique in our framework.

We established in Chapter 2 that some of the recent studies of the Wnt pathway identified post translational modifications of Axin and LRP6 as important steps that lead to deactivation of the destruction complex. To our knowledge, none of the mathematical models of the Wnt pathway have focused on this interaction and its role in deactivation of the destruction complex. We therefore proposed twelve candidate models in Chapter 4 that describe the interactions between Axin and LRP6. We explained why we focused on LRP6 phosphorylation at S1490, and Axin phosphorylation at S497/500. We used our model selection framework and results by Kim et al. (2013) to show that four of our original twelve models were consistent with experimental observations. We proposed a new *in vitro* experiment to discriminate between the remaining four models. Without suitable experimental data, we ended Chapter 4 by establishing why one of the candidate models (model H_{21}) may be the most suitable for further studies. In order to ensure the problem of model selection is computationally tractable, we simplified this model, and showed that it can still reproduce several experimental observations. Due to the lack of suitable experimental results, we fitted the new simplified model, which neglected certain interactions between Axin and LRP6, to model output from our candidate model H_{21}.

Having identified a suitable experiment to discriminate between the four remaining candidate models; in Chapter 5 we described the methods and results for carrying out this experiment. Our preliminary results suggested that the models H_{21} and H_{22} may be the most appropriate models of the four remaining candidates. We discussed why further work is required to completely validate our results.

In Chapter 6, we proposed new candidate models that extended the simplified model from Chapter 4 to include β-catenin and a more detailed description of the destruction complex. We carried out this extension in two steps; first introducing β-catenin synthesis and degradation, and then introducing β-catenin phosphorylation. We applied our model selection framework to the new candidate models, and ended Chapter 6 with what we think is an exciting contribution to modelling of the canonical Wnt pathway; a mathematical model of the pathway that reconciles seemingly inconsistent experimental observations from three different experimental studies of the Wnt pathway.

Our model is focused on the first few hours after Wnt stimulation and describes interactions between Axin, LRP6 and β-catenin. We found different model parameterisations that describe the *in vitro* observations by Kim et al. (2013), Azzolin et al. (2014) and Li et al. (2012). The acceptance of this particular model, and the rejection of alternatives allowed us to make several observations. Firstly, simply assuming that binding of Wnt ligands increases the rate of phosphorylation of LRP6 at S1490 (and other PPPSP motifs) by GSK3 is sufficient to describe the signalling cascade observed in the first few hours after Wnt stimulation. Secondly, our mathematical model suggests that recruitment of β-catenin to LRP6 via Axin seems to be an important factor in describing the observed experimental dynamics. To our knowledge, this conclusion has not been investigated by other mathematical models of the Wnt pathway. Finally, one of the discrepancies in the existing models of the Wnt pathway concerns the identification of which functions of the destruction complex are altered upon Wnt stimulation. Our model suggests that the following two events lead to deactivation of the destruction

complex upon Wnt stimulation:

- a reduction in the rate at which β-catenin is recruited to Axin, due to Axin dephosphorylation at S497/500,
- and, a slowdown in the rate of β-catenin phosphorylation, due to inhibition of GSK3 by pS1490 LRP6.

In fact rejection of candidate models (N_{12} and N_{22}) in Chapter 6 suggests that Axin in complex with pS1490 LRP6 must continue to degrade already phosphorylated β-catenin.

We ended Chapter 6, by carrying out *in silico* experiments on our mathematical model of the Wnt pathway. We established that our model reproduces additional *in vitro* observations by Kim et al. (2013), Li et al. (2012) and Azzolin et al. (2014). This again highlights the fact that the different results in these studies are not inconsistent and the competing verbal models proposed by these studies are not required to describe the observed experimental results. This illustrates why care is needed in developing verbal models of signalling pathways from such experimental data.

7.2.1 A note on reproducibility of experimental results

The work of Chapter 5 did illustrate a noticeable phenomenon in experimental studies; namely that the materials and methods sections of publications do not necessarily provide enough details for a experimentalist to reproduce the results quickly. My aim to reproduce and extend the experimental results of Kim et al. (2013) within six months seemed realistic to me, whereas, my experimentalist colleagues felt it too ambitious. The main reason for this discrepancy is that any experimental procedure needs to be optimised for the problem of interest. This raises an interesting question: with the almost unlimited availability of resources online, why do the materials and methods sections of papers limit the description of a one week procedure to just one paragraph? A simple solution would be to require a detailed materials and methods section online. The field of computer science is moving towards open sourcing code bases used to produce results. We hope this trend continues and that it will be extended to experimental studies in biological sciences.

I experienced other problems that were beyond my control. For example, I lost a month of work due to a faulty batch of Wnt ligands, which we later discovered is a common problem. I also lost four months of work because Kim et al. (2013) stated the wrong antibody in their paper. By the time I received the new antibody, I only had one month to carry out the experimental work.

7.3 Future work

There are many potential avenues for extending the work proposed in this thesis. As the very first step, it might be appropriate to extend the original candidate model H_{21}, instead of the simplified model S_1 to study a more complete picture of the Wnt pathway as we did in Chapter 6. There are also several issues we did not address. We did not include the Dvl, APC or Frizzled proteins which are known to influence the pathway dynamics. We did not model several other phosphorylation sites on LRP6, Axin and β-catenin.

Of these, we believe APC is a strong candidate for future work. APC is mutated in 75% of colorectal cancer cases and yet its role in the canonical Wnt pathway remains

poorly understood. Comparing the results of *in silico* experiments on our mathematical model with existing *in vitro* studies involving APC will be a good first step in understanding the role APC plays in Wnt signalling. We should then be able to use these results to introduce APC explicitly in our model.

Our model treats the membrane, cytoplasm and the nucleus as a well-mixed compartment. Several compartmentalised mathematical models of the Wnt pathway have been proposed in the past (MacLean et al., 2015b; Schmitz et al., 2013; Haack et al., 2015). A suitable extension to our model will be to investigate how compartmentalisation could contribute to the observed dynamics involving Axin, β-catenin and LRP6. Although experimental procedures exist to study protein localisations around the cell, extended experimental results are still lacking which will make discrimination between any proposed candidate models of the pathway difficult. Such a study needs to be combined with careful experimental collaboration to ensure that experimental procedures exist for collection of suitable experimental data.

Crosstalk between signalling pathways can lead to interesting and important responses within the cell. Some of the recent mathematical models of the Wnt pathway have investigated crosstalk involving the Wnt pathway (Chen et al., 2014; Kay et al., 2017). Recently the first mathematical model of the Hippo pathway has been developed (Sun et al., 2016). Another area for future work is the cross talk between the Hippo pathway and the canonical Wnt pathway. We touched on this problem briefly in Chapter 6, demonstrating the role that YAP/TAZ, which are the Hippo pathway targets, might play in recruitment of Axin to LRP6. It will be interesting to study this crosstalk further *in silico*. A model incorporating this crosstalk could be well-suited for study in a multiscale model of the intestinal crypts where both of these pathways are known to play important roles (Imajo et al., 2014; Clevers and Nusse, 2012). The mechanotransductional properties of YAP/TAZ alongside their role in Wnt signalling might provide new insights into the dynamics of the intestinal crypts.

Given the qualitative nature of the experimental data in studies of signalling pathways, parameter inference is a problem we do not tackle in our framework. An interesting extension to our work may be to study the size of the parameter space that is consistent with the experimental observations. It will be useful to establish a protocol to investigate how pathway outputs change as parameter values vary. In particular, it would be interesting to study the importance of levels of Axin, which have been observed to vary from 0.02 nM (Lee et al., 2003) to 150 nM (Tan et al., 2012) in different cell lines.

We established in Chapter 6 that with different parameterisations, our mathematical model can reproduce different experimental observations. However, we did not establish what these parameters tell us about the state of the system that reproduces each set of results. A good next step will be to study the minimum number of changes required to switch from one feasible qualitative model output (e.g. one that fits results by Kim et al. (2013)) to another (e.g. one that fit results by Azzolin et al. (2014)). What do these changes tell us about the state of the cells and the procedures in different experimental labs? If we can establish that changes in a particular model parameter (e.g. total levels of Axin) can describe this difference, can we replicate and validate such result *in vitro* (e.g. by overexpressing or suppressing Axin)?

We focused our modelling on the first few hours after Wnt stimulation. Doing so allowed us to ignore various feedback loops (see Chapter 2 for details). Another

avenue for model extension would be to study the pathway over longer time periods, including the various feedback loops involving Axin and LRP6. Recently, Brunt and Scholpp (2017) carried out a detailed review of the function of endocytosis in Wnt signalling. It would be interesting to use mathematical modelling to investigate the role of endocytosis, and in the first instance, LRP6 recycling in Wnt signalling.

On the experimental side, the first piece of future work is to optimise the protocol detailed in Chapter 5 further. We hope the groundwork in this chapter and the detailed materials and methods will help future students who continue this work.

Our framework provides a tool that can be used to discriminate between alternative models of signalling pathways using qualitative data. For example, two different models have been proposed about the role of YAP phosphorylation in the Hippo pathway (Downward and Basu, 2008). First, YAP phosphorylation has been observed to lead to its cytoplasmic retention (Harvey et al., 2013; Hao et al., 2008; Zhao et al., 2007). Second, YAP phosphorylation has been observed to promote its binding to p73 tumour suppressor in the nucleus (Pefani and O'Neill, 2016; Matallanas et al., 2007). A detailed study of these interactions could elucidate the underlying mechanism that leads to these discrepancies.

Another example where our framework could be applied is the role of homodimerization and heterodimerization of STAT proteins in JAK-STAT signalling (Delgoffe and Vignali, 2013). For example, heterodimerization could lead to reducing the number of available STAT molecules (Ho and Ivashkiv, 2006), or heterodimers and homodimers may lead to transcription of different genes (Collison et al., 2012). Mathematical modelling has been used to study the role of dimerization and phosphorylation in signalling via STAT1 in mammalian cells (Shudo et al., 2007). Further mathematical modelling using a framework such as one proposed here could help clarify these interactions further.

7.4 Final remarks

In this thesis, we have established a new framework for studying the dynamics of signalling pathways. We have shown that care must be taken when using qualitative and semi-quantitative experimental data to propose new models of signalling pathways, and how, with careful model selection, we may be able to discriminate between competing models.

We have applied our framework to the canonical Wnt pathway and proposed a mathematical model that elucidates how post translational modification of LRP6 and Axin lead to deactivation of the destruction complex. We were able to reconcile seemingly inconsistent experimental observations with a single mathematical model.

We also showed how our framework can be used to guide the design of new experiments that may discriminate between competing model structures of a signalling pathway. Our framework, as implemented in python using PySB, SciPy and CMA-ES packages, allows for quick prototyping of new mathematical models and as such could be generalised to study other signalling pathways. We hope that our work encourages new collaborations between mathematical modellers and experimental biologists, and in particular, helps the experimentalists with the design of future experiments.

Part I

Appendices

Appendix A

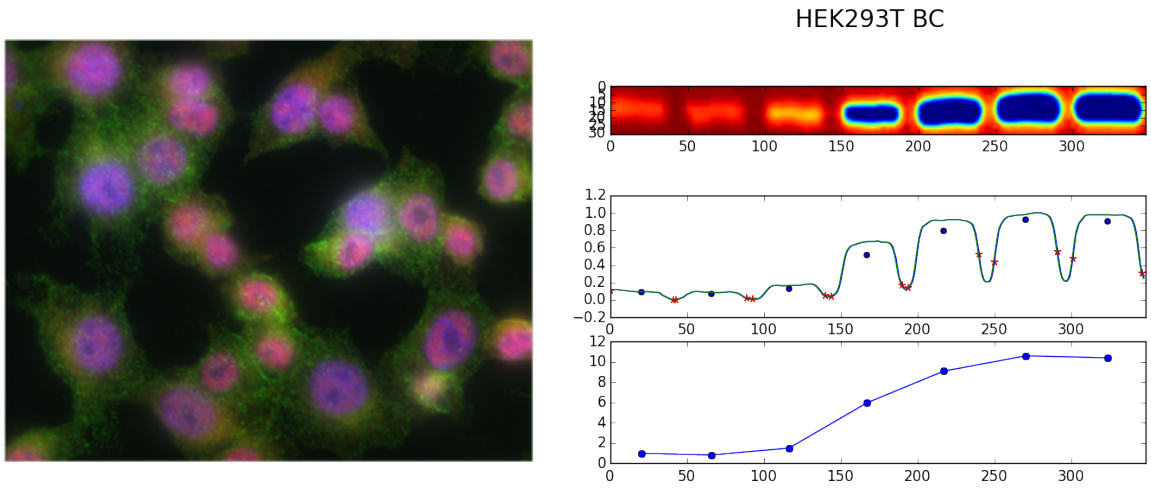
Theoretical methods

A.1 Image segmentation

In the few months we spent in the lab when we carried out immunofluorescence experiments, we collected over 22 GB worth of images. It is hence essential to come up with a robust automated segmentation algorithm. All image analysis was done in Python using the Numpy, Scipy and CV2 scientific packages. Images were saved in Nikon nd2 format, which were loaded using a modified version of SLOTH (http://pythonhosted.org/SLOTH).

A cytoplasmic mask for the images is calculated using a *k-means* clustering algorithm, trained over the intensity of randomly selected subset of the image pixels in all image channels. The nuclear mask is calculated using a simple adaptive thresholding algorithm on the DAPI channel.

Once the masks are defined, we simply calculate the average pixel intensity in various channels (taking into account the manual intensity multiplier on the microscope) to measure the relative protein concentration in different cellular compartments. We subtract the average background intensity calculated from empty channels from a few images from the final intensity value. We used a value of 15 A.U. for the background noise/intensity level. The algorithm only segments cells from the background and not individually. In most of the collected images, segmenting individual cells by eye is also extremely difficult if not impossible (Figure A.1A).



(A) (B)

FIGURE A.1: (A) RKO cells stained for β-catenin (green), YAP antibodies and DAPI (blue). It is difficult to segment RKO cells individually. (B) Quantification of blot in Figure S5A of Kim et al. (Kim et al., 2013).

A.2 Estimating number of Wnt ligands and receptors

A.2.1 Number of Wnt ligands in a typical *in vitro* experiment

We start *in vitro* experiments in 10cm-diameter dishes when cells are at 60%-70% confluency. This corresponds to about 5 million cells per dish. Bafico et al. (2001) estimate 2500-5000 LRP6 co-receptors per NIH3T3 cells; thus assuming a similar number of co-receptors in HEK293T cells used in our experiments, we estimate 2×10^{10} LRP6 co-receptors per well.

Wnt3A is a $44\mathrm{Da}$ protein, which is equivalent to $44 \times 10^{3}\mathrm{g/mol}$ molecular mass. Assuming a typical concentration of $100\mathrm{ng/ml}$ of Wnt3A for a typical experiment and $10\mathrm{ml}$ media, we have approximately $2 \times 10^{-11}\mathrm{mol}$ of Wnt3A ligands. This gives us approximately $6 \times 10^{23} \times 2 \times 10^{-11} \approx 10^{13}$ ligands in a typical experiment.

This suggests the number of Wnt3A ligands is approximately 500 times more than LRP6 co-receptors, and hence it is unlikely that exhaustion of Wnt ligands is the primary reason behind the behaviours observed experimentally.

A.3 Western blot quantification

We developed a Python script that enables us to quantify the relative intensity of different blots in these publications efficiently. The input is a simple blot image, plus the expected number of wells in the given image. The algorithm calculates local minima in the image intensity, which are assumed to be the gap between the two separate gel runs. The results are then adjusted, using the control protein if required (Figure A.1B).

Appendix B

Cost vectors used in Chapters 4 and 6

This appendix includes the elements of the cost vectors we use to compare our candidate models to various experimental results by Kim et al. (2013), Li et al. (2012) and Azzolin et al. (2014). The quantity of interest (Y_i), calculated from the model outputs, is the value used to calculate the cost element (J_i). The exact levels of the satisfaction boundaries are chosen to achieve a qualitative match to the experimental observations. The weights w_i are evolved during the fitting process to give more importance to particular qualitative behaviour that were missed in earlier optimisations.

In Section 3.5.2 of Chapter 3, we introduced the satisfaction metrics and gave a description of how we propose each element of the cost vectors. Here, we provide further examples of how we write down each cost element below.

- **Levels of LRP6/Axin complex should double after 30 minutes of Wnt stimulation:** To enforce this behaviour, we look at the fold change in this complex, and define the cost to be the distance from 2 if this level is below 2, or 0 otherwise

$$\max\left(0, 2 - \frac{X(0.5h)}{X(0h)}\right), \tag{B.1}$$

- **Phosphorylated Axin should not reach steady state too quickly:** We enforce this be ensuring levels of phospho Axin at $t = 0.5h$ minutes and $t = 1h$ are not close to each other. We calculate the difference between phospho Axin at these two time points and normalize it using the level at $t = 0$. We set the cost to the reciprical of this value unless this level is greater than 5%

$$\frac{1}{\frac{X(0.5h)-X(1h)}{X(0)}} \quad \text{if } \left|\frac{X(0.5h) - X(1h)}{X(0)}\right| < 0.05. \tag{B.2}$$

B.1 Cost vectors for Chapter 4

Qualitative Requirement	Output Variable (X)	Quantity of Interest (Y_i)	Value (J_i)	Weight (w_i)
Levels of phosphorylated Axin should drop to $10\% - 40\%$ of the initial level	$A_p + C_1 + C_3$	$\frac{X(t_{\text{final}})}{X(0)}$	$\lvert Y_i - 0.4\rvert$ if $Y_i > 0.4$, $\lvert Y_i - 0.1\rvert$ if $Y_i < 0.1$	2
Levels of phosphorylated LRP6 should increase between two and ten fold.	$L_p + C_2 + C_3$	$\frac{X(t_{\text{final}})}{X(0)}$	$\lvert Y_i - 2\rvert$ if $Y_i < 2$, $\lvert Y_i - 10\rvert$ if $Y_i > 10$	2
Levels of phosphorylated Axin should decrease monotonically	$A_p + C_1 + C_3$	$\frac{X(t_{i+1}) - X(t_i)}{\delta t}$, $t_i = 0, \ldots, t_{\text{final}-1}$	$\max_{t_j=0,\ldots,t_{\text{final}-1}}(Y_i(t_j), 0)$	10
Levels of phosphorylated LRP6 should increase monotonically	$L_p + C_2 + C_3$	$\frac{X(t_{i+1}) - X(t_i)}{\delta t}$, $t_i = 0, \ldots, t_{\text{final}-1}$	$\min_{t_j=0,\ldots,t_{\text{final}-1}}(Y_i(t_j), 0)$	10
Levels of LRP6/Axin complex should double after 30 minutes of Wnt stimulation	$C_0 + C_1 + C_2 + C_3$	$\frac{X(0.5h)}{X(0)}$	$\max(0, 2 - Y_i)$	10
Levels of LRP6/Axin complex should drop to within 20% and no less than the initial level	$C_0 + C_1 + C_2 + C_3$	$\frac{X(2h)}{X(0)}$	$\max(0, Y_i - 1.2) + \min(0, 1 - Y_i)$	20
Phosphorylated LRP6 and phosphorylated Axin should reach their steady state within 90 minutes	$A_p + C_1 + C_3$, $L_p + C_2 + C_3$	$\frac{X(t_{\text{final}})}{X(1.5h)}$	$\lvert Y_i - 1\rvert$	1
Phosphorylated Axin should not reach steady state too quickly	$A_p + C_1 + C_3$	$\lvert\frac{X(0.5h) - X(1h)}{X(0)}\rvert$	$\frac{1}{Y_i}$ if $Y_i < 0.05$	1
All dependent variables must be positive	All dependent variables	$X_i(t)$	$\sum_i \min_t(X_i(t), 0)$	1

TABLE B.1: Cost vector for qualitative fit to results by Kim et al. (2013) as displayed in Figure 4.4.

B.2 Cost vectors for Chapter 6

Cost vector elements displayed in Table B.2 are applied to all model selection runs and include in particular the qualitative requirements for total levels of β-catenin, which is shared between all experimental results and added to all cost vectors in Chapter 6.

Qualitative Requirement	Output Variable (X)	Quantity of Interest (Y_i)	Value (J_i)	Weight (w_i)
Concentration of β-catenin should not be too low	$B + D + E$	X	$Y_i > 1$	1
β-catenin should start to reach steady state by 4 hours	$B + D + E$	$\frac{X(4h) - X(3h)}{X(3h)}$	$Y_i - 0.05$ if $Y_i > 0.05$	10
Levels of β-catenin should increase monotonically	$B + D + E$	$\frac{X(t_{i+1}) - X(t_i)}{\delta t}$, $t_i = 0, \ldots, t_{\text{final}-1}$	$\min_{t_j=0,\ldots,t_{\text{final}-1}}(Y_i(t_j), 0)$	10
Levels of β-catenin should increase between 1.5 and 20 fold.	$B + D + E$	$\frac{X(t_{\text{final}})}{X(0)}$	$\lvert Y_i - 1.5\rvert$ if $Y_i < 1.5$, $\lvert Y_i - 20\rvert$ if $Y_i > 20$	1
All dependent variables must be positive	All dependent variables	$X_i(t)$	$\sum_i \min_t(X_i(t), 0)$	1

TABLE B.2: Requirements shared between all cost vectors in Chapter 6

Qualitative Requirement	**Output Variable (X)**	**Quantity of Interest (Y_i)**	Value (J_i)	**Weight (w_i)**
Monotonic decrease in levels of phospho Axin	$A_p+C+D+E$	$\frac{X(t_{i+1})-X(t_i)}{\delta t}$, $t_i = 0, \ldots, t_{\text{final}-1}$	$\max_{t_j=0,\ldots,t_{\text{final}-1}}(Y_i(t_j), 0)$	10
Levels of phosphorylated Axin should drop to below 60% of the initial level.	$A_p+C+D+E$	$\frac{X(t_{\text{final}})}{X(0)}$	$\max(0, Y_i - 0.6)$	1
Monotonic increase in levels of phospho LRP6	$L_p + C + E$	$\frac{X(t_{i+1})-X(t_i)}{\delta t}$, $t_i = 0, \ldots, t_{\text{final}-1}$	$\min_{t_j=0,\ldots,t_{\text{final}-1}}(Y_i(t_j), 0)$	10
Levels of LRP6/Axin complex should increase within half hour	$C + E$	$\frac{X(0.5h)}{X(0)}$	$\max(0, 2 - Y_i)$	10
Levels of LRP6/Axin complex should drop by three hours	$C + E$	$\frac{X(0.5h)}{X(3h)}$	$\max(0, 1.2 - Y_i)$	10
Levels of LRP6/Axin complex should stay above the original non-stimulated levels	$C + E$	$\frac{X(3h)}{X(0)}$	$\max(0, 1.5 - Y_i)$	10
Levels of Axin/β-catenin should not have a sharp increase in the first half hour	$D + E$	$\frac{X(0.5h)}{X(0)}$	$\max(0, Y_i - 1.1)$	1
Levels of Axin/β-catenin increase over three hours	$D + E$	$\frac{X(3h)}{X(0)}$	$\max(0, 1.5 - Y_i)$	1
Maximum levels of LRP6/Axin complex should be reached between 5 minutes and 60 minutes.	$C + E$	$\arg\max_t X_i(t)$	$\lvert Y_i - 1\rvert$ if $Y_i > 1$, $\lvert Y_i - 5/60\rvert$ if $Y_i < 5/60$	1

TABLE B.3: Cost vector for qualitative fit of Extension 1 to results by Kim et al. (2013) as displayed in Figure 6.5.

Qualitative Requirement	**Output Variable (X)**	**Quantity of Interest (Y_i)**	Value (J_i)	**Weight (w_i)**
Monotonic decrease in levels of phospho Axin	$A_p+C+D+E$	$\frac{X(t_{i+1})-X(t_i)}{\delta t}$, $t_i = 0, \ldots, t_{\text{final}-1}$	$\max_{t_j=0,\ldots,t_{\text{final}-1}}(Y_i(t_j), 0)$	10
Levels of phosphorylated Axin should drop to below 60% of the initial level.	$A_p+C+D+E$	$\frac{X(t_{\text{final}})}{X(0)}$	$\max(0, Y_i - 0.6)$	1
Monotonic increase in levels of phospho LRP6	$L_p + C + E$	$\frac{X(t_{i+1})-X(t_i)}{\delta t}$, $t_i = 0, \ldots, t_{\text{final}-1}$	$\min_{t_j=0,\ldots,t_{\text{final}-1}}(Y_i(t_j), 0)$	10
Levels of LRP6/Axin complex should increase within half hour	$C + E$	$\frac{X(0.5h)}{X(0)}$	$\max(0, 2 - Y_i)$	10
Levels of LRP6/Axin complex should drop by three hours	$C + E$	$\frac{X(0.5h)}{X(3h)}$	$\max(0, 1.5 - Y_i)$	10
Levels of LRP6/Axin complex should stay above the original non-stimulated levels	$C + E$	$\frac{X(3h)}{X(0)}$	$\max(0, 1.5 - Y_i)$	10
Levels of Axin/β-catenin should not have a sharp increase in the first half hour	$D + E$	$\frac{X(0.5h)}{X(0)}$	$\max(0, Y_i - 1.1)$	1
Levels of Axin/β-catenin increase over four hours	$D + E$	$\frac{X(3h)}{X(0)}$	$\max(0, 1.5 - Y_i)$	1
Maximum levels of LRP6/Axin complex should be reached between 5 minutes and 60 minutes.	$C + E$	$\arg\max_t X(t)$	$\lvert Y_i - 1\rvert$ if $Y_i > 1$, $\lvert Y_i - 5/60\rvert$ if $Y_i < 5/60$	1
Levels of phosphorylated β-catenin should drop within the first hour	$D_p + E_p$	$\frac{X(1h)}{X(0)}$	$\lvert Y_i - 0.5\rvert$ if $Y_i > 0.5$	1
Levels of phosphorylated β-catenin should return to within 25% of the original value within 4 hours.	$D_p + E_p$	$\frac{X(4h)}{X(0)}$	$\lvert Y_i - 0.75\rvert$ if $Y_i < 0.75$, $\lvert Y_i - 1.25\rvert$ if $Y_i > 1.25$	1

TABLE B.4: Cost vector for qualitative fit of Extension 2 to results by Kim et al. (2013) as displayed in Figure 6.12A.

Qualitative Requirement	**Output Variable (X)**	**Quantity of Interest (Y_i)**	Value (J_i)	**Weight (w_i)**
Levels of Axin/LRP6 complex should increase between 0 and 4 hours	$C + E + E_p$	$\frac{X(4h)}{X(0)}$	$\lvert Y_i - 3\rvert$ if $Y_i < 3$	10
Levels in phosphorylated LRP6 should be monotonically increasing	L_p+C+E+E_p	$\frac{X(t_{i+1})-X(t_i)}{\delta t}$, $t_i = 0, \ldots, t_{\text{final}-1}$	$\min_{t_j=0,\ldots,t_{\text{final}-1}}(Y_i(t_j), 0)$	10
Levels of phosphorylated β-catenin should not increase too quickly	$D_p + E_p$	$\frac{X(0.5h)}{X(0)}$	$\lvert Y_i - 1.1\rvert$ if $Y_i < 1.1$	1
Levels of phosphorylated β-catenin should increase over 2 hours.	$D_p + E_p$	$\frac{X(2h)}{X(0)}$	$\lvert Y_i - 1.5\rvert$ if $Y_i < 1.5$	1

TABLE B.5: Cost vector for qualitative fit of Extension 2 to results by Li et al. (2012) as displayed in Figure 6.12B

Qualitative Requirement	**Output Variable (X)**	**Quantity of Interest (Y_i)**	Value (J_i)	**Weight (w_i)**
Levels of Axin/LRP6 complex should increase at least 1.5 fold	$C + E + E_p$	$\frac{X(t_{\text{final}})}{X(0)}$	$\lvert Y_i - 1.5\rvert$ if $Y_i < 1.5$	10
Levels of Axin/LRP6 complex should increase monotonically	$C + E + E_p$	$\frac{X(t_{i+1})-X(t_i)}{\delta t}$, $t_i = 0, \ldots, t_{\text{final}-1}$	$\min_{t_j=0,\ldots,t_{\text{final}-1}}(Y_i(t_j), 0)$	10
Levels of Axin/β-catenin compelex should drop at least 80%	D+E+D_p+E_p	$\frac{X(t_{\text{final}})}{X(0)}$	$\lvert Y_i - 0.8\rvert$ if $Y_i > 0.8$	1
Levels of Axin/active β-catenin complex should drop at least 80%	$D + E$	$\frac{X(t_{\text{final}})}{X(0)}$	$\lvert Y_i - 0.8\rvert$ if $Y_i > 0.8$	1
Levels of Axin/β-catenin complex should decrease monotonically	D+E+D_p+E_p	$\frac{X(t_{i+1})-X(t_i)}{\delta t}$, $t_i = 0, \ldots, t_{\text{final}-1}$	$\max_{t_j=0,\ldots,t_{\text{final}-1}}(Y_i(t_j), 0)$	1
Levels of Axin/LRP6 complex should not increase too quickly	$C + E + E_p$	$\frac{X(2h)}{X(0.5h)}$	$\lvert Y_i - 1.2\rvert$ if $Y_i < 1.2$	1

TABLE B.6: Cost vector for qualitative fit of Extension 2 to results by Azzolin et al. (2014) as displayed in Figure 6.12C

Appendix C

Parameter values for candidate models in Chapter 4

Model	Index	k_4	k_{-5}	k_{-2}	k_2	k_3	k_5	K_3	K_7	K_5	k_{-6}	k_6	k_1	k_{-1}	τ	w_3	A_{tot}
H_{11}	0	3228.7	122.7	4.162e-03	1.167e-04	3.323e-04	12404.8	204.4	313.5	35.60	5.691	1.465e-02	2.641e-02	2.777e-04	11.10	50.93	2.190
H_{11}	1	3.117	1.951	1.069e-04	3.562e-04	1.501e-04	468938.6	436.0	4039.6	2.552	0.177	7.515e-03	1.006e-02	1.132e-04	14.57	53.44	9.638
H_{11}	2	6356.0	1448.3	0.188	67.81	8847.3	1831.8	2378.9	457.0	1.140e-02	0.125	1.127	3.897e-03	1.004e-04	8.406	9.241	144.5
H_{11}	3	1802.0	177.5	1.239e-04	1.154e-04	1.540e-04	10.96	2462.6	1184.3	0.663	21.67	4.880	9.963e-03	1.046e-04	16.88	29.58	43.88
H_{11}	4	0.323	104.0	1.028e-04	1.206e-04	10.16	6.262e-02	820.7	84.89	158.8	330.2	612.2	7.543e-03	1.028e-04	17.54	7.110	98.18

TABLE C.1: Parameter sets found using the multi-start CMA-ES algorithm for model H_{11} that reproduce experimental observations by Kim et al. (2013).

Model	Index	k_4	k_{-5}	k_{-2}	k_2	k_3	k_5	K_3	K_7	K_5	k_{-6}	k_6	k_1	k_{-1}	τ	w_4	A_{tot}
H_{21}	0	26.31	20.15	0.483	1.225e-03	405.9	10338.1	983.6	18.33	0.588	0.421	68.01	7.140e-03	3.567e-04	15.15	5.343	115.4
H_{21}	1	1.944e-03	4.120e-03	3.740e-02	2.335e-04	1379.2	274.5	549.1	0.496	0.453	0.532	168.5	1.467e-02	8.934e-03	8.458	96.02	111.7
H_{21}	2	57.00	1985.7	408.7	46.89	0.366	5053.9	2539.6	7448.5	5.518e-02	0.304	1.042	1.226e-03	4.417e-03	15.17	88.88	149.9
H_{21}	3	51.71	19.15	8.501e-03	0.163	9.693e-03	7182.6	955.5	6110.7	1.124	3.178	351.7	1.424e-02	3.434e-04	10.11	8.080	52.84
H_{21}	4	6.843e-03	9.416e-03	3.823e-02	4.638e-04	1.413e-03	0.105	3542.6	575.6	30.51	578.6	3.785	5.572e-03	2.078e-04	5.041	35.69	81.14
H_{21}	5	677.8	2523.6	8.743e-02	4.040e-04	2.365e-03	1106.0	361.2	2734.6	0.536	64.34	1216.2	1.107e-04	2.149e-02	7.922	13.93	106.4
H_{21}	6	5063.5	2084.9	7.229e-02	0.309	68.66	11160.9	218.3	118.1	1.129e-02	282.2	3177.9	0.726	7.274	8.892	5.717	3.359
H_{21}	7	62.10	114.7	9.381	26.45	5.960e-02	98808.7	9167.7	7409.3	2.746e-02	0.183	0.404	5.202e-03	1.119e-04	19.79	73.30	150.0
H_{21}	8	1476.9	1597.3	1147.6	4.583	600278.8	938942.9	1379.2	1.081	0.744	0.205	8.160	2.624e-03	2.281e-03	14.44	6.166	103.1
H_{21}	9	816.5	3120.6	2.195e-02	127.3	2.201	173.3	465.6	222.9	1.139e-02	25.82	378.0	1.111e-02	1.227e-02	9.614	56.45	64.21
H_{21}	10	1644.7	7836.0	1.231e-02	378.5	4.381	3873.1	426.5	641.5	1.047e-02	20.66	673.7	4.045e-02	0.196	10.08	48.12	81.87
H_{21}	11	178.3	500.0	4.204e-02	4.858e-03	8.442e-04	79673.1	500.9	288.0	36.20	1786.9	272.2	6.088e-03	1.203e-04	14.84	40.75	118.1
H_{21}	12	0.424	0.339	1.444e-02	1.029e-03	3308.5	750.4	5718.1	0.282	129.3	3.342	877.2	1.076e-02	1.077e-04	11.76	17.37	150.0
H_{21}	13	56.29	208.5	4.166e-04	8.567	7.381	397.5	204.1	299.6	1.092e-02	32.97	977.9	0.313	2.951e-04	14.11	59.30	68.06
H_{21}	14	2597.7	3817.3	3.822e-04	4.649e-04	98.71	46206.6	73.99	106.9	1.000e-02	402.0	5041.9	15.51	16.39	15.72	12.58	8.043
H_{21}	15	59.49	95.84	115.2	0.204	20182.2	283513.4	9426.2	0.165	2.958	1.821	4.902e-04	3.587e-03	2.337e-04	14.63	7.766	35.60

TABLE C.2: Parameter sets found using the multi-start CMA-ES algorithm for model H_{21} that reproduce experimental observations by Kim et al. (2013).

Model	Index	k_4	k_{-5}	k_{-2}	k_2	k_3	k_5	K_3	K_7	K_5	k_{-6}	k_6	k_1	k_{-1}	τ	w_4	A_{tot}
H_{22}	0	0.628	1.030	2.333e-02	5.490e-04	1.614e-04	411.0	590.7	1089.4	3.984e-02	517.5	407.4	4.052e-03	1.218e-02	1.491	28.97	149.9
H_{22}	1	88.26	2517.9	139.1	39.26	0.252	173.6	2328.7	3320.9	0.653	0.536	1.614	1.366e-02	1.006e-04	11.19	89.35	39.41
H_{22}	2	180.7	3460.1	262.8	2.428	0.144	2576.6	3897.8	7372.4	1.514e-02	0.808	4.453	1.241e-03	1.896e-04	11.01	36.07	4.551
H_{22}	3	38.62	161.3	0.259	1.414e-03	4.351e-04	2591.0	1777.1	4158.8	5.515	300.0	845.9	9.298e-04	6.463e-03	9.124	11.44	114.3
H_{22}	4	911.8	854.1	150.9	2.024	1.850	6020.2	2044.0	2594.2	3.573	0.415	0.195	6.037e-03	1.644e-04	13.61	11.08	21.18
H_{22}	5	0.184	5.092	0.862	2.845e-02	3.541e-03	220.9	577.0	617.9	0.152	0.334	0.418	8.132e-03	1.486e-04	13.94	55.03	3.465
H_{22}	6	239.2	1040.3	642.5	0.783	7.755	33801.1	695.7	1266.8	7.551e-02	0.250	0.668	2.176e-03	8.077e-04	12.66	13.02	2.776
H_{22}	7	119.2	415.6	0.189	1.201e-04	1.900e-04	8297.3	3093.5	9949.1	4.805	1000.4	230.7	1.139e-02	3.162e-04	7.875	8.816	3.855
H_{22}	8	162.0	5238.0	651.3	55.72	0.459	4794.4	5787.6	3174.4	7.054	1.278	2.635	2.033e-03	1.665e-04	8.169	84.92	146.5
H_{22}	9	4.130	8.020	1.608e-02	0.121	4.028e-04	2957.8	2144.6	11.48	12.34	0.497	0.289	7.511e-03	1.506e-03	13.31	36.36	129.0

TABLE C.3: Parameter sets found using the multi-start CMA-ES algorithm for model H_{22} that reproduce experimental observations by Kim et al. (2013).

Model	Index	k_4	k_{-5}	k_{-2}	k_2	k_3	k_5	K_3	K_7	K_5	k_{-6}	k_6	k_1	k_{-1}	τ	w_3	w_7	A_{tot}
H_{31}	0	1508.8	827.8	6.397e-02	1.000e-04	2.104e-05	434.8	4383.7	8344.1	330.6	6386.1	549.9	2.501e-02	1.891e-03	9.488	5.193	26.38	68.27
H_{31}	1	101.8	128.5	22.77	0.473	250037.2	7.326e-04	25.13	1.001e-02	128.2	2.888e-03	174.8	4.490e-02	0.527	11.84	73.56	66.75	1.883
H_{31}	2	3450.7	603.0	1.010e-04	2.394e-04	3.867e-04	232.1	304.7	14.25	13.18	238.2	11.35	6.371e-02	0.198	11.99	98.28	29.46	1.172
H_{31}	3	5.720e-02	3.029	1.236e-04	1.022e-04	7748.8	0.141	15.36	1.003e-02	12.43	4.029	3.282	9.451e-02	2.251e-04	19.95	80.18	4.894	1.482e-03
H_{31}	4	5.137e-02	4.208	1.834e-04	2.051e-04	3.509e-02	126603.1	15.40	86.90	242.6	23.04	8.460	0.436	0.129	19.98	99.98	94.95	1.011e-03
H_{31}	5	98.79	25.27	7.112e-03	1.318e-03	2.255e-03	39.05	86.18	1.014	121.5	2.134	1.157e-02	1.339e-02	3.726e-02	18.24	95.41	22.43	0.444
H_{31}	6	40.91	8497.3	2.005e-02	4.656e-03	1.665e-03	1.296e-02	55.92	147.6	328.9	15.05	2.529e-04	2.680e-03	5.146e-04	14.64	18.91	99.78	4.851
H_{31}	7	9999.9	1089.7	0.881	0.657	45855.0	479.1	1199.7	1.203e-02	1.130e-02	18.02	60.62	7.113e-02	1.162e-04	12.14	5.828	6.737	6.940
H_{31}	8	8.411e-02	0.572	1.560e-02	2.006e-04	1.158e-02	0.461	18.86	9.503	1.007e-02	1.441	1.281	1.097	536.7	20.00	65.12	65.98	2.723e-03
H_{31}	9	0.429	0.121	2.851e-02	5.890e-04	2.261e-03	5.786	847.1	0.725	102.8	152.2	3.927	1.048e-03	4.542e-03	13.96	14.48	74.90	59.68
H_{31}	10	8403.6	4382.0	2.353e-03	6.024e-02	0.160	570.3	3817.5	1312.5	68.41	133.5	7460.4	1.810e-02	2.380	14.63	5.018	66.40	16.90

TABLE C.4: Parameter sets found using the multi-start CMA-ES algorithm for model H_{31} that reproduce experimental observations by Kim et al. (2013).

Model	Index	k_4	k_{-5}	k_{-2}	k_2	k_3	k_5	K_3	K_7	K_5	k_{-6}	k_6	k_1	k_{-1}	τ	w_3	w_7	A_{tot}
H_{32}	0	607.0	8385.6	10.36	47.95	18396.2	9301.2	33.22	325.6	21.19	0.168	0.313	2.371e-03	5.680e-04	10.46	12.35	86.81	6.534
H_{32}	1	42.57	441.9	4.234e-04	2.029	92.90	6444.8	479.9	663.9	19.18	0.446	2.128	2.609e-04	1.202e-04	8.533	3.989	99.36	31.44
H_{32}	2	41.63	363.6	0.109	1.401e-04	1.986e-04	176.1	407.7	173.8	717.5	326.8	27.75	3.021e-03	1.131e-04	7.765	4.247	99.51	36.39
H_{32}	3	1623.0	3060.5	0.331	1.006	2088.9	13169.5	2517.4	3381.4	3.018	2.451	56.90	2.256e-04	1.151e-04	9.893	4.433	99.28	52.73
H_{32}	4	62.09	7521.0	0.273	1.536	96.36	63.01	18.75	2156.8	129.0	0.668	8.249e-02	3.054e-03	1.707e-04	12.84	23.72	79.24	3.061
H_{32}	5	121.9	826.5	4.034e-02	1.041	9534.5	143.9	671.9	1044.3	1288.2	3.366	20.17	5.893e-03	5.588e-04	8.577	3.129	98.32	34.29
H_{32}	6	4263.8	642.8	3.517e-02	1.007e-04	5.132e-05	1247.5	1304.0	73.14	1821.4	4453.3	14.43	5.746e-03	6.903e-04	7.753	11.55	54.09	47.52
H_{32}	7	346.7	865.1	7.712e-02	2.432	585004.3	9.200	277.1	177.3	48.01	0.643	2.541	1.007e-04	1.053e-04	10.84	5.573	99.33	27.64
H_{32}	8	0.251	0.373	6.855e-04	1.472e-04	13280.5	6215.6	3621.2	1270.9	1702.6	1711.1	646.6	1.620	33.03	17.44	8.915	98.81	123.5

TABLE C.5: Parameter sets found using the multi-start CMA-ES algorithm for model H_{32} that reproduce experimental observations by Kim et al. (2013).

Model	Index	k_4	k_{-5}	k_{-2}	k_2	k_3	k_5	K_3	K_7	K_5	k_{-6}	k_6	k_1	k_{-1}	τ	w_4	w_7	A_{tot}
H_{61}	0	1477.8	996.8	6.673e-02	1.020e-04	9.401e-05	8092.8	5457.6	9047.8	1.884	1878.5	5416.1	3.111e-02	1.072e-04	12.10	9.066	14.46	0.476
H_{61}	1	57.30	95.72	1.000e-04	0.242	3.626	63.62	68.90	0.882	1.432e-02	16.67	35.16	0.132	1.788e-02	9.104	35.89	7.331	12.12
H_{61}	2	253.6	139.6	2.152e-04	1.621	65.62	746014.9	182.6	17.01	2.019e-02	66.21	4233.0	0.715	0.129	9.610	14.87	6.612	30.56
H_{61}	3	196.6	626.6	3.868e-02	2.751e-04	2.029e-04	158.6	541.9	1481.7	0.144	284.4	401.2	6.319e-03	7.079e-03	1.838	14.58	1.540	0.229
H_{61}	4	263.8	1321.1	0.729	7.884e-03	2.657e-04	1942.6	6147.7	1104.7	2.115	409.5	696.8	1.717e-03	1.423e-02	11.04	10.80	11.58	65.00
H_{61}	5	113.3	371.2	6.311e-02	1.701e-04	5.073e-04	360.2	373.9	14.43	8.407e-02	1465.6	558.0	1.200e-03	1.141e-02	10.53	10.68	22.15	21.84
H_{61}	6	1103.2	4312.6	1.309	312.5	75.19	1357.7	282.9	100.2	1.443e-02	3.677	1636.4	2.828e-02	2.272e-03	9.047	68.99	52.59	35.14
H_{61}	7	7.787	30.53	7.007	0.290	366692.4	3922.1	70.00	1.018e-02	2.404e-02	0.105	26.88	1.849e-02	1.029e-04	8.707	27.29	16.10	31.08
H_{61}	8	46.17	95.55	1.290e-02	0.538	8887.5	594.9	225.7	1.437e-02	0.143	42.50	624.5	0.137	0.362	9.441	25.01	11.61	65.48
H_{61}	9	180.9	31.96	1.290e-04	1.447e-02	0.842	500.0	2576.8	6.050	1.138e-02	542.4	1435.7	9.031e-02	1.501	9.308	3.023	14.73	34.13
H_{61}	10	481.6	25.43	3.634e-03	0.858	0.372	37.81	3011.2	24.21	1.222e-02	12.66	545.1	7.440e-02	6.722e-04	9.882	14.96	17.21	15.12
H_{61}	11	4407.7	2262.1	9.523e-04	0.204	3.084e-02	6807.7	2119.7	77.20	6.601e-02	7486.9	8084.5	1.951e-02	1.774	9.262	4.307	3.677	73.25
H_{61}	12	878.8	3094.1	9.254e-02	1.010e-04	3.619e-04	77.53	939.2	959.7	9.809	2802.7	358.6	3.732e-03	1.947e-04	6.375	11.17	1.125	17.67
H_{61}	13	241.2	269.7	0.321	15.10	2276.1	202.5	842.8	1.957e-02	1.279e-02	201.1	2303.5	2.595e-02	0.146	9.178	17.99	60.55	18.44
H_{61}	14	226.4	460.8	1.552e-02	3.771	10.72	1198.6	301.4	1.471	2.155	91.84	108.5	0.122	0.147	9.671	20.15	14.50	57.78
H_{61}	15	750.6	658.8	1.196e-02	8.471e-02	7867.6	2076.9	92.60	1.179	1.000e-02	10.28	1044.6	0.183	1.822	11.43	15.32	7.321	5.312
H_{61}	16	1918.5	4327.6	1.872e-02	58.94	330.9	1625.2	106.5	0.467	1.009e-02	4921.1	7145.3	23.63	1.016	12.23	38.02	15.10	24.15
H_{61}	17	76.28	302.6	5.194	20.43	1486.6	417.7	116.3	2.952	1.004e-02	30.81	6776.4	2.118e-02	5.246e-02	11.49	54.90	14.85	26.76
H_{61}	18	856.9	5266.6	2.768	142.3	6.138	42.79	367.9	24.91	0.111	64.53	3181.3	4.265e-02	4.578e-02	11.28	49.11	64.75	74.04
H_{61}	19	13.89	193.8	5.723e-02	0.690	0.114	0.908	183.3	371.0	1.064e-02	30.73	3612.0	2.013e-04	5.686e-03	13.31	73.40	6.926	4.981
H_{61}	20	58.52	29.89	7.010e-02	0.389	823.8	880.0	3849.5	1.285e-02	41.22	47.14	310.3	1.766e-04	3.579e-02	13.57	8.513	16.98	58.91
H_{61}	21	591.8	4168.2	4.703e-04	187.7	4.828	80.18	310.6	2.417	1.065e-02	79.35	336.8	1.553	1.134e-04	18.28	98.75	46.08	83.67

TABLE C.6: Parameter sets found using the multi-start CMA-ES algorithm for model H_{61} that reproduce experimental observations by Kim et al. (2013).

Model	Index	k_4	k_{-5}	k_{-2}	k_2	k_3	k_5	K_3	K_7	K_5	k_{-6}	k_6	k_1	k_{-1}	τ	w_4	w_7	A_{tot}
H_{62}	0	106.5	470.3	4.792e-02	2.540e-04	5.458e-04	223.4	296.0	177.8	6.215e-02	242.4	2217.8	1.551e-02	1.894e-02	9.038	19.00	42.91	87.55
H_{62}	1	1.092e-02	2.562e-02	2.459e-02	1.652e-04	8.429e-04	259.8	138.2	22.12	4.554e-02	338.3	179.7	6.321e-03	3.059e-04	5.617	61.09	2.037	40.16
H_{62}	2	249.0	360.1	1.954e-02	4.360e-03	4.308e-04	1209.1	263.1	0.553	2.526e-02	25.06	9.643	4.088e-03	1.018e-04	7.719	31.48	7.282	66.94
H_{62}	3	409.4	342.9	4.642	8.119e-02	6.917	689.2	2576.4	674.8	11.61	0.889	4.871e-02	1.266e-02	1.001e-04	14.45	9.426	88.32	122.3
H_{62}	4	3.317e-02	0.136	3.427e-02	3.482e-03	4.600e-04	57.64	711.4	3.838	355.9	593.3	17.78	8.201e-03	1.328e-04	7.302	61.91	34.90	79.88
H_{62}	5	59.33	312.2	73.12	9.123	2.898	465.2	201.6	1804.8	3.405e-02	0.210	3.403	1.882e-02	1.065e-04	15.02	36.02	70.89	44.13
H_{62}	6	1683.9	821.0	1.641e-02	2.113e-02	1.613e-03	22414.1	506.4	236.4	4.674e-02	66.92	1395.4	4.888e-04	5.678e-04	14.03	15.79	8.153	67.45
H_{62}	7	1.358	1.818	5.573e-02	1.026e-04	4.998e-04	3240.2	642.0	1611.0	1.365	83.10	430.4	1.577e-02	1.504e-04	12.95	20.96	3.323	4.531
H_{62}	8	0.519	1.843	2.957e-02	1.321e-04	1.970e-03	32.91	55.07	2323.5	1.215e-02	2.686	1557.0	1.160e-04	1.415e-04	2.095	43.27	8.397	15.76
H_{62}	9	4.796	13.68	4.116e-02	4.897e-04	9.845e-05	449643.3	1287.6	2762.2	0.530	296.3	479.4	3.060e-03	1.855e-02	13.27	21.95	1.927	46.41
H_{62}	10	0.165	0.514	2.374e-02	2.297e-04	4.918e-04	416.5	354.6	21.84	6.435	475.4	185.5	2.080e-03	1.008e-04	9.792	39.50	1.547	97.01
H_{62}	11	1.909	5.094	3.372e-02	1.043e-04	3.370e-04	469.5	699.0	19.17	30.10	3252.0	535.9	2.605e-03	6.053e-04	13.76	33.24	2.490	122.8
H_{62}	12	9270.5	1160.4	8.044e-02	1.740e-03	1.153e-03	78478.9	1377.7	39.67	1.013e-02	32.10	1334.2	1.474e-04	2.347e-03	7.290	2.850	77.03	1.452
H_{62}	13	359.0	4219.8	219.3	60.39	0.132	212.2	6498.4	9483.6	8.179	1.173	651.9	1.318e-03	1.214e-02	10.48	38.46	61.47	115.4
H_{62}	14	19.74	30.81	6.553e-03	0.649	1.694e-03	578.8	1376.6	61.22	0.699	5.197	215.0	2.528e-03	3.659e-03	13.86	19.53	86.99	100.1
H_{62}	15	225.6	307.8	3.986e-02	1.016e-02	3.312e-04	14.48	501.0	67.72	2.833e-02	579.7	527.8	4.299e-03	1.376e-03	17.68	12.97	1.000	52.52
H_{62}	16	713.8	339.6	3.991e-04	1.219e-04	1.316e-02	240.5	7446.6	1279.6	169.0	1.967	9.561	1.400e-02	1.013e-04	17.06	9.808	78.69	106.4
H_{62}	17	11.20	53.40	0.457	0.201	0.806	3112.6	3898.9	190.1	31.18	0.432	2.217	5.446e-03	1.306e-04	13.42	73.45	99.16	0.103

TABLE C.7: Parameter sets found using the multi-start CMA-ES algorithm for model H_{62} that reproduce experimental observations by Kim et al. (2013).

k_{-2}	k_2	k_3	K_3	K_4	k_1	k_{-1}	τ	w_4	A_{tot}
0.130	7.959e-03	1.133e-02	887.0	1567.8	9.362e-03	1.214e-02	16.29	38.50	71.76
71.58	2.455	12.28	77.26	5.050e-02	1.006e-04	2.634e-02	19.99	51.78	148.4
34.41	3.702e-03	64.76	3946.7	52.35	2.793e-03	9.671e-03	13.98	19.85	27.00
161.2	4.121e-03	19.07	185.8	2186.3	3.058e-04	7.880e-03	11.17	9.073	149.6
137.3	7.111e-04	84.70	52.29	133.4	2.130e-03	2.068e-02	11.11	20.97	150.0
884.7	3.202e-03	387.8	2292.6	686.4	9.233e-04	2.352e-02	11.19	15.37	148.0
0.322	3.606e-03	0.125	0.244	0.278	1.001e-04	6.091e-03	18.87	65.04	147.7
365.8	4.018e-03	55.83	66.90	80.44	3.527e-03	2.043e-02	11.53	21.96	149.4

TABLE C.8: Parameter sets found using the multi-start CMA-ES algorithm for our simplified reduced model that reproduce experimental observations by Kim et al. (2013).

Appendix D

Parameter values for candidate models in Chapter 6

Model	Index	k_{-2}	k_2	k_3	K_3	K_4	k_1	k_{-1}	k_5	K_5	s	d	τ	w_2	A_{tot}
M_{13}	0	245.4	0.352	7.649e-02	0.727	2.528	1.615e-03	3.385e-02	52.65	758.4	0.987	435.6	14.61	99.70	6.864
M_{13}	1	14.45	0.170	0.508	10.36	0.250	7.715e-05	2.197e-02	423975.8	193.4	0.582	120.3	19.89	52.76	76.37
M_{13}	2	2.149e-02	2.940e-03	2.664e-02	11.77	1.832	9.120e-03	4.656e-04	391176.6	1.039e-02	2.634e-02	2.966e-02	19.83	29.23	6.397
M_{13}	3	116.1	7.898	8.642e-03	5.059	7.632	1.614e-05	1.424e-02	10032.7	14.93	0.107	3552.8	9.314	24.67	0.558

TABLE D.1: Parameter sets found using the multi-start CMA-ES algorithm for model M_{31} that reproduce experimental observations by Kim et al. (2013).

Model	Index	k_{-2}	k_2	k_3	K_3	K_4	k_1	k_{-1}	k_5	K_5	s	d	τ	w_2	w_{-4}	A_{tot}
M_{23}	0	890.1	1.892	9.445e-02	0.142	0.922	3.177e-03	8.633e-02	30.09	4807.5	7.851e-02	4112.9	20.00	81.08	3.705	2.746
M_{23}	1	397.7	55.50	7.404e-03	0.257	24.02	5.994e-06	2.603e-04	237.3	330.9	0.284	2138.9	6.688	19.45	0.547	60.34
M_{23}	2	8.488e-02	9.837e-05	130.8	1.347	1.050e-02	7.465e-03	1.967e-02	26.50	153.7	0.601	26.50	16.01	61.36	0.620	14.55
M_{23}	3	9.138	1.287	5.418e-03	1.597	47.21	4.031e-03	3.631e-03	22675.9	6.400	0.255	2.037	8.050	83.33	0.401	4.681
M_{23}	4	98.66	1.574	4.413	3.119	3.726e-02	3.828e-03	2.951e-05	159813.1	52.16	0.850	13.52	19.35	11.88	0.537	3.515

TABLE D.2: Parameter sets found using the multi-start CMA-ES algorithm for model M_{32} that reproduce experimental observations by Kim et al. (2013).

Model	Index	k_{-2}	k_2	k_3	K_3	K_4	k_1	k_{-1}	k_5	K_5	s	d	k_6	k_{-6}	τ	w_2	A_{tot}
N_{13}	0	2.852e-02	9.228e-05	0.319	0.441	2.489	1.571e-02	2.399e-03	5.142e-02	2.541	0.338	1.066	0.613	1.455e-05	5.717	96.92	134.8
N_{13}	1	2.748e-02	3.645e-04	0.226	0.611	0.859	1.222e-02	3.714e-03	570.9	1.006e-02	6.059e-02	0.178	8.336e-02	5.498e-03	9.212	60.30	73.58

TABLE D.3: Parameter sets found using the multi-start CMA-ES algorithm for model N_{13} that reproduce experimental observations by Kim et al. (2013).

Model	Index	k_{-2}	k_2	k_3	K_3	K_4	k_1	k_{-1}	k_5	K_5	s	d	k_6	k_{-6}	τ	w_2	A_{tot}
N_{13}	0	20.11	0.529	12.29	1.711e-02	2.098	7.222	6222.6	2.706	1.565e-02	0.513	119.2	642.7	5847.0	15.98	27.38	22.62
N_{13}	1	17.57	0.300	12.03	0.347	4.769	7.239	18.93	15732.0	637.5	0.746	511.4	12.06	27.03	20.00	42.76	12.88
N_{13}	2	81.75	1.094	125.7	1.096	6.173	11.26	232.3	5.053	362.4	0.531	4149.2	13.98	82.81	18.47	94.67	71.59
N_{13}	3	58.43	3.348	7.315	1.383	2.878	6.562	46.68	0.621	42.82	0.412	62.24	18.99	167.2	19.21	84.06	6.867
N_{13}	4	14.16	0.104	10.81	2.927e-02	0.629	4.896	12.88	11046.4	6932.5	0.394	20.94	1374.6	6.932	15.47	42.98	1.492
N_{13}	5	209.3	1.004	27.76	0.521	1.020	8170.2	70.42	2.005e-02	4140.3	0.345	362.6	221.1	5620.4	13.69	90.15	14.84
N_{13}	6	7.006	0.290	78.80	1.093e-02	7.979	3.792	359.5	448.4	30.55	4.340e-02	3649.8	7.927	283.7	19.82	46.89	19.49
N_{13}	7	53.61	0.344	2.132	0.635	2.610	3.339e-02	2.758	536.5	45.26	0.103	21.51	12.20	1.126e-05	17.66	57.08	23.35
N_{13}	8	108.1	0.536	2.345e-02	0.499	8.266e-02	314.1	33.04	377.0	368.6	5.686e-02	0.972	1094.6	43.26	19.88	12.93	1.193
N_{13}	9	92.54	0.134	1.088e-02	0.173	1.030	175.6	13.26	2.206	55.52	6.793e-02	8.225	104.6	36.20	19.79	76.22	0.236

TABLE D.4: Parameter sets found using the multi-start CMA-ES algorithm for model N_{13} that reproduce experimental observations by Li et al. (2012). Showing only 10 of 54 fits found.

Model	Index	k_{-2}	k_2	k_3	K_3	K_4	k_1	k_{-1}	k_5	K_5	s	d	k_6	k_{-6}	τ	w_2	A_{tot}
N_{13}	0	28.50	0.407	22.50	233.3	26.90	370.0	0.675	5.190e-02	22.54	0.626	6.295	9.446	11.74	19.82	12.45	10.23
N_{13}	1	64.66	0.153	27.62	12.32	35.78	17.55	632.8	28.50	6.955e-02	0.615	40.77	38.34	1530.1	20.00	20.73	4.618
N_{13}	2	1897.8	3.124	48.69	97.00	38.05	4.259	86.84	11.44	0.301	0.348	46.16	14.38	1807.1	19.84	36.97	23.27
N_{13}	3	19.68	0.129	19.21	4.394	8743.7	126.9	24.42	0.311	48.00	0.754	10.82	13.71	5.605	19.83	9.680	2.729
N_{13}	4	55.87	0.560	43.91	3330.7	50.33	2.627	19.26	1.680	4.134e-02	0.374	4.310	20.91	196.3	19.97	15.05	5.225
N_{13}	5	196.0	0.442	693.8	141.1	11.72	167.7	33.00	0.394	73.13	0.790	74.72	12.23	110.8	19.61	21.41	15.80
N_{13}	6	33.43	0.129	41.69	950.1	44.15	0.772	59.26	8.164	2.856e-02	0.987	5.651	20.31	34.82	19.77	17.89	4.752
N_{13}	7	10.93	0.132	22.45	12.24	716.2	7781.4	4.320	0.441	1.423	0.306	7.679	54.98	91.37	19.95	12.59	0.638
N_{13}	8	13.00	0.179	5.936	46.16	52.63	8.779	343.8	2.690	0.114	0.519	6.377	4.479	12.19	19.79	8.379	9.459
N_{13}	9	31.04	0.210	63.46	178.0	161.0	1023.4	20.05	0.328	40.21	0.843	40.69	38.93	2744.8	20.00	28.72	20.15
N_{13}	10	4369.9	60.35	182090.3	1755.4	1.478	3432.0	995.9	2.214e-02	474.8	0.891	685.6	911.8	1704.1	19.97	9.376	20.67

TABLE D.5: Parameter sets found using the multi-start CMA-ES algorithm for model N_{13} that reproduce experimental observations by Azzolin et al. (2014). Showing 10 of the 93 fits found.

Bibliography

Alberghina, L. (Lilia) and Hans V. Westerhoff (2005). Systems biology : definitions and perspectives. Springer, p. 408.

Alon, Uri (2007). An introduction to systems biology : design principles of biological circuits. Chapman & Hall/CRC.

Amerongen, Renée van (2012). Alternative Wnt pathways and receptors. *CSH Perspect. Biol.* 4.10.

Amit, Sharon, Sharon Amit, Ada Hatzubai, Ada Hatzubai, Yaara Birman, Yaara Birman, Jens S Andersen, Jens S Andersen, Etti Ben-shushan, Etti Ben-shushan, Matthias Mann, Matthias Mann, Yinon Ben-neriah, Yinon Ben-neriah, Irit Alkalay, and Irit Alkalay (2002). Axin-mediated CKI phosphorylation of. *Genes Dev.* Pp. 1066–1076.

Aragona, Mariaceleste, Tito Panciera, Andrea Manfrin, Stefano Giulitti, Federica Michielin, Nicola Elvassore, Sirio Dupont, and Stefano Piccolo (2013). A mechanical checkpoint controls multicellular growth through YAP/TAZ regulation by actin-processing factors. *Cell* 154.5, pp. 1047–59.

Azzolin, Luca, Tito Panciera, Sandra Soligo, Elena Enzo, Silvio Bicciato, Sirio Dupont, Silvia Bresolin, Chiara Frasson, Giuseppe Basso, Vincenza Guzzardo, Ambrogio Fassina, Michelangelo Cordenonsi, and Stefano Piccolo (2014). YAP/TAZ incorporation in the β-Catenin Destruction Complex Orchestrates the Wnt Response. *Cell* 158.1, pp. 157–70.

Azzolin, Luca, Francesca Zanconato, Silvia Bresolin, Mattia Forcato, Giuseppe Basso, and Silvio Bicciato (2012). Role of TAZ as Mediator of Wnt Signaling. *Cell* 151.7, pp. 1443–1456.

Bafico, A, G Liu, A Yaniv, A Gazit, and S A Aaronson (2001). Novel mechanism of Wnt signalling inhibition mediated by Dickkopf-1 interaction with LRP6/Arrow. *Nat. Cell Biol.* 3.7, pp. 683–6.

Baker, Monya (2016). 1,500 scientists lift the lid on reproducibility. *Nature* 533.7604, pp. 452–454.

Barua, Dipak and William S Hlavacek (2013). Modeling the effect of APC truncation on destruction complex function in colorectal cancer cells. *PLoS Comput. Biol.* 9.9, e1003217.

Bass, J. J., D. J. Wilkinson, D. Rankin, B. E. Phillips, N. J. Szewczyk, K. Smith, and P. J. Atherton (2017). An overview of technical considerations for Western blotting applications to physiological research. *Scand. J. Med. Sci. Sports* 27.1, pp. 4–25.

Bazigou, Eleni and Charalampos Rallis (2007). Cell signaling and cancer. *Genome Biology* 8.7, p. 310.

Behrens, J, B A Jerchow, M Würtele, J Grimm, C Asbrand, R Wirtz, M Kühl, D Wedlich, and W Birchmeier (1998). Functional interaction of an axin homolog, conductin, with beta-catenin, APC, and GSK3beta. *Science* 280.5363, pp. 596–9.

Bilic, Josipa, Ya-Lin Huang, Gary Davidson, Timo Zimmermann, Cristina-Maria Cruciat, Mariann Bienz, and Christof Niehrs (2007). Wnt induces LRP6 signalosomes and promotes dishevelled-dependent LRP6 phosphorylation. *Science* 316.5831, pp. 1619–22.

Bovolenta, Paola, Pilar Esteve, Jose Maria Ruiz, Elsa Cisneros, and Javier Lopez-Rios (2008). Beyond Wnt inhibition: new functions of secreted Frizzled-related proteins in development and disease. *J. Cell Sci.* 121.Pt 6, pp. 737–46.

Bradford, M M (1976). A rapid and sensitive method for the quantitation of microgram quantities of protein utilizing the principle of protein-dye binding. *Anal. Biochem.* 72, pp. 248–54.

Brocardo, Mariana, Inke S Näthke, and Beric R Henderson (2005). Redefining the subcellular location and transport of APC: new insights using a panel of antibodies. *EMBO Rep.* 6.2, pp. 184–190.

Brunt, Lucy and Steffen Scholpp (2017). The function of endocytosis in Wnt signaling. *Cell. Mol. Life Sci.*

Cai, Jing, Anirban Maitra, Robert a Anders, Makoto M Taketo, and Duojia Pan (2015). β-Catenin destruction complex- independent regulation of Hippo – YAP signaling by APC in intestinal tumorigenesis. *Genes Dev.* Pp. 1–14.

Carballido-Landeira, Jorge and Bruno Escribano (2016). Nonlinear dynamics in biological systems, p. 128.

Cedersund, Gunnar and Jacob Roll (2009). Systems biology: Model based evaluation and comparison of potential explanations for given biological data. *FEBS J.* 276.4, pp. 903–922.

Chen, Jiawen, Zhong-Ru Xie, and Yinghao Wu (2014). Computational modeling of the interplay between cadherin-mediated cell adhesion and Wnt signaling pathway. *PLoS One* 9.6.

Chitalia, Vipul C., Rebecca L. Foy, Markus M. Bachschmid, Liling Zeng, Maria V. Panchenko, Mina I. Zhou, Ajit Bharti, David C. Seldin, Stewart H. Lecker, Isabel Dominguez, and Herbert T. Cohen (2008). Jade-1 inhibits Wnt signalling by ubiquitylating β-catenin and mediates Wnt pathway inhibition by pVHL. *Nat. Cell Biol.* 10.10, pp. 1208–1216.

Clevers, Hans and Roel Nusse (2012). Wnt/β-catenin signaling and disease. *Cell* 149.6, pp. 1192–205.

Coghill, George M., Ashwin Srinivasan, and Ross D. King (2008). Qualitative system identification from imperfect data. *J. Artif. Intell. Res* 32, pp. 825–877.

Collison, Lauren W., Greg M. Delgoffe, Clifford S. Guy, Kate M. Vignali, Vandana Chaturvedi, Delisa Fairweather, Abhay R. Satoskar, K. Christopher Garcia, Christopher A. Hunter, Charles G. Drake, Peter J. Murray, and Dario A.A. Vignali (2012). The composition and signaling of the IL-35 receptor are unconventional. *Nat. Immunol.* 13.3, pp. 290–299.

Collu, Giovanna M and Ana Hidalgo (2014). Wnt – Notch signalling crosstalk in development and disease, pp. 3553–3567.

Conacci-Sorrell, Maralice, Inbal Simcha, Tamar Ben-Yedidia, Janna Blechman, Pierre Savagner, and Avri Ben-Ze'ev (2003). Autoregulation of E-cadherin expression by cadherin-cadherin interactions: the roles of beta-catenin signaling, Slug, and MAPK. *J. Cell Biol.* 163.4, pp. 847–57.

Cselenyi, Christopher S., Kristin K. Jernigan, Emilios Tahinci, Curtis A. Thorne, Laura A. Lee, and Ethan Lee (2008). LRP6 transduces a canonical Wnt signal independently of Axin degradation by inhibiting GSK3's phosphorylation of β-catenin. *Proc. Natl. Acad. Sci. U.S.A.* 105.23.

Danos, Vincent, Jérôme Feret, Walter Fontana, and Jean Krivine (2007). Scalable Simulation of Cellular Signaling Networks. *Programming Languages and Systems*. Berlin, Heidelberg: Springer Berlin Heidelberg, pp. 139–157.

Delgoffe, Greg M. and Dario A.A. Vignali (2013). STAT heterodimers in immunity. *JAK-STAT* 2.1, e23060.

Downward, Julian and Subham Basu (2008). YAP and p73: A Complex Affair. *Mol. Cell* 32.6, pp. 749–750.

Duchartre, Yann, Yong Mi Kim, and Michael Kahn (2016). The Wnt signaling pathway in cancer. *Critical Reviews in Oncology/Hematology* 99, pp. 141–149.

Ellison, Phillipp, Haixia Ji, Daniel Knight, and Martin Feinberg (2014). Chemical Reaction Network Theory Toolbox.

Ferlay, J, I Soerjomataram, M Ervik, R Dikshit, S Eser, C Mathers, M Rebelo, DM Parkin, D Forman, and F Bray (2012). Globocan 2012: Estimated Cancer Incidence, Mortality and Prevalence Worldwide in 2012.

Feroz, F., M. P. Hobson, and M. Bridges (2009). MultiNest: An efficient and robust Bayesian inference tool for cosmology and particle physics. *Mon. Not. R. Astron. Soc.* 398.4, pp. 1601–1614.

Fiedler, Marc, Carolina Mendoza-Topaz, Trevor J Rutherford, Juliusz Mieszczanek, and Mariann Bienz (2011). Dishevelled interacts with the DIX domain polymerization interface of Axin to interfere with its function in down-regulating β-catenin. *Proc. Natl. Acad. Sci. U.S.A.* 108.5, pp. 1937–42.

Flunkert, V. and E. Schoell (2009). Pydelay - a python tool for solving delay differential equations.

Gammons, Melissa V., Miha Renko, Christopher M. Johnson, Trevor J. Rutherford, and Mariann Bienz (2016). Wnt Signalosome Assembly by DEP Domain Swapping of Dishevelled. *Mol. Cell* 64.1, pp. 92–104.

Gassmann, Max, Beat Grenacher, Bianca Rohde, and Johannes Vogel (2009). Quantifying Western blots: Pitfalls of densitometry. *Electrophoresis* 30.11, pp. 1845–1855.

Gelfand, Alan and Adrian F. M. Smith (1990). Sampling-Based Approaches to Calculating Marginal Densities. *J. Am. Stat. Assoc.* 85.410, pp. 398–409.

Gillespie, Daniel T (1976). A general method for numerically simulating the stochastic time evolution of coupled chemical reactions. *J. Comput. Phys.* 22.4, pp. 403–434.

Glinka, A, W Wu, H Delius, A P Monaghan, C Blumenstock, and C Niehrs (1998). Dickkopf-1 is a member of a new family of secreted proteins and functions in head induction. *Nature* 391.6665, pp. 357–62.

Goentoro, Lea and Marc W. Kirschner (2009). Evidence that Fold-Change, and Not Absolute Level, of β-Catenin Dictates Wnt Signaling. *Mol. Cell* 36.5, pp. 872–884.

Gottardi, Cara J. and Barry M. Gumbiner (2004). Distinct molecular forms of β-catenin are targeted to adhesive or transcriptional complexes. *J. Cell Biol.* 167.2, pp. 339–349.

Gould, Nicholas I. M. and Sven Leyffer (2003). An Introduction to Algorithms for Nonlinear Optimization. Springer Berlin Heidelberg, pp. 109–197.

Gregorieff, Alex, Daniel Pinto, Harry Begthel, Olivier Destrée, Menno Kielman, and Hans Clevers (2005). Expression pattern of Wnt signaling components in the adult intestine. *Gastroenterology* 129.2, pp. 626–638.

Ha, Nam-Chul, Takashi Tonozuka, Jennifer L Stamos, Hee-Jung Choi, and William I Weis (2004). Mechanism of phosphorylation-dependent binding of APC to beta-catenin and its role in beta-catenin degradation. *Mol. Cell* 15.4, pp. 511–21.

Haack, Fiete, Heiko Lemcke, Roland Ewald, Tareck Rharass, and Adelinde M Uhrmacher (2015). Spatio-temporal model of endogenous ROS and raft-dependent WNT/beta-catenin signaling driving cell fate commitment in human neural progenitor cells. *PLoS Comput. Biol.* 11.3, e1004106.

Habib, S J, B C Chen, F C Tsai, K Anastassiadis, T Meyer, E Betzig, and R Nusse (2013). A localized Wnt signal orients asymmetric stem cell division in vitro. *Science* 339.6126, pp. 1445–1448.

Hansen, Nikolaus (2006). The CMA evolution strategy: A comparing review. *Studies in Fuzziness and Soft Computing* 192.2006, pp. 75–102.

Hao, Yawei, Alex Chun, Kevin Cheung, Babak Rashidi, and Xiaolong Yang (2008). Tumor suppressor LATS1 is a negative regulator of oncogene YAP. *The Journal of biological chemistry* 283.9, pp. 5496–509.

Hart, M., J-P. Concordet, I. Lassot, I. Albert, R. del los Santos, H. Durand, C. Perret, B. Rubinfeld, F. Margottin, R. Benarous, and P. Polakis (1999). The F-box protein β-TrCP associates with phosphorylated β-catenin and regulates its activity in the cell. *Curr. Biol.* 9.4, pp. 207–211.

Harvey, K F, X Zhang, and D M Thomas (2013). The Hippo pathway and human cancer. *Nat Rev Cancer* 13.4, pp. 246–257.

He, Xi, Mikhail Semenov, Keiko Tamai, and Xin Zeng (2004). LDL receptor-related proteins 5 and 6 in Wnt/beta-catenin signaling: arrows point the way. *Development* 131.8, pp. 1663–77.

Hendriksen, Jolita, Marnix Jansen, Carolyn M Brown, Hella van der Velde, Marco van Ham, Niels Galjart, G Johan Offerhaus, Francois Fagotto, and Maarten Fornerod (2008). Plasma membrane recruitment of dephosphorylated beta-catenin upon activation of the Wnt pathway. *J. Cell Sci.* 121.Pt 11, pp. 1793–802.

Hernández, Ana R, Allon M Klein, and Marc W Kirschner (2012). Kinetic Responses of β-catenin Specify the Sites of Wnt Control. *Science* 338.6112, pp. 1337–40.

Herzig, M, F Savarese, M Novatchkova, H Semb, and G Christofori (2007). Tumor progression induced by the loss of E-cadherin independent of beta-catenin/Tcf-mediated Wnt signaling. *Oncogene* 26.16, pp. 2290–8.

Hines, Keegan E, Thomas R Middendorf, and Richard W Aldrich (2014). Determination of parameter identifiability in nonlinear biophysical models: A Bayesian approach. *J. Gen. Physiol* 143.3, pp. 401–16.

Ho, Hao H. and Lionel B. Ivashkiv (2006). Role of STAT3 in type I interferon responses: Negative regulation of STAT1-dependent inflammatory gene activation. *J. Biol. Chem.* 281.20, pp. 14111–14118.

Huang, Shih-Min A, Yuji M Mishina, Shanming Liu, Atwood Cheung, Frank Stegmeier, Gregory A Michaud, Olga Charlat, Elizabeth Wiellette, Yue Zhang, Stephanie Wiessner, Marc Hild, Xiaoying Shi, Christopher J Wilson, Craig Mickanin, Vic Myer, Aleem Fazal, Ronald Tomlinson, Fabrizio Serluca, Wenlin Shao, Hong Cheng, Michael Shultz, Christina Rau, Markus Schirle, Judith Schlegl, Sonja Ghidelli, Stephen Fawell, Chris Lu, Daniel Curtis, Marc W Kirschner, Christoph Lengauer, Peter M Finan, John A Tallarico, Tewis Bouwmeester, Jeffery A Porter, Andreas Bauer, and Feng Cong (2009). Tankyrase inhibition stabilizes axin and antagonizes Wnt signalling. *Nature* 461.7264, pp. 614–20.

Huber, Andrew H. and William I. Weis (2001). The Structure of the β-Catenin/E-Cadherin Complex and the Molecular Basis of Diverse Ligand Recognition by β-Catenin. *Cell* 105.3, pp. 391–402.

Huels, David J, Rachel A Ridgway, Sorina Radulescu, Marc Leushacke, Andrew D Campbell, Sujata Biswas, Simon Leedham, Stefano Serra, Runjan Chetty, Guenievre Moreaux, Lee Parry, James Matthews, Fei Song, Ann Hedley, Gabriela Kalna, Fatih Ceteci, Karen R Reed, Valerie S Meniel, Aoife Maguire, Brendan Doyle, Ola Söderberg, Nick Barker, Alastair Watson, Lionel Larue, Alan R Clarke, and Owen J Sansom (2015). E-cadherin can limit the transforming properties of activating β-catenin mutations. *EMBO J.* e201591739.

Imajo, Masamichi, Miki Ebisuya, and Eisuke Nishida (2014). Dual role of YAP and TAZ in renewal of the intestinal epithelium. *Nat. Cell Biol.* 17.1.

Itasaki, N. (2003). Wise, a context-dependent activator and inhibitor of Wnt signalling. *Development* 130.18, pp. 4295–4305.

Janda, Claudia Y., Deepa Waghray, Aron M. Levin, Christoph Thomas, and K. Christopher Garcia (2012). Structural Basis of Wnt Recognition by Frizzled. *Science* 337.6090.

Janson, Natalia B. (2012). Non-linear dynamics of biological systems. *Contemporary Physics* 53.2, pp. 137–168.

Jho, Eek-hoon, Stavros Lomvardas, and Frank Costantini (1999). A GSK3β Phosphorylation Site in Axin Modulates Interaction with β-Catenin and Tcf-Mediated Gene Expression. *Biochem. Biophys. Res. Commun.* 266.1, pp. 28–35.

Jho, Eek-hoon, Tong Zhang, Claire Domon, Choun-Ki Joo, Jean-Noel Freund, and Frank Costantini (2002). Wnt/beta-catenin/Tcf signaling induces the transcription of Axin2, a negative regulator of the signaling pathway. *Mol. Cell. Biol.* 22.4, pp. 1172–83.

Jones, Eric, Travis Oliphant, and Pearu Peterson (2001). {SciPy}: Open source scientific tools for {Python}.

Kaiser, Jocelyn (2017). Rigorous replication effort succeeds for just two of five cancer papers. *Science*.

Kass, Robert and Adrian Raftery (1995). Bayes Factors. *J. Amer. Statist. Assoc.* 90.430, pp. 773–795.

Kay, Sophie K., Heather A. Harrington, Sarah Shepherd, Keith Brennan, Trevor Dale, James M. Osborne, David J. Gavaghan, and Helen M. Byrne (2017). The role of the Hes1 crosstalk hub in Notch-Wnt interactions of the intestinal crypt. *PLoS Comput. Biol.* 13.2.

Khan, Zahid, Sapna Vijayakumar, Teresa Villanueva de la Torre, Sabrina Rotolo, and Anna Bafico (2007). Analysis of endogenous LRP6 function reveals a novel feedback mechanism by which Wnt negatively regulates its receptor. *Mol. Cell. Biol.* 27.20, pp. 7291–7301.

Kim, S.-E., H. Huang, M. Zhao, X. Zhang, A. Zhang, M. V. Semonov, B. T. MacDonald, X. Zhang, J. G. Abreu, L. Peng, and X. He (2013). Wnt Stabilization of β-Catenin Reveals Principles for Morphogen Receptor-Scaffold Assemblies. *Science* 340.6134, pp. 867–870.

Kimelman, D and W Xu (2006). β-Catenin destruction complex: insights and questions from a structural perspective. *Oncogene* 25.57, pp. 7482–7491.

Kirk, Paul, Thomas Thorne, and Michael P H Stumpf (2013). Model selection in systems and synthetic biology. *Curr. Opin. Biotechnol.* 24.4, pp. 767–774.

Kishida, S, H Yamamoto, S Hino, S Ikeda, M Kishida, and A Kikuchi (1999). DIX domains of Dvl and axin are necessary for protein interactions and their ability to regulate beta-catenin stability. *Mol. Cell. Biol.* 19.6, pp. 4414–22.

Kogan, Yuri, Karin E. Halevi-tobias, Gili Hochman, Anna K. Baczmanska, Luc Leyns, and Zvia Agur (2012). A new validated mathematical model of the Wnt signalling pathway predicts effective combinational therapy by sFRP and Dkk. *Biochem. J.* 444, pp. 115–125.

Krstic, Jelena, Marietta Herrmann, Ivana Gadjanski, and Slavko Mojsilovic (2017). Editorial: Microenvironment-Derived Stem Cell Plasticity. *Front. Cell Dev. Biol.* 5, p. 82.

Lee, Ethan, Adrian Salic, Roland Krüger, Reinhart Heinrich, and Marc W Kirschner (2003). The roles of APC and Axin derived from experimental and theoretical analysis of the Wnt pathway. *PLoS Biol.* 1.1, E10.

Leeuwen, Ingeborg M M van, Helen M Byrne, Oliver E Jensen, and John R King (2007). Elucidating the interactions between the adhesive and transcriptional functions of beta-catenin in normal and cancerous cells. *J. Theor. Biol.* 247.1, pp. 77–102.

Leung, Janet Y, Frank T Kolligs, Rong Wu, Yali Zhai, Rork Kuick, Samir Hanash, Kathleen R Cho, and Eric R Fearon (2002). Activation of AXIN2 expression by beta-catenin-T cell factor. A feedback repressor pathway regulating Wnt signaling. *J. Biol. Chem.* 277.24, pp. 21657–65.

Li, Q., Tomo-O Ishikawa, Masanobu Oshima, and Makoto M Taketo (2005a). The Threshold Level of Adenomatous Polyposis Coli Protein for Mouse Intestinal Tumorigenesis. *Cancer Res.* 65.19, pp. 8622–8627.

Li, Vivian S W, Ser Sue Ng, Paul J. Boersema, Teck Y. Low, Wouter R. Karthaus, Jan P. Gerlach, Shabaz Mohammed, Albert J R Heck, Madelon M. Maurice, Tokameh Mahmoudi, and Hans Clevers (2012). Wnt Signaling through Inhibition of β-Catenin Degradation in an Intact Axin1 Complex. *Cell* 149.6, pp. 1245–1256.

Li, Xiaofeng, Yazhou Zhang, Heeseog Kang, Wenzhong Liu, Peng Liu, Jianghong Zhang, Stephen E Harris, and Dianqing Wu (2005b). Sclerostin binds to LRP5/6 and antagonizes canonical Wnt signaling. *J. Biol. Chem.* 280.20, pp. 19883–7.

Liepe, Juliane, Chris Barnes, Erika Cule, Kamil Erguler, Paul Kirk, Tina Toni, and Michael P H Stumpf (2010). ABC-SysBio–approximate Bayesian computation in Python with GPU support. *Bioinformatics* 26.14, pp. 1797–9.

Liu, Chunming, Yiming Li, Mikhail Semenov, Chun Han, Gyeong-Hun Baeg, Yi Tan, Zhuohua Zhang, Xinhua Lin, and Xi He (2002). Control of β-Catenin Phosphorylation/Degradation by a Dual-Kinase Mechanism. *Cell* 108.6, pp. 837–847.

Liu, Jun, Jeffery Stevens, Cynthia a. Rote, H. Joseph Yost, Yaoxiong Hu, Kristi L. Neufeld, Raymond L. White, and Nori Matsunami (2001). Siah-1 mediates a novel beta-catenin degradation pathway linking p53 to the adenomatous polyposis coli protein. *Mol. Cell* 7.5, pp. 927–936.

Lloyd-Lewis, Bethan, Alexander G Fletcher, Trevor C Dale, and Helen M Byrne (2013). Toward a quantitative understanding of the Wnt/β-catenin pathway through simulation and experiment. *WIRES Syst. Biol. Med.* 5.4, pp. 391–407.

Lopez, C. F., J. L. Muhlich, J. A. Bachman, and P. K. Sorger (2014). Programming biological models in Python using PySB. *Molecular Systems Biology* 9.1, pp. 646–646.

Luo, Wen, Annita Peterson, Benjamin A Garcia, Gary Coombs, Bente Kofahl, Reinhart Heinrich, Jeffrey Shabanowitz, Donald F Hunt, H Joseph Yost, and David M Virshup (2007). Protein phosphatase 1 regulates assembly and function of the beta-catenin degradation complex. *EMBO J.* 26.6, pp. 1511–21.

MacDonald, Bryan T and Xi He (2012). Frizzled and LRP5/6 receptors for Wnt/β-catenin signaling. *CSH Perspect. Biol.* 4.12.

MacDonald, Bryan T, Chika Yokota, Keiko Tamai, Xin Zeng, and Xi He (2008). Wnt signal amplification via activity, cooperativity, and regulation of multiple intracellular PPPSP motifs in the Wnt co-receptor LRP6. *J. Biol. Chem.* 283.23, pp. 16115–23.

MacLean, Adam L., Heather A. Harrington, Michael P. H. Stumpf, and Helen M. Byrne (2015a). Mathematical and Statistical Techniques for Systems Medicine: The Wnt Signaling Pathway as a Case Study. *Systems Medicine*. Springer.

MacLean, Adam L., Zvi Rosen, Helen M. Byrne, and Heather A. Harrington (2015b). Parameter-free methods distinguish Wnt pathway models and guide design of experiments. *Proc. Natl. Acad. Sci. U.S.A.* 112.9, p. 201416655.

Mah, Amanda T., Kelley S. Yan, and Calvin J. Kuo (2016). Wnt pathway regulation of intestinal stem cells. *J. Physiol.* 594.17, pp. 4837–4847.

Maretzky, Thorsten, Karina Reiss, Andreas Ludwig, Julian Buchholz, Felix Scholz, Erhardt Proksch, Bart de Strooper, Dieter Hartmann, and Paul Saftig (2005). ADAM10 mediates E-cadherin shedding and regulates epithelial cell-cell adhesion, migration, and beta-catenin translocation. *Proc. Natl. Acad. Sci. U.S.A.* 102.26, pp. 9182–7.

Marjoram, Paul, John Molitor, Vincent Plagnol, and Simon Tavare (2003). Markov chain Monte Carlo without likelihoods. *Proc. Natl. Acad. Sci. U.S.A.* 100.26, pp. 15324–8.

Matallanas, David, David Romano, Karen Yee, Katrin Meissl, Lucia Kucerova, Daniela Piazzolla, Manuela Baccarini, J. Keith Vass, Walter Kolch, and Eric O'Neill (2007). RASSF1A Elicits Apoptosis through an MST2 Pathway Directing Proapoptotic Transcription by the p73 Tumor Suppressor Protein. *Mol. Cell* 27.6, pp. 962–975.

Mazemondet, Orianne, Mathias John, Stefan Leye, Arndt Rolfs, and Adelinde M Uhrmacher (2012). Elucidating the sources of β-catenin dynamics in human neural progenitor cells. *PLoS One* 7.8.

McCartney, Brooke M and Inke S Näthke (2008). Cell regulation by the Apc protein Apc as master regulator of epithelia. *Curr. Opin. Cell Biol.* 20.2, pp. 186–93.

Metcalfe, C. and M. Bienz (2011). Inhibition of GSK3 by Wnt signalling - two contrasting models. *J. Cell Sci.* 124.21, pp. 3537–3544.

Mikels, A. J. and R Nusse (2006a). Wnts as ligands: processing, secretion and reception. *Oncogene* 25.57, pp. 7461–7468.

Mikels, Amanda J and Roel Nusse (2006b). Purified Wnt5a protein activates or inhibits beta-catenin-TCF signaling depending on receptor context. *PLoS Biol.* 4.4, e115.

Miller, Mayumi F, Ethan David Cohen, Julie E Baggs, Min Min Lu, John B Hogenesch, and Edward E Morrisey (2012). Wnt ligands signal in a cooperative manner to promote foregut organogenesis. *Proc. Natl. Acad. Sci. U.S.A.* 109.38, pp. 15348–53.

Mirams, Gary R (2008). Subcellular Phenomena in Colorectal Cancer. Thesis submitted to The University of Nottingham for the degree of Doctor of Philosophy.

Molnar, Cristina, Martin Resnik-Docampo, Maria F., Mercedes Martin, Covadonga F., and Jose F. de Celis (2011). Signalling Pathways in Development and Human Disease: A Drosophila Wing Perspective. *Human Genetic Diseases*. InTech.

Morin, P. J., A B Sparks, V Korinek, N Barker, H Clevers, B Vogelstein, and K W Kinzler (1997). Activation of β-Catenin–Tcf Signaling in Colon Cancer by Mutations in β-Catenin or APC. *Science* 275.5307, pp. 1787–1790.

Neyman, J. and E. S. Pearson (1933). On the Problem of the Most Efficient Tests of Statistical Hypotheses. *Philosophical Transactions of the Royal Society A: Mathematical, Physical and Engineering Sciences* 231.694-706, pp. 289–337.

Niehrs, Christof (2012). The complex world of WNT receptor signalling. *Nat. Rev. Mol. Cell Biol.* 13.12, pp. 767–79.

Niehrs, Christof and Jinlong Shen (2010). Regulation of Lrp6 phosphorylation. *Cell. Mol. Life Sci.* 67.15, pp. 2551–2562.

Northrup, S H and H P Erickson (1992). Kinetics of protein-protein association explained by Brownian dynamics computer simulation. *Proc. Natl. Acad. Sci. U.S.A.* 89.April, pp. 3338–3342.

Nusslein-Volhard, C., E. Wieschaus, and H. Kluding (1984). Mutations affecting the pattern of the larval cuticle in Drosophila melanogaster. *Wilhelm Roux's Archives of Developmental Biology* 193.5, pp. 267–282.

Ozawa, M, H Baribault, and R Kemler (1989). The cytoplasmic domain of the cell adhesion molecule uvomorulin associates with three independent proteins structurally related in different species. *EMBO J.* 8.6, pp. 1711–7.

Pargett, Michael and David M Umulis (2013). Quantitative model analysis with diverse biological data: applications in developmental pattern formation. *Methods* 62.1, pp. 56–67.

Pefani, Dafni E. and Eric O'Neill (2016). Hippo pathway and protection of genome stability in response to DNA damage. *The FEBS Journal* 283.8, pp. 1392–1403.

Piao, Shunfu, Sun-Hye Lee, Hyunjoon Kim, Soohwan Yum, Jennifer L. Stamos, Yongbin Xu, Su-Jin Lee, Jaewon Lee, Sangtaek Oh, Jin-Kwan Han, Bum-Joon Park, William I. Weis, and Nam-Chul Ha (2008). Direct Inhibition of GSK3β by the Phosphorylated Cytoplasmic Domain of LRP6 in Wnt/β-Catenin Signaling. *PLoS One* 3.12, e4046.

Piccolo, Stefano, Sirio Dupont, and Michelangelo Cordenonsi (2014). The Biology of YAP/TAZ: Hippo Signaling and Beyond. *Physiological reviews* 94.4, pp. 1287–1312.

Pritchard, J K, M T Seielstad, A Perez-Lezaun, and M W Feldman (1999). Population growth of human Y chromosomes: a study of Y chromosome microsatellites. *Mol. Biol. Evol.* 16.12, pp. 1791–1798.

Pronobis, Mira I, Natalie Deuitch, Vinya Posham, Yuko Mimori-Kiyosue, and Mark Peifer (2017). Reconstituting regulation of the canonical Wnt pathway by engineering a minimal β-catenin destruction machine. *Mol. Biol. Cell* 28.1, pp. 41–53.

Radtke, Freddy and Hans Clevers (2005). Self-renewal and cancer of the gut: two sides of a coin. *Science* 307.5717, pp. 1904–9.

Raue, Andreas, C. Kreutz, T. Maiwald, J. Bachmann, M. Schilling, U. Klingmüller, and J. Timmer (2009). Structural and practical identifiability analysis of partially observed dynamical models by exploiting the profile likelihood. *Bioinformatics* 25.15, pp. 1923–1929.

Raue, Andreas, Marcel Schilling, Julie Bachmann, Andrew Matteson, Max Schelke, Daniel Kaschek, Sabine Hug, Clemens Kreutz, Brian D. Harms, Fabian J. Theis, Ursula Klingmüller, and Jens Timmer (2013). Lessons Learned from Quantitative Dynamical Modeling in Systems Biology. *PLoS One* 8.9.

Reya, Tannishtha and Hans Clevers (2005). Wnt signalling in stem cells and cancer. *Nature* 434.7035, pp. 843–50.

Roberts, David M, Mira I Pronobis, John S Poulton, Eric G Kane, and Mark Peifer (2012). Regulation of Wnt signaling by the tumor suppressor adenomatous polyposis coli does not require the ability to enter the nucleus or a particular cytoplasmic localization. *Mol. Biol. Cell* 23.11, pp. 2041–56.

Rose, Z. B. and S. Dube (1976). Rates of phosphorylation and dephosphorylation of phosphoglycerate mutase and bisphosphoglycerate synthase. *J. Biol. Chem.* 251.16, pp. 4817–4822.

Rosenbluh, Joseph, Deepak Nijhawan, Andrew G Cox, Xingnan Li, James T Neal, Eric J Schafer, Travis I Zack, Xiaoxing Wang, Aviad Tsherniak, Anna C Schinzel, Diane D Shao, Steven E Schumacher, Barbara A Weir, Francisca Vazquez, Glenn S Cowley, David E Root, Jill P Mesirov, Rameen Beroukhim, Calvin J Kuo, Wolfram Goessling, and William C Hahn (2012). β-Catenin-driven cancers require YAP1 transcriptional complex for survival and tumorigenesis. *Cell* 151.7, pp. 1457–73.

Sato, Toshiro, Robert G. Vries, Hugo J. Snippert, Marc van de Wetering, Nick Barker, Daniel E. Stange, Johan H. van Es, Arie Abo, Pekka Kujala, Peter J. Peters, and Hans Clevers (2009). Single Lgr5 stem cells build crypt–villus structures in vitro without a mesenchymal niche. *Nature* 459.7244, pp. 262–265.

Schmitz, Yvonne, Katja Rateitschak, and Olaf Wolkenhauer (2013). Analysing the impact of nucleo-cytoplasmic shuttling of β-catenin and its antagonists APC, Axin and GSK3 on Wnt/β-catenin signalling. *Cellular signalling* 25.11, pp. 2210–21.

Schwarz-Romond, Thomas, Christien Merrifield, Benjamin J. Nichols, and Mariann Bienz (2005). The Wnt signalling effector Dishevelled forms dynamic protein assemblies rather than stable associations with cytoplasmic vesicles. *J. Cell Sci.* 118.22.

Schweizer, Liang and Harold Varmus (2003). Wnt/Wingless signaling through beta-catenin requires the function of both LRP/Arrow and frizzled classes of receptors. *BMC Cell Biol.* 4.1, p. 4.

Semënov, Mikhail, Keiko Tamai, and Xi He (2005). SOST is a ligand for LRP5/LRP6 and a Wnt signaling inhibitor. *J. Biol. Chem.* 280.29, pp. 26770–26775.

Shin, Sung-Young, Oliver Rath, Armin Zebisch, Sang-Mok Choo, Walter Kolch, and Kwang-Hyun Cho (2010). Functional roles of multiple feedback loops in extracellular signal-regulated kinase and Wnt signaling pathways that regulate epithelial-mesenchymal transition. *Cancer Res.* 70.17, pp. 6715–6724.

Shudo, Emi, Jin Yang, Akihiko Yoshimura, and Yoh Iwasa (2007). Robustness of the signal transduction system of the mammalian JAK/STAT pathway and dimerization steps. *J. Theor. Biol.* 246.1, pp. 1–9.

Sisson, S. A., Y. Fan, Mark M. Tanaka, Mark D. McDonnell, Bruno Goncalves, and Jaroslaw Dziadek (2007). Sequential Monte Carlo without likelihoods. *Proc. Natl. Acad. Sci. U.S.A.* 104.6, pp. 1760–1765.

Skilling, John and John (2004). Nested Sampling. *AIP Conf. Proc.* 735, pp. 395–405.

Song, Je Hoon, David J. Huels, Rachel a. Ridgway, Owen J. Sansom, Boris N. Kholodenko, Walter Kolch, and Kwang Hyun Cho (2014). The APC network regulates the removal of mutated cells from colonic crypts. *Cell Rep.* 7.1, pp. 94–103.

Song, Li, Zhuo-yu Li, Wei-ping Liu, Mei-rong Zhao, Li Song, Zhuo-yu Li, Wei-ping Liu, and Mei-rong Zhao (2015). Gli signaling pathways in colon cancer and implications for therapy Crosstalk between Wnt / b -catenin and Hedgehog / Gli signaling pathways in colon cancer and implications for therapy. 4047.December.

Stamos, Jennifer L and William I Weis (2013). The β-catenin destruction complex. *CSH Perspect. Biol.* 5.1, a007898.

Stelling, Jörg, Uwe Sauer, Zoltan Szallasi, Francis J Doyle, John Doyle, R.Y. Pinter, U. Alon, H. Margalit, I. Simon, J. Zeitlinger, and et Al. (2004). Robustness of cellular functions. *Cell* 118.6, pp. 675–85.

Stockinger, Andreas, Andreas Eger, Julia Wolf, Hartmut Beug, and Roland Foisner (2001). E-cadherin regulates cell growth by modulating proliferation-dependent beta-catenin transcriptional activity. *J. Cell Biol.* 154.6, pp. 1185–1196.

Strovel, E T, D Wu, and D J Sussman (2000). Protein phosphatase 2Calpha dephosphorylates axin and activates LEF-1-dependent transcription. *J. Biol. Chem.* 275.4, pp. 2399–403.

Su, YunYun, Chunjiang Fu, Shinji Ishikawa, Alessandra Stella, Masayuki Kojima, Kazuhisa Shitoh, Emanuel M. Schreiber, Billy W. Day, and Bo Liu (2008). APC is essential for targeting phosphorylated beta-catenin to the SCFbeta-TrCP ubiquitin ligase. *Mol. Cell* 32.5, pp. 652–61.

Sun, Meng, Fabian Spill, and Muhammad H. Zaman (2016). A Computational Model of YAP/TAZ Mechanosensing. *Biophys. J.* 110.11, pp. 2540–2550.

Swat, Maciej, Alexander Kel, and Hanspeter Herzel (2004). Bifurcation analysis of the regulatory modules of the mammalian G1/S transition. *Bioinformatics* 20.10, pp. 1506–11.

Taelman, Vincent F., Radoslaw Dobrowolski, Jean-Louis Plouhinec, Luis C. Fuentealba, Peggy P. Vorwald, Iwona Gumper, David D. Sabatini, and Edward M. De Robertis (2010). Wnt Signaling Requires Sequestration of Glycogen Synthase Kinase 3 inside Multivesicular Endosomes. *Cell* 143.7, pp. 1136–1148.

Takebe, Naoko, Pamela J Harris, Ronald Q Warren, and S Percy Ivy (2011). Targeting cancer stem cells by inhibiting Wnt, Notch, and Hedgehog pathways. *Nat. Rev. Clin. Oncol.* 8.2, pp. 97–106.

Tamai, Keiko, Xin Zeng, Chunming Liu, Xinjun Zhang, Yuko Harada, Zhijie Chang, and Xi He (2004). A Mechanism for Wnt Coreceptor Activation. *Mol. Cell* 13.1, pp. 149–156.

Tan, Chin Wee, Bruce S Gardiner, Yumiko Hirokawa, Meredith J Layton, David W Smith, and Antony W Burgess (2012). Wnt signalling pathway parameters for mammalian cells. *PLoS One* 7.2, e31882.

Taylor, Sean C., Thomas Berkelman, Geetha Yadav, and Matt Hammond (2013). A defined methodology for reliable quantification of western blot data. *Mol. Biotechnol.* 55.3, pp. 217–226.

Tetsu, O and F McCormick (1999). Beta-catenin regulates expression of cyclin D1 in colon carcinoma cells. *Nature* 398.6726, pp. 422–6.

Toni, Tina, David Welch, Natalja Strelkowa, Andreas Ipsen, Michael P H M.P.H Stumpf, Tina Toni, David Welch, Natalja Strelkowa, and Andreas Ipsen (2009). Approximate Bayesian computation scheme for parameter inference and model selection in dynamical systems. *Interface* 6.31, pp. 187–202.

Tyson, John J., Katherine C. Chen, and Bela Novak (2003). Sniffers, buzzers, toggles and blinkers: Dynamics of regulatory and signaling pathways in the cell. *Curr. Opin. Cell Biol.* 15, pp. 221–231.

Tyson, John J and Béla Novák (2010). Functional motifs in biochemical reaction networks. *Annu. Rev. Phys. Chem.* 61.1, pp. 219–40.

Valenta, Tomas, Bahar Degirmenci, Andreas E. Moor, Patrick Herr, Dario Zimmerli, Matthias B. Moor, George Hausmann, Claudio Cantù, Michel Aguet, and Konrad Basler (2016). Wnt Ligands Secreted by Subepithelial Mesenchymal Cells Are Essential for the Survival of Intestinal Stem Cells and Gut Homeostasis. *Cell Reports* 15.5, pp. 911–918.

Valenta, Tomas, George Hausmann, and Konrad Basler (2012). The many faces and functions of β-catenin. *EMBO J.* 31.12, pp. 2714–36.

Valvezan, Alexander J., Fang Zhang, J. Alan Diehl, and Peter S. Klein (2012). Adenomatous Polyposis Coli (APC) regulates multiple signaling pathways by enhancing glycogen synthase kinase-3 (GSK-3) activity. *J. Biol. Chem.* 287.6, pp. 3823–3832.

Veelen, Wendy van, Ngoc H Le, Werner Helvensteijn, Lau Blonden, Myrte Theeuwes, Elvira R M Bakker, Patrick F Franken, Léon van Gurp, Frits Meijlink, Martin A van der Valk, Ernst J Kuipers, Riccardo Fodde, and Ron Smits (2011). β-catenin tyrosine 654 phosphorylation increases Wnt signalling and intestinal tumorigenesis. *Gut* 60.9, pp. 1204–12.

Vermeulen, Louis, Felipe De Sousa E Melo, Maartje van der Heijden, Kate Cameron, Joan H de Jong, Tijana Borovski, Jurriaan B Tuynman, Matilde Todaro, Christian Merz, Hans Rodermond, Martin R Sprick, Kristel Kemper, Dick J Richel, Giorgio Stassi, and Jan Paul Medema (2010). Wnt activity defines colon cancer stem cells and is regulated by the microenvironment. *Nat. Cell Biol.* 12.5, pp. 468–76.

Vert, Grégory and Joanne Chory (2011). Crosstalk in cellular signaling: background noise or the real thing? *Dev. Cell* 21.6, pp. 985–91.

Vyshemirsky, Vladislav and Mark A. Girolami (2008). Bayesian ranking of biochemical system models. *Bioinformatics* 24.6, pp. 833–839.

Wang, Lili, Xiaoyong Liu, Ekaterina Gusev, Chuanxin Wang, and François Fagotto (2014). Regulation of the phosphorylation and nuclear import and export of β-catenin by APC and its cancer-related truncated form. *J. Cell Sci.* 127.Pt 8, pp. 1647–59.

Wang, Yanshu, Hao Chang, Amir Rattner, and Jeremy Nathans (2016). Frizzled Receptors in Development and Disease. *Curr. Top. Dev. Biol.* 117, pp. 113–39.

Wei, Qiou, Chika Yokota, Mikhail V. Semenov, Brad Doble, Jim Woodgett, and Xi He (2007). R-spondin1 is a high affinity ligand for LRP6 and induces LRP6 phosphorylation and β-catenin signaling. *J. Biol. Chem.* 282.21, pp. 15903–15911.

Wilkinson, Darren J. (2007). Bayesian methods in bioinformatics and computational systems biology. *Brief. Bioinform.* 8.2, pp. 109–116.

Willert, K, S Shibamoto, and R Nusse (1999). Wnt-induced dephosphorylation of axin releases beta-catenin from the axin complex. *Genes Dev.* 13.14, pp. 1768–73.

Willert, Karl, Marcel Brink, Andreas Wodarz, Harold Varmus, and Roel Nusse (1997). Casein kinase 2 associates with and phosphorylates dishevelled. *EMBO J.* 16.11, pp. 3089–3096.

Wolf, Joshua, Todd R Palmby, Julie Gavard, Bart O Williams, and J Silvio Gutkind (2008). Multiple PPPS/TP motifs act in a combinatorial fashion to transduce Wnt signaling through LRP6. *FEBS Lett.* 582.2, pp. 255–61.

Wu, Geng and Xi He (2006). Threonine 41 in β-Catenin Serves as a Key Phosphorylation Relay Residue in β-Catenin Degradation. *Biochemistry* 45.16, pp. 5319–5323.

Wu, Geng, He Huang, Jose Garcia Abreu, and Xi He (2009). Inhibition of GSK3 Phosphorylation of β-Catenin via Phosphorylated PPPSPXS Motifs of Wnt Coreceptor LRP6. *PLoS One* 4.3, e4926.

Wu, Ximei, Xiaolin Tu, Kyu Sang Joeng, Matthew J. Hilton, David A. Williams, and Fanxin Long (2008). Rac1 Activation Controls Nuclear Localization of β-catenin during Canonical Wnt Signaling. *Cell* 133.2, pp. 340–353.

Yamamoto, H, S Kishida, M Kishida, S Ikeda, S Takada, and A Kikuchi (1999). Phosphorylation of axin, a Wnt signal negative regulator, by glycogen synthase kinase-3beta regulates its stability. *J. Biol. Chem.* 274.16, pp. 10681–4.

Yamamoto, Hideki, Hideyuki Komekado, and Akira Kikuchi (2006). Caveolin Is Necessary for Wnt-3a-Dependent Internalization of LRP6 and Accumulation of β-Catenin. *Dev. Cell* 11.2, pp. 213–223.

Yamamoto, Hideki, Hiroshi Sakane, Hideki Yamamoto, Tatsuo Michiue, and Akira Kikuchi (2008). Wnt3a and Dkk1 Regulate Distinct Internalization Pathways of LRP6 to Tune the Activation of β-Catenin Signaling. *Dev. Cell* 15.1, pp. 37–48.

Ye, Xin, Yanshu Wang, Amir Rattner, and Jeremy Nathans (2011). Genetic mosaic analysis reveals a major role for frizzled 4 and frizzled 8 in controlling ureteric growth in the developing kidney. *Development* 138.6.

Yost, C, M Torres, J R Miller, E Huang, D Kimelman, and R T Moon (1996). The axis-inducing activity, stability, and subcellular distribution of beta-catenin is regulated in Xenopus embryos by glycogen synthase kinase 3. *Genes Dev.* 10.12, pp. 1443–54.

Yu, Huimin, Xin Ye, Nini Guo, and Jeremy Nathans (2012). Frizzled 2 and frizzled 7 function redundantly in convergent extension and closure of the ventricular septum and palate: evidence for a network of interacting genes. *Development* 139.23, pp. 4383–94.

Zeng, Xin, He Huang, Keiko Tamai, Xinjun Zhang, Yuko Harada, Chika Yokota, Karla Almeida, Jianbo Wang, Brad Doble, Jim Woodgett, Anthony Wynshaw-Boris, Jen-Chieh Hsieh, and Xi He (2008). Initiation of Wnt signaling: control of Wnt coreceptor Lrp6 phosphorylation/activation via frizzled, dishevelled and axin functions. *Development* 135.2, pp. 367–75.

Zeng, Xin, Keiko Tamai, Brad Doble, Shitao Li, He Huang, Raymond Habas, Heidi Okamura, Jim Woodgett, and Xi He (2005). A dual-kinase mechanism for Wnt co-receptor phosphorylation and activation. *Nature* 438.7069, pp. 873–7.

Zhan, T, N Rindtorff, and M Boutros (2017). Wnt signaling in cancer. *Oncogene* 36.11, pp. 1461–1473.

Zhao, Bin, Xiaomu Wei, Weiquan Li, Ryan S Udan, Qian Yang, Joungmok Kim, Joe Xie, Tsuneo Ikenoue, Jindan Yu, Li Li, Pan Zheng, Keqiang Ye, Arul Chinnaiyan, Georg Halder, Zhi-Chun Lai, and Kun-Liang Guan (2007). Inactivation of YAP oncoprotein by the Hippo pathway is involved in cell contact inhibition and tissue growth control. *Genes & development* 21.21, pp. 2747–61.